Experimental weathering of Aboriginal rock art from the Murujuga Peninsula, Western Australia

Do emissions from the local industry have an impact on the rock art weathering rate?

Dissertation

zur

Erlangung des Doktorgrades (Dr. rer. nat.)

der

Mathematisch-Naturwissenschaftlichen Fakultät

der

Rheinischen Friedrich-Wilhelms-Universität Bonn

vorgelegt von

Jolam Tjako Neumann

aus

Alfter

Bonn, Februar 2025

Angefertigt mit Genehmigung der Mathematisch-Naturwissenschaftlichen Fakultät
der Rheinischen Friedrich-Wilhelms-Universität Bonn

Gutachter/Betreuer: Prof. Dr. Thorsten Geisler-Wierwille

Gutacher: PD Dr. Martin Kilo

Tag der Promotion: 16.05.2025

Erscheinungsjahr: 2025

Abstract

One of the most important cultural heritage sites in Australia is located on the Murujuga peninsula on the northern coast of Western Australia. On the peninsula and the surrounding islands over one million petroglyphs, carved into rock surfaces across the area, can be found. These petroglyphs depict animals, plants, and even human figures, some of which are believed to be up to 30,000 years old. They are visible due to the colour contrast between the thin removed surface layer, called rock varnish, and the underlying brighter weathered rind of the host rocks. This collection of rock art remains of great cultural and spiritual importance to the local Aboriginal community and might become an UNESCO World Heritage Site in the near future, as the federal government nominated the petroglyphs on Murujuga for heritage status in 2023.

As with many other cultural heritage sites worldwide that are endangered due to anthropogenic impacts such as climate change and environmental pollution, concerns about a potential threat to the Murujuga petroglyphs have arisen decades ago. Continuous industrial development on the peninsula led to increasing emissions of industrial pollutants, particularly NO_x and SO_x. As these pollutants cause lower pH levels in the local rainwater, and therefore on the rock surfaces, it is crucial to determine how and if these pH changes accelerate the degradation of petroglyphs on the peninsula compared to natural weathering rates.

To date, there is no scientific consensus on whether the increase in pollutant emissions on Murujuga negatively impacts the conservation of the petroglyphs, despite various studies that were published on this topic and some monitoring programmes that were carried out on Murujuga over the past years. Therefore, in this work, two different experiments were conducted to gain new insights and potentially answer the question if industrial emissions on Murujuga accelerate the weathering rate of the rock varnish.

The mineralogical and chemical composition of the rock varnish was determined by Raman spectroscopy, X-ray diffraction, and chemical electron microprobe analyses, revealing that the varnish mainly consists of birnessite, hematite, and kaolinite, along with minor components such as todorokite, quartz, anatase, rutile, and carbonaceous matter. It was shown that different types of varnish found on Murujuga can be differentiated by colour, with black varnish being the type with the highest Mn content. This type of varnish was also found to have a fine layering, primarily in its outermost parts. A comparison with an older varnish sample from 1994, which has been less affected by industrial pollution, indicated that the rock varnish on Murujuga

might already be depleted in Mn. This was supported by specially designed irrigation experiments using artificial rainwaters with different pH levels, which revealed a significantly larger increase of the dissolution rate for Mn-oxides than for hematite (the main Fe-phase in the varnish) below a pH of 5.

These irrigation experiments allowed the examination of the pH dependence of the dissolution rates of the main components of the varnish by analysing the element concentrations in artificial rainwater samples that had been in contact with rock varnish samples. It was shown that the dissolution rates of Mn-oxide-phases increased significantly at pH < 5, a pH level regularly observed on Murujuga to date. The dissolution rates of Mn-oxides were significantly higher than those of kaolinite, whose dissolution rates also increased at pH < 5. Hematite was found to be the most stable main component of the varnish, with dissolution rates increasing only at pH < 4 and overall low dissolution rates. The observed Mn release, normalised to the Mn content on the surface, was at least 100 times higher than the normalised Fe release.

As the main part of this study, an accelerated, semi-actualistic long-term weathering experiment was carried out over 12 months, simulating six years of Murujuga-like conditions using two types of artificial rainwater with pH 5 and 7. The varnish-bearing rock samples from Murujuga that were artificially weathered in the experiment were closely monitored using various analytical techniques (p-XRF, colour measurements, μ-CT, high resolution optical imaging) to detect surface changes including the additional extraction of DNA samples to also monitor the development of the microbial community.

It was found that varnish weathering is already accelerated at a pH of 5, even though the dissolution rates observed at pH 5 and pH 7 were within a comparable range. Overall, the changes of the colour, chemical composition, surface properties, and sample weight were greater in the sample groups weathered under slightly acidic conditions (pH 5). The experiment also revealed significant differences between the different types of varnish and their relative vulnerability to weathering effects. The extraction of DNA samples revealed significant differences depending on the pH and rock type.

Additionally, in this long-term experiment, glass dosimeters with different compositions, provided by the Fraunhofer Institute for Silicate Research (ISC), were employed to monitor and quantify the simulated alteration in the chamber. As the alteration behaviour of these dosimeters is well known and they have been used for many decades to monitor cultural heritage sites, their application allows for comparability of the simulated conditions and facilitates the comparison of the simulated alteration with real-world conditions.

Based on the results, it is concluded that the degradation of the rock varnish on petroglyph-bearing rocks from Murujuga is highly likely impacted by local industrial pollution, with weathering rates most likely already accelerated due to the lower pH of the rainwater on Murujuga to date. Furthermore, it is highly probable

that weathering rates will increase further if the pH continues to decrease, as the dissolution rates of the primary phases of the varnish tended to rise at lower pH values. Additionally, new insights into the composition and microstructures of the rock varnish, as well as the microbial communities on the rock varnish were obtained and it is hypothesised that the varnish in Murujuga might already be significantly depleted in Mn-phases due to increased dissolution rates in the past.

Zusammenfassung

Eine der wichtigsten kulturellen Stätten Australiens befindet sich auf der Murujuga-Halbinsel an der Nordküste Westaustraliens. Auf der Halbinsel und den umliegenden Inseln finden sich mehr als eine Million Petroglyphen, die in die Gesteine des Gebietes geritzt wurden. Diese Petroglyphen stellen Tiere, Pflanzen und sogar menschliche Figuren dar und es wird angenommen, dass sie bis zu 30.000 Jahre alt sind. Sie sind aufgrund des Farbkontrasts zwischen der dünnen, abgetragenen Oberflächenschicht, dem so genannten „Rock Varnish“ (dt. Wüstenlack) und der darunter liegenden, helleren, verwitterten Schicht des Wirtsgesteins sichtbar. Diese Sammlung von Felszeichnungen ist nach wie vor von großer kultureller und spiritueller Bedeutung für die örtliche Aborigine-Gemeinschaft und könnte in naher Zukunft zum UNESCO-Weltkulturerbe erklärt werden, da die australische Regierung die Felszeichnungen auf Murujuga im Jahr 2023 für den Status als UNESCO-Weltkulturerbe nominiert hat.

Wie bei vielen anderen kulturellen Stätten weltweit, die aufgrund anthropogener Einflüsse wie Klimawandel und Umweltverschmutzung gefährdet sind, gibt es seit Jahrzehnten Sorgen bezüglich einer möglichen Bedrohung der Petroglyphen auf Murujuga, da die kontinuierliche industrielle Entwicklung auf der Halbinsel zur zunehmenden Emission von Industrieschadstoffen, insbesondere NO_x und SO_x, geführt hat. Da diese Schadstoffe zu einer Senkung des pH-Werts des örtlichen Regenwassers und damit auch auf den Gesteinsoberflächen geführt haben und führen, ist es von entscheidender Bedeutung festzustellen, ob und wie sich diese pH-Veränderungen auf die Gesteinsoberflächen auf der Halbinsel auswirken, in die die Petroglyphen geritzt wurden.

Bis heute gibt es keinen wissenschaftlichen Konsens darüber, ob sich die Zunahme der Schadstoffemissionen auf Murujuga auf den Erhalt der Petroglyphen auswirkt, trotz verschiedener Studien, die zu diesem Thema veröffentlicht wurden, sowie einiger Überwachungsprogramme, die in den letzten Jahren auf Murujuga durchgeführt wurden. In dieser Arbeit wurden daher verschiedene Experimente und Analysen durchgeführt, um neue Erkenntnisse zu gewinnen und, bestenfalls, die Frage zu beantworten, ob industrielle Emissionen auf Murujuga die Verwitterungsrate der Gesteinsoberflächen beeinflussen.

Die mineralogische und chemische Zusammensetzung des „Varnish“ wurde durch Raman-Spektroskopie, Röntgenbeugung und Elektronenstrahlmikrosondenanalysen bestimmt und es konnte gezeigt werden, dass der „Varnish“ hauptsächlich aus Birnessit, Hämatit und Kaolinit besteht, zusätzlich zu kleineren Bestandteilen aus Todorokit, Quarz, Anatas, Rutil und kohlenstoffhaltigen Phasen. Es wurde gezeigt,

dass die verschiedenen „Varnish“-Typen auf Murujuga anhand ihrer Farbe unterschieden werden können, wobei schwarzer „Varnish“ der Typ mit dem höchsten Mn-Gehalt ist. Außerdem wurde festgestellt, dass dieser „Varnish“-Typ vor allem in seinen äußersten Teilen eine feine Lamination aufweist. Ein Vergleich mit einer älteren Probe aus dem Jahr 1994, die weniger von der industriellen Verschmutzung betroffen war, deutet darauf hin, dass die Gesteinsoberflächen auf Murujuga bereits an Mn verarmt sein könnten. Dies wird auch durch die Ergebnisse von speziell konzipierten Beregnungsexperimenten mit künstlichem Regenwasser mit unterschiedlichen pH-Werten gestützt, die einen signifikant höheren Anstieg der Auflösungsraten der Mn-Oxid-Phasen im Vergleich zu Hämatit (der Fe-Hauptphase) unterhalb pH 5 gezeigt haben.

Diese Beregnungsexperimente ermöglichten die Untersuchung der pH-Abhängigkeit der Auflösungsraten der Hauptbestandteile des „Varnish“ durch Analysen der Elementkonzentrationen in den künstlichen Regenwasserproben, die mit den Gesteinsoberflächen in Kontakt waren. Es hat sich gezeigt, dass die Auflösungsraten der Mn-Oxid-Phasen bei einem pH-Wert < 5, einem schon jetzt auf Murujuga regelmäßig beobachteten pH-Wert, deutlich zugenommen haben. Die Auflösungsraten von Mn-Oxiden waren deutlich höher als die von Kaolinit, dessen Auflösungsraten ebenfalls bei einem pH-Wert von < 5 zugenommen haben. Hämatit erwies sich als die stabilste Hauptkomponente des „Varnish“, wobei die Auflösungsraten nur bei einem pH-Wert von < 4 zugenommen haben und die Auflösungsraten insgesamt vergleichsweise niedrig sind. Es wurde festgestellt, dass die Mn-Konzentrationen in den Wasserproben, normiert auf den Mn-Gehalt an der Oberfläche, mindestens 100 Mal höher als die normierten Fe-Konzentrationen waren.

Als Hauptteil dieser Arbeit wurde ein beschleunigtes, semi-aktualistisches Langzeit-Verwitterungsexperiment über 12 Monate durchgeführt, bei dem sechs Jahre Murujuga-ähnlicher Bedingungen mit zwei Arten von künstlichem Regenwasser mit einem pH-Wert von 5 und 7 simuliert wurden. Die Gesteinsproben mit „Varnish“ aus Murujuga, die in dem Experiment künstlich verwittert wurden, wurden mit verschiedenen Analysetechniken (p-XRF, Farbmessungen, µ-CT, hochauflösende Bilder) genau überwacht, um Oberflächenveränderungen festzustellen. Zusätzlich wurden DNA-Proben genommen, um auch die Entwicklung der mikrobiellen Population zu überwachen. Es wurde nachgewiesen, dass die „Varnish“-Verwitterung bereits bei pH 5 beschleunigt ist, obwohl die bei pH 5 und pH 7 beobachteten Auflösungsraten in einem vergleichbaren Bereich lagen. Insgesamt waren die Veränderungen der Farbe, der chemischen Zusammensetzung, der Oberflächenstruktur und des Probengewichts bei den Probengruppen, die unter leicht sauren Bedingungen (pH 5) künstlich verwittert wurden, größer. Das Verwitterungsexperiment hat auch signifikante Unterschiede zwischen den verschiedenen „Varnish“-Typen und ihrer relativen Anfälligkeit für Verwitterung gezeigt. Die Extraktion der DNA-Proben ergab signifikante Unterschiede in Abhängigkeit von pH-Wert und Gesteinsart. Zusätzlich wurden in diesem Langzeitexperiment vom Fraunhofer-Institut für Silicatforschung (ISC) zur Verfügung

gestellte Glasdosimeter mit unterschiedlichen Zusammensetzungen eingesetzt, um die simulierten Bewitterungsbedingungen in der Kammer zu überwachen und zu quantifizieren. Da das Alterationsverhalten dieser Dosimeter gut erforscht ist und sie seit vielen Jahrzehnten zur Überwachung von Kulturgütern eingesetzt werden, ermöglicht ihre Verwendung eine Vergleichbarkeit der simulierten Bedingungen und erleichtert den Vergleich der simulierten mit realen Bedingungen.

Die Ergebnisse lassen den Schluss zu, dass die Verwitterung des „Rock Varnish“ auf den Gesteinen von Murujuga, die als Untergrund für die Petroglyphen dienen, höchstwahrscheinlich durch die lokale industrielle Verschmutzung beeinflusst wird, wobei die Verwitterungsraten aufgrund des niedrigeren pH-Werts des Regenwassers auf Murujuga sehr wahrscheinlich bereits beschleunigt sind. Darüber hinaus ist es sehr wahrscheinlich, dass die Verwitterungsraten weiter zunehmen werden, wenn der pH-Wert weiter sinkt, da die Auflösungsraten der primären Phasen des „Varnish“ bei niedrigeren pH-Werten tendenziell ansteigen. Außerdem wurden neue Erkenntnisse über die Zusammensetzung und die Mikrostrukturen des „Varnish“, sowie über die mikrobiellen Populationen auf dem „Varnish“ gewonnen, und es wurde die Hypothese aufgestellt, dass der „Varnish“ auf Murujuga aufgrund gestiegener Auflösungsraten bereits erheblich an Mn-Mineralphasen verarmt sein könnte.

Acknowledgements

At first, I would like to thank everyone who supported me during the work on this thesis and helped to make this project possible, whether through numerous discussions, practical assistance, proofreading, or technical support.

My deepest gratitude goes to my doctoral supervisor, Thorsten Geisler-Wierwille, who came up with the project, first as a master thesis and then in the following as a PhD project. He made my doctorate possible, offering support whenever questions arose, while also giving me the freedom to plan the project independently and explore my own ideas. He also assisted with carrying out the Raman measurements as well as analysing and presenting their results.

I would also like to thank the members of the Murujuga Rock Art Conservation Project, especially Prof. Dr. Benjamin Smith and Dr. John Black, without whose support it would not have been possible to obtain samples from Murujuga or secure permission to use them from the Murujuga Aboriginal Corporation. The Murujuga Aboriginal Corporation also deserves special thanks for approving my project. Additionally, I would like to thank Dr. Ken Mulvaney for collecting some of the samples from Murujuga, as well as Prof. Dr. Robert Bednarik for providing an older sample from Murujuga.

My sincere thanks also go to the Fraunhofer Institute for Silicate Research, which provided glass dosimeters and analysed them. In particular, Gabriele Maas-Diegeler and PD Dr. Martin Kilo, who also served as my second supervisor, offered valuable support and deserve special thanks.

I would also like to thank the other two members of my doctoral committee, Prof. Dr. Christian März and Prof. Dr. Jan Bemmann.

Many individuals supported me during my analytical work. I wish to thank Dr. Patricia Roeser and Dagmar Wenzel for their assistance with the ICP-OES analyses, Holger Becker and Marina Westkamp for allowing me to use their p-XRF while ours was experiencing issues, Dr. Seven Oliver Franz for carrying out the XRF measurements, Dr. Andreas Lang for conducting the µ-CT scans, Dr. Frank Tomaschek and Manuel Kunz for assisting with the EMP analyses and sample coating, respectively, Hans-Henning Friedrich for carrying out and helping to evaluate the XRD measurements, Johannes Kehren and the group of Prof. Dr. Olaf Krause at the Hochschule Koblenz for letting me use their high-resolution optical microscope, and especially Dr. Sabina Karačić for her help with collecting DNA samples, extracting the DNA, and analysing, presenting, and interpreting the acquired microbiological data.

Thomas Schulz, Dieter Lülsdorf, Philipp Krämer, Henrik Blanchard, and Nils Jung contributed to designing and building the experimental setups and preparing the rock samples used and I am deeply grateful for their valuable assistance and work. I would also like to thank Daniela Bungartz and Dagmar Hambach for their repeated help in resolving bureaucratic challenges. Additionally, I extend my gratitude to Dr. Johanna Mäsgen for proofreading my thesis.

Furthermore, I would like to thank the Rosa-Luxemburg-Foundation for supporting my bachelor's and master's degrees, as well as my PhD project, through a scholarship.

Finally, I would especially like to thank Fe for her patience and support throughout this project, regardless of my mood and stress level, as well as for proofreading my thesis and making an effort to understand everything I did and described. I am also immensely grateful to my parents, Jutta and Micha, who enabled and encouraged me to decide freely what to study, to discover my enthusiasm for science, and who supported me my whole life to achieve everything I have accomplished to this day.

Contents

List of Figures

List of Tables

1 Introduction

Murujuga is a peninsula in the north of Western Australia, located near the small city of Karratha (Fig. 1.1). The peninsula and the surrounding islands are renowned for their Aboriginal rock art. The Murujuga Aboriginal corporation (MAC), that represents the traditional custodial groups in the region, states that:

> "With an estimated one to two million petroglyphs, Murujuga is home to one of the largest, densest and most diverse collections of rock art in the world, and is of continuing cultural and spiritual significance to the Traditional Owners and Custodians. It also has significant state, national and international heritage value."
>
> (Murujuga Aboriginal Corporation, 2024)

The Murujuga petroglyphs depict a wide variety of motifs (Fig. 1.1; see Chapter 1.4), including tracks, local animals, plants, and even humans (McDonald & Veth, 2009) and some of them are believed to be up to 30,000 years old (McDonald, 2005; Mulvaney, 2010, 2013; McDonald, 2015). Due to their vast number it was not possible to document all of them to this date. As the petroglyphs represent an important part of their cultural heritage, the Aboriginal community is advocating for their preservation since decades.

Figure 1.1: Map and petroglyphs of Murujuga depicting weapons, geometric figures, and a kangaroo. All photos were taken by T. Geisler-Wierwille in 2019.

Most parts of the peninsula were listed as a national heritage site in July 2007 (McDonald & Veth, 2009). In 2020, the archaeological sites on Murujuga were added to UNESCO's tentative list to become a world heritage site (UNESCO, 2020), and in 2023, the federal government formally nominated the peninsula for world heritage listing (ABC News, 2023).

The petroglyphs were carved into the rock surface by the Aboriginal people who inhabit the area at least since 30,000 years (Law et al., 2010). They used different techniques to create the petroglyphs all of which include removing the outermost layer of the rocks, known as the rock varnish, which creates a colour contrast making the petroglyphs visible (Fig. 1.1), even if they are only carved a few millimetres deep into the rock (Vinnicombe, 2002). Different kinds of rock varnish can be found all over the world in arid to semi arid climates as on Murujuga and the varnish mainly consists of Mn- and Fe-oxides, as well as clay minerals (see Chapter 1.4).

Similar to other archaeological sites and cultural objects worldwide, which are threatened by industrial pollution and climate change leading to increased weathering rates and erosion (Camuffo, 1992; Di Turo et al., 2016; Sesana et al., 2021), it is feared that the petroglyphs on Murujuga might be endangered due to industrial pollutants as the industrial development on the peninsula over the past decades led to an increasing amount of pollutants released into the local atmosphere (see Chapter 1.1). Due to this, the pH of the rainwater and therefore of the rock surfaces got lower over the time, raising concerns that this might increase the weathering rates of the rock varnish, which could lead to an irretrievable loss of the petroglyphs, which are only visible as long as the rock varnish stays intact (Bednarik, 1994, 2002; Black et al., 2017a; Smith et al., 2022).

Different researchers attempted to examine the alteration rates and processes, as well as their potential acceleration, over the past decades since concerns about the endangerment of the petroglyphs first arose in the 1970s (Wright, 1974). The underlying question is whether the increased emissions of various pollutants from industrial sites on Murujuga, and the consequent decrease in rainwater and rock surface pH, have accelerated the weathering rates of the petroglyph-bearing rock varnish and how, or if, a further decrease in pH could affect the rock surfaces on Murujuga (see Chapter 1.2) . After criticism of the lack of monitoring (e.g. Bednarik, 2002), various studies were conducted on Murujuga by different research groups trying to examine if there is a potential endangerment of the rock art (MacLeod, 2005; Lau et al., 2007; Gillett, 2008; Lau et al., 2010; Markley et al., 2015; Duffy et al., 2017; Ramanaidou et al., 2017; MacLeod, 2018, 2019, 2021; MacLeod & Fish, 2021; MRAMP, 2022, 2023). The results of some of these studies, as well as the analytical methods and techniques employed, were criticised by other researchers, raising further concerns about the endangerment of the petroglyphs as further detailed in Chapter 1.1 (Bednarik, 2009; Black et al., 2017a, 2017b; Smith et al., 2022).

As it was not possible to definitively answer the underlying questions about the impact of industrial pollution on Murujuga and as there is no scientific consensus to date, it remains essential to evaluate how variations in rainwater pH might change the dissolution rates of different minerals in the rock varnish, as well as to observe the impact of weathering processes at different pH levels and the resulting alteration of the rock varnish under varying weathering conditions (see Chapter 1.2). Additionally, it is necessary to examine the varnish composition and mineralogy, as well as the differences between the types of rock varnish found on Murujuga (see Chapter 3.1.3).

In order to gain new insights on these topics, a long-term weathering experiment under controlled conditions in a climate chamber (see Chapter 4) was conducted for a total of 12 months, simulating six years of Murujuga climate (see Chapter 1.5). In the used climate chamber the temperature, humidity, solar radiation, and precipitation were simulated using climate data from Murujuga to create Murujuga-like conditions. The setup enabled the weathering of two sets of rock varnish-bearing samples from Murujuga with different artificial rainwater compositions at different pH levels. Over the course of this experiment the color, chemical composition, and the structures of the rock sample surfaces were monitored, as well as the loss of weight of the samples. In addition samples of the artificial rainwater that was rinsed over the varnish-bearing samples were analysed to examine their chemical composition in order to determine the amount of material dissolved. DNA samples were extracted from separate rock samples weathered in the climate chamber to analyse the change of the microbial community composition on the rock varnish surfaces over time. This experiment was conducted to identify weathering processes and surface changes on the samples and to determine if the pH changes of the rainwater observed on Murujuga lead to significant differences in the weathering processes, the amount of surface changes, and the weathering rates.

Furthermore, some irrigation experiments at various pH levels were carried out with varnish-bearing rock samples to determine the pH dependence of the dissolution rates of the main mineral components in the varnish and therefore the pH dependence of the weathering rates of the rock varnish on Murujuga (see Chapter 5). For these experiments also the used artificial rainwater that was in contact with the rock varnish was analysed, as well as the colour and chemical composition of the varnish to detect possible changes over the course of the experiments at different pH levels.

Thin sections of the varnish were additionally prepared and analysed to determine the chemical and mineralogical composition of the thin rock varnish layer, as well as its microstructures to achieve a better understanding of how the varnish degrades (see Chapter 6).

1.1 State of the Art

It is well known that climate change and industrial pollution can pose major threats to historical buildings, monuments, cultural objects, statues, and ancient rock art around the world, as they contribute to increase weathering and degradation rates, like the effects caused by acid rain (Charola, 1987; Camuffo, 1992; Reis et al., 2012; Di Turo et al., 2016; Sesana et al., 2021). For instance, acid rain, resulting from anthropogenic pollutants, is progressively destroying the cultural heritage of Mexico's Maya civilization, which is primarily constructed from limestone. Limestone dissolves when it comes into contact with acid rain, leading to the erosion of inscriptions (Heckel et al., 2007; Castillo-Miranda et al., 2017). This issue might become even more severe in the near and mid-future, as anthropogenic climate change is expected to cause significant shifts in the climate at many locations worldwide (IPCC, 2023), including Europe, likely resulting in degradation patterns of cultural heritage sites that differ from those seen in recent decades. While the impact of air pollution on the deterioration of cultural heritage objects and monuments made of limestone, sandstone, various metals (Cu, Fe, Zn & Al), alloys (bronze), polymeric materials, and glass is considered reasonably well understood (Tidblad et al., 2012), the situation is different when it comes to the Aboriginal rock art (Figs. 1.1 & 1.3) on Murujuga carved into rock varnish layers.

First concerns about an endangerment of the petroglyphs date back to 1974, after the first industrial sites were built and the first petroglyphs were removed (Wright, 1974). Industrial development on Murujuga began in 1964 with the construction of an iron ore export terminal, followed by a salt production facility in 1970. In the 1980s, several natural gas processing complexes were added. Additional liquefied natural gas (LNG) production plants were built in 1995 and 2007. In 2006, an ammonium fertilizer plant was established and in 2017, an ammonium nitrate facility was added (Gillett, 2006). There are ongoing plans for further expansions of industrial complexes on Murujuga by various companies (Mulvaney, 2022). It is estimated that by the mid-1980s, up to 25 % of the petroglyphs on Murujuga had already been destroyed, mainly through removal from construction sites (Bednarik, 2002).

Results from chemical deposition monitoring in 2012-2014 provided by Woodside, one of the companies operating on Murujuga, revealed that up to 34 % of the emitted NO_2 was deposited on the rocks (Woodside, 2019). However, emissions of SO_x, particularly from shipping, are also extremely high and might have a similarly profound impact on the rock patinas of Murujuga, as they form sulphuric acid during periods of light rainfall. Woodside recently reported annual emissions of 8,720 tons of NO_x and 117 tons of SO_x (Department of the Environment and Energy, 2023). Since 2017, there have also been additional NO_x emissions from Yara Pilbara Nitrates, contributing 620 tons of NO_x and 58 tons of ammonia annually (Department of the Environment and Energy, 2023). In total, including emissions from other facilities and the Dampier Port, 10,270 tons of NO_x and 157 tons of SO_x were emitted on Murujuga in 2023 (Department of the Environment and Energy, 2023). Satellite imagery measuring NO_2 concentrations in the atmosphere showed significantly higher concentrations over large parts of Murujuga compared to the surrounding areas (Gillett, 2006; Smith et al., 2022). It is known that NO_x and SO_x contribute to acid rain (Norton & Vesela, 2003) and these emissions, along with the resulting acid rain, lead to increased nitrite and nitrate concentrations on the rock surfaces, which in turn can lead to microbial growth (MacLeod, 2005). This organisms can release acids and lower the surface pH (MacLeod, 2005, 2021). In other environments, acidic industrial emissions have been shown to lower the pH of rock surfaces, leading to their destruction (Giesen et al., 2014; Dorn, 2020). Reports indicate that acid rain with a pH below 5.6 frequently occurs on Murujuga, with an average pH of 4.6 (Bednarik, 2007) and that the environment has become more acidic over time (MacLeod, 2005). Most recent studies measured pH values mostly around 5 on Murujuga (MacLeod & Fish, 2021; MRAMP, 2023).

Due to this and other findings concerns about an endangerment of the petroglyphs grew over time, prompting numerous studies to investigate whether industrial pollution and the associated acid rain are accelerating the natural weathering of the petroglyphs (Bednarik, 2002; MacLeod, 2005; Lau et al., 2007; Gillett, 2008; Lau et al., 2010; Markley et al., 2015; Duffy et al., 2017; Ramanaidou et al., 2017; MacLeod, 2018, 2019, 2021; Black et al., 2017b; MacLeod & Fish, 2021; Smith et al., 2022; Neumann et al., 2022; MRAMP, 2022, 2023). Some of these studies, however, have delivered highly controversial results and conclusions, which will be further detailed in the following. In response to concerns raised by authors such as Bednarik (2002), the government established the Burrup Rock Art Monitoring Management Committee which was tasked with the implementation of some studies that were carried out in 2004-2005 and 2007-2008 by the Commonwealth Scientific and Industrial Research Organisation (CSIRO)(Lau et al., 2007, 2010). The CSIRO continued taking colour measurements on Murujuga for more then ten years until 2016 (Duffy et al., 2017). In addition some extreme weathering experiments were carried out by CSIRO (Ramanaidou et al., 2017). Today, the Murujuga Rock Art Strategy has replaced the Burrup Rock Art Monitoring Management Committee, overseeing the monitoring of the petroglyphs and conducting scientific studies (DWER, 2019). As part of the Murujuga Rock Art Strategy, the Murujuga Rock Art Monitoring Program (MRAMP) was launched, and a first report from its field studies was published at the end of 2023. The programme is conducted by Curtin University and Calibre (MRAMP, 2023), in cooperation with the Murujuga Aboriginal Corporation (MAC).

Previously, in 2002, Robert Bednarik criticised the lack of a management plan for the peninsula and its petroglyphs. He proposed nominating the peninsula as world heritage (which was finally achieved in 2023), returning the land to the Aboriginal community, and increasing the effort for the conservation of the petroglyphs (Bednarik, 2002). He warned that changes in pH levels could lead to the destruction of the rock varnish, as already observed on some sites on the peninsula due to bird droppings with a pH of around 5.9. Bednarik also reported observable changes on some of the rock surfaces which he describes as “bleaching” (Bednarik, 2002, p. 36). Colour changes were also reported using a method of colour calibration applied to pictures that were taken in the past. With this method, he predicted that shallow petroglyphs could disappear between 2025 and 2035 (Bednarik, 2002). However, this prediction has proven to be overly pessimistic, as the vast majority of petroglyphs still exists today. The method used to examine colour changes is now considered inaccurate, given today's understanding of how complex it is to measure and track colour changes precisely (Neumann, 2021; MRAMP, 2023). Nevertheless, Bednarik's publications and his actions made the concerns publicly known and led to further research and funding for studies on Murujuga. Also other groups working to protect the Murujuga rock art formed, as for example the Friends of Australian Rock Art (FARA). Their activities, as well as the work of other groups, led to the including of Murujuga to the National Heritage List in 2007 (Mulvaney, 2022).

The first publication of a progress report of colour change and spectral mineralogy, along with a final report on fumigation experiments and dust deposition, was published by the CSIRO in 2007 (Lau et al., 2007), followed by more interim reports on the colour change (e.g. Lau et al., 2010). The group monitored dust deposition on Murujuga to evaluate the composition and deposition rates of dust, aiming to determine if there are differences in the dust deposition near the industrial sites compared to areas further away (Lau et al., 2007). For this purpose, synthetic rock surfaces made up of polyurethane polymer were exposed on three different sites on Murujuga, initially for three months and afterwards for one year. Over time, the collected amount of dust did not change, leading the researchers to conclude that the amount of accumulated dust is limited, with a continuous process of deposition and removal occurring. They also discovered that dust far from the industrial sites had a different composition than dust near the sites, the latter containing more Fe-oxides (Lau et al., 2007). Additionally, the group conducted a fumigation experiment, in which they collected rocks with desert varnish from Murujuga, crushed them, and subjected them to fumigation with different mixtures of pollutants. One sample group was fumigated with no air pollutants as a control group and two other groups were fumigated with the anticipated level of air pollution on Murujuga and one with ten times those levels. After 720 hour of fumigation cycles with different temperatures, they analysed the samples and compared the results with pre-fumigation measurements. They stated that they could not find any evidence for changes on the rock surface (Lau et al., 2007), although other studies stated that the data they collected does show significant changes (Black et al., 2017a).

The group also measured the surface colour at seven different sites, with multiple spots and measurements per spot since 2004. Five of the seven spots were located on central Murujuga, near industrial sites, while the other two spots being far north on Gidley and Dolphin Island. For their measurements they used a BYK Gardner chroma meter and the L*a*b colour space and calculated the colour change ΔE (Lau et al., 2007, 2010). At each site, they measured spots on engravings and on the surrounding rock, combining at least seven measurements per sampling point. They mention the importance to protect the measured area during the measurement from natural light, as light conditions can vary between measurements, and used black fabric “when necessary” (Lau et al., 2010, p. 5) to exclude natural light from their measurements. It is unclear, however, whether or how they ensured that the exact same area was measured each time, which is critical for accuracy, as discussed in Chapter 2.1. However, they admitted that some large colour differences may be influenced by the placement of the chroma meter due to the roughness of the rock surface (Lau et al., 2007). They concluded that “there was no consistent perceptible increase in colour change over the 2004–09 period” (Lau et al., 2010, p. 27). It should be noted that they primarily focused on the change from year to year and not on the change over the whole period of six years in which they performed their measurements. When viewed over the whole period, the measured changes from 2004 to 2009 varied between a ΔE of 3.25 and 13.49 (Lau et al., 2010), which are significant changes, considering that a $\Delta E > 1$ is visible to the human eye. It is highly questionable whether these measured values reflect real changes in surface colour, due to inadequacies within the measurement process such as the lack of consistent repositioning of the chroma meter on the exact same spot as mentioned above. For example measurements from one spot (site 7, spot 1 engraving) had a ΔE of 23.71 (Lau et al., 2010) from one year to the next, which is an unrealistically high value. The results of the study were later heavily criticised, as the chroma meter used was not designed for rough surfaces or the temperatures and humidity that regularly occur on Murujuga (Black et al., 2017a). Lau et al. (2007, 2010) also measured all spots with an ASD FieldSpec Pro reflectance spectroscope, which measured the reflected light from the surface to observe changes in mineralogy, but concluded that no changes had occurred (Lau et al., 2010).

The colour and reflectance spectroscopy measurements continued until 2016 (Duffy et al., 2017), with more interim reports published in various years (e.g. Markley et al., 2015). The group measured the same seven sites as before but added two more spots per site since 2013, along with three additional sites close to the Yara Pilbara Nitrates Production Facility. In 2009, the BYK Gardner chroma meter was replaced with a Konic Minolta CM-700d (Duffy et al., 2017). This new device delivered significantly different L*a*b values than the BYK Gardner chroma meter, making it challenging to compare the data from 2008 and earlier with the new data from 2009 and later. Nevertheless, the overall change was reported after converting the older data in a manner that was not described. The inadequacies in the measurement process, as previously mentioned (positioning of the chroma meter, rough surface), persisted throughout all measurements. The average colour change for the period from 2004 to 2016 remained high, with a ΔE of 11.97 for the sites close to the industry and 13.80 for the northern sites, which are far from the industry (Markley et al., 2015; Duffy et al., 2017). It is highly questionable whether these measured values reflect a real change in surface colour for the reasons mentioned earlier. The report concluded that “None of the instruments demonstrates a difference in the rate of change between the northern control sites and the southern sites closer to industry” (Duffy et al., 2017, p. 142), consistent with earlier reports that also concluded that there was no evidence for a consistent trend in colour change (Lau et al., 2007, 2010; Markley et al., 2015).

In addition to the aforementioned issues regarding colour measurements, a group of researchers criticised that the study does not include any statistical analyses (Black et al., 2017a), referring to Markley et al. (2015). Afterwards, statistical analyses were carried out, but the results were withheld by the Western Australian Government, requiring the authors to sign a confidentiality agreement (Black et al., 2017a). The authors also criticised the change in measurement devices and expressed concerns about whether the same area was measured each time, which could lead to further inaccuracies due to the inhomogeneous surface of the rocks (Black et al., 2017a). Furthermore, it was pointed out that the used instruments only provide precise results for temperatures below 35 °C and a humidity below 85 %. Both values are often exceeded on Murujuga (Bednarik, 2009). Bednarik (2009) also criticised the colour measurements, which were carried out, due to the lack of consistency, emphasizing that it is crucial to measure the same point each time. This assertion is supported by findings in a previous study (Neumann, 2021) and is further discussed in Chapter 2.1. The reflectance spectroscopy measurements also did not show systematic changes according to Duffy et al. (2017). Following the criticisms from Black et al. (2017a), which deemed the methodology inadequate and the results inaccurate and non-reproducible, the CSIRO ceased the annual colour and reflectance spectroscopy measurements (MacLeod & Fish, 2021). Instead, Yara Pilbara Nitrates, a company operating industrial sites on Murujuga, contracted Warren Fish and Ian MacLeod to continue the colour monitoring on the same sites (MacLeod & Fish, 2021).

In 2008, the CSIRO published another report investigating air pollution on a total of 10 sites on Murujuga (Gillett, 2008). The authors measured the concentrations of NO_2, SO_2, HNO_3, ammonia gases, and other air pollutants. They also collected suspended particles and rainwater samples from different sites. Far away from the industrial sites lower concentrations of some air pollutants were detected than close to them (Gillett, 2008). They also observed slightly higher acid deposition from the industrial complexes but concluded that the amount was too small to impact the petroglyphs on Murujuga. This conclusion was based on the underlying assumption of a very high buffering capacity of up to 200 meq/m^2/year for the soils on Murujuga (Gillett, 2008). However, this conclusion was questioned by Black et al. (2017a), as it was based on a map that shows buffering capacities with a scale of 1:5,000,000 classifying the entire area around Murujuga with a size of approximately 300,000 km^2 as one type of soil (Cinderby et al., 1998), despite Murujuga itself being only 110 km^2 in size. Even one of the map's authors pointed out that it is not possible to draw conclusions for the critical loads on Murujuga using the map (Black et al., 2017a). The authors concluded that the rocks on Murujuga can only withstand low acid loads due to their slow weathering rates, with the most sensitive rocks only capable of buffering 25 meq/m^2/year of sulphur (Black et al., 2017a). Maximum loads of 32 meq/m^2/year were measured on Murujuga in 2007/2008 (Black et al., 2017a; Gillett, 2008).

In addition, Yara Pilbara Nitrates published air quality monitoring reports between 2017 and 2022 (Yara Pilbara, 2017, 2018, 2019, 2020, 2021, 2022). For the measurements, three sites around the Yara facilities were chosen, all of which had already been used for other studies conducted by the CSIRO (Duffy et al., 2017). The concentrations of NH_3, NO_2, and SO_2 were measured, along with the dust deposition rates. From the measured gases, the annual deposition rates were calculated in meq/m^2/year (Yara Pilbara, 2017, 2019, 2020, 2021, 2022). The first study was designed as a baseline assessment, establishing investigation levels (Yara Pilbara, 2017). These investigation levels were set at around 50 meq/m^2/year at two sites (Yara Pilbara, 2019), which exceeded the maximum measured load from 2007/2008 (Black et al., 2017a; Gillett, 2008). For the third site, the investigation level was set to 27.1 meq/m^2/year (Yara Pilbara, 2019) and was regularly exceeded over longer time periods (Yara Pilbara, 2022). The average NO_2 concentrations at the first site increased nearly constantly from 3.60 to 4.88 µg/m^3, with two small decreases in 2018 and 2021. At the second site, the average concentrations also have risen from 2.56 to 3.59 µg/m^3 over the years, with the same exceptions. The same is valid for the third site with a lower increase from only 2.31 to 2.56 µg/m^3 with the lowest overall concentrations (Yara Pilbara, 2017, 2018, 2019, 2020, 2021, 2022). The SO_2 concentrations decreased at all sites, falling nearly continuously from 1.39, 0.96, and 0.83 µg/m^3 in 2017 to 0.18, 0.12, and 0.11 µg/m^3 in 2022, with values never exceeding the maximum measured in 2017 (Yara Pilbara, 2017, 2018, 2019, 2020, 2021, 2022). Dust deposition on the sites did not vary significantly after a slight increase between 2018 and 2019, rising from around 0.7 g/m^2/month to values between 0.8 and 1.2 g/m^2/month across all sites. There was one exception at the second site in 2021, which recorded a deposition rate of 1.9 g/m^2/month (Yara Pilbara, 2018, 2019, 2020, 2021, 2022).

In another study, conducted by CSIRO, weathering experiments were performed and the results were published in 2017 (Ramanaidou et al., 2017). For these experiments, granophyre and gabbro samples were collected from locations previously used for colour measurements (Lau et al., 2007, 2010; Markley et al., 2015; Duffy et al., 2017). A total of 126 cylindrical samples, each with a diameter of 10 mm and an intact rock varnish surface, were cut from the collected granophyre and gabbro rocks. The researchers created silicone casts for the cylindrical samples and protected them with additional resin to ensure that only the rock varnish was exposed to the simulated weathering conditions, while other parts of the rock remained sealed (Ramanaidou et al., 2017). This method is similar to the Araldite® coating used for the rock samples in this study (Chapter 4.1.3). The samples were then placed in 100 ml of various solutions, including HNO_3 (pH 2.0 to 4.4), H_2SO_4 (pH 1.9 to 4.3), NH_4NO_3 (pH 4.8 & 5.3), and NH_3 (pH 9.2 & 11.5), as well as distilled water (pH 7) as a control group. The samples were kept in these solutions for 3 days or for one month at 50 °C . The experimental solutions were measured using ICP-AES (inductively coupled plasma - atomic emission spectroscopy). Additionally, colour measurements, reflectance spectroscopy measurements, and scanning electron microscopy were employed (Ramanaidou et al., 2017).

The colour measurements were performed in a more reliable manner by placing the cylindrical holders with the samples over the measurement head of the used Konica Minolta CM-700d chroma meter and measuring them 10 times while rotating them by an angle of 40°. However, this method still has room for improvement, as the 10 rotations added up to more than one full rotation, and it was not ensured that the measurements starts at the same position, leading to duplicate measurements at the starting position. According to Ramanaidou et al. (2017), they found that for the gabbro varnish, dissolution of Al, Mn, and Fe starts below pH 3 and for Al also above 11. Some results, indicating the dissolution of Mn at pH levels of 4.9, 5.8, and in distilled water (pH 7), were excluded, because this “would mean that under rainwater (pH = 5.5), Mn will be dissolved in natural condition which is clearly not the case, as otherwise, Mn would not be present on the surface of the Burrup weathered rocks as they have been subjected to thousands of years of rain.” (Ramanaidou et al., 2017, p. 12). For granophyre varnish, they concluded that dissolution begins at pH 3.2 and below for Al, Mn and Fe, as well as above pH 11 for Al. Again, some samples containing dissolved Mn at higher pH levels were excluded for the same reasons as mentioned above. For the colour measurements and the other used methods they state that they did not observe any changes (Ramanaidou et al., 2017). However, the claim that there is no dissolution above pH 3.0 or 3.2 and the reported zero concentrations for most samples should be questioned, given a detection limit of 0.1 mg/l (100 ppb) for Fe and 0.03 mg/l (30 ppb) for Mn. This limit is significant considering a volume of 100 ml solution and an exposed varnish area of only 10 mm in diameter. Recent publications have indicated that a single simulated weathering event using a solution with pH 5 is sufficient to measure significant changes in the composition of the rainwater that was in contact with the varnish surface compared to a blank sample that was not in contact with varnish surface (Neumann et al., 2022). Additionally, the conclusion that there cannot be dissolution at the pH levels assumed for rainwater on Murujuga because there would be no varnish left is inadequate for several reasons: (1) other studies have indicated that the pH was higher before industrial development (Bednarik, 2007; MacLeod, 2005); (2) evidence shows that there is a loss of Fe and Mn under the most acidic conditions on Murujuga (MacLeod, 2005, 2021; MacLeod & Fish, 2021); (3) it is known that there is some erosion on Murujuga occurring at relatively low rates (Pillans & Fifield, 2013); and (4) the varnish is continuously regrowing (Chapter 1.4). The varnish would only disappear if the erosion rate consistently exceeded the growth rate for a considerable time, which is a concern raised by some researchers due to industrial developments and the therefore increased industrial emissions (Bednarik, 2002; Black et al., 2017b; Smith et al., 2022; Mulvaney, 2022).

In 2017, a study tried to theoretically assess the effects of emissions on the rock surfaces on Murujuga (Black et al., 2017b). The authors used data of the acidity of the rock surface from Murujuga, compared to older pieces that were collected on

Murujuga before the industrial development by MacLeod (2005). They concluded that the acidity of the rock surfaces has increased, leading to an increased solubility of Mn and Fe and increased dissolution rates of Fe- and Mn-bearing phases. They state that due to this the varnish could become more unstable and thinner (Black et al., 2017b).

MacLeod published annual reports of the colour measurements for Yara Pilbara from 2018 to 2021, which also included pH measurements, analyses of the mobilisation of metal cations, and various other measurements (MacLeod, 2018, 2019, 2021). The studies only included sites close to the industrial complexes and no measurements were performed at the remote sites on Dolphin and Gidley island, unlike in the previous CSIRO research (MacLeod, 2021; Duffy et al., 2017). MacLeod collected wash solutions from different sites by rinsing an area of 200 cm^2 with distilled water. These solutions were analysed using ICP-MS (inductively coupled plasma – mass spectrometry) to determine the metal ion content. Fe was detected in 7 of 16 samples with a detection limit of only 6 ppb. Mn was also found at various sites with concentrations of < 10 ppb. The author noted that, as indicated in unpublished data from rock washings in 2017, Mn compounds are significantly more soluble than their Fe analogues, with up to 60 times greater solubility (MacLeod, 2021). Here it has to be noted, that the dissolution rates more important than the overall solubility because the maximum solubility will likely not be reached during the low time of contact. The pH measurements on the rock surfaces indicate an increase of the pH between 2019 and 2021, which has decreased the solubility of Mn according to MacLeod (MacLeod, 2021). The pH on the rock surface directly corresponds to the NO_3^- concentration on the rock surface and can also be connected to major rainfall events on Murujuga, such as cyclone Damien in February 2020, which brought 235 mm of rain within 24 hours. The author suggested that these major rainfall events washed the surface, resetting the acidity. For example, after an extended period with no major rainfall events, the pH recorded at some sites was at its lowest (MacLeod, 2021). Between 2017 and 2021, the measured pH of the granophyre surfaces ranged from approximately 4.0 to 6.5, with most sites averaging between 4.5 and 5.5. The gabbro surfaces exhibited comparable pH levels, with a minimum of 4.5 and a maximum around 6.5. Notably, the pH at nearly all sites increased between 2019 and 2021 (MacLeod, 2021). The author also compared the acquired data from older nitrate and pH measurements that were taken more than a decade ago (MacLeod, 2005). The new data indicated an overall increase in pH (MacLeod, 2021), because the lowest pH was measured in 2003 / 2004 (MacLeod, 2005) and also a decrease in NO_3^- concentrations was noted, which were higher in 2003 / 2004. It is important to note that the sites, where measurements were taken differ between the two studies (MacLeod, 2005, 2021).

For the colour measurements, MacLeod measured the same spots at the same sites previously studied by CSIRO (Lau et al., 2007, 2010; Markley et al., 2015; Duffy et al., 2017), but only reported the ΔE value for the colour difference between the background and the engravings. The author suggested a correlation between the colour measurements and the measured surface pH (MacLeod, 2021). However, it is unclear whether MacLeod increased the reliability of the colour measurements compared to the measurements carried out by the CSIRO staff. It is known that the same chroma meter used in previous measurements was employed, indicating that some criticisms (Black et al., 2017a; Smith et al., 2022) also applies to MacLeod's new measurements.

MacLeod and Fish published summarised data in 2021 (MacLeod & Fish, 2021). In this publication, they highlight the impact of the major rainfall events once again as an explanation for the fluctuating measured pH levels. They connect the pH to the chloride concentration on the surface, which is affected by seawater, as well as to the nitrate concentration. The colour changes are correlated with the measured pH (MacLeod & Fish, 2021). The authors concluded that their research shows that pH changes of only 0.3 change the surface chemistry from Mn dissolution to Mn precipitation, which explains the shifts in surface colour and the changing contrast between background and engraving. They also suggest that the dissolution of Fe and Mn is mitigated by major rainfall events and the deposition of ammonia and sea salts. The comparison of their data from 2003 / 2004 with data collected between 2017 and 2019 indicates a reduced amount of nitrate, which, according to the authors, contributes to a stabilisation of the rock varnish (MacLeod & Fish, 2021). The average pH measured for all monitored sites was 5.29 in 2017, 5.51 in 2018, and 4.71 in 2019 (MacLeod & Fish, 2021; Smith et al., 2022). However, they stated that "the present monitoring data shows that there is presently no adverse impact on the rock engravings from industrial pollution [...]" (MacLeod & Fish, 2021, p. 8).

This statement, as well as parts of the reports MacLeod published between 2018 and 2021 (MacLeod, 2018, 2019, 2021), were heavily criticised by Smith et al. (2022). First of all, it was pointed out that the statement made by MacLeod and Fish stands in contrast to results of other researchers published over the past decades, which were aforementioned. Specifically, the fact that this claim is supported by only a limited number of measurements performed at just seven different sites was criticised (Smith et al., 2022). Additionally, the lack of a control group outside of the polluted area makes the results even more questionable. It is well known and widely accepted that pH plays a crucial role in the weathering of the Murujuga rock varnish, which is also acknowledged by MacLeod and Fish (2021), who even stated that a pH change of 0.3 can have a significant impact on the weathering process (MacLeod, 2021). The Pourbaix diagrams for Fe and Mn support these assumptions (Pedeferri, 2018; Pourbaix, 1974) and are referenced by different authors (Black et al., 2017a; Smith et al., 2022; MacLeod, 2021). The proposition that "the natural pH of local weathered gabbro and granophyre is 5.5 ± 0.2" (MacLeod & Fish, 2021, p. 4) is rejected by Smith et al. (2022), because other findings indicate that rock varnish will not even form if the pH is 5.6 or less (Bednarik, 2009), or that Mn is leached if the pH falls to 5.7 or below (Goldsmith et al., 2014). The measured pH on various sites is below these values, and the average for the 2017-2019 period is also below these thresholds. At one site near the Woodside petrochemical plant the pH average is even below 4.0 for the 2017-2019 period (Smith et al., 2022; MacLeod & Fish, 2021). The assumption from MacLeod and Fish (2021) that rainfall events reset the decay and acidity of rocks is also questioned by Smith et al. (2022). On the contrary it is stated, that the mixing of rainwater with deposited material on the rock surface can lead to increased acidity (Smith et al., 2022). Smith et al. (2022) suggest that only major rainfall events can positively affect the acidity of the rock surface, but these events only occur twice a decade (Smith et al., 2022; Holmes, 2021). With respect to the statement made by MacLeod and Fish (2021), it is important to note that they assume that nitrate levels are now lower than in 2003-2004 when the first measurements were conducted (MacLeod, 2005). This was also criticised by Smith et al. (2022), because the nitrate concentrations were measured at different sites and it was not mentioned that nitrate levels measured before industrial development were significantly lower (only 0.3 ppm) according to MacLeod himself (MacLeod, 2005). Smith et al. (2022) also point out that the NO_x emissions are still very high when compared to the emissions from 2003 and 2004.

As aforementioned, the most recent report comes from the Murujuga Rock Art Monitoring Program (MRAMP), for which a first analysis plan was published in 2022 (MRAMP, 2022), and a first report was published at the end of 2023 (MRAMP, 2023). For this report, scientists from the Curtin University in Perth carried out different measurements on Murujuga in cooperation with calibre and MAC. The team conducted four fieldwork campaigns between March 2022 and March 2023, including colour and spectral measurements, portable X-ray fluorescence (p-XRF), and surface measurements of pH and other parameters on over 60 rock samples on Murujuga. They also collected rock varnish samples to analyse the microbial population (MRAMP, 2023). In addition, a total of 18 weather stations that also measure the air quality were set up by the team all over Murujuga. For the purpose of these here presented studies, the colour, p-XRF, and pH measurements are of most interest.

The pH measurements were conducted within each field campaign across Murujuga, providing the most detailed insights into the rock surface pH. Their method was based on the technique described by MacLeod and Fish (2021; MRAMP, 2022). The measured pH from the first campaign, with a median close to neutral conditions, differed significantly from the pH measured during the three following campaigns, which showed quite acidic and decreasing median pH values below a pH of 5. These differences are also clearly visible in a spatial interpolation of the measured pH (MRAMP, 2023). The variation between the first campaign and the subsequent ones might be explainable by different weather conditions, such as temperature and days since the last major rainfall event, as suggested by the authors (MRAMP, 2023).

The colour measurements were carried out using a JAZ spectrophotometer, which is no longer produced or officially supported by the manufacturer. The measurements are displayed as reflectivity spectra by the instrument. This complicates comparisons with previous measurements and studies that used the more common L*a*b colour space. During the campaigns, the team run into problems with cooling the device and had to place it in a freezer cube (MRAMP, 2023). The results in the report are all presented as plots showing the wavelength and reflectance of the measured spots. There are observable differences between the different field campaigns (MRAMP, 2023), but the results are not comparable to other colour measurements conducted on Murujuga. The team aimed to address problems encountered in previous studies related to colour measurements, which failed to ensure that the same area was measured each time, and were therefore criticised (Lau et al., 2007, 2010; Markley et al., 2015; Duffy et al., 2017; Black et al., 2017a). To tackle this, the MRAMP team used a method to relocate the measured area by comparing pictures from prior measurements with live views provided by a phone camera connected to the spectrometer probe using a frame. The frame also shielded the measured area from ambient light sources. The device used for colour measurements is highly sensitive to the measurement angle, so a holder tube was added to the frame to ensure the same angle and distance to the sample (MRAMP, 2023). Despite difficulties with data conversion and the right placement of the device, the authors claimed to have achieved standard deviations for $L^* = 0.28$, for $a^* = 0.21$, and for $b^* = 0.19$ (MRAMP, 2023), which are still quite high compared to the standard deviations determined in this study (Chapter 4.2.1.1) and previous work (Neumann et al., 2022).

For the p-XRF measurements, the authors assume a penetration depth of up to 5 mm, which leads them to conclude that their measurements reflect not only the rock varnish composition, but also the weathering rind and the bulk rock (MRAMP, 2023). This conclusion is partly questionable, given that other p-XRF measurements of the rock varnish have yielded results consistent with the expected varnish composition, such as the Fe-oxide concentration, indicating that most of the measured volume is made up of the varnish (Neumann, 2021). Instead of monitoring the change on the rock surface from campaign to campaign to observe possible changes in the chemical composition of the surface, as done in other studies (Neumann et al., 2022), the authors only use the data to differentiate the different rock types found on Murujuga (MRAMP, 2023).

The air quality monitoring has already been set up and started and first results show that CO, NO_2, NH_3, H_2SO_4, and SO_2 concentrations are highly increased over the central part of the peninsula, where the industrial complexes are located, compared to remote sites (MRAMP, 2023). However, the comparison of the measured pH with the gas concentrations shows not clear correlation (MRAMP, 2023).

The MRAMP study is by far the most extensive research conducted on Murujuga to date, and especially the initial results from the pH measurements appear promising. Additionally, the establishment of a dense network of weather and air quality monitoring stations across Murujuga is highly beneficial. However, some methodological approaches may have inherent flaws and could be prone to inaccuracies, such as the colour measurements, which are known to depend heavily on precise sample repositioning (Neumann et al., 2022; see Chapter 2.1).

All the aforementioned studies show that, to this day, there has been no systematic and reliable study employing diverse analytical methods to assess both chemical and physical weathering effects, nor any study comparing weathering rates from Murujuga with those from areas unaffected by anthropogenic pollution but subjected to similar weather and climate conditions. Such an actualistic experimental approach could yield robust and reliable data, potentially guiding governmental decisions about further industrial developments on Murujuga and aiding in the creation of strategies to protect the rock art. Nevertheless, there are three intrinsic challenges that make it extremely difficult to accurately quantify the overall natural weathering rates of the varnish surface:

(1) At surface temperature conditions, the weathering of the varnish and natural rocks is a relative slow process compared to the typical human lifespan, making it analytically difficult to precisely quantify surface weathering rates through short-term laboratory or field tests. This challenge has prompted researchers to apply more extreme weathering conditions, such as lower pH or elevated temperatures, in their experiments to accelerate chemical reactions and transport processes (Lau et al., 2007; Přikryl et al., 2003; Sitzia et al., 2021). However, such studies face the issue that reactions and / or transport mechanisms, and thus the kinetics of weathering, may change with varying conditions, leading to the valid counterargument that the results cannot safely be extrapolated back to natural surface conditions (Sulzbach & Geisler, 2024).

(2) Natural rocks and, particularly, desert varnishes are mineralogically, texturally, biologically, and chemically heterogeneous materials, which inherently exhibit varied local responses to acid solutions or, more generally, to any chemical, biological, and physical weathering processes.

(3) The exposure of the rocks (e.g. petroglyphs) to environmental factors such as sunlight, wind, rain, and marine aerosols from the sea can differ significantly from site to site. This leads to variations in the physico-chemical conditions experienced by individual cultural objects, further complicating the assessment of weathering rates and the effects of pollution.

Considering the first problem, recent research shows that it is possible to detect significant chemical, colour, and textural changes on the varnish surface after artificial weathering of Murujuga rock varnish samples in a climate chamber for up to four months (simulating two years on Murujuga) using portable X-ray fluorescence (p-XRF) spectrometry, colorimetry, and micro-computed X-ray tomography (μ-CT; Neumann et al., 2022). This study found that colour changes on the rock surface can already be detected after only one month of artificial weathering with much lower standard deviations compared to previous (Lau et al., 2007, 2010; Markley et al., 2015; Duffy et al., 2017) and ongoing studies (MRAMP, 2023). It was also possible do determine significant changes in the chemical composition due to the artificial weathering including a decrease in the surface MnO concentration (Neumann et al., 2022). These results were only made possible by specific analytical and data evaluation protocols that ensured exact and accurate measurements of the same rough surface before and after weathering - an essential requirement for producing reliable and usable data. Other studies to date lack these critical methodological standards. Moreover, it was demonstrated that even a single rainfall event can dissolve measurable amounts of material, particularly Fe and Mn, as shown by ICP-MS analysis with a very low detection limit (Neumann et al., 2022) compared to other similar studies (Ramanaidou et al., 2017). Neumann et al. (2022) also showed that the rate of weathering and degradation is highly dependent on the rock type and the properties of the varnish. The degree of chemical and physical weathering was found to vary and could be resolved analytically on a centimetre scale (Neumann et al., 2022). This study was designed as preliminary work for a more extensive investigation that is presented in this work, simulating accelerated weathering in a controlled climate chamber experiment included different sample groups exposed to conditions that simulate both the present environment on Murujuga and anticipated conditions before industrial development.

The second problem, as well as the third, is harder to overcome, as the range of conditions in natural environments is vast, and it will not be possible to simulate such a large number of different conditions. Therefore, it is necessary to focus weathering experiments on the main components that influence weathering processes (e.g. pH). Additionally, it is essential to use varnish samples with a wide variety of varnish types to account for the heterogeneity of varnish surfaces.

1.2 Objectives of this study

The natural weathering of rock varnish, such as those associated with the petroglyphs on Murujuga, is a highly complex process that depends on a large number of parameters, including (1) the precipitation rate and rainwater composition, (2) air and varnish surface temperature, (3) rock surface inclination, (4) humidity, (5) varnish composition and texture, (6) solar radiation, (7) wind, (8) atmospheric marine aerosol concentration, and (9) microbial activity. These parameters even vary on a very local scale on Murujuga, which is directly reflected by the observable variations in the degradation of the petroglyphs. This variability makes it extremely difficult to precisely quantify the overall natural weathering rate of the petroglyphs and rock varnish. As a result, it also complicates the reliable quantification of any additional impacts from anthropogenic pollution on the degradation rate. This study aims to overcome the problems faced in previous studies, while accounting for the known difficulties in investigating and analysing the weathering processes, as well as the physical and chemical effects on the rock varnish (see Chapter 1.1). It is crucial to provide robust and comparable data to proof or disproof the hypothesis that the local industrial emissions on Murujuga are accelerating the weathering of the rock varnish and the petroglyphs carved into it. Additionally, the study seeks to enhance the understanding of the entire weathering process. The study's concept acknowledges the complexity of the problem by integrating two experimental sets, where the degree of complexity increases progressively. In these experiments, the most significant parameters were controlled.

The first part of this study aims to understand the varnish chemistry, mineralogy, and structures, which were not investigated in detail to this day. Therefore the chemical composition of the varnish surfaces, as well as the microstructures of the varnish and its mineralogy were determined using XRD, p-XRF, Raman spectroscopy, and EMP analyses (see Chapter 3.1.3).

To test the impact of the rainwater composition and pH on the rock varnish and its weathering, the second part of this study involved a climate chamber experiment. In this experiment, varnish-bearing granophyre and gabbro samples from Murujuga were subjected to weathering under controlled conditions for a total of one year, simulating six years of Murujuga climate. In contrast to a previous study, which proved that it is possible to quantify chemical and physical changes in the varnish over small time periods with the right analytical methods (Neumann et al., 2022), this study utilised two different groups of samples that were weathered simultaneously in the same climate chamber. These samples were subjected to different artificial rainwater compositions, representing the anticipated composition without industrial emissions (pH $\approx$ 7.0) and with the influence of industrial emissions (pH $\approx$ 5.0). The used rock samples were measured before, after, and during short breaks in the weathering experiment with various methods like p-XRF, colour measurements, high-resolution optical imaging, and µ-CT scanning, which have provided reliable and robust data in previous studies (Neumann et al., 2022). This experiment, conducted under controlled conditions, aims to determine whether the changes in rainwater composition and pH, that have occurred on Murujuga due to industrial emissions, affect the weathering rates of the petroglyphs (see Chapter 4).

Since the varnish texture and mineralogy significantly affect the weathering rate of the varnish, each sample may weather differently (Neumann et al., 2022). Therefore, glass dosimeters provided by the Fraunhofer Institute for Silicate research (ISC) additionally were placed in the climate chamber experiment to monitor the simulated weathering. The data from the climate chamber experiment will be used to calibrate the degree of weathering of the glass dosimeters against chemical, textural, mineralogical, and colour changes of the varnish surface. The Fraunhofer Institute has utilised different types of silicate glass as dosimeters, depending on the expected corrosion potential of the studied conditions. In this study three different types of glass compositions were tested.

Furthermore, to investigate the pH dependence of rock varnish dissolution and degradation, including the dissolution dependence on the dip of the varnish surface, irrigation experiments were conducted using artificial rainwater with a pH ranging from 8.0 to 3.0, along with rock samples from Murujuga with an intact varnish layer which were irrigated at different surface angles. The artificial rainwater was collected and analysed using inductively-coupled optical emission spectroscopy (ICP-OES, see Chapter 5). It has already been demonstrated that significant changes in the artificial rainwater composition can be observed after just a 15 minute long weathering event conducted in the same manner (Neumann et al., 2022).

The main hypothesis tested in this study is if anthropogenic pollution from various industrial sites on Murujuga accelerates the degradation of the Murujuga petroglyphs, which are carved in the rock varnish of the different rocks on the peninsula. To test this hypothesis, an experimental programme under controlled conditions, using different compositions of rainwater and pH levels was designed, as outlined above and in more detail in Chapter 4.1 and 5.1.

In addition, this study aims to provide new insights to the Muruujga rock varnish chemistry and mineralogical compositions, as well as to the pH dependence of the dissolution rates of the main components of the varnish. Also the conducted experiments are aimed to provide necessary information on how a long-term field study on Murujuga could yield further insights into the mechanisms controlling the degradation of the varnish, particularly the impact of anthropogenic pollution on these processes. Such a field study has to consider the different conditions based on the location on the peninsula, including (1) the recorded chemical and colour changes on the varnish surface on various sites, (2) the distance from industrial sites, (3) the recorded very local weather conditions, (4) the local aerosol corrosion potential, and (5), if data is available, the distribution of air pollutants across the peninsula.

1.3 Geology of Murujuga

Murujuga, also known as Burrup peninsula, is located on the northern coast of Western Australia. Murujuga translates to “hip bone sticking out” (Bird & Hallam, 2006, p. 15) in the Aboriginal language, referring to the shape of the peninsula. The main part of the peninsula extends approximately 25 km from north to south and 6 km from east to west with an area of around 110 km^2. It is also called Burrup peninsula due to Mount Burrup, the highest point on the peninsula (Ramanaidou & Fonteneau, 2019). The peninsula is surrounded by numerous island. North of the peninsula are Dolphin, Angel, Gidley, and Legendre Islands, while in the west the East Lewis, West Lewis, Malus, Enderby, and Rosemary Islands are located. A few kilometres south of the peninsula is the town of Karratha. The Murujuga National Park occupies the eastern part of the peninsula (Fig. 1.2), whereas the western part contains large industrial facilities and the town of Dampier, including the port of Dampier. The peninsula and surrounding islands formed only around 7,000 years ago due to rising sea levels (Mulvaney, 2022). The Geological Survey of Western Australia has mapped the whole area at a scale of 1:100,000. All rocks found on the peninsula, the surrounding islands, and south of the peninsula are part of the Pilbara Craton (Hickman, 1997), which is one of the few Archaeon cratons in the world and contains some of the oldest rocks found on Earth (Donaldson & Bednarik, 2011). Some parts of the craton have been dated at 3.27 Ga old (Hickman et al., 2006) and can be found south of Karratha. The oldest rocks on Murujuga are granites that are around 3.12 Ga old (Hickman, 1997) and can be found on a few outcrops all over the peninsula. The main part of this so-called Dampier Granitoid Complex lies between Karratha and the peninsula (Hickman, 1997), but is overlaid by Holocene sediments (Fig. 1.2). The Dampier Granitoid Complex dips at an angle of 25° to the north-west, along with the overlying younger rocks of the Hamersley Basin (Donaldson & Bednarik, 2011). The rocks of the Hamersley Basin have been dated by radiogenic methods at 2,725 ± 5 Ma old (Wingate, 1997), making up the vast majority of rocks found on Murujuga and the surrounding islands. The mainland of the peninsula and Dolphin Island consist of granophyre (also called Gidley granophyre) in the western part and gabbro in the eastern part. The gabbro is divided into normal gabbro in contact with the granophyre and a quench gabbro in the most eastern part of the peninsula and Dolphin Island (Hickman, 1997). Angel and Gidley Islands, west of Dolphin Island, are composed entirely of granophyre. Some parts of the Peninsula and the islands are covered by Holocene sediments (Fig. 1.2). The islands west of the peninsula consist of igneous rock from the Fortescue Group, which also belongs to the Hamersley Basin, and is primarily composed of basalts (Hickman, 1997). Some smaller outcrops of gabbro and granophyre can also be found (Hickman, 1997; Ramanaidou & Fonteneau, 2019).

The quench gabbro in the easternmost part contains some needle-like pyroxene crystals that can reach lengths of up to a metre, indicating rapid cooling of the magma. This gabbro has a slightly different chemical composition compared to the overlying gabbro, making it unsuitable for rock art. Consequently, very few petroglyphs can be found on the surfaces of quench gabbro rocks (Donaldson & Bednarik, 2011). The overlying gabbro is coarser-grained, and its mineral texture indicates a very slow cooling rate (Donaldson & Bednarik, 2011). The uneven and rough surface, due to the coarse grain size - some minerals reaching diameters of nearly a centimetre - makes it quite unsuitable for engravings (Donaldson & Bednarik, 2011). Most petroglyphs are therefore found engraved into the granophyre rocks on the eastern part of the peninsula, as well as on Dolphin and Gidley Island (Bird & Hallam, 2006). This granophyre is fine-grained and can be found as pillars formed by cooling fractures at certain sites. These cooling fractures form a landscape dominated by large boulders that are scattered around and are stacked upon each other (Ramanaidou & Fonteneau, 2019). Due to the small grain size, the surface of the granophyre is smoother and more even than that of the gabbro (Donaldson & Bednarik, 2011).

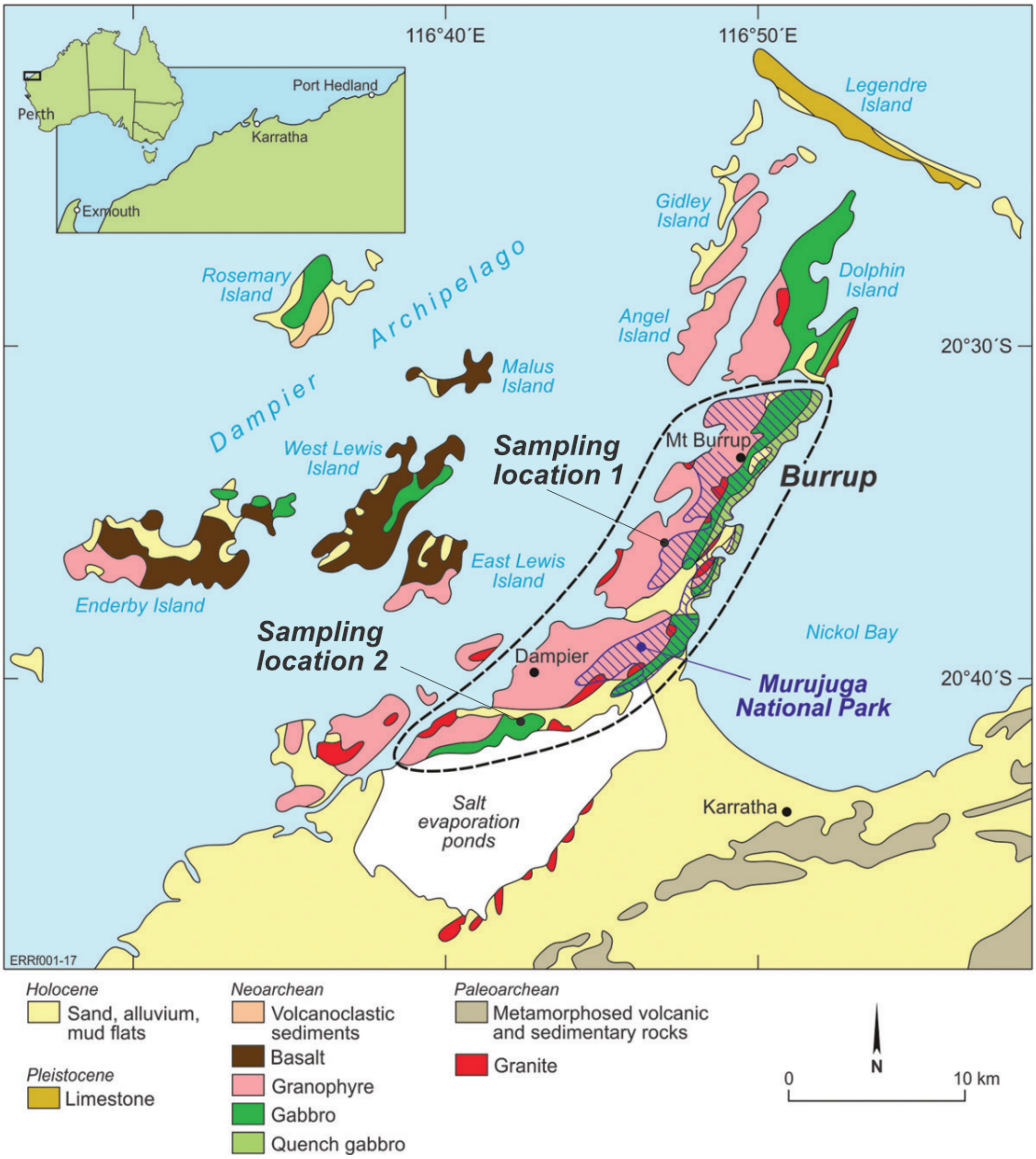

Figure 1.2: Geological map of Murujuga. The Murujuga National Park as well as the sampling locations where the used rock samples were collected are shown on the map. Adapted from Ramanaidou & Fonteneau (2019).

The rock types were classified due to their chemical and mineralogical composition. The chemical composition was examined by Donaldson & Bednarik (2011) and also by Neumann (2021), revealing significant differences. Quench gabbro and gabbro are relatively similar in their composition, both having a SiO_2 content of around 50 wt. %. The gabbro contains far less SiO_2 than the granophyre, which has around 70 wt. %, but more Al_2O_3 as well as approximately ten times the amount of CaO (around 10 & 1-2 wt. %, respectively; Tab. 1.1). The Fe_2O_3 content of the gabbro is also higher than that of the granophyre, as well as the MgO content. Both rock types contain nearly no MnO with concentrations of only 0.15 wt. % in the gabbro and

0.07 to 0.08 wt. % in the granophyre samples. Both types of rock also contain small amounts of P_2O_5 and SO_3, as well as around 0.5 wt. % TiO_2. The Na_2O and K_2O contents of the granophyre are higher than of the gabbro (Tab. 1.1).

Table 1.1: Chemical composition of the granophyre and gabbro host rock from different sources. The bulk rock composition was examined by Geoscience Australia (Donaldson & Bednarik, 2011) and in an earlier study (Neumann, 2021).

Element (oxides)	**Gabbro* (wt. %)**	**Gabbro$^+$ (wt. %)**	**Granophyre* (wt. %)**	**Granophyre$^+$ (wt. %)**
SiO_2	52.10	50.25	71.44	70.23
Al_2O_3	16.72	17.03	12.40	12.35
Fe_2O_3	7.59	8.86	4.39	4.69
MnO	0.15	0.15	0.08	0.07
MgO	7.70	7.55	1.08	1.82
CaO	11.12	10.95	1.66	0.69
Na_2O	1.79	2.00	3.56	4.53
K_2O	0.69	0.45	3.75	2.57
TiO_2	0.48	0.48	0.52	0.54
P_2O_5	0.05	0.02	0.14	0.12
SO_3	0.05	0.09	0.03	0.07
LOI	0.92	2.58	0.56	1.06
Total	99.84	100.55	99.81	98.85

*(Donaldson & Bednarik, 2011)

$^+$(Neumann, 2021)

Gabbro and granophyre are hard and dense rocks that resist chemical and physical weathering, which is why they remain preserved despite their old age (Donaldson & Bednarik, 2011). On both rock types, a weathering rind with a thickness of up to 10 mm can be found (Bednarik, 2002). This rind consists mainly of clay minerals as kaolinite from weathered feldspar, unweathered quartz crystals and some Fe-oxides from weathered pyroxene on the granophyre (Donaldson & Bednarik, 2011). In other parts of Western Australia, similar rocks exhibit a much thicker weathering rind due to relatively low erosion rates compared to the area around Murujuga. As a result, the rocks on Murujuga appear relatively fresh given their age (Donaldson & Bednarik, 2011). The angular-shaped boulders are slowly rounded over time trough erosion and spalling (Bednarik, 2002). The outermost layer of the rocks is a very thin layer known as desert varnish, which is crucial for the petroglyphs that were pecked into the rock surface and will be described in the following.

For the conducted experiments varnish-bearing samples of the granophyre and gabbro rocks from Murujuga were used, which were collected on Murujuga in different locations shown in Fig. 1.2. The sample characterisation and preparation is further detailed in Chapter 3.1.1.

1.4 Petroglyphs of Murujuga and rock varnish

Petroglyphs appearance

Murujuga is renowned for its vast number of petroglyphs, which are scattered across the peninsula and some of the surrounding islands. It is estimated that more than one million petroglyphs exist throughout the area, making it the region with the densest concentration of rock art in the world (Bird & Hallam, 2006). These petroglyphs are believed to be up to 30,000 years old (McDonald, 2005; Mulvaney, 2010, 2013; McDonald, 2015). Some sources mention that they might perhaps be as old as the first settlements in Australia around 50,000 years ago (Bird & Hallam, 2006). Determining the exact age of the petroglyphs is challenging, and estimates vary between sources (Vinnicombe, 2002; Bednarik, 2007). However, it is known through C-14 dating that the Pilbara region, which Murujuga is a part of, has been inhabited for at least 30,000, and perhaps as long as 35,000 years (Law et al., 2010).

The petroglyphs were carved into the rock by the Aboriginal people living in the area. To this day, it has not been possible to document all of the petroglyphs (McDonald & Veth, 2009). The entire landscape with its petroglyphs provides valuable insights into the secular and sacred live and traditions of the Aboriginal people (Bird & Hallam, 2006), making it one of the most important heritage sites in Australia. This significance has been recognised since the 1960s, leading to various archaeological field trips that confirmed the area's immense value for scientific research and as a cultural heritage site (Bird & Hallam, 2006). Despite this recognition, industrial development continued and concerns about the threat to the petroglyphs have grown over the past years (Chapter 1.1). As a result, the petroglyphs on the peninsula were nominated for the National Trust Endangered Places List in 2002. In 2003, Murujuga became the first site in Australia to be added to the World Monuments Fund's list of the most endangered places (Bird & Hallam, 2006). Subsequently, in 2004, a large part of Murujuga was nominated for the National Heritage List and it was officially included in July 2007 (Donaldson & Bednarik, 2011). In 2020, the archaeological sites on Murujuga were added to the tentative list of the UNESCO to become world heritage (UNESCO, 2020). In 2023, the federal government formally nominated the peninsula for the world heritage listing despite the possible endangerment (ABC News, 2023). The petroglyphs remain of great importance to the Aboriginal community on Murujuga and in the surrounding areas, even tough no new petroglyphs are being carved any more. Some of the sites are still used for ceremonial purposes. The Murujuga Aboriginal Cooperation (MAC) overseas everything regarding the petroglyphs including their protection and development (Murujuga Aboriginal Corporation, 2024).

The petroglyphs display a wide range of motifs (Figs. 1.1 & 1.3), including geometric shapes, animals, animal tracks, and even humans or anthropomorphous figures. Some motifs also show other objects like weapons (Vinnicombe, 2002) and the distribution of these motifs varies from site to site. Within the groups of motifs there is also a wide variety. For example, the animal figures include turtles (Fig. 1.3), fish, birds, reptiles, and mammals such as kangaroos (Fig 1.1). The human or anthropomorphous motifs also exhibit a great level of variety, from simple stick figures to filled-in figures with varying body proportions (Vinnicombe, 2002; McDonald & Veth, 2009). Due to the age of the petroglyphs, some depict now extinct animals. For instance, various depictions of the Thylacine, commonly known as Tasmanian tiger, have been found on Murujuga (Mulvaney, 2009). Most of the motifs are smaller than 30 cm, while others range between 30 and 60 cm with only a few images exceeding 60 cm in size (Veth et al., 1993). The smallest motifs are less than 4 cm in diameter and show all kinds of figures and the largest reach up to 150 cm (Vinnicombe, 2002).

The petroglyphs are not evenly distributed across Murujuga, due to the various types of rock found on the peninsula. The gabbro located on the eastern part of the peninsula and the northern islands has a rougher and more uneven surface compared to the granophyre in the western part of the peninsula and northern islands (Donaldson & Bednarik 2011, see Chapter 1.3). This aligns with the sites listed in Bird & Hallam (2006) and other sources (Pillans & Fifield, 2013). There are more sites in the western part of the peninsula and Dolphin island, with a high concentration near the western coastline. Fewer sites are listed along the eastern coastline. On the islands west of the peninsula (Fig. 1.2), a few sites with petroglyphs have been found in areas consisting of basalt, granophyre, and gabbro (Bird & Hallam, 2006).

Various techniques were used to create the petroglyphs. The instruments employed ranged from small, fine tools used for drawing narrow lines, to simpler tools for pecking marks in the rock surface, or other instruments that were rubbed across the surface to produce lines (Vinnicombe, 2002). Most motifs were pecked into the surface with tools of different diameters, varying from a few millimetres to a centimetre or more (Vinnicombe, 2002). Depending on the method, the petroglyphs penetrate the rock to different depths, either deeper or more shallow (Bednarik, 2002; Mulvaney, 2009). One type of petroglyphs was created by merely removing the dark varnish, exposing the brighter, weathered layer beneath, which creates a sharp colour contrast. These petroglyphs have nearly no relief, making them vulnerable to weathering. If new rock varnish forms after engraving or the leftover rock varnish erodes, the petroglyphs become nearly invisible (Bednarik, 2002). The other type of petroglyphs is pecked deeper into the rock, removing not only the varnish but also parts of the underlying weathered rind. This type of petroglyphs can have a relief of more than 10 mm. While the contrast may also diminish over time due to varnish growth or weathering, the higher relief ensures they remain visible (Bednarik, 2002). The different stages of weathering result in varying degrees of contrast, as described by Mulvaney (2009), ranging from ancient petroglyphs with no visible colour contrast, which are only discernible by their deep relief, to petroglyphs with moderate contrast, and those with a sharp colour contrast that remain visible despite a shallow relief.

Figure 1.3: Various examples of the petroglyphs found on Murujuga and the typical landscape with large boulders stacked over each other (uppermost picture). The images show different types of petroglyphs displaying animals, tracks and geometrical figures characterised by a different degree of degradation. The picture in the lower left corner shows flaking due to physical weathering. All photos were taken by T. Geisler-Wierwille in 2019.

Due to the different types of petroglyphs and the varying depth of their relief, the colour contrast - and consequently the rock varnish itself - is crucial for the visibility of a large number of petroglyphs on Murujuga. Accelerated weathering of the varnish could lead to the irretrievable destruction of some of these petroglyphs (see Chapter 1.1). On top of that, since the beginning of the industrial development on Murujuga, a significant number of petroglyphs have already been destroyed or damaged due to various construction projects across the peninsula (Bednarik, 2002).

Rock varnish composition and formation

The chemical and mineralogical composition of rock varnish differs from that of the weathered rind of granophyre and gabbro or the bulk rock itself. Rock varnish, sometimes also refereed to as dessert varnish, can be found in various locations all over world, primarily in arid to semi-arid climate zones (Potter & Rossman, 1979; Dorn, 2007, 2009; Krinsley et al., 2017; Macholdt et al., 2017; Lingappa et al., 2021; Rabbachin et al., 2022). Petroglyphs have been carved into this thin varnish in different locations and across various time periods (Rabbachin et al., 2022; Donze et al., 2024). The varnish is generally enriched in Fe- and Mn-oxides and it is also composed of clay minerals (Potter & Rossman, 1977, 1979; Dorn, 2009; Krinsley et al., 2017; Gleeson et al., 2018). This definition of rock varnish composition, first provided by Potter & Rossman (1977), has been widely accepted and remains unchanged (Dorn, 2024). The Mn-oxides in the varnish of samples from California were identified as mainly birnessite with a particle size below 0.1 µm, while the Fe-oxides were found to be predominantly hematite (Potter & Rossman, 1979). Other studies reported todorokite and birnessite as the main Mn-oxide-phases in samples from various locations in the United States (McKeown & Post, 2001). In rock varnish samples from Arizona, fine-grained ($<$ 100 nm) minerals from the hollandite-todorokite group were identified, alongside birnessite and buserite, all of which contain Mn. The Fe-oxides were determined to be hematite and goethite by other researchers (Garvie et al., 2008). In rock varnish samples from India birnessite was found in all samples, but not in the associated host rock. Here, only goethite was found in the rock varnish samples and hematite and magnetite were only identified in the host rock samples (Chaddha et al., 2024).

The outermost 5 to 10 µm of the varnish in samples from the Negev Desert in Israel were found to be depleted in Mn compared to the rest of the varnish (Goldsmith et al., 2014), while on other samples researchers proved that this thin, outermost layer was enriched in Pb (Broecker & Liu, 2001). Several researchers observed a layering of the varnish, with some layers being rich in clay minerals and others containing higher concentrations of Mn- and Fe-oxides (T. Liu & Broecker, 2008; Xu et al., 2019). The clay minerals were found to be predominantly montmorillonite and illite (Potter & Rossman, 1977), while other researchers also identified smectite and kaolinite (Garvie et al., 2008). In rock varnish from the Gobi Desert, additional minerals, including goethite, anatase, rutile, and quartz, were identified alongside birnessite and hematite (Xu et al., 2019). The mineralogy of rock varnish samples from Murujuga has not yet been fully analysed and only one very recent has confirmed that the described layering is also present in the rock varnish from Murujuga and tried to examine the mineralogy of the varnish (MRAMP, 2023).

Depending on the source, the estimated varnish thickness varies from up to 200 µm (T. Liu & Broecker, 2000; Gleeson et al., 2018) to 500 µm (Potter & Rossman, 1979), or even between 5 µm and 1 mm (Krumbein & Jens, 1981). Varnish samples from the Pilbara region, near Murujuga, were found to be 75-150 µm thick (Flood et al., 2003). Rock varnish can consist of up to 70 % of clay minerals, primarily kaolinite and montmorillonite (Black et al., 2017b), and may also contain quartz, carbonates, and organic material (Krumbein & Jens, 1981). Some chemical analyses show that other types of rock varnish consist of up to 23 wt. % of MnO and up to 21 wt. % FeO (Potter & Rossman, 1979). Varnish samples from various other sources were found to contain less Mn than the samples analysed by Potter & Rossman (1979). For example the samples analysed by Dorn which contained between 5 % (Peru) and 22 % (South Australia) Mn and between 12 % (Peru) and 23 % (Egypt) Fe (Dorn, 2020). The Fe-Mn ratio varied from 0.6 to 2.4 (Dorn, 2020). Potter & Rossman (1979) differentiated between black varnish, which has Fe-Mn ratios between 0.5 and 1.3, and orange varnish, which contains nearly no Mn, leading to ratios of up to 100. Similar results were found by other researchers who measured black and red varnish and found a Fe-Mn ratio of 2.5 on the black varnish and 5.9 on the red varnish, which only contained 0.8 % Mn (Rabbachin et al., 2022). Rock varnish samples from the Negev Desert in Israel showed no correlation between Mn and Fe concentrations. However, most analysed samples had Fe contents ranging from 7.5 to 15 wt. %, while Mn concentrations were approximately 10 to 20 wt. %. The majority of these samples contained more Mn than Fe, resulting in Fe-Mn ratios of less than 1 (Goldsmith et al., 2014). Varnish samples from the Gobi Desert predominantly contained 8 to 13 % MnO, with FeO contents measured mostly between 8 and 11 %, yielding Fe-Mn ratios around 1 for most samples. This study also found no correlation between Fe and Mn content (Xu et al., 2019). Varnish samples from California and Nevada were found to have a wide range of Mn and Fe concentrations, ranging from 0.08 to 14.12 wt. % and 4.01 to 16.20 wt. %, respectively (Harmon et al., 2021). Other samples from the United States were found to have Mn contents ranging from 10 to 15 wt. % and Fe-Mn ratios < 1, due to Fe contents of only 5 to 13 wt. % (Wayne et al., 2006).

Due to the different compositions of rock varnish and the various environments where it can be found worldwide, a classification of different types of varnish was proposed. The varnish was categorised based on its origin and chemical composition. This classification resulted in five proposed types of varnish, three of which are relevant for this study. The first proposed type occurs in arid deserts and exhibits a fine laminated structure, with a slightly lower Mn content compared to types II and III. These latter types are typically found in semi-arid to arid and semi-arid environments, respectively and lack distinguishable layering but exhibit a higher Mn content than the laminated type. Types II and III can be further distinguished by their Pb content, which is significantly lower in type III compared to type II (Macholdt et al., 2017). The samples used to define these categories originated from various sites and, except for some samples collected near rivers (which were categorised as another type), contained approximately 2 to 30 wt. % Mn and 4 to 10 wt. % Fe. The Fe-Mn ratios in most samples ranged from < 1 to approximately 6 (Macholdt et al., 2017).

The varnish samples analysed for this study contained between < 1 wt. % and 9.10

wt. % MnO and < 10 to 41.85 wt. % Fe_2O_3, leading to Fe-Mn ratios between 3 and > 100 (Tab. 3.1). A more detailed analysis of the varnish samples can be found in Chapter 3.1.3.1. It should be noted that all rock samples were measured using p-XRF (Chapters 2.2.2 & 3.1.3.1) and therefore parts of the samples that are not composed entirely of the varnish can also be included in the measurements due to a varying penetration depth and some parts of the samples with no intact varnish on them. The measurements indicate that the analysed varnish samples were enriched in Fe and Mn compared to the underlying weathered rind and bulk rock (Tab. 1.1), even though the Mn content is significantly lower than in varnish samples from other sources mentioned before. The Fe-Mn ratios of the rock varnish on Murujuga, along with the varnish composition and structure of the rock samples used from Murujuga, are further examined and discussed in Chapter 3.1.3.

Due to the high contents of Fe- and Mn-oxides, rock varnish is mostly described as reddish-brown, brown, or even black (Krumbein & Jens, 1981; Potter & Rossman, 1979; Gleeson et al., 2018). On Murujuga, the varnish varies in its colour, with some parts being red or orange, while others are darker, ranging from brown to black (Figs. 1.1, 1.3, 3.1, 3.2 & 3.3). In addition to variations in thickness and colour, the surface structure of rock varnish also differs. It is thinly layered (Gleeson et al., 2018; Lingappa et al., 2021), and while some samples have uneven, rough surfaces with visible pores, others appear more even, with metallic lustre, and show no visible pores or cracks (Fig. 3.1).

It is not yet fully understood how rock varnish forms or which processes lead to the relative enrichment of Fe- and Mn-oxides. An abiotic theory, suggesting that varnish is formed by the oxidation of Mn and Fe, has been around for multiple decades (Krinsley et al., 2017; Goldsmith et al., 2014; Gleeson et al., 2018). This theory states that carbonic acid in rainwater leaches Mn from the accumulated dust on the rock surface, which then re-precipitates due to a slight pH increase caused by the evaporation of rainwater (Dorn, 2007; Krinsley et al., 2017). However, the anticipated growth rates for this mechanism are much higher than the observed or calculated rates, which argues against this mechanism (Krinsley et al., 2017). Furthermore, the theory fails to explain the enrichment of Fe-oxides (Dorn, 2024), as the small pH differences may not be enough to dissolve the Fe, which has a lower mobility than Mn but is also enriched in the rock varnish (Goldsmith et al., 2014). Recent publications argue strongly against a model that explains the varnish formation solely through abiotic processes (Chaddha et al., 2024; Dorn, 2024).

Another theory explains the formation of the rock varnish with the presence of a silicate gel created by bacterial activity, which incorporates material into the varnish (Perry & Kolb, 2004; Perry et al., 2005). This theory, while not as widely discussed as the others, has also faced criticism because it cannot explain all aspects of rock varnish formation (Dorn, 2024).

It is widely accepted that the presence of budding bacteria, capable of processing Mn and Fe, as well as enriching and cementing Fe- and Mn-oxides, plays a role in the varnish formation process. These bacteria have been found at many different sites with rock varnish (Krumbein & Jens, 1981; Flood et al., 2003; Krinsley et al., 2012; Esposito et al., 2015; Krinsley et al., 2017; Gleeson et al., 2018; Lingappa et al., 2021). Some theories try to explain varnish formation entirely with biotic processes, such as the presence of *Cyanobacteria* growing on the rock (Lingappa et al., 2021), or through the activity of large microbial communities (Krumbein & Jens, 1981). Just as theories excluding biotic processes have faced criticism, these theories, which exclude abiotic processes, have also been recently criticised (Dorn, 2024).

Lingappa et al. (2021) observed a high number of *Cyanobacteria* on the varnish surface in various samples they analysed, and demonstrated that a specific *Cyanobacteria*, called *Chroococcidiopsis*, can absorb Mn-oxides that arrive as dust on the rock surface and are then reduced by different processes. These *Cyanobacteria* can concentrate Mn by up to 50 times compared to the surrounding environment. They proposed a model for varnish formation, in which these *Cyanobacteria* play the most important role: growing on sun-lit surfaces, their Mn-enriched biomass is oxidised after they die, which then forms the Mn-oxides found in the varnish (Lingappa et al., 2021). This hypothesis was criticised for focussing solely on Mn enrichment. It fails to explain the Fe enrichment in varnish, the formation of clay minerals that make up a significant portion of the varnish, as well as providing no explanation for varnish found on surfaces that are not exposed to sunlight (Dorn, 2024).

Based on the known presence of budding bacteria and the problems with theories that only involve biotic or abiotic processes, a polyenetic model of varnish formation has been proposed by various authors, combining both biotic and abiotic elements (Dorn, 2009; Krinsley et al., 2012, 2017; Dorn, 2024). In this model, it is assumed that the components needed for varnish formation are first deposited on the rock surface, for example, by wind-blown dust. Then, the budding bacteria incorporates Fe and Mn into their cells. These bacteria are later broken down by abiotic processes, which fragment the Fe- and Mn-rich cells. These fragments are then transported into the clay minerals of the rock varnish through abiotic processes (Krinsley et al., 2012, 2017; Dorn, 2024). Recent publications assert that this hypothesis can explain major challenges faced by other theories, such as Fe enrichment, the small number of microfossils within rock varnish, and the slow growth rates (Dorn, 2024; Chaddha et al., 2024). One of the primary issues is explaining the very slow growth rate of varnish, estimated to be between < 1 and 40 µm per 1,000 years (T. Liu & Broecker, 2000). Analyses of varnish samples with known ages at sites with faster growth rates compared to warm desert environments, such as Murujuga, suggest that even the occurrence of one budding bacterium every 400 years could result in a growth rate of around 20 µm per 10,000 years (Krinsley et al., 2017). Considering these estimated slow growth rates, the existence of rock varnish is linked to very slow rates of erosion. For Murujuga, these erosion rates have been estimated at around 0.34–2.30 mm per 1,000 years on vertical surfaces and 0.15–0.48 mm per 1,000 years on flat surfaces (Pillans & Fifield, 2013). These proposed erosion rates are higher than the expected rates of varnish growth. The fact that the varnish on Murujuga remains intact suggests that either the growth rates must be significantly higher, or the erosion rates were overestimated. Additionally, the low Mn content of the Murujuga rock varnish compared to other types of rock varnish elsewhere remains noteworthy.

In summary, the question of how rock varnish forms on Murujuga is not easy to answer, but it is most likely a combination of biotic and abiotic processes that leads to varnish formation. The presence of budding bacteria appears to be necessary. The exact process on Murujuga, as well as the growth rates, still need to be analysed in detail, along with the question of why the Fe-Mn ratio is comparably high in most of the rock varnish samples from Murujuga.

1.5 Climate and weather on Murujuga

Murujuga is located around 20.6° south and has been described as having a tropical arid climate (Gentilli, 1971). The winter between June and September is warm and dry, while the summer, from October to May, is significantly hotter and wetter (Jones, 2004). There are no weather stations on Murujuga itself that are operated by an official government institution with available datasets over several years. The closest station that is run by the Bureau of Meteorology of the Australian Government, is located at the Karratha Airport (20.71°S, 116.77°E), with data available since 1971.

The highest temperatures have been recorded between December and February with a very recent all time maximum of 48.4 °C in January 2022. The highest mean maximum temperature is also reached in January with 36.1 °C. Only between June and August the mean maximum temperature is below 30 °C. These three months are also the only ones with a mean minimum temperature below 15 °C. The lowest ever recorded temperature was 6.9 °C in July 2006. In summer, the mean minimum daily temperatures are around 26 °C (Australian Government, Bureau of Meteorology, 2023).

Rainfall occurs mostly during the warm summer months, reaching the highest mean rainfall of 76.4 mm in February, with an average of 5.1 days of rain. The winter months are much drier, especially September, October and November, with a mean rainfall of below 1.5 mm and less than one day of rain. The mean annual rainfall between 1972 and 2023 was 297.2 mm. Heavy rainfall events occur irregularly over the summer months due to cyclones, such as in February 2020 (ABC News, 2020). These and other events can result in very high precipitation in certain months or years, such as those in February 2011 with a total of 348.8 mm, or the year 2006 with an annual rainfall of 855.4 mm (Australian Government, Bureau of Meteorology, 2023). Some single major rainfall events, like cyclone Damien in 2020, can bring up to 235 mm of rain within 24 hours (MacLeod, 2021).

Due to its proximity to the equator, solar exposure is relatively high, with a mean daily solar exposure of 6.33 kWh/m^2. May to July are the only months with a mean daily solar exposure below 5 kWh/m^2. Between November and January, values of up to 7.94 kWh/m^2 per day are reached (Australian Government, Bureau of Meteorology, 2023).

Table 1.2: Climate data used for the simulation in the climate chamber. All data is from the weather station at the Karratha Airport run by the Bureau of Meteorology of the Australian Government (Australian Government, Bureau of Meteorology, 2023), with the exception of the humidity data, which was obtained from an alternative source, but originally recorded by the same weather station (Weather Underground, 2023).

Month	Temp.* max. (°C)	Temp.* min. (°C)	Hum.** max. (%)	Hum.** min. (%)	Prec.*** (mm)	Mean days of rain	Solar exposure (kWh/m^2/d)
Jan	36.1	26.9	83	45	45.7	4.0	7.5
Feb	35.7	26.8	85	46	76.4	5.1	7.1
Mar	36.2	26.1	83	40	45.8	3.9	6.6
Apr	34.4	23.0	81	34	17.4	1.8	5.7
May	30.0	18.4	78	33	32.2	3.2	4.7
Jun	26.5	15.2	80	35	34.4	3.2	4.2
Jul	26.5	13.9	78	30	14.0	1.9	4.7
Aug	28.3	14.4	77	25	4.0	1.1	5.6
Sep	31.0	17.1	75	23	1.4	0.4	6.6
Oct	34.0	20.8	76	28	0.4	0.3	7.5
Nov	35.0	23.1	75	30	1.3	0.4	7.9
Dec	36.0	25.7	78	36	14.4	1.4	7.9

* Temperature; ** Humidity; *** Precipitation

Unlike other climatic parameters, the Bureau of Meteorology does not publish maximum and minimum daily humidity data. However, the hourly values of all parameters that are recorded by the weather station at the Karratha Airport are available (Weather Underground, 2023) and the daily maximum and minimum humidity was analysed for the years 2018 to 2022 to calculate mean maximum and minimum daily values for every month. Between July and November the mean daily humidity is the lowest with mean maximum values between 75 and 78 % and mean minimum values between 23 and 30 %. The highest humidity with a mean daily maximum of 85 % and minimum of 46 % occurs in February, which is also the month with the highest average mean rainfall.

For the climate simulation performed in this study the weather data from the Bureau of Meteorology of the Australian Government was used. The monthly mean maximum and minimum temperatures were based on data collected over the past 30 years, while the mean monthly rainfall was derived from records spanning the last 46 years. The monthly values for mean daily solar exposure were available for the past 33 years and the mean number of rainy days per month has been reported for the last 50 years (Australian Government, Bureau of Meteorology, 2023). As previously mentioned, the mean daily maximum and minimum humidity was not published. The data was thus collected from an alternative source that provides humidity data for a duration of only five years (Weather Underground, 2023). All data utilised in the climate simulation is presented in Tab. 1.2.

2 Analytical methods

2.1 Colorimetry

The colour measurements were carried out with a CR-410 chroma meter from Konica Minolta at the Institute for Geosciences of the University of Bonn. All calculations were performed using the L*a*b colour space, as it allows for easy calculation of the colour difference ΔE. Additionally, this colour space is commonly used in other published research on Murujuga petroglyphs and rocks, facilitating straightforward comparisons (Lau et al., 2007; Markley et al., 2015). Although the initial measurements were taken with the XYZ colour space, these values were converted to the L*a*b colour space. This was necessary since the used software from Konica Minolta can only process values within the XYZ colour space.

The measured area of the CR-410 chroma meter has a diameter of 50 mm, which is the reason why all rock samples weathered in the climate chamber were cut into a disk-like shape with this diameter. Colour measurements of smaller samples that do not completely fill the measured area present a problem: the measured colour does not represent the actual colour of the sample, and the calculated ΔE values may not be as precise due to white space in the background which, however is also measured (Neumann et al., 2022). Furthermore, measuring samples smaller than the total measured area increases susceptibility to errors, as it must be precisely ensured that the background used for the measurements remains unchanged. For the chroma meter, the manufacturer specifies a standard deviation of ± 0.07 for the calculated ΔE values. This requires measurements to be taken within the operating range of the chroma meter (0-40 °C & a maximum humidity of 85 %). The measured area with a diameter of 50 mm is illuminated by a pulsed xenon lamp (Konica Minolta, 2020).

For the measurements, all samples were placed on a Teflon© plate to ensure consistent sample placement and alignment of the chroma meter. This Teflon© plate had 16 marks around the measured area, as all samples were rotated during the measurements to average the influence of surface roughness and varying reflections on the sample surfaces based on its position (Fig. 2.1). This rotation process resulted in 16 individual measurements per full measurement on each sample. Each sample was measured four times during each session (equivalent to 4 sets of 16 individual measurements). Across all 11 measurement cycles of the climate chamber samples a total of 11,264 single measurements were carried out on the 16 rock samples used (11 measurement phases with 4 sets of 16 measurements for each of the 16 samples).

Additionally the samples used for the irrigation experiments were also measured with the same analytical protocol.

For calculating the colour change ΔE after each measurement, an average of the 4 sets of measurements was calculated, following an initial average calculation of the 16 individual measurements to combine them into a single total. The propagated measurement errors are provided within a 95 % confidence interval. The first measurements, taken before the weathering or irrigation experiments began, served as the reference values for calculating the colour change ΔE. Additionally, for the climate chamber experiment, step-to-step changes were calculated using two consecutive measurements.

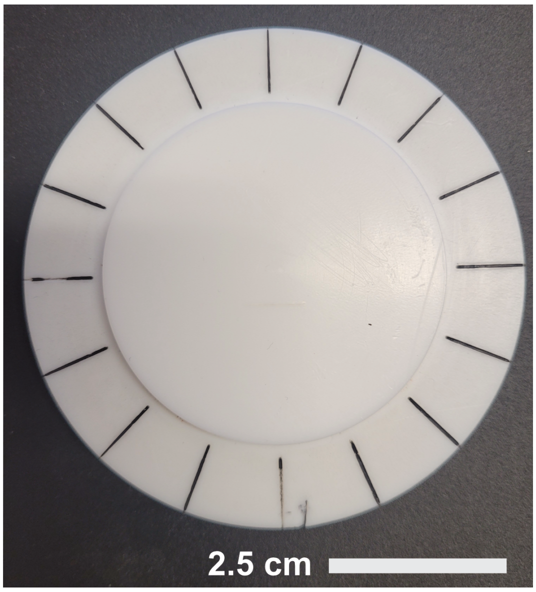

Figure 2.1: The Teflon© plate that was used for the colour measurements. The marks on the outer ring were used to turn the chroma meter by the same angle during every measurement.

The colour difference ΔE, along with changes in brightness (ΔL*) and the chromatic components (Δa* and Δb*) of the samples, were examined. ΔL* is a significant parameter in addition to ΔE, as changes in brightness are crucial for addressing the underlying research questions. This is due to the fact that petroglyphs are visible primarily because of the colour contrast between the dark rock varnish and the brighter underlying rock, which becomes exposed when the varnish is removed. If the varnish gradually dissolves or its brightness changes, reducing the contrast, the petroglyphs could eventually disappear (Bednarik, 2002).

ΔL*, Δa* and Δb* were calculated using the following formulas:

$$\Delta L^* = L_1^* - L_2^*$$

$$\Delta a^* = a_1^* - a_2^*$$

$$\Delta b^* = b_1^* - b_2^*$$

Here, L_1^*, a_1^*, and b_1^* represent the initial values measured before the weathering experiment began, while L_2^*, a_2^*, and b_2^* are the values, measured during the intermediate pauses of the weathering experiment, as well as the final values measured after the weathering experiment.

The colour difference ΔE was calculated using the following formula (International Organization for Standardization, 2020):

$$\Delta E = \sqrt{(L_1^* - L_2^*)^2 + (a_1^* - a_2^*)^2 + (b_1^* - b_2^*)^2}$$

The actual measured colours were displayed and visually compared using the programme Affinity. For this purpose the L*a*b colours converted into HEX colour codes, as none of the available image processing software could display L*a*b colours with two decimals.

The rock cubes for the irrigation experiments were also measured using the CR-410 chroma meter from Konica Minolta. Unlike the samples for the weathering experiment, the rock cubes were smaller than the measured area, which causes minor issues as aforementioned, as well as described in Neumann et al. (2022). Despite this, the rock cubes were measured using a similar Teflon© plate with the same size and markings around it (Fig. 2.1). The only difference between this plate and the one used for the weathering experiment samples was a small mark in the centre of the plate to ensure that the rock cubes were properly positioned within the centre of the measured area. If the samples were not centred, the results from the 16 circular measurements taken per full measurement would vary widely, leading to a larger error. The rock cubes were measured before the irrigation experiments and after every two experiments with the same type of artificial rainwater. Each measurement cycle consisted of 4 full measurements per rock cube, calculated from 16 individual measurements taken at different angles. The first measurements, taken before the initial irrigation experiment, served as the reference values for calculating the colour change. The propagated measurement errors are reported at the 95 % confidence level.

It should be noted that the results from the irrigation experiments do not reflect the actual colour of the samples, as the samples, with dimensions of 2 x 2 cm^2, account for only 20 % of the chroma meter's measured area. The background, which constitutes approximately 80 % of the measured area, remains unchanged throughout the measurements. Consequently, all calculated values for ΔE, ΔL*, Δa*, and Δb* represent only around one-fifth of the actual change on the sample surface.

2.2 X-ray fluorescence spectrometry

2.2.1 Benchtop X-ray fluorescence spectrometry (XRF)

A Malvern Panalytical Axios WDXRF (wavelength-dispersive X-ray fluorescence) analyser, located at the Institute for Geosciences of the University of Bonn, was used for the benchtop XRF measurements. Na, Mg, Al, Si, P, S, K, Ca, Ti, Mn, and Fe were measured as main elements using currents of 50–120 mA and voltages of 24–60 kV, depending on the element. Each element was measured for 12 to 24 seconds, resulting in a total measuring time of 16 minutes per sample. In addition various trace elements were measured with the same settings. The rock and varnish samples used for the XRF measurements were taken from spare parts of the collected rock samples (Chapter 3.1.1). A total of six samples were analysed: one varnish sample from the gabbro, one from the granophyre, and two samples from each rock type without varnish. Prior to the measurements, the samples were ground and compressed into press tablets. Additionally, the loss on ignition (LOI) was determined before compressing the samples. Since Mn was measured only as a trace element, its concentration in the varnish samples exceeded the calibration range.

2.2.2 Portable X-ray fluorescence spectrometry (p-XRF)

For the p-XRF measurements of the samples weathered in the climate chamber, an X-MET 7500 mining analyser from Oxford Instruments was used (Oxford Instruments, 2013). The device consists of a large-area silicon drift detector and a 45 kV X-ray tube, which is capable of detecting all elements between Mg and U (Oxford Instruments, 2013). The measured area is a circle with a diameter of 10 mm (Neumann, 2021). The X-MET 7500 comes with some factory-calibrated measurement programmes, but it is also possible to create and calibrate custom measurement programmes. In contrast to previous work (Neumann, 2021), an individual programme was developed and calibrated using samples of the rock and rock varnish employed in the study. These samples were measured with a XRF at the Institute for Geosciences of the University of Bonn (Chapter 2.2.1).

The written programme calculates the Cr, Sr, and Ba contents in ppm and the MgO, K_2O, SO_3, Fe_2O_3, TiO_2, SiO_2, P_2O_5, MnO, Al_2O_3, and CaO contents in wt. %. Cr, Sr, and Ba were chosen as trace elements due to their relatively high concentrations compared to other trace elements that were measured with the benchtop XRF. All elements lighter than Fe are measured using a voltage of 13 kV and a current of 10 mA with the $f = 0.4$ filter, while heavier elements are measured at 45 kV and the same current, also using the $f = 0.4$ filter. The programme was calibrated using a total of 6 pressed tablets composed of gabbro and granophyre varnish (one each) and host rock (two per rock type), all measured with the benchtop XRF. These samples were measured three times for 120 s each to serve as calibration standards. For the calibration, the X-MET 7500 compares the given results for the calibration samples with the measured intensities and the relationship between these two values was described for all elements using a linear equation. After excluding individual values for some elements, all linear equations had a correction coefficient of R > 0.9. The standard measurement time for this programme was 60 s, divided into two times 30 s for the two different analytical settings described above.

All rock samples for the climate chamber experiment, including the reference samples, were measured before and after the weathering experiment as well as during each measurement pause (Fig. 4.2), resulting in a total of 11 sets of data. Each sample was measured 15 times for 60 s per measurement, leading to a total of 11 sets of 15 measurements per sample, and 2,640 individual measurements across the entire experiment. An average value was calculated from each of these 15 single measurements. These average values were then normalized to 100 % because the total sum of the measured elements varied over the time on all samples. This was likely due to a slightly different distance between the sample an the measuring head, even if the samples were always placed as close as possible to the measuring head. This led to different absolute values which would falsify the calculated changes without a normalization to 100 %.

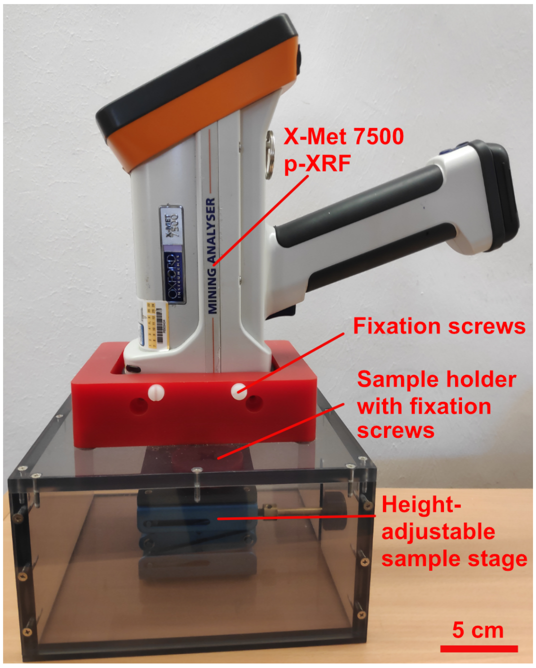

Figure 2.2: Sample holder for the X-Met 7500 consisting of a holder for the p-XRF with fixation screws on four sides around the measuring head and a height adjustable table with a holder for the rock samples with fixation screws on two sides.

Due to the inhomogeneous surface of the samples, the measured values for the different elements varied from sample to sample. For better comparability of the observed changes, the change Δ_{el} (%) was calculated as a percentage value using the initial measurements taken before the start of the climate chamber experiment as a reference. This allowed the Δ_{el} (%) for the different measured elements to be compared across all samples in a consistent manner. It was noted that the values for the reference samples changed from measurement cycle to measurement cycle more than expected, despite the fact that these samples were stored under controlled conditions throughout the experiment (see Chapters 4.1.1 & 4.2.1.4). To correct for this, the mean Δ_{el} (%) of the reference samples for each measurement cycle was subtracted from the observed Δ_{el} (%) of the samples weathered in the climate chamber to correct the results. The propagated measurement errors are reported at the 95 % confidence level.

Ensuring that the exact same area of the sample surfaces is measured during each cycle is crucial, as small changes in positioning can lead to significantly different results. To achieve consistent measurements, a sample holder developed for previous research was utilised (Neumann, 2021). This sample holder includes a stand for the p-XRF, with fixation screws on four sides around the measuring head, which points downward into an acrylic glass casing containing a small percentage of lead to protect against X-rays. Beneath the measuring head is a height-adjustable table with a plastic holder for the rock samples, equipped with fixation screws on two sides (Fig. 2.2). After each individual measurement, the rock samples were unscrewed and reinserted into the holder to minimise systematic errors that could arise from slight variations in the positioning of the sample and the p-XRF. This measurement setup allows for the generation of reproducible data from inhomogeneous samples (Neumann et al., 2022).

The rock cubes used in the irrigation experiments were measured using a Niton XL3t GOLDD+ analyser from Thermo Fisher Scientific at the LVR Museum in Bonn. This analyser is equipped with an energy-dispersive silicon drift detector. The 50 kV X-ray tube, featuring a silver anode, improves detection limits for light elements. An 8 mm measuring spot and a polypropylene measuring window (4 µm) were selected for the measurements. The analyses were conducted using the Mining Cu/Zn measurement programme, which measures various elements with different filters over a duration of 95 seconds per measurement (Tab. 2.1). For the ‘Low programme’, only 5 seconds were selected, as the elements within this setting are not relevant to this study, and the results from these elements were not used. It was not possible to skip this programme or reduce the time to less than 5 seconds. The rock cubes were measured before the irrigation experiments and after every two experiments with the same type of artificial rainwater, resulting in a total of 7 measuring cycles. Each cube was measured 10 times per cycle. As with the p-XRF measurements using the X-MET 7500, it was essential to ensure that the same area on the rock cubes was measured each time. For this reason, a special sample holder was constructed from plastic, which could be placed in the same position on the external case, where the p-XRF was clamped during measurements. The sample holder featured four small pins that fit into pre-drilled holes in the external case and screws on two sides to secure the rock cubes (Fig. 2.3), similar to the sample holder used for the X-Met 7500 (Fig. 2.2). The rock cubes were removed and reinserted between each of the 10 measurements.

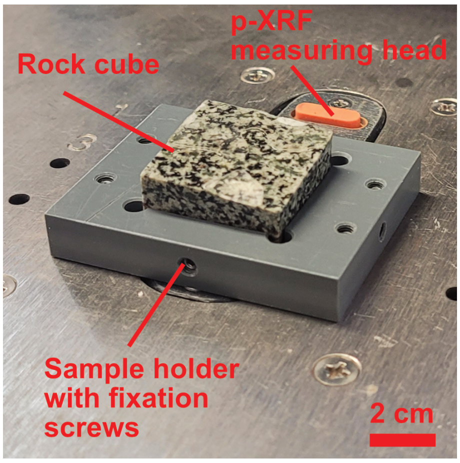

Figure 2.3: Backside view of the p-XRF setup that was used for measuring the rock cubes that consists of an external case for the p-XRF from Thermo Fisher Scientific and a special designed sample holder made out of plastic with two fixation screws to hold the rock cubes and small pins to hold the sample holder in place.

Table 2.1: Measured elements and acquisition time of the Mining Cu/Zn programme that was used for the samples employed in the irrigation experiments.

Programme	Elements	Time (s)
Standard	Mn, Fe, Co, Ni, Cu, Zn, As, Se, Rb, Sr, Zr, Nb, Y, Mo, Hf, Ta, W, Re, Au, Pb, Bi	30
Light	Mg, Al, Si, P, S, Cl	30
Medium	K, Ca, Ti, V, Cr	30
Low	Pd, Ag, Cd, Sn, Sb, Ba	5

The results from the measurements taken with the p-XRF from Thermo Fisher Scientific were reported as elemental weight percent rather than oxide weight percent, unlike the measurements from the X-MET 7500. The results also included a balance, which represents the percentage of elements present in the sample, but not measured by the programme. For the measurements taken, this balance was relatively high, at around 60 %. This may be due to the uneven surface of the samples, which leaves air between the sample and the measuring head, reducing the signal intensity. Due to this, the elemental results were normalised to account for the balance, improving the internal accuracy of the data. For instance, the Fe content measured, including the balance, ranged from 3 to 12 wt. %, and after normalising to the balance, it increased to between 9 and 40 wt. %, which aligns more closely with the results from the X-MET 7500. It is noted here that the errors of relative concentration changes are more important than the error of the absolute concentration. To ensure comparability, the change Δ_{el} (%) was calculated as a percentage value in the same manner as described previously, using the initial measurements taken before the start of the irrigation experiments as a reference.

2.3 Micro-computed tomography (μ-CT)

The μ-CT measurements were conducted at the Palaeontology Department of the Institute for Biology of the University of Bonn using a v|tome|x scanner from GE Sensing & Inspection Technologies GmbH, equipped with a 240 kV X-ray tube. All 16 rock samples used in the climate chamber experiment were measured once before and once after the experiment. The image stacks, consisting of 800 to 1,500 TIFF files depending on the sample height, were captured at a resolution of approximately 1,500 by 1,500 pixels, resulting in a total of about 1.5 to 3.5 billion voxels per scan, with a voxel size of 38 μm. This provides an approximately ten times lower resolution than the optical images taken (see Chapter 2.6). For prior research an other μ-CT with a significantly higher resolution of 6 μm was used (Neumann, 2021) but unfortunately the samples used for the weathering experiment in the climate chamber were to big to be scanned with the higher resolution μ-CT.

To analyse the changes that may have occurred during the climate chamber experiment, the models were compared using Dragonfly (Comet Technologies Canada Inc., 2024). Dragonfly automatically calculates the best-fit greyscale threshold to determine whether a voxel belongs to the sample. These values were used as thresholds. It was not possible to apply the same threshold for each pair of scans, as the greyscale values of the scans taken before and after the experiment differed. The programme can superimpose the loaded scans to reveal structural changes and detect material loss. For this purpose, Dragonfly performs a 3D registration, where the programme compares both models and superimposes them. The scale changes are evaluated with a step size of 0.001, the rotation with a step size of 0.5°, and the translation along all three axes with a step size of 0.001 mm. This method allows for the detection of material loss within the given resolution. Afterwards, with the use of different colour schemes, it is possible to make changes between the scan taken before and after the weathering experiment visible.

Two sets of scans from two of the samples could not be processed reliably due to their density and resulting dark colours, which made it impossible to determine proper greyscale boundaries to differentiate between the sample itself and the surrounding air. Due to this only 14 out of the 16 sets of scans were processed.

2.4 Inductively-coupled optical emission spectroscopy (ICP-OES)

The ICP-OES measurements were performed at the Institute for Geosciences of the University of Bonn using an iCAP PRO X DUO from Thermo Fischer Scientific. A total of 42 water samples collected during the climate chamber experiment and another 84 samples from the irrigation experiments were analysed. All samples were collected in Teflon© containers (Fig. 2.4), which were cleaned before each use (see Chapter 4.1.1). After collection, the water was transferred to plastic tubes, cleaned similarly, and 30 µl of concentrated HNO_3 were added per ml of sample to stabilise them. The samples were stored in a fridge until they were analysed.

The water samples from the climate chamber experiment were analysed for their P, S, Mn, Fe, Mg, Si, Ca, Sr, Ba, Na, Li, and K concentrations. For the measurements, 40 µl of a Sc solution and 40 µl of a Y solution, each with a concentration of 1000 ppm, were added as internal standards to 3 ml of sample. Calibration was performed using a stock solution containing various elements (Tab. 2.2; for these analyses, a solution without Al was used). Calibration solutions with dilution factors (DF) of 100, 250, 500, and 1000, along with a blank sample, were employed. SLRS-6 reference material (Yang et al., 2015) was used for calibration, once with a DF of 3 and once with a DF of 2, mixed with the stock solution at DF 250.

Figure 2.4: The different types of used Teflon© containers for collecting artificial rainwater samples. All containers have a lid that is removable to ensure that only water that was in contact with the rock varnish is collected in the containers. The larger containers (right) were used for the larger samples in the climate chamber experiment and the smaller containers (left) were used for the rock cubes from the irrigation experiment. One of the rock cubes with an angle of 30° can be seen on the top left side.

The samples from the irrigation experiments were analysed for Al concentrations and the same elements as the previous samples (Tab. 2.2). The stock solution used for the calibration standards was identical to that used for the other measurements, except that Al was added to the solution. Calibration standards with the same dilution factors (DF), along with an additional blank sample, were employed as previously described. Unlike before, 3.5 ml of each sample were used, and only 30 µl of Sc and 30 µl of Y solutions were added as internal standards. Due to Mn and S concentrations far exceeding the calibration range, some measurements had to be repeated. For these repeated measurements, only 20 out of the 84 samples were re-analysed, focusing solely on S and Mn content. Six calibration solutions, containing between 5 and 400 ppb of Mn and between 0.1 and 8 ppm of S were used, along with an additional blank solution. As internal standards, 30 µl each of In and Sc were added to 3.5 ml of the samples. SLRS-6 reference material (Yang et al., 2015) was again used for calibration.

Table 2.2: Contents of the stock solution used for ICP-OES calibration.

Element	Concentration
Ca	400 ppm
K	100 ppm
Mg	100 ppm
Na	100 ppm
S	100 ppm
Si	100 ppm
Mo	250 ppb
Ba	500 ppb
Li	500 ppb
Mn	5000 ppb
P	5000 ppb
Sr	5000 ppb
Fe	10000 ppb
As	10000 ppb
Al	9901 ppb

The artificial rainwater was made using demineralised water, which was subsequently mixed with a prepared stock solution to incorporate specific pollutants and achieve the desired pH values (Chapter 4.1.3.3). As a result, this rainwater contained very low concentrations of various elements. For data analysis, the element concentrations of the blank samples, collected alongside the other samples, were subtracted from those of the corresponding artificial rainwater samples that had been in contact with the rock varnish. This approach enabled the determination of the actual amount of material released into the collected water.

The accuracy and precision of the measurements were calculated using the internal SLRS-6 standard (Yang et al., 2015), which was measured a total of 39 times alongside the collected water samples. The accuracy for P was fairly good at 104 %, although

Table 2.3: Accuracy and precision of the elements measured using ICP-OES.

	Climate chamber experiment		Irrigation experiments	
Element	Accuracy (%)	Precision (%)	Accuracy (%)	Precision (%)
Si	84	3	84	1
Al	-	-	87	4
Mg	99	3	98	1
Fe	92	9	93	1
Mn	97	7	89	7
S	94	6	96	2
Ca	96	3	94	1
K	96	3	92	3
Na	93	2	93	1
Ba	79	17	79	1
P	104	43	63	38
Li	96	3	98	3

some measurements deviated significantly from the expected values, resulting in a precision of only ± 43 % for the samples from the climate chamber experiment. Despite this variability, the P results were included in the evaluation, as the large number of samples measured should provide a reliable overall mean value. For the irrigation experiments the accuracy for P was only 63 % and the precision was ± 38 %. Therefore the P results were excluded. The accuracy and precision for all other elements is given in Tab. 2.3 for both groups of samples.

For the samples from the irrigation experiments Mn and S concentrations exceeded the calibration range in the initial measurements and 20 samples were therefore re-analysed with an extended calibration range. All repeated measurements were within a range of ± 5 % of the initial values, demonstrating that the original calibration still provided reliable results even far outside the calibrated range. The results of the samples measured twice were averaged.

Element concentrations were calculated using multiple measurements for each element, where feasible. For all elements, one to three different wavelengths were measured in both axial and radial modes, resulting in two to six values per element. Only settings with a relative standard deviation of less than 6 % were used to calculate the mean concentrations for each element. Certain samples were excluded from the analysis due to issues with the internal standards, which produced unreliable results for these specific samples.

2.5 Raman spectroscopy

Raman measurements were carried out using a Horiba Scientific LabRam Evolution Raman spectrometer located at the Institute of Geosciences of the University of Bonn. The Raman spectrometer is equipped with a 2 W frequency-doubled Nd:YAG laser ($\lambda = 532.09$ nm), an electron-multiplier CCD detector, an automated x-y-z stage, and an Olympus BX41 microscope. For all measurements a grating with 600 grooves/mm, covering a wavenumber range from 70 to 1715 cm^{-1}, and a 50 and 75 μm spectrometer entrance slit was used, resulting in a spectral resolution of 2.1 ± 0.1 cm^{-1} and 2.8 ± 0.1 cm^{-1}, respectively, as given by the width of a Ne line at 1707.06 cm^{-1} that was recorded as "internal" frequency standard in all spectra by placing a Ne lamp into the beam path. A 50x long-working distance objective with a numerical aperture (NA) of 0.5 and a 100x objective (NA = 0.9) were used for measurements of surface phases and Raman mapping of varnish layers in polished thin section, respectively. With this setting, the diffraction-limited, theoretical lateral and axial (depth) resolution of a Raman measurements with the focus at the sample surface was 1.3 and 8.5 μm, respectively. However, these values should be understood as rough estimates as, e.g. the axial resolution at the surface also depends on the visible light absorption properties of the material investigated which is high for Fe- and Mn-phases.

Point-by-point hyperspectral Raman images were recorded with a 1 or 2 μm step size in x and y direction. Due to the sensitivity of Fe- and Mn-oxides against laser heating, which may cause phase transformations, the laser power at the sample surface was set to ≈ 1.0 mW. The Raman intensity at each point therefore had to be recorded for 40 to 90 s. The mineral phases were identified by the characteristic positions and relative intensities of their fundamental Raman bands using the RRuff data base (Lafuente et al., 2015) and data from previous Raman studies (De Faria et al., 1998; Julien et al., 2003; Chernyshova et al., 2007; Ostrooumov, 2017; Bernardini et al., 2019; Marshall et al., 2020). The data reduction and creation of hyperspectral false colour Raman images was carried out using the LabSpec 6 programme (Horiba, 2024). The Raman images show the 2-dimensional, micrometre-scale distribution of the identified mineral phases. However, as the varnish phases were intergrown with each other at the sub-micrometre scale, mixed spectra were unavoidable due to the limitation in the spatial resolution. The dominant mineral phase captured in a given Raman spectrum was therefore determined by the classical least-squares (CLS) fitting procedure. This mathematical procedure assumes that a multiphase spectrum is a simple mixture of the spectrum of each individual phase. At each point within the multidimensional spectral field, the CLS matching procedure finds a linear combination of reference spectra from the pure phases that best describe the respective raw spectrum, as described in more detail in Hauke et al. (2019). This procedure, at least partly, considers differences in the Raman cross sections of the different phases. Eventually, the image is generated by colouring each pixel (point) relative to the proportion of individual components in the spectrum. The false-coloured hyperspectral Raman images are presented in the unmixed mode that displays the phase with the highest fractional intensity within a Raman spectrum with a colour assigned to that phase (Hauke et al., 2019). The colour shading of a pixel from bright to dark further renders the total fraction of that phase, with bright and dark coding reflecting higher and lower fractions, respectively.

2.6 High-resolution optical imaging

High-resolution optical images of the rock samples were captured at the Westerwald campus of Hochschule Koblenz using a VHX-7000 from Keyence. The VHX-7000 is capable of producing high-resolution composite images of large surfaces with a wide depth of focus, allowing for sharp images of the rock samples regardless of surface irregularities. All samples were illuminated with the built-in ring light of the Keyence VHX-7000. A 30x magnification, combined with the integrated 4K camera, was used to capture the composite images, except for one sample (SR2), which was analysed at a 50x magnification. The depth of field was individually selected based on the surface characteristics of each sample but was consistently extended above and below the highest and lowest points of the sample by approximately 100 µm.

The light intensity was controlled by a manual rotary controller, which was set to one-quarter of the maximum intensity for all samples. The resulting resolution of the composite images was approximately 15,000 by 15,000 pixels, yielding a pixel size of 3 to 4 µm. The images were processed using Affinity and sets of three samples were manually adjusted to match the colour and lighting of the first image taken before the weathering experiment as good as possible. To visualise the changes that occurred between the images taken before and after the experiment, the colours of the post-experiment images were inverted and superimposed with the pre-experiment images, which retained their natural colours and were displayed with 50 % transparency. This method highlighted areas that became brighter during the weathering experiment, appearing in inverted colours - primarily blue and white tones - while areas that darkened were visible in the natural colours of the underlying images, mainly brown and reddish tones. The areas with visible changes were then compared side by side to illustrate the transformations that occurred. Due to different exposure of the images that were compared some areas on the samples, especially very bright areas, falsely looked as if they changed. Because of this it was not reliably possible to quantify the occurred surface changes and they were only analysed qualitatively. Some composite images had to be taken multiple times because the initial lighting intensity was set too high, resulting in overexposed pictures and a loss of detail.

The optical images of the glass dosimeters were taken by the Fraunhofer Institute for Silicate Research (ISC) at their Bronnbach site, with a Keyence VHX-970X. Single images were taken with both coaxial and ring lighting turned on at 100x and 300x magnifications. All images were captured immediately after the completion of the FT-IR measurements, without further delay, to ensure that the surface structures remained as close as possible to their condition when removed from the climate chamber.

2.7 DNA extraction

One granophyre and one gabbro rock were initially selected to investigate the microbial communities associated with rock varnish and their response to simulated weathering conditions. These rocks were carefully handled and split into four samples, representing the four sample groups in the long-term weathering experiment. One sample of each rock type was placed in the climate chamber experiment at each of the sides with different simulated conditions at pH 5 (acidic) and pH 7 (neutral). Samples of the rock varnish were collected at three distinct points during the experiment to monitor changes in microbial communities over time: (1) before the weathering experiment to establish baseline microbial community composition, (2) after 5 days of weathering, representing an early response to the simulated conditions, (3) after the weathering experiment (360 days), to assess long-term effects of the treatments.

The rocks were broken into smaller pieces using a disinfected hammer and chisel rather than a water-cooled table saw that was used to cut the other samples used in the long-term weathering experiment, which would have introduced external contaminants through the used tap water. A sterile scalpel was used to scrape small amounts of the surface material into sterile DNA-free tubes to collect parts of the rock varnish. This method minimised potential contamination during sample collection. The scraped off powders were then stored at -20 °C in a freezer until the final sampling was completed and DNA was extracted. However, to evaluate the potential contamination caused by the sawing process, one additional granophyre sample was cut and DNA samples were collected from its surface before and after sawing. It has to be noted that the collected samples not only contain parts of the varnish but also parts of the underlying weathered rind because the varnish was to thin to scrape it off without removing parts of the underlying layer.

DNA was extracted from the rock samples using the FastDNA Spin Kit for Soil (MP Biomedicals, 2024), following the manufacturer's protocol. A total of 42 DNA extractions were performed, corresponding to the collected samples from the four rock types and time points. The quality and concentration of extracted DNA were assessed using a NanoDrop spectrophotometer from Thermo Fisher Scientific. Out of these, 28 samples yielded DNA of sufficient quality for further sequencing and bioinformatic analysis.

The microbial community composition was analysed by amplifying the 16S rRNA gene, specifically the V4 hypervariable region, using the primers 16S-515F (GTGCCAGCMGCCGCGGTAA) and 16S-806R (GGACTACVSGGGTATCTAAT). The amplification was carried out using the HotStarTaq Plus Master Mix Kit (QIAGEN) under the following cycling conditions: Initial denaturation at 95 °C for 5 minutes, Followed by 30–35 cycles of denaturation (95 °C for 30 s), annealing (53 °C for 40 s), and elongation (72 °C for 60 s), with a final elongation step at 72 °C for 10 minutes. The amplified products were sequenced using the Illumina MiSeq platform at BMK Gene in Münster, Germany, following standard protocols.

The raw sequencing data was processed using the QIIME2 pipeline (Bolyen et al., 2019), with quality control, denoising, and chimera removal performed using the DADA2 (Callahan et al., 2017) to generate amplicon sequence variants (ASVs). Taxonomic classification of the 16S rRNA sequences was conducted using the Silva 138 database (Quast et al., 2012). The processed ASV and taxonomy data were integrated and analysed in R (R Core Team and others, 2013) using a combination of phyloseq (McMurdie & Holmes, 2013), microeco (C. Liu et al., 2021), ampvis2 (Albertsen et al., 2015), vegan (Oksanen et al., 2019) and ggplot (Wickham, 2016). Data visualisation included the generation of bar plots and heatmaps to highlight the relative abundance of dominant microbial taxa. Non-metric multidimensional scaling (NMDS) plots based on Bray-Curtis dissimilarities were used to assess community composition patterns among treatments.

Diversity metrics, including ASV richness and Simpson's evenness, were calculated for each sample. Differences in these metrics between rock types and experimental treatments were assessed using ANOVA. The microbial community composition was analysed using PERMANOVA, performed with the adonis2 function in the vegan package. Pairwise comparisons between groups were conducted with pairwise.adonis2. To further evaluate differences in microbial community composition, heatmaps of the most abundant genera were generated, and clustering patterns were examined.

The sampling, DNA extraction, as well as the data evaluation and interpretation were conducted in close cooperation with Dr. Sabina Karačić from the Institute for Medical Microbiology, Immunology and Parasitology of the University Hospital Bonn.

2.8 X-ray diffraction (XRD)

The mineral composition of the powder samples from the granophyre and gabbro varnish, which were used to produce press tablets, as well as the composition of the residue left in both glass tanks after the weathering experiment, were analysed using XRD at the Institute for Geosciences of the University of Bonn. The powder samples were placed in a standard sample holder. The XRD measurements were conducted with a D500 diffractometer from Siemens, which consists of a Siemens Kristalloflex 710D X-ray generator operating at 40 kV and 40 mA, a theta-2theta goniometer employing a graphite single crystal monochromator, and a scintillation detector. All samples were measured at angles ranging from 4° to 70° (2Θ) with a step size of 0.02° and an aperture of 0.2 mm. The measurement time per angle was set to 80 s, resulting in a total measurement time per sample of approximately 3 days.

The resulting spectra were analysed using Brukers TOPAS programme (Bruker AXS, 2024b) for quantitative and EVA programme (Bruker AXS, 2024a) for qualitative assessments of the mineralogy of the samples.

2.9 Electron microprobe (EMP)

To determine the chemical composition and the elemental distribution within parts of the rock varnish of the thin sections, a JEOL 8200 Superprobe electron microprobe (EMP) was used at the Institute for Geosciences of the University of Bonn. The thin sections were coated with Pd using a Cressington Sputter Coater 108 Auto for a duration of 40 seconds per thin section at the Palaeontology Department of the Institute for Biology of the University of Bonn. Pd coating was chosen instead of carbon coating to allow the examination of the carbon content on the samples.

The thin sections were analysed with an energy of 20 kV and a beam current of $2x10^{-8}$ A. Backscattered electron (BSE) images of all mapped areas on the thin sections were acquired. On the mapped areas, the abundance of Fe, Al, Si, S, Mn, C, Na, P, and Ti was measured. A total of four maps were acquired from four thin sections, which were cut from granophyre and gabbro rocks collected on Murujuga, as well as from a granophyre sample which was provided by Robert Bednarik. The element distribution maps were acquired at the same positions as the maps acquired by Raman spectroscopy. In Addition on the same areas some quantitative point measurements were taken with an energy of 15 kV and a beam current of $1.5x10^{-8}$ A. With this analyses the contents of Mg, Na, Fe, K, Ti, Si, Al, Mn, and Ca were examined.

2.10 Fourier-transform infrared spectroscopy (FT-IR)

The FT-IR measurements were conducted by the Fraunhofer Institute for Silicate Research (ISC) at their Bronnbach site, using a Nicolet 700 infrared spectrometer from Thermo Fischer Scientific to assess the state of glass corrosion. All measurements were performed in transmission mode, covering a spectral range from 400 to 4000 cm^{-1}. All dosimeters were measured prior to the start of the climate chamber experiment to determine its E0-value, which indicates the water content. This value is determined by the width of the OH absorption band at 3300 cm^{-1} in the infrared spectrum. After removal from the climate chamber, the dosimeters were shipped to the ISC within one day and stored there in a desiccator for 24 hours before being re-measured. The newly obtained E1-value allows for the quantification of the weathering effect by calculating the ΔE_{IR} value, which is the difference between the E0- and E1-values and reflects the extent of glass corrosion.

Each glass dosimeter was measured only once, as the measurements are highly accurate and precise. The reproducibility was therefore empirically determined by measuring six samples multiple times, yielding an estimated standard error of ± 0.002 given at the a 95 % confidence level. This standard error was applied to all measurements. Any measurements that deviated from the expected values were repeated at least twice to rule out measurement errors.

3 Sample characterisation

3.1 Rock samples with desert varnish

3.1.1 Rock sample preparation and collection

The used granophyre samples were collected on Murujuga by Prof. Dr. Benjamin Smith from the University of Western Australia in May 2022. A total of seven pieces of varying sizes were collected near a road close to the Karratha Gas Plant at 20°36’03.0”S and 116°46’56.2”E, at an elevation of 51 m. Two separate gabbro samples were collected by Dr. Ken Mulvaney on Murujuga in August 2022 from an old quarry site south of Dampier at 20°41’03.6”S and 116°42’33.7”E (Fig. 1.2). All samples were collected with the permission of the Murujuga Aboriginal Cooperation (MAC).

Subsequently, the samples were sealed in clean plastic bags and sent to the University of Bonn. After taking the first set of DNA samples, the pieces of granophyre and gabbro were cut and prepared (Chapter 4.1.3). The cut rock samples exhibited a wide range of varnish surfaces on the granophyre and gabbro. The differences on the granophyre surfaces were more pronounced than those on the gabbro surfaces. Some of the granophyre samples were very porous and contained deep holes in the varnish (Fig. 3.1; NR1 & SR1), while others had a very smooth surface without any visible pores but with a metallic lustre (Fig. 3.1; SR2 & N3). Due to the size of the granophyre pieces collected, it was not possible to cut out larger numbers of samples from the same pieces. From three pieces, two samples were cut and placed in the climate chamber in different sample groups (NR3 & SR2 were from the same piece, as were NR2 & SR3, as well as NR1 & SR1; Fig. 3.1). The reference samples were cut from different pieces that were too small to produce more than one sample per piece. The colours of the rock varnish also varied significantly. While the porous samples SR1 and NR1 had darker, often nearly black surfaces with some lighter, orange to brown and red areas, the samples NR2 and SR3 were overall lighter, displaying a more reddish-brown colour with only a few dark, nearly black spots. There were also visible differences between the samples within the same group. For instance, sample NR1 had significantly more red areas than its counterpart SR1. The third pair of samples, with more even surfaces, exhibited a red to black colour and was the most uniform compared to the other samples. It was evident that in some samples, parts of the varnish on the edges had potentially chipped off during the cutting process due to the physical force and movement exerted by the core drill used (Fig. 3.1).

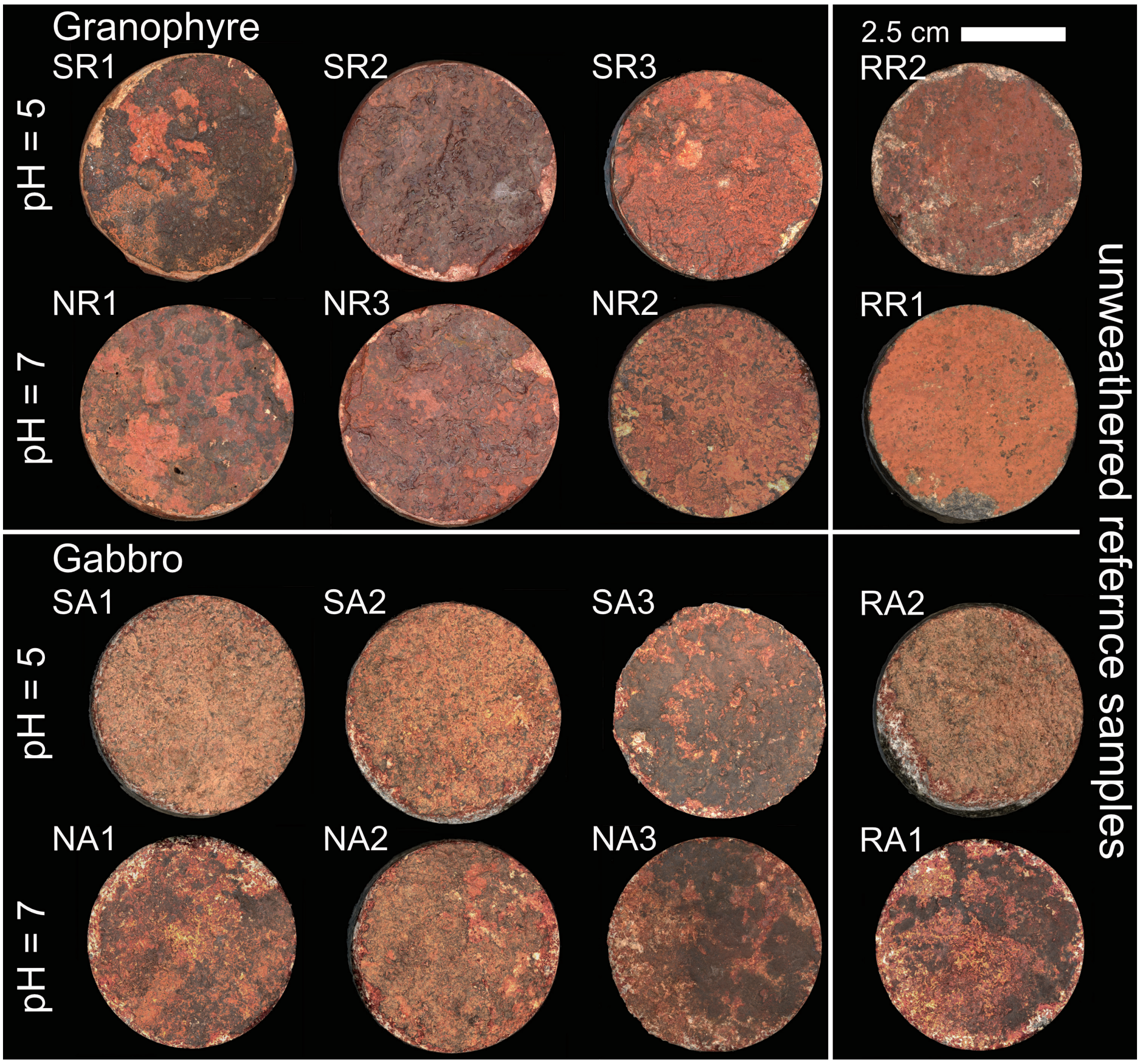

Figure 3.1: High-resolution optical microscope images of all 16 rock samples that were used for the artificial weathering experiment. Samples with a 'S' as first letter were weathered with artificial rainwater with pH ≈ 5.0 and samples with a 'N' as first letter were weathered with artificial rainwater with pH ≈ 7.0. The four samples on the right side with a first letter 'R' were not weathered.

The two collected gabbro samples were larger and had more homogeneous surfaces than the granophyre samples. The smaller of the two samples had a dark, nearly black, and relatively smooth surface, with some areas where the varnish had already chipped off, exposing an underlying brighter layer with orange to brown colours (Fig. 3.1; SA3, NA3 & RA1). From this piece, a total of three samples were cut, one of which was placed in each sample group in the climate chamber, while one was used as a reference sample. The second piece of gabbro collected had a more porous and uneven surface, which appeared slightly brighter, more orange-brown, and less metallic compared to the other piece of gabbro and most granophyre samples (Fig. 3.1; SA1, SA2, NA1, NA2 & RA2). Sample NA1 is an exception due to its surface, which differed slightly from the other samples cut from this piece of gabbro. Some areas on sample NA1 were darker and more similar to the gabbro samples cut from the first piece of rock.

For the irrigation experiment, a total of six cubes with dimensions of around 2 × 2 cm^2 and a height between 1.5 and 2 cm were used. Three of these cubes were cut from a piece of granophyre and the other three from a piece of gabbro. Both rocks were collected in 2019 by Thorsten Geisler-Wierwille on Murujuga, with permission from MAC, for previous research (Neumann et al., 2022). The surface of the gabbro cubes was significantly darker than most parts of the samples used in the climate chamber experiment. Moreover, because they were cut from the same piece, the gabbro cubes exhibited greater uniformity compared to the samples used in the climate chamber experiment. The surface of the cubes resembled certain parts of the gabbro samples SA3 and NA3 (Fig. 3.1), which were used in the climate chamber experiment.

Overall, the varnish on the granophyre samples was also darker than most parts of the varnish on the samples used in the climate chamber experiment. However, in comparison to the granophyre cubes, some additional orange areas were visible (Fig. 3.2). The surface of the granophyre cubes was less rough than the samples used in the climate chamber experiment, with fewer pores. The granophyre cubes were most similar to the samples SR1 and NR1, which were weathered in the climate chamber (Fig. 3.1).

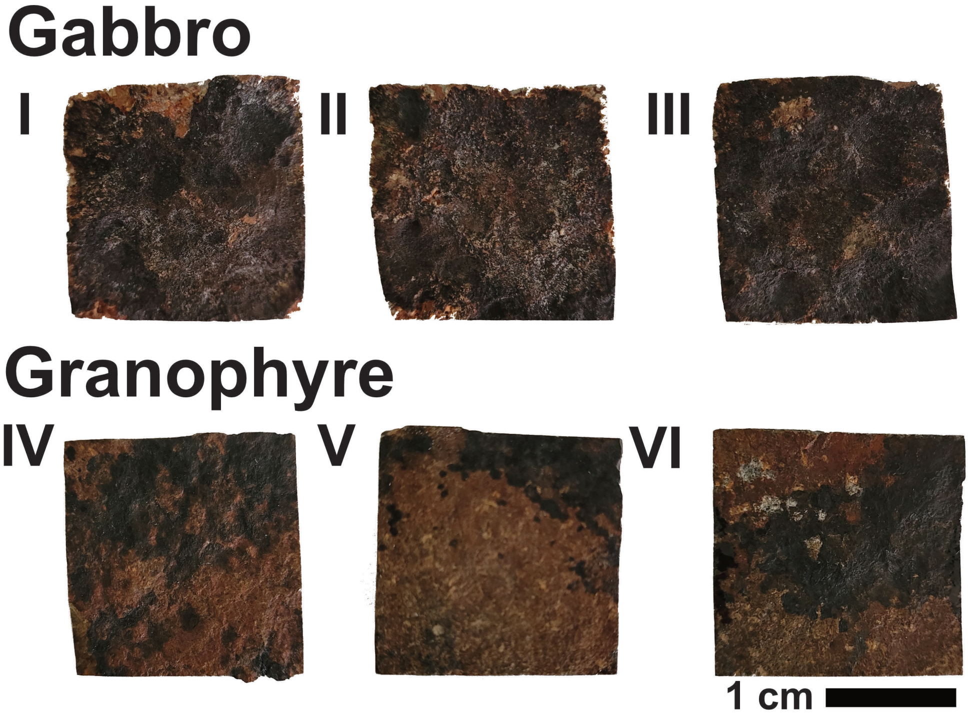

Figure 3.2: Images of the rock cubes used for the irrigation experiments.

In addition, a small granophyre sample with intact varnish was used to determine whether the varnish composition has already changed over time. The sample was provided by Prof. Dr. Robert Bednarik, who collected it in 1994 near the Woodside gas treatment facility on the west coast of Murujuga, a few kilometres north of Dampier. On the sample surface, intact black, orange, and red rock varnish was observed (Fig. 3.3), which was analysed using p-XRF. Additionally, a thin section was prepared to analyse the mineralogy and chemistry of the varnish using Raman spectroscopy and EMP.

It is known that varnish differs in colour and its composition also varies depending on the varnish colour (Potter & Rossman, 1979; Rabbachin et al., 2022). The varnish observed on the rock samples used in this study also exhibited considerable variation in colour, as shown in Figs. 3.1, 3.2, and 3.3. Some parts of the varnish were black and very dense, while others were red with a metallic lustre and a comparatively smooth surface. Most parts of the varnish on the samples could be described as orange to orange-brown, with a rougher and more porous surface structure compared to the red and black varnish. The granophyre samples SR1 and NR1 were the only samples with three types of varnish on their surface (Fig. 3.1), whereas the other samples exhibited only one or two types of varnish. The red varnish was found exclusively on the granophyre samples and not on the gabbro. The varnish described as orange differed between the granophyre and gabbro samples, appearing more brown on the gabbro samples, with a much more porous and rough surface (Fig. 3.1; RR1 & SA2).

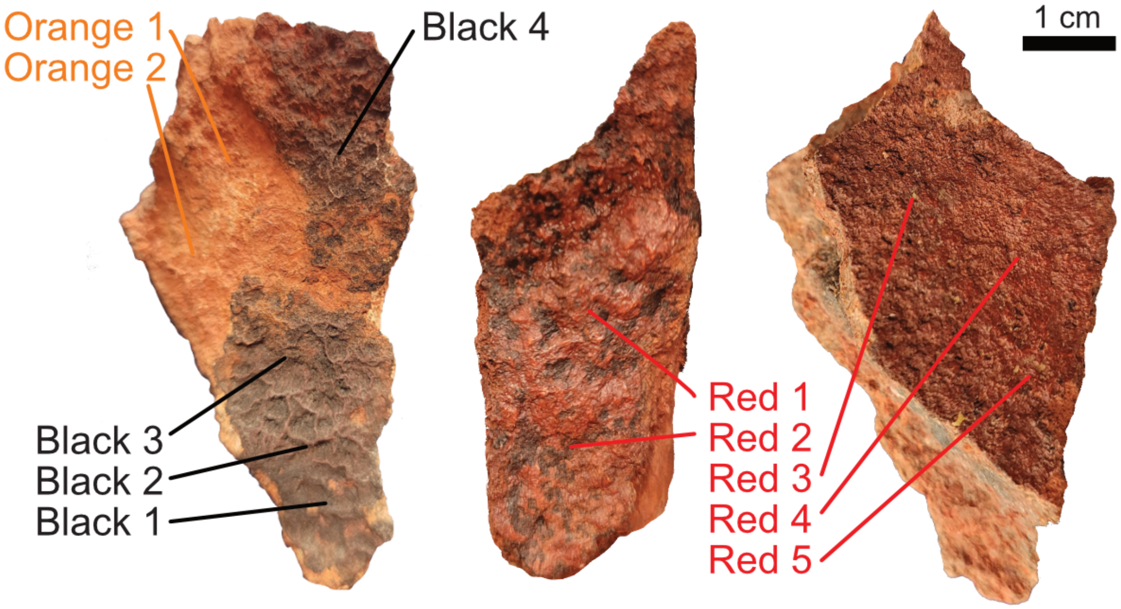

Figure 3.3: Different sides of the granophyre sample provided by Robert Bednarik with differently coloured varnish. The lines point towards the points where p-XRF measurements were taken to analyse the varnish composition (Tab. 3.2).

3.1.2 Hostrock petrography

A total of six thin sections from the granophyre and gabbro pieces collected in 2022 were prepared for further analyses. All thin sections included both the varnish and the weathered layer beneath, as well as the unweathered host rock. Under a petrographic microscope with polarised light, the mineralogical composition and structure of the different rock types were observed. The gabbro varnish was found to be partially destroyed and very thin compared to that of the granophyre. Beneath the varnish, a thick altered layer of up to 1 cm was visible (Fig. 3.4a). The intact gabbro contains small quartz and feldspar crystals, mainly plagioclase. Other mineral phases, such as rutile, were also visible (Fig. 3.4b & c). Additionally, mica, hornblende, and pyroxene were identified, as reported in a previous study (Neumann, 2021). The granophyre exhibits a thicker, more intact varnish, visible under the microscope as a small black rind. The weathered layer is thinner than that of the gabbro. The structure of the underlying rock is partly fine-grained but also contains larger alkali feldspar crystals that display twinning under polarised light (Fig. 3.4f). The granophyre also contains larger clinochlore crystals (Fig. 3.4e). Other minerals observed included needle-like pyroxene, mica, quartz, and some rutile crystals.

The chemical composition of the bulk rock from the samples collected in 2019 was previously analysed in another study (Neumann, 2021) and is presented in Tab. 1.1, alongside results from an earlier study by Donaldson & Bednarik (2011). The compositions of both rock types were consistent with expectations for a gabbro and a granophyre, with the granophyre containing more SiO_2 than the gabbro. Differences in the chemical composition of the two rock types are further detailed in Chapter 1.3 and are shown in Tab. 1.1. The host rock composition of the samples collected in 2022 was not re-examined and is believed to be similar to the composition shown in Tab. 1.1.

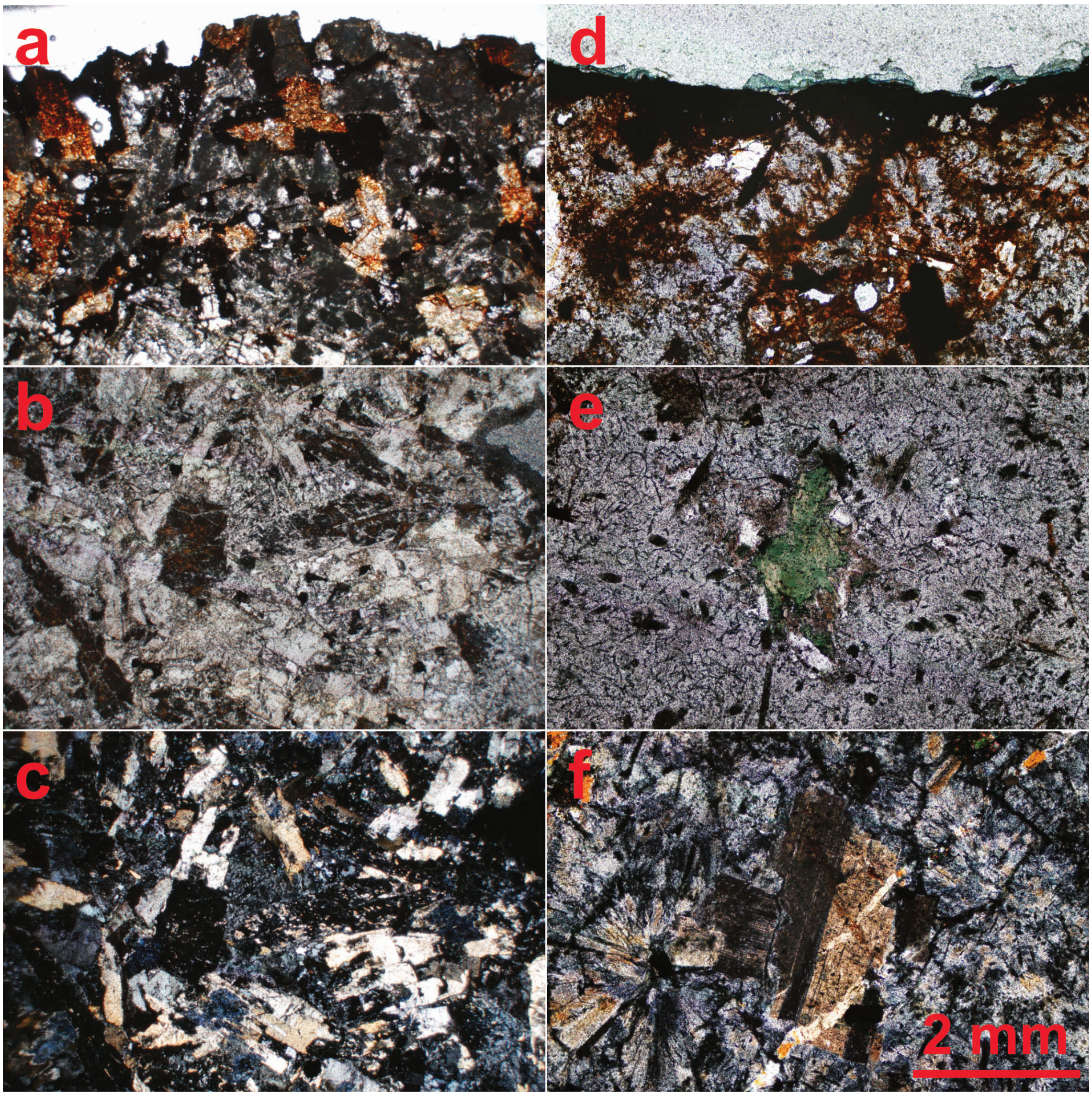

Figure 3.4: Optical images of thin sections from (a–c) gabbro and (d–f) granophyre taken under a petrographic microscope using normal lighting (a, b, d & e) and polarised light (c & f). Under transmitted light (b), the structure of the gabbro, with small quartz and plagioclase crystals (white), is visible. These crystals exhibit white to grey interference colours under polarised light (c). Additionally, some opaque phases, likely metal oxides, are visible (b & c; upper right corner). Both the gabbro and granophyre contain rutile, as seen in the gabbro in (b) as a brown crystal that turned nearly black under polarised light (c). The granophyre varnish is thicker and more intact compared to the gabbro samples (d). The granophyre structure is fine-grained, with some larger crystals such as green clinochlore (e) and large alkali feldspars that display twinning (f). The granophyre also contains needle-like pyroxene (e; black phase) and quartz (f).

3.1.3 Varnish petrography

3.1.3.1 Chemistry

The chemical composition of the rock varnish was determined using p-XRF measurements, which were conducted prior to the start of the weathering experiment in the climate chamber. It should be noted that the measured area was always consistent due to the sample holder used (Chapter 2.2.2). However, this area is not necessarily representative of the entire sample surface because of its inhomogeneous surface and composition. The differences between the various types of varnish were determined by measuring specific areas on the different samples. Due to sections with no intact varnish and variations in varnish thickness across different spots, the measurements represent not only the varnish composition but also portions of the underlying weathered rind of the samples. This limitation is further influenced by the penetration depth of the p-XRF, which may exceed the thickness of the varnish in some cases.

Consequently, the results do not solely represent the varnish composition, but provide an overall insight into the chemical properties of the sample surfaces. All results were normalised to 100 % due to some measurements yielding totals exceeding 100 %. This discrepancy is at least partly attributed to high Fe contents, particularly in granophyre samples NR3 and SR2, which exceeded the calibration range of the measurement programme used.

The resulting chemical compositions for all granophyre and gabbro samples, as well as the average compositions, are presented in Tab. 3.1. For most measured elements, the intra-group variability was relatively high and significant differences were observed between the average values of the gabbro and granophyre samples. Using p-XRF, the trace elements Ba, Cr, and Sr were also measured. The Cr and Sr concentrations in the granophyre samples were significantly higher than in the gabbro samples. Notably, one pair of granophyre samples (NR3 & SR2), which also had the highest concentrations of P_2O_5, Fe_2O_3, and SO_3 (Tab. 3.1), exhibited exceptionally high Cr and Sr contents, with approximately 900 and 1300 ppm Cr and around 2700 and 3000 ppm Sr, respectively.

From the measured chemical compositions, the Fe-Mn ratios were calculated (Tab. 3.1). Due to significant variations, primarily in the measured MnO concentrations, the ratios varied considerably between different samples, reaching maximum values exceeding 100 in the two granophyre samples SR2 and NR3. Conversely, the ratio reached a minimum value of 2.06 in one of the granophyre rock cubes used for the irrigation experiment. The ratios measured on the rock samples used in the climate chamber experiment were higher than those observed in the cubes used for the irrigation experiment. Compared to Fe-Mn ratios from other studies, which regularly reported ratios around 1, these values were still higher than expected (Potter & Rossman, 1979; Goldsmith et al., 2014; Macholdt et al., 2017; Xu et al., 2019; Dorn, 2020; Rabbachin et al., 2022).

Table 3.1: Varnish composition of all samples measured with p-XRF. All values, except the Fe-Mn ratio are given in wt. % and represent mean values of a total of 10 (irrigation samples) and 15 (climate chamber samples) single measurements. The errors are not shown but are within a range of ± 0.02 to 0.20 wt. % for all measured elements.

Sample	**MgO**	**K_2O**	**SO_3**	**Fe_2O_3**	**TiO**	**SiO_2**	**P_2O_5**	**MnO**	**Al_2O_3**	**CaO**	**Fe/Mn**
RA1	3.79	1.31	0.24	21.90	1.48	47.91	0.75	1.81	16.94	3.87	10.9
RA2	3.11	1.28	0.13	17.35	1.74	55.15	0.29	2.61	15.53	2.81	6.0
NA1	4.19	1.27	0.21	20.76	1.28	49.43	0.60	0.74	16.97	4.54	25.5
NA2	3.51	1.62	0.23	20.81	1.39	48.69	0.63	4.54	16.13	2.44	4.1
NA3	3.28	1.28	0.25	22.70	1.48	45.44	1.23	3.04	18.57	2.75	6.8
SA1	3.33	1.39	0.19	19.56	1.41	54.00	0.31	1.78	15.01	3.03	9.9
SA2	2.84	1.30	0.21	19.95	1.92	53.47	0.33	2.22	14.51	3.26	8.1
SA3	3.36	1.38	0.16	22.35	1.37	44.40	0.86	5.24	18.32	2.57	3.9
I	3.19	1.07	0.34	30.56	1.54	38.84	0.95	9.10	13.21	1.20	3.0
II	4.14	0.83	0.36	23.27	1.27	46.34	0.59	1.96	15.39	5.85	10.7
III	3.82	0.89	0.38	28.55	1.32	42.16	0.91	4.51	14.24	3.22	5.7
Mean Gabbro	**3.47**	**1.27**	**0.23**	**21.92**	**1.49**	**48.37**	**0.65**	**3.30**	**16.06**	**3.23**	**5.9**
RR1	1.82	1.70	0.11	12.81	1.33	58.77	0.46	0.48	21.19	1.34	24.0
RR2	2.67	1.08	0.15	24.98	1.31	44.09	1.87	3.28	19.70	0.86	6.9
NR1	2.15	2.15	0.24	16.16	< d.l.	53.31	1.46	3.96	19.71	1.00	3.7
NR2	2.36	1.13	0.41	24.97	1.22	42.69	3.07	6.06	17.17	0.92	3.7
NR3	2.32	0.74	1.11	41.85	1.19	31.95	4.61	0.16	14.99	1.07	239.4
SR1	2.31	1.17	0.45	19.58	1.08	50.42	1.26	3.86	18.74	1.13	4.6
SR2	1.80	0.42	2.21	41.26	1.30	30.04	7.27	0.08	13.92	1.69	492.9
SR3	2.47	1.31	0.18	26.03	1.74	46.73	1.20	5.30	14.45	0.59	4.4
IV	2.12	2.04	0.24	15.99	0.95	52.71	2.59	4.01	18.91	0.43	3.6
V	2.17	2.99	0.16	8.76	0.59	62.76	1.80	0.26	19.52	0.98	30.7
VI	1.98	1.85	0.32	12.36	0.94	51.01	3.16	5.42	19.75	3.21	2.1
Mean Grano*	**2.22**	**1.47**	**0.53**	**23.24**	**1.06**	**47.35**	**2.56**	**2.74**	**17.83**	**1.00**	**8.7**

< d.l.: concentration below detection limit

*Granophyre

Other studies have reported significant differences in Fe-Mn ratios depending on the varnish colour, primarily due to lower Mn content. Darker areas contained significantly more Mn and, consequently, exhibited very low Fe-Mn ratios compared to brighter areas, described as red or orange, where Fe-Mn ratios were higher (Potter & Rossman, 1979; Rabbachin et al., 2022). Therefore, areas with different colours were additionally measured on the samples used in the climate chamber experiment and on the sample provided by Robert Bednarik. These areas were categorised as black, orange, and red.

Black varnish is known to have the highest Mn concentrations and, therefore, the lowest Fe-Mn ratios (Potter & Rossman, 1979; Rabbachin et al., 2022). Measurements of the black varnish on the samples used in the climate chamber experiment confirmed this assumption. In all spots, the Fe_2O_3 contents were also high, aligning with the mean values calculated for the granophyre and gabbro (Tab. 3.1). This resulted in Fe-Mn ratios mostly around three (Tab. 3.2).

The black varnish on the sample provided by Robert Bednarik exhibited MnO contents ranging from 12 to 20 wt. %, which is significantly higher than the concentrations measured on the samples collected in 2022. The Fe_2O_3 content was also slightly higher than on the surface of the samples used in the climate chamber experiment. This resulted in Fe-Mn ratios which are significantly lower than for all measurements on the samples collected in 2022 (Fig. 3.5). The measurements on the older sample fell within the range expected based on known compositions published by other researchers (Potter & Rossman, 1979; Goldsmith et al., 2014; Macholdt et al., 2017; Xu et al., 2019; Dorn, 2020; Rabbachin et al., 2022), although it must be noted that the samples used in the cited studies were collected from locations other than Murujuga.

Table 3.2: Fe and and Mn concentrations (wt. %) and Fe-Mn ratios obtained from different spots on the sample provided by Robert Bednarik (left half) and on the rock samples weathered in the climate chamber (right half) differentiated by the colour of the rock varnish. The colours were classified as black, orange, and red.

	Sample	Fe_2O_3	MnO	Fe/Mn	Sample	Fe_2O_3	MnO	Fe/Mn
Black varnish	**Bednarik 1**	28.32	17.41	1.5	**SR1 1**	25.40	7.97	2.9
	Bednarik 2	33.27	20.20	1.3	**SR1 2**	24.86	7.46	3.0
	Bednarik 3	32.36	17.35	1.5	**SR1 3**	24.13	7.16	3.0
	Bednarik 4	26.57	12.05	1.8	**NR1**	19.12	5.24	3.3
					SA3	20.19	4.24	4.3
					NA1	20.42	3.01	6.1
					NA3	24.53	4.64	4.8
					RA1	21.61	7.45	2.6
Orange varnish	**Bednarik 1**	10.56	0.17	54.6	**SR1 1**	17.21	2.16	7.2
	Bednarik 2	10.34	0.63	14.9	**SR1 2**	16.31	1.27	11.6
					NR1	9.82	0.48	18.3
					NA1	19.94	0.66	27.1
					NA3	22.02	1.08	18.5
					RR1	23.63	0.80	26.8
Red varnish	**Bednarik 1**	19.51	3.71	4.8	**SR2**	42.66	0.09	452.4
	Bednarik 2	19.49	3.74	4.7	**NR2**	27.36	5.08	4.9
	Bednarik 3	29.62	0.80	33.3	**NR3**	40.62	0.07	534.7
	Bednarik 4	34.68	1.15	27.2	**RR2**	23.98	3.14	6.9
	Bednarik 5	33.67	1.05	29.1				

The second type of varnish, characterised by its orange colour, exhibited a lower MnO content across all spots, resulting in higher Fe-Mn ratios (Tab. 3.2), which are consistent with ratios reported for varnish samples analysed by other researchers (Potter & Rossman, 1979; Rabbachin et al., 2022). Two orange spots measured on the sample provided by Robert Bednarik had MnO contents < 1 wt. %, yielding high

Fe-Mn ratios. The orange-coloured surface on the Bednarik sample likely represented the remaining surface layer after the original black varnish chipped off (Fig. 3.3). Consequently, the measured area may primarily consist of weathered remains of the underlying gabbro, explaining the significantly lower MnO content compared to the orange varnish on the rock samples weathered in the climate chamber. The measured spots on these samples represented an intact varnish layer with an orange colour, as evident on the granophyre samples NR1 and RR1 in Fig. 3.1.

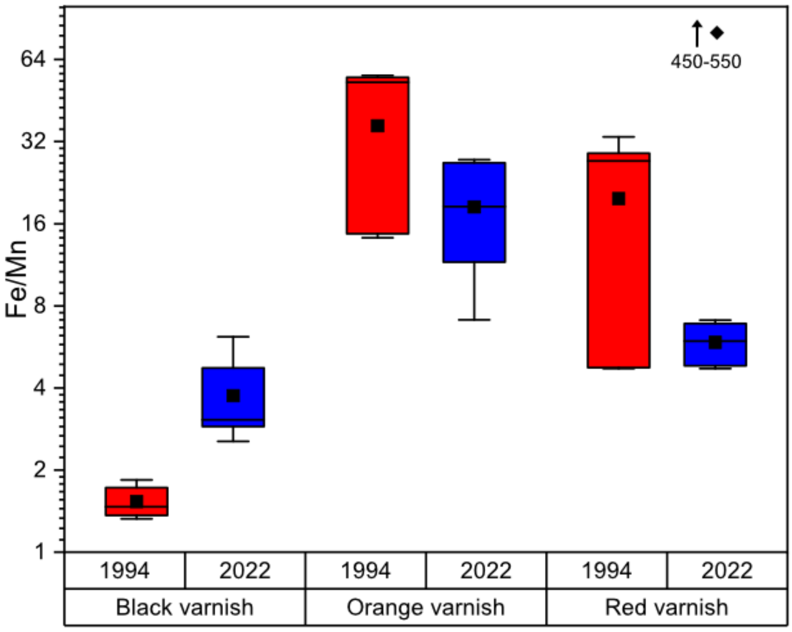

Figure 3.5: Comparison of the Fe-Mn ratios of the rock varnish depending on its colours and year the samples were collected. The sample from 1994 was provided by Robert Bednarik and the samples from 2022 were the samples used in the climate chamber experiment.

The red varnish on the sample provided by Robert Bednarik exhibited notable variability. The measured spots were located on two different sides of the sample, each showing a distinguishable type of red varnish. Although the red tones were consistent, one side included additional black spots in the varnish, while the other side was purely red with a slightly more porous and uneven structure (Fig. 3.3). Measurements on the side with black inclusions exhibited significantly higher MnO contents than those on the side with pure red varnish (Tab. 3.2). The red varnish spots on the rock samples weathered in the climate chamber also displayed substantial variability. Two spots were located on samples with red varnish that included darker regions, leading to higher MnO contents. The other two spots, found on granophyre samples SR2 and NR3, formed exceptions in many parameters. The MnO content in these spots was < 0.1 wt. %, while the Fe_2O_3 content was the highest among all samples, resulting in Fe-Mn ratios > 100. These were considered non-representative outliers and were excluded from Fig. 3.5, as indicated in the presented boxplot.

The results of these additional p-XRF measurements demonstrated that the chemical composition of the varnish depends on its colour. The black varnish exhibits a comparable composition irrespective of the rock type and is chemically distinguishable from other parts of the varnish due to its high MnO content, resulting in relatively low Fe-Mn ratios. Nonetheless, this ratio remains noticeably high in the samples used for this study compared to data from other researchers and the significantly older sample from Murujuga provided by Robert Bednarik, as shown in Fig. 3.5. The reasons for the low MnO content, even in spots that appeared as dark as the varnish on the Bednarik sample, warrant further discussion and are of considerable interest, given that Mn is a key element in varnish formation and plays a crucial role in its stability (see Chapter 1.4).

The varnish classified as orange and red did not exhibit a clear correlation between colour and chemical composition or MnO content, suggesting that colour alone is not a reliable indicator for the properties for this type of varnish. Moreover, the differences between the samples used in this study and the older sample provided by Robert Bednarik were less pronounced for orange and red varnish compared to black varnish. Some parts of the surface, such as those on the Bednarik sample, appeared to lack intact rock varnish entirely. The variety of varnish types and, consequently, the surfaces of the rocks on Murujuga is remarkably high.

3.1.3.2 Mineralogy

The mineral composition of the varnish was determined using Raman spectroscopy, EMP data from the prepared thin sections, and XRD measurements of powdered samples comprising a mixture of varnish and parts of the underlying weathered rind. It was possible to identify all main components of the analysed varnish samples using at least one of these three methods, as shown in Tab. 3.3. The primary phases of the varnish are birnessite, hematite, and kaolinite, which are predominantly composed of Mn, Fe, Al, and Si. Smaller quantities of todorokite, anatase, rutile, carbonaceous matter, and quartz were also identified in the varnish itself. Additionally, lepidocrocite and albite crystals were observed on the surface of the varnish layer in some of the samples as secondary minerals (Chapter 4.2.1.2).

The Fe- and Mn-oxide-phases were all identified by Raman spectroscopy, as shown in Fig. 3.8. The identification of the different Mn-oxide-phases was particularly challenging due to variations in their band positions and widths, which reflect differences in crystallite sizes and chemical and structural disorder. Hematite was present in at least two distinct forms, as illustrated in Fig. 3.9, and these were also distinguishable through their Raman spectra (Fig. 3.8a). Quantitative EMP data further helped differentiating Fe- and Mn-oxide-phases based on their varying CaO content, which was highest in todorokite, and their MnO_2 to $MnO_2 + Fe_2O_3$ ratios (Fig. 3.11a). Despite the presence of significant todorokite concentrations in the outermost layers of one varnish map (Fig. 3.7), its overall abundance was too low for identification in the XRD spectra, unlike birnessite (Figs. A5 & A6).

Table 3.3: Identified mineral phases in the rock varnish.

Mineral	Chemical formula	Raman	XRD	EMP	Remarks
Hematite	α-Fe_2O_3	+	+	+	Raman spectra and EMP data indicate that hematite occurs as variably disordered, chemically impure nano-crystals as shown in Fig. 3.8a (Chernyshova et al., 2007).
Lepidocrocite	γ-FeO(OH)	+			Yellow aggregates at the varnish surface (Figs. 3.8a & 4.12. Fraction too low to be detected by XRD.
Birnessite	(Na,Ca)(Mn^{4+},Mn^{3+})$_2O_4 \bullet 1.5H_2O$	+	+	+	Main Mn-oxide-phase in the varnish. Raman spectra indicate that the birnessite is variably disordered, and likely mainly in the hexagonal state (Fig. 3.8b; Julien et al., 2003).
Todorokite*	(Ca,Na,K)(Mn^{4+},Mn^{3+})$_6O_{12} \bullet nH_2O$	+		+	Fraction in the varnish too low to be detected by XRD. Raman spectra indicate that it occurs as variably disordered, chemically impure nano-crystals (Fig. 3.8b; Ostrooumov, 2017).
Anatase	TiO_2	+			Isolated, micrometre-size bipyramidal crystals at the surface and within the varnish (Fig. A1; Neumann et al., 2022). Fraction in the varnish too low to be detected by XRD.
Rutile	TiO_2	+			Very rare inside the varnish. Identified only in one location (Fig. A1). Fraction in the varnish too low to be detected by XRD.
Kaolinite	$Al_2Si_2O_5(OH)_4$		+	+	Variably intergrown with Fe-Mn-oxides throughout the varnish layer (Fig. 3.11b). Kaolinite is a very weak Raman scatterer and could not be detected by Raman spectroscopy.
Albite	$NaAlSi_3O_8$	+	+		Small white particles at the surface (Chapter 4.3.2.1; Fig. 4.13) of one sample. Albite was detected by XRD (Figs. A5 & A6) and Raman spectroscopy (Fig. A1).
Amorphous carbon	C	+		+	Partly laminarly intergrown with the Fe- and Mn-oxides (Figs. 3.7 & A1).

*It is noted that the Raman spectrum is very similar to those of ranciéite and cryptomelane with basically one strong and broad band centred between 620 and 640 cm^{-1} (Julien et al., 2003; Bernardini et al., 2019). However, cryptomelane can be excluded due to low K concentrations of < 1 wt. % and the high Ca content measured by EMP (Tab. 3.4). Ranciéite is expected to show weak Raman bands near 292 and 343 cm^{-1} (Bernardini et al., 2019), which, however, are not observed (Fig. 3.8b). Still, ranciéite and cryptomelane cannot be completely ruled out, but based on the available data, todorokite seems to be the most likely possibility.

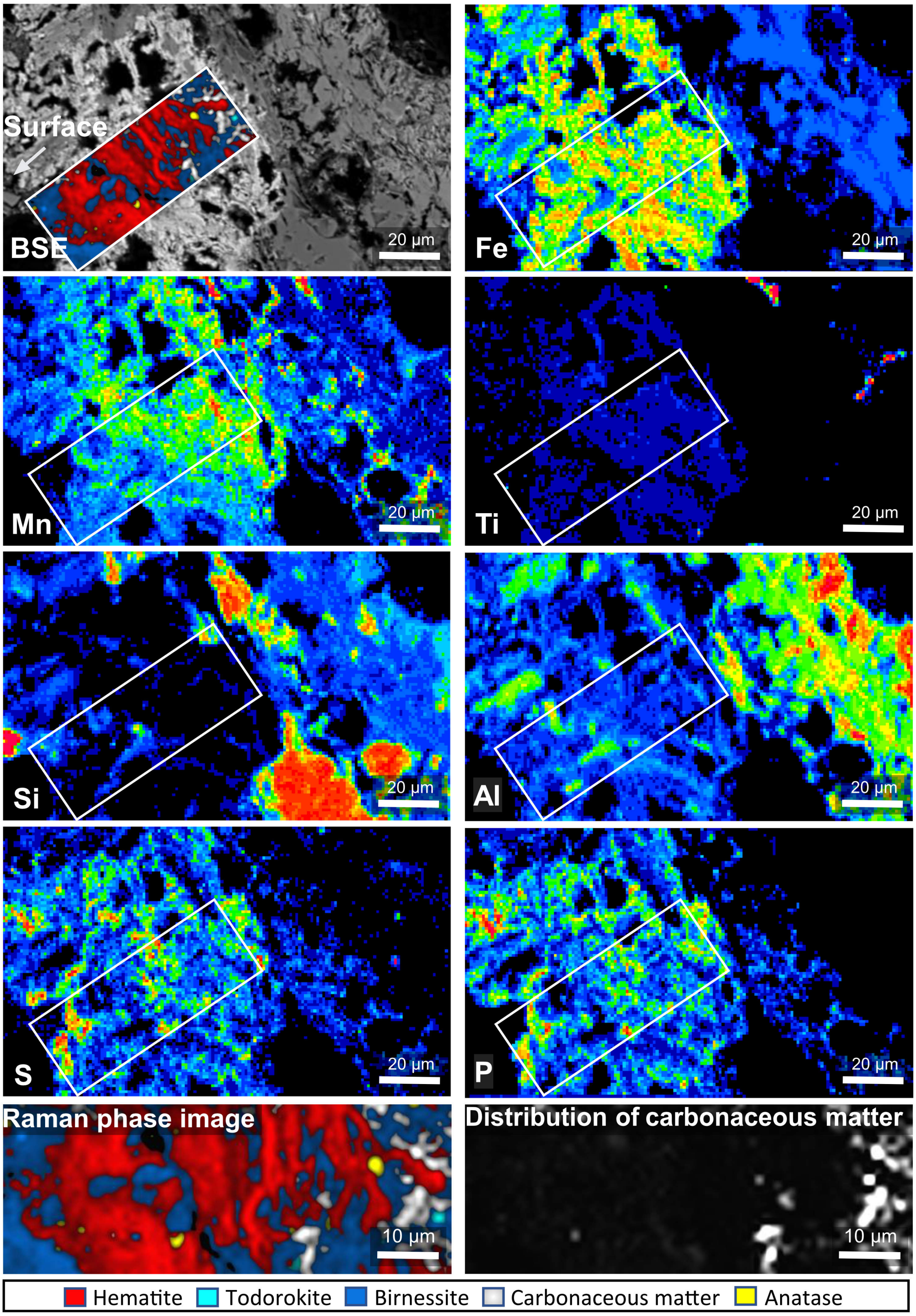

Figure 3.6: Backscattered electron (BSE), element distribution (Fe, Mn, Ti, Si, Al, S & P), and hyperspectral Raman images from the gabbro varnish (rock sample NA1). The hyperspectral Raman image is superimposed on the BSE image and its location is marked by a rectangle in the element distribution images. Colour coding of the element distribution images varies from red for high to blue for low abundances and is scaled between the maximum and minimum content observed within the measured area. The Raman image in the lower right corner shows the distribution of carbonaceous matter only.

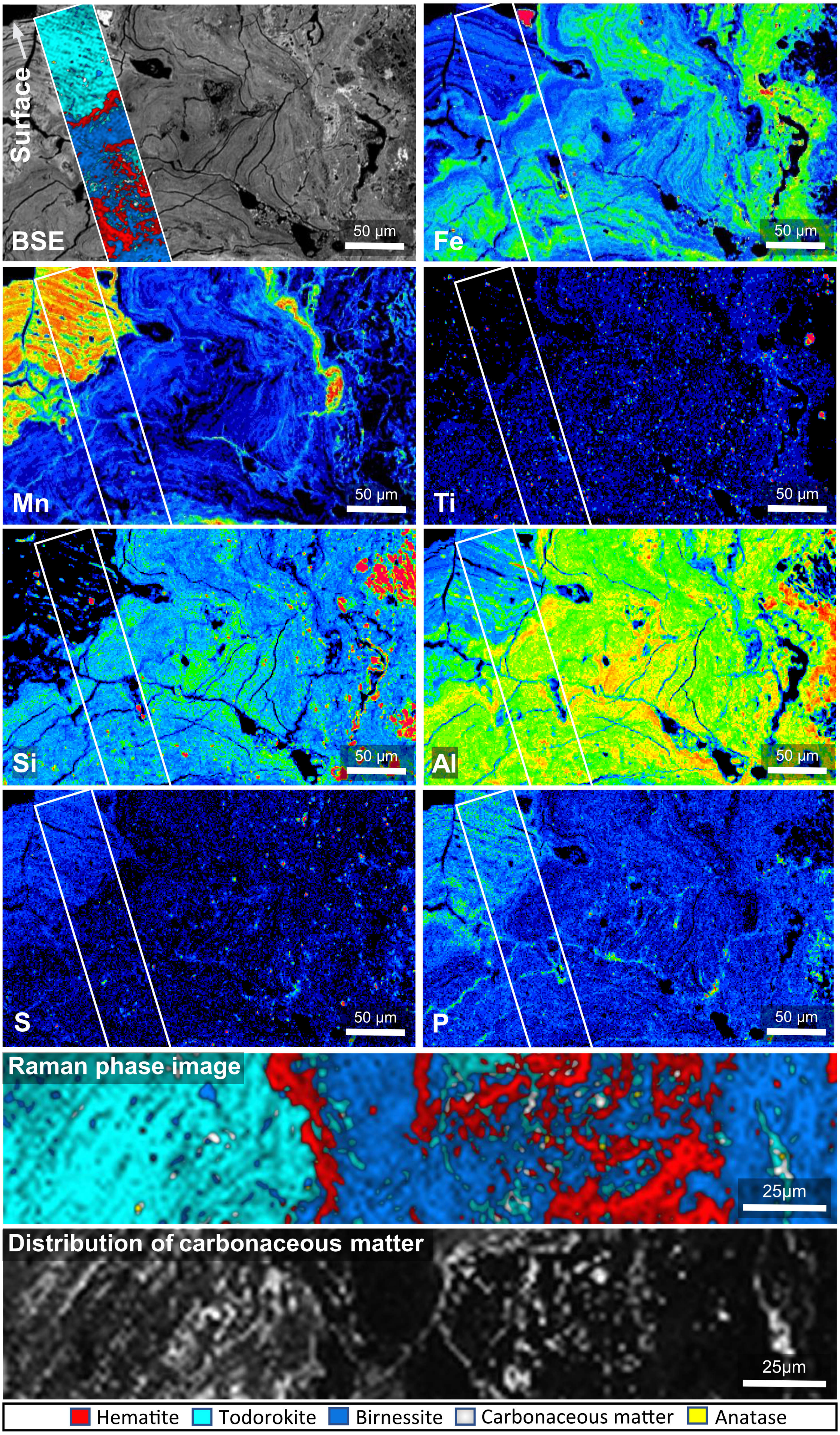

Surface
BSE
50 µm
Fe
50 µm
Mn
50 µm
Ti
50 µm
Si
50 µm
Al
50 µm
S
50 µm
P
50 µm
Raman phase image
25µm
Distribution of carbonaceous matter
25µm
🟥 Hematite
🟦 Todorokite
🟦 Birnessite
⬜ Carbonaceous matter
🟨 Anatase

Figure 3.7: Backscattered electron (BSE), element distribution (Fe, Mn, Ti, Si, Al, S & P), and hyperspectral Raman images from the granophyre varnish (sample NR1). The hyperspectral Raman image is superimposed on the BSE image and its location is marked by a rectangle in the element distribution images. Colour coding of the element distribution images varies from red for high to blue for low abundances and is scaled between the maximum and minimum content observed within the measured area. The Raman image in the lower right corner shows the distribution of carbonaceous matter only.

Kaolinite could not be identified through Raman spectra, as it is a very weak Raman scatterer. However, it was identifiable using quantitative EMP data, as the observed Al to Si ratios in Fe-rich areas of the samples matched those of kaolinite (Fig. 3.11b). High concentrations of Si and Al were also evident in the element distribution maps and coincided with regions where lower Mn and higher Fe contents were measured (Figs. 3.6, 3.7, 3.9 & 3.10). It is therefore likely that kaolinite is intergrown with the Fe- and Mn-oxides. Kaolinite was also identified in the powder samples analysed by XRD (Figs. A5 & A6). Furthermore, the quantitative EMP data revealed that birnessite- and todorokite-rich areas contained up to 12 wt. % excess Al_2O_3, indicating that these Mn-oxides incorporated some Al into their structure (Fig. 3.11b).

The combination of BSE images, Raman maps, and EMP chemical imaging made it possible to determine the mineral and element distribution in selected varnish areas. Four areas on thin sections of the varnish from one gabbro sample (Fig. 3.6) and two granophyre samples (Figs. 3.7 & 3.9) have been investigated that were taken from the same rock pieces as gabbro sample NA1 and granophyre samples NR1 and NR2, respectively. A fourth area was mapped from a thin section of the granophyre sample obtained from Robert Bednarik, which he collected in 1994. It is important to note that the Raman phase images (Figs. 3.6, 3.7, 3.9 & 3.10) display only the dominant mineral phases determined using CLS fitting (Chapter 2.5). As the element distribution maps and quantitative EMP data (Tab. 3.4) illustrate, most varnish areas contain Fe, Mn, Al, and Si, suggesting that the main phases are intergrown. This assumption is supported by high-resolution optical images, which revealed that both orange and black varnish areas contain a mixture of black, red, and white areas, which are mainly composed of birnessite, hematite, and kaolinite in variable proportions (Fig. A3).

In the granophyre varnish, fine layering was particularly evident in BSE images, especially in the outermost parts, which primarily consisted of birnessite (Fig. 3.10) or todorokite in one sample. These todorokite layers are partly intergrown with carbonaceous matter (Fig. 3.7). Hematite-rich areas also exhibit layering, as shown in Fig. 3.9. These outermost layers are not only enriched in Mn (except for sample

NR2; Fig. 3.9) but also in S and P. The Na content of the outermost layer is also higher compared to the underlying parts of the varnish (Fig. A4). In all varnish samples, Al concentrations tend to increase towards deeper layers, suggesting a higher kaolinite content, whereas Fe and Mn are most abundant in the outer layers. Si and Ti element distribution maps revealed the presence of quartz, anatase, and very few rutile grains in the varnish (Figs. 3.6, 3.7, 3.9 & 3.10).

The investigated gabbro varnish exhibited no discernible layering. However, similar to the granophyre varnish, Mn and Fe concentrations are higher in the outer layers, while Al concentrations increas in the deeper layers. This trend also applies to S and P concentrations (Fig. 3.6). In the gabbro varnish, numerous quartz grains exceeding 20 µm in size were also observed.

It should be noted that the analysed varnish areas represent the thickest varnish sections found on the prepared thin sections. The observed thickness of up to 200 µm is not representative for the overall varnish, as most areas are much thinner. In some parts of the thin sections, no intact varnish was found and the outermost parts in this areas are made up of the weathered rind of the host rocks. Additionally, it is possible that parts of the varnish were removed during the sawing and polishing processes due to the physical forces applied but were intact before.

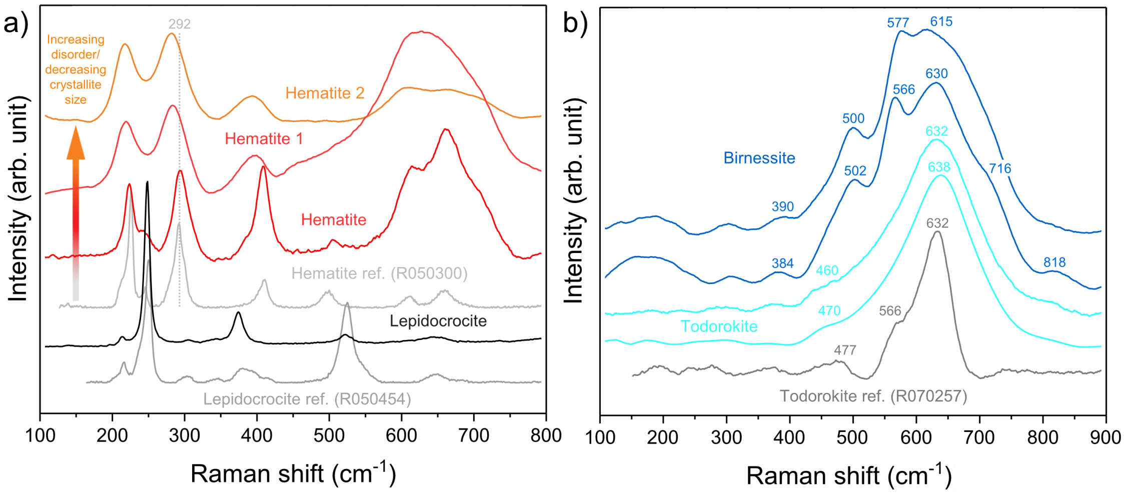

Figure 3.8: Representative Raman spectra from all so far identified (a) Fe-oxide and (b) Mn-oxide-phases. Numbers refer to wavenumbers of band maxima. The hematite spectra were scaled by eye to the same intensity of the band at 292 cm^{-1}. The reference spectra were taken from the RRuff Raman database (Lafuente et al., 2015). Note the differences of band positions and widths within the spectra from one oxide phase, which indicates variable structural and chemical disorder and / or different nano-crystallite sizes (Julien et al., 2003; Chernyshova et al., 2007; Ostrooumov, 2017).

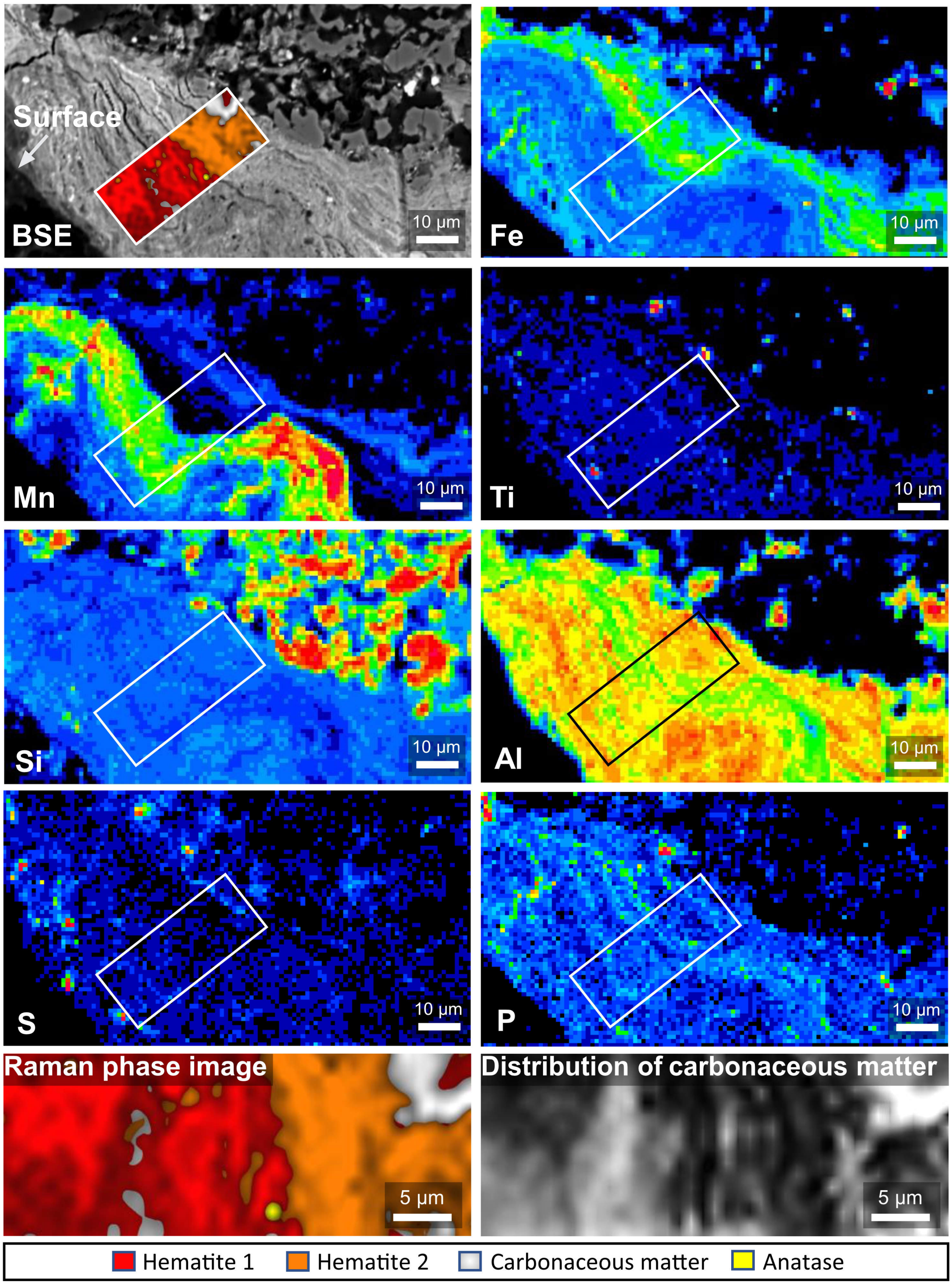

Figure 3.9: Backscattered electron (BSE), element distribution (Fe, Mn, Ti, Si, Al, S & P), and hyperspectral Raman images from the granophyre varnish (sample NR2). The hyperspectral Raman image is superimposed on the BSE image and its location is marked by a rectangle in the element distribution images. Colour coding of the element distribution images varies from red for high to blue for low abundances and is scaled between the maximum and minimum content observed within the measured area. Note the occurrence of two distinct hematite phases which are characterised by different chemistry and clearly distinguishable Raman spectra (Fig. 3.8a). The Raman image in the lower right corner shows the distribution of carbonaceous matter only.

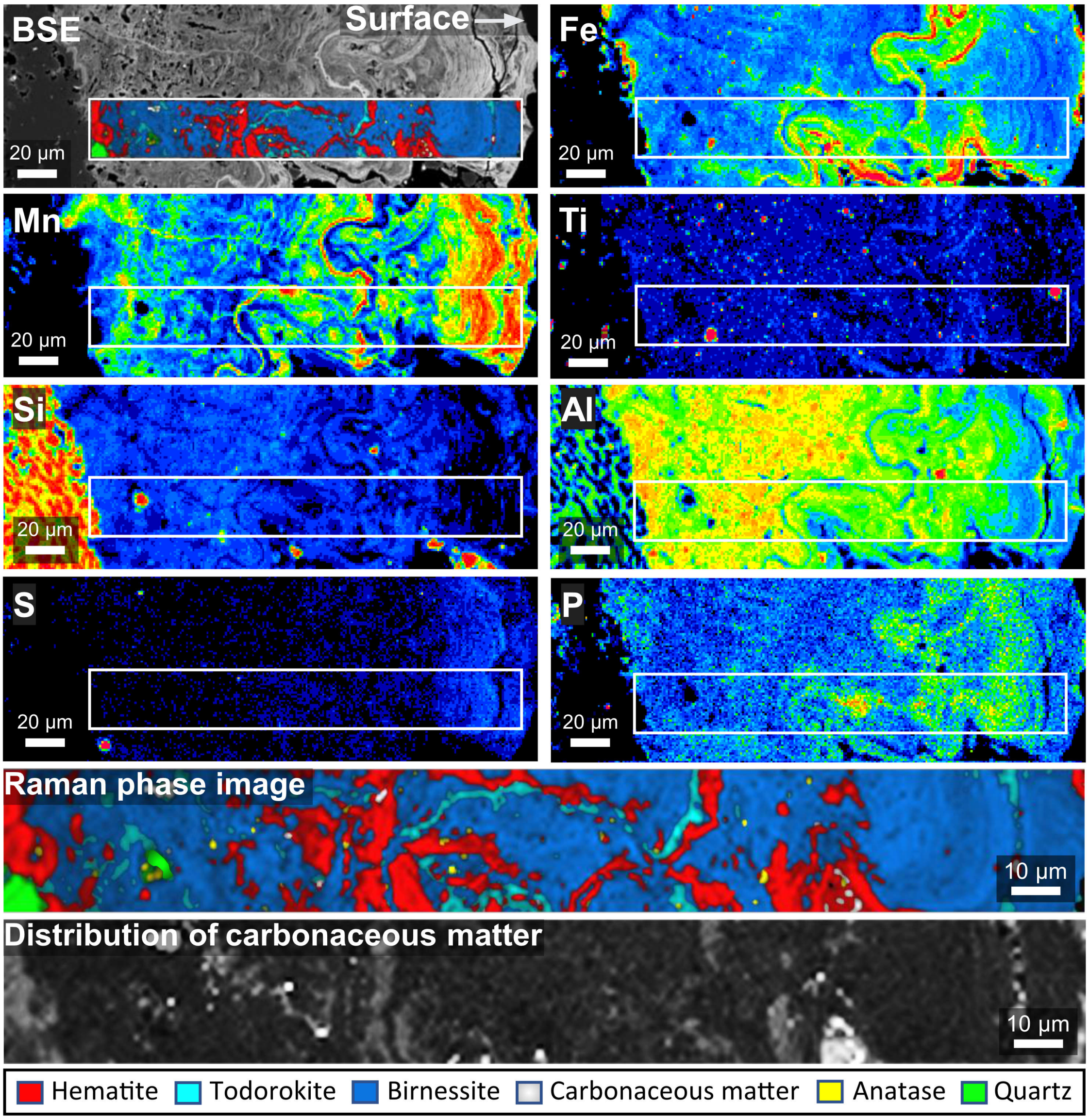

Figure 3.10: Backscattered electron (BSE), element distribution (Fe, Mn, Ti, Si, Al, S & P), and hyperspectral Raman images from the granophyre varnish of the sample collected by Robert Bednarik in 1994. The hyperspectral Raman image is superimposed on the BSE image and its location is marked by a rectangle in the element distribution images. Colour coding of the element distribution images varies from red for high to blue for low abundances and is scaled between the maximum and minimum content observed within the measured area. The Raman image in the lower right corner shows the distribution of carbonaceous matter only.

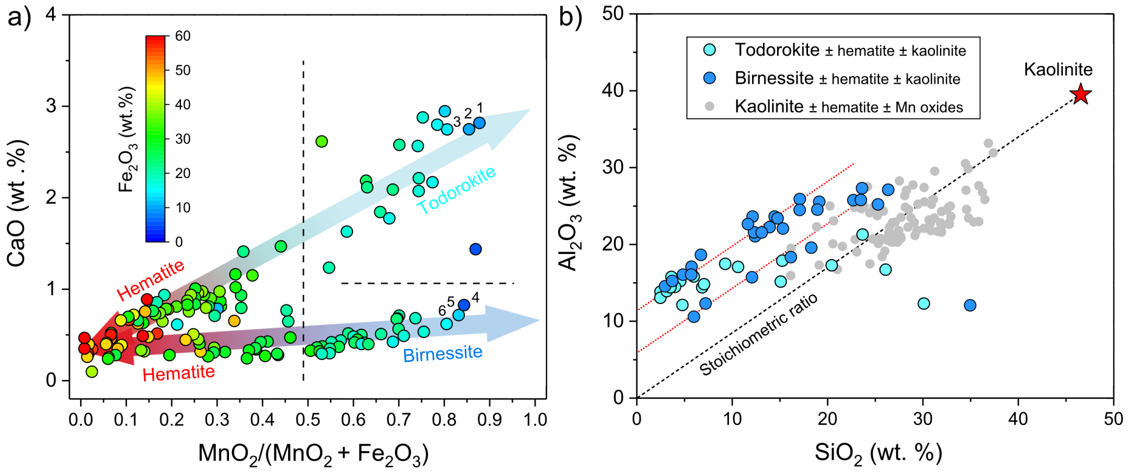

Figure 3.11: EMP from the rock varnish of the granophyre (sample from 1994, NR1 & NR2) plotted in a diagram of (a) CaO vs. $MnO_2/(MnO_2 + Fe_2O_3)$ and (b) Al_2O_3 vs. SiO_2. Note the two hematite-Mn-oxide mixing trends that are defined by data from birnessite- and todorokite-dominated regions as verified by Raman spectroscopy. The numbers at the symbols in (a) refer to analyses given in Tab. 3.4. Note that in (b) the Al to Si ratio of the Fe- (hematite-)rich regions (grey symbols) basically matches well with those of kaolinite, whereas the todorokite- and birnessite-dominated regions mostly plot away from the stoichiometric ratio of kaolinite (stippled black line) towards higher Al_2O_3 contents (dotted red lines), which suggests that both Mn-oxides contain significant amounts of Al_2O_3 of up to about 12 wt. %, which, would at least partly explain the observed Raman band broadening and frequency shifts (Fig. 3.8b).

Table 3.4: Representative EMP analyses from todorokite- (1-3) and birnessite-dominated (4-6) varnish areas. The full data set is given in the digital supplementary material.

	Todorokite[1]			**Birnessite**[1]		
Spot[2]	**1**	**2**	**3**	**4**	**5**	**6**
MnO_2 [3]	61.6	56.63	56.53	64.4	62.12	54.06
Fe_2O_3 [3]	8.58	9.63	13.55	13.02	15.01	23.48
TiO_2	0.04	0.06	0.06	0.32	0.3	0.27
MgO	1.07	0.99	1.02	0.66	1.99	0.15
CaO	2.82	2.75	2.75	0.72	0.62	0.68
K_2O	0.58	0.46	0.42	0.52	0.44	0.29
Na_2O	0.32	0.26	0.31	0.23	0.1	0.37
SiO_2	2.48	3.14	3.63	5.99	7.21	2.96
Al_2O_3	13.84	13.92	14.98	10.58	12.32	14.56

[1] ± hematite ± kaolinite

[2] See Fig. 3.11a

[3] Total Mn and Fe is calculated as MnO_2 and Fe_2O_3, but both minerals contain Mn in the divalent oxidation state, the amount of which is unknown. This can lead to totals that are too high.

3.1.3.3 Varnish types and composition

The observed surface structures on the analysed samples (Chapter 3.1.1), in combination with the measured chemical composition of the varnish samples depending on their colour (Chapter 3.1.3.1) and the analysed mineralogy and chemistry of individual varnish samples (Chapter 3.1.3.2), allow for the classification of different types of varnish present on the studied rock samples (Fig. 3.12).

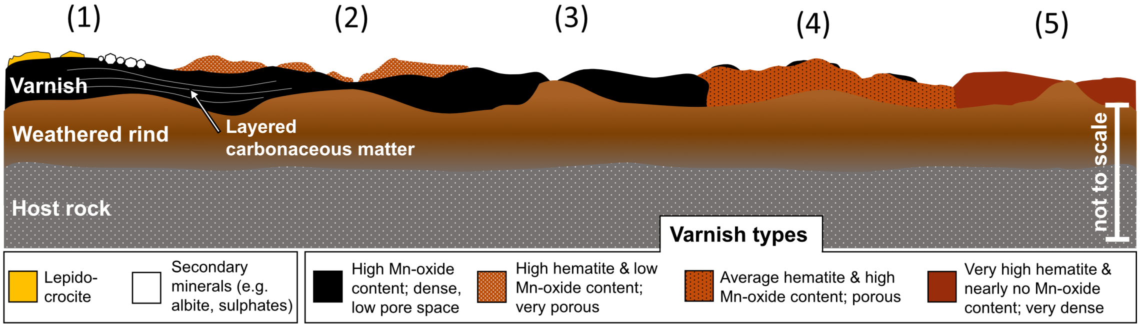

Figure 3.12: Schematic illustration of identified varnish types on the rock sample surfaces with the underlying weathered rind and host rock. In addition to the observed varnish types some areas that are characterised by the occurrence of secondary minerals at the surface are here defined as varnish type (1).

Besides (1) some minor components, such as secondary minerals and organic material deposited on the sample surfaces (e.g. lepidocrocite & albite on samples NR3 & SR1, respectively), the varnish of the samples can be classified into four distinct types that could be analysed more detailed. The most abundant type of varnish (2) is orange to brown, has a highly porous structure, and overlays darker, denser parts of the varnish. This type was found on some of the gabbro (NA2, SA1 & SA2) and granophyre (NR1 & SR1) samples and is mainly composed of haematite with a comparably low Mn content. The (3) darker, nearly black, denser varnish, was not only present underneath the type (2) varnish, but also occurred independently on some samples (gabbro samples NA1, NA3 & SA3; granophyre samples NR1 & SR1). It has a low pore space and contains relatively high amounts of Mn-oxides. This type of varnish was also found to include some layered carbonaceous matter (Fig. 3.7). A distinct type of varnish (4), composed of a mixture of orange to red and black components with very high Mn contents and moderate density and pore space, was found on only two granophyre samples (NR2 & SR3). The final classified type of varnish (5) is very dense, red to brown in colour, has a very high Fe and low Mn content, and exhibits a metallic lustre. This type was found exclusively on two granophyre samples (NR3 & SR2).

Additionally, some red varnish spots were identified on the gabbro samples NR1 and SR1, as well as on the sample from 1994 provided by Robert Bednarik. These were also measured using p-XRF (Tab. 3.2) but were too small to be reliably described, as they are mostly intergrown with parts of the black varnish, as observed in the high-resolution images of the samples (Figs. 3.1 & 3.3).

3.2 Glass dosimeters

The chemical compositions of the three types of glass dosimeters that were used in the climate chamber are shown in Tab. 3.5. The most stable glass type M3 is the most simple type of glass that was used, which only consists of SiO_2, K_2O, and CaO. The other two glass types MI and M5, that are more vulnerable to alteration, additionally consist of Na_2O, MgO, Al_2O_3, and P_2O_5, making them more complex. The only difference between glass types MI and M5 is, that type M5 additionally contains MnO_2 and Fe_2O_3. Therefore the K_2O and CaO content is a little lower than in type MI.

Table 3.5: Chemical composition of the three types of glass dosimeters used in the climate chamber experiment. All values are given in wt. %.

Glass type	**SiO_2**	**K_2O**	**CaO**	**Na_2O**	**MgO**	**Al_2O_3**	**P_2O_5**	**MnO_2**	**Fe_2O_3**
MI	48.0	25.5	15.0	3.0	3.0	1.5	4.0	0.0	0.0
M5	48.0	24.5	14.0	3.0	3.0	1.5	4.0	1.0	1.0
M3	60.0	15.0	25.0	0.0	0.0	0.0	0.0	0.0	0.0

4 Climate chamber experiment

4.1 Experimental approach

4.1.1 Experimental procedure

In the long-term experiment a total of 16 rock samples from Murujuga (Fig. 3.1) were weathered for one year in a climate chamber together with glass dosimeters. The entire simulation was accelerated by a factor of six, effectively simulating a total of 6 years of weather cycles within this one-year period. The climate data used for the simulation is given in Tab. 1.2. Due to this acceleration, each simulated day lasted only 4 hours. The daily cycle commenced with the minimum temperature and maximum humidity, reflecting conditions around 5 a.m. The climate chamber was programmed to maintain these conditions for 15 minutes. Following this, the temperature was raised to the maximum while the humidity decreased to the minimum over a period of 90 minutes. After holding these values for 30 minutes, the temperature was decreased, and the humidity increased over another 90 minutes. The maximum humidity and minimum temperature were again maintained for 15 minutes. Solar radiation was simulated before and after the maximum temperature was reached, utilizing Ultra Vitalux® lamps from Osram (see Chapter 4.1.2). While the lamps effectively heated the samples, a simulation of continuous daily solar radiation without breaks would have resulted in excessively high and unrealistic surface temperatures. Therefore, solar radiation was simulated before and after reaching the maximum temperature of the simulated daily cycle. Precipitation was introduced between the two phases of solar radiation when the chamber reached maximum temperature and minimum humidity (Fig. 4.1). As intended and as observed in nature, humidity increased during and after the simulated precipitation due to evaporation.

To simplify the experimental programme, each simulated month consisted of a total of 30 simulated days, equating to 5 days in real time. The number of rainfall events per simulated month varied based on the average number of rainy days per month, ranging from none to a maximum of five (Tab. 1.2). Rainfall events were evenly distributed throughout the simulated month, allowing for a maximum of one rainfall event per day in real time.

The weathering experiment was divided into ten phases, each with measurement pauses in between. Over the course of the experiment, the phases increased in duration, ranging from five, ten, and fifteen days for the first three steps to two months each for the last four steps (Fig. 4.2). The measurement pauses were essential

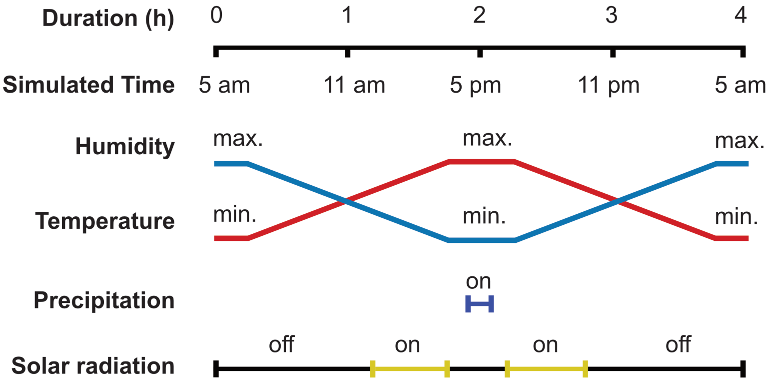

Figure 4.1: Scheme of the daily cycle that was simulated in the climate chamber.

for the planned analytical programme. Depending on the intended measurements, the availability of the climate chamber for other groups, and necessary maintenance, these pauses varied from three to 17 days, totalling 64 days. With the additional 360 days of simulated weathering, the overall experiment duration amounted to 424 days. During the pauses, all rock samples and glass dosimeters were taken out of the chamber and stored in the same laboratory as the reference samples. To protect them from sunlight, the laboratory was permanently darkened, with temperature and humidity controlled between 20 to 23 °C and 40 to 50 %, respectively, using a climate control unit.

Colour and p-XRF measurements were conducted before the weathering was started and after each weathering phase, resulting in a total of 11 sets of measurements. A set of three glass dosimeters (one from each glass type) from each of the two sample groups was removed from the climate chamber and analysed with FT-IR after each weathering phase and imaged with an optical microscope (Fig. 4.2). Unlike the rock samples, the glass dosimeters were not returned to the climate chamber after measurement. Reference glass dosimeters and those placed above the experimental setup to gauge atmospheric alterations in the climate chamber were analysed once after 180 days of weathering and then measured again at the end of the experiment. Here, the same dosimeters were measured twice. High-resolution optical images of the rock samples were taken before the weathering experiment, after 180 days of weathering, and after termination of the weathering experiment.

Before and after the weathering experiment µ-CT scans of all rock samples were taken, as well as DNA samples from additional rock samples that were also placed in the climate chamber. DNA samples were also collected after five days of weathering. The DNA samples were collected from separate rock samples that had not been cut with a tablesaw to prevent altering the biogenic surface conditions (Chapter 2.7). Additionally, DNA samples from a single piece of rock were collected, after which the rock was cut in the same manner as the other rock samples used in the climate chamber experiment. DNA samples were then taken again immediately afterwards to estimate the changes inflicted by the cutting process, which all other rock samples had undergone.

Samples of the artificial rainwater, that interacted with the rock samples, were collected alongside blank samples during the last three weathering phases and analysed using ICP-OES to assess the amount of material dissolved by the artificial rainwater when in contact with the rock samples from both groups (Fig. 4.2). For the artificial rainwater collection, Teflon© containers were employed (Fig. 2.4), which were rinsed in demineralised water and afterwards treated for 12 hours with 10 % HNO_3 to dissolve any contamination from residual materials. The water samples were taken while simulating the climate conditions of February (Tab. 1.2), which was the month with the most precipitation and the longest precipitation duration per day. As only a single set of seven Teflon© containers was available, it was necessary to take the samples from each side weathered under different conditions in two consecutive days, resulting in 14 samples per weathering phase and a total of 42 samples collected.

Additionally, all rock samples were weighed before the experiment, after 180 days of weathering, and after the weathering experiment to detect any potential material loss.

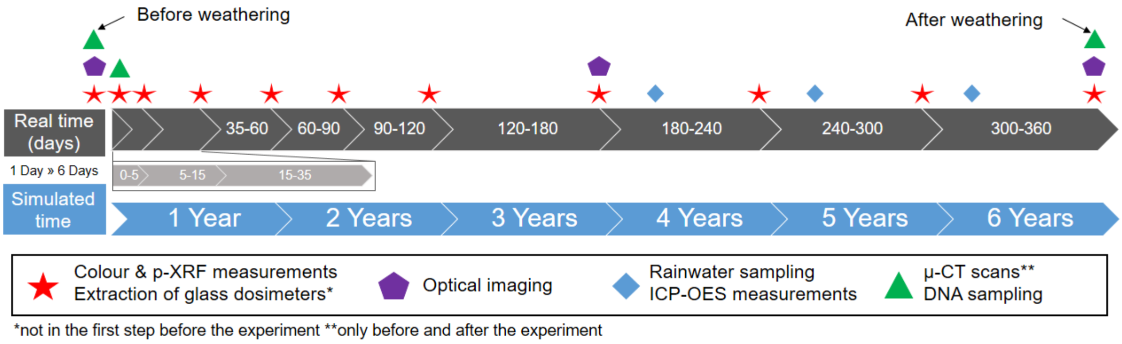

Figure 4.2: Scheme of the experimental procedure and the analytical steps and methods.

Over the course of the experiment, some material accumulated in both glass tanks. This material was extracted from the tanks, weighed, and subsequently analysed also by p-XRF and XRD.

4.1.2 Experimental setup

For the long-term weathering experiment, a Clime Event C/180/70a/3 chamber from Weisstechnik was used. The climate chamber is capable of simulating temperature and humidity in the necessary range, with cooling and heating rates of 3.8 and 4.0 K/min, respectively. The temperature variance is maintained at ± 0.1 to ± 0.3 K over time and ± 0.5 to ± 1.0 K spatially, depending on the simulated temperature. Humidity is controlled with a variance of ± 1 to ± 3 % over time, also depending on the temperature (Weiss Technik, 2021).

To simulate solar radiation and precipitation while keeping the two sample groups separate and ensuring that they do not come into contact with the artificial rainwater used for the other group, an additional setup was constructed in the climate chamber. This setup primarily consisted of two glass tanks, each with a volume of 25 litres, equipped with an irrigation system and Ultra Vitalux® lamps from Osram on top. A modified nozzle was installed in each corner of the tanks to ensure an even distribution of artificial rainwater (Fig. 4.3). Each nozzle was connected to a pump specific to each tank, along with additional valves to control pressure and flow. Unlike earlier experiments (Neumann et al., 2022), the water was not nebulised by the nozzles; instead, the droplets were significantly larger and closer to real rainfall. The artificial rainwater was stored in large 20-litre canisters. Ambient air was pumped into the artificial rainwater in each canister half an hour before each simulated rainfall event to maintain equilibrium with the CO_2 in the air, thus ensuring a constant pH value. The pH of both types of rainwater was controlled 5 to 10 minutes before every simulated rainfall event. Additionally, the rock sample and glass dosimeter positions in the experimental setup were rotated before every simulated month that included at least one rainfall event, ensuring that all samples were exposed to the same conditions over time and received an equal amount of simulated precipitation. During and after each simulated rainfall event, the artificial rainwater was removed from the experimental setup using an additional pump to prevent the samples from becoming partially submerged. This also ensured that only a small amount of water remained in the chamber to evaporate. If not managed, the evaporating water could influence the humidity control of the climate chamber for an extended period. In any case, the small amount of evaporating water temporarily increased humidity after each rainfall event, which is not considered to be problematic, as natural humidity also increases due to evaporation following rainfall events.

The Ultra Vitalux® lamps, each with a power of 300 W, emit UVA, UVB and visible light (Tab. 4.1). Additionally, they radiate heat. These lamps are rated for 1000 hours of burning time, but the amount of emitted light decreases over time (Tab. 4.1). Consequently, the lamps were replaced after every simulated year, resulting in a total of six sets being used, which corresponds to 364.5 hours of burning time per lamp. After this duration, the emitted light remains close to the initial values (Tab. 4.1). The sample surfaces heat up rapidly, making it necessary to switch the lamps off after half of the daily simulated solar radiation, followed by a brief pause to allow the sample surfaces to cool (Fig. 4.1). The burning time was calculated based on the mean daily solar radiation per month (Tab. 1.2). Given the radiated surface in each of the two used glass tanks (22 x 33 cm^2) and one Ultra Vitalux® lamp above, the radiation times varied between 76 minutes in November and 31 minutes in June per simulated day (with a total simulated daily duration of 4 hours). The Ultra

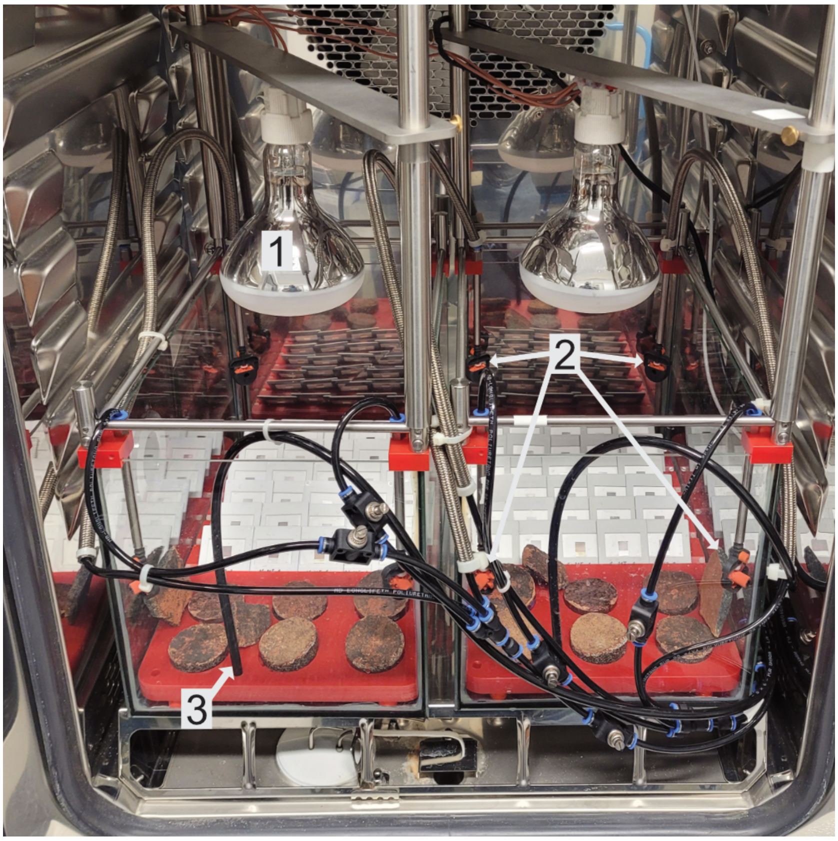

Figure 4.3: Experimental setup in the climate chamber with the tanks for each sample group. Each side of the setup consists of (1) an Ultra Vitalux® lamp, (2) four nozzles for irrigation, (3) a pipe to pump out the water during the simulated rainfall events, and a sample holder (red) for the rock samples and glass dosimeters.

Vitalux® lamps were turned on after 40 % of the non-illuminated time had elapsed. Following 50 % of the illumination time, a break was implemented for 20 % of the non-illuminated duration, after which the second half of the solar radiation was simulated. For example, in January, this resulted in 1 hour and 7 minutes without solar radiation, followed by a period of 36 minutes with solar radiation, then a break of 34 minutes. After this, the second half of the solar radiation was simulated for another 36 minutes, followed by a break of 1 hour and 7 minutes (Fig. 4.1).

The surface temperatures of the rock samples reached 60.6 °C or 55.6 °C, depending on the starting temperature, after 30 minutes of simulated solar radiation (with starting temperatures of 36.5 °C & 26.5 °C, respectively; Tab. 4.2). Approximately 60 °C is the maximum surface temperature that should be attained; therefore, a short cooling pause, as described above, was implemented between the simulated solar radiation sessions. Measurements taken before the start of the experiment indicated that the maximum surface temperatures on the samples ranged from 62.5 °C in December to 52.5 °C in June.

The materials used for the experimental setup were selected for their UV stability and resistance to acids, allowing them to withstand the heat and UV radiation emitted

Table 4.1: Luminous flux and light emission of the Ultra Vitalux® lamps depending on the burning time (Osram, 2023).

Burning Time (h)	Luminous flux (lx)	UVB (W/m^2) 280-315 nm	UVA (W/m^2) 315-400 nm	visible light (W/m^2) 380-780 nm
1	14400	3.0	13.6	41.4
500	13700	1.8	11.0	39.0
1000	10800	1.1	7.3	29.7

Table 4.2: Temperature of the rock sample surfaces depending on the burning time of the Ultra Vitalux® lamps.

Time (min)	Start	10	15	20	30
Temp (°C)	36.5	53.0	56.5	59.3	60.6
Temp (°C)	26.5	46.5	50.2	52.7	55.6

by the Ultra Vitalux® lamps. However, the surface of the sample holders placed in each glass tank (Fig. 4.3; red plastic) darkened over time. The cause of this color change remains undetermined, but it appears to be related to the drilling performed on the surface and may be associated with the oil used for cooling during the drilling process. A test comparing two pieces of the used plastic, one with a drilled hole and one without, showed significantly less darkening on the piece without the drilled hole. Additionally, the sample holder in the tank that was weathered with the neutral artificial rainwater (pH 7) exhibited less darkening, suggesting that the slightly acidic artificial rainwater (pH 5) contributes to the colour change. Importantly, the color change on the surface of the plastic sample holders did not impact their stability, and it is assumed that the color change, along with any potential evaporation of components from the plastic sample holders, did not affect the overall results of the weathering experiment.

The sample holders on each side featured six milled grooves with a 45° angle in the upper part to accommodate 30 glass dosimeters per side. Due to the limited space within the glass tanks, it was necessary for the slide frames containing the glass dosimeters to overlap slightly. The 45° angle was chosen to ensure that all glass dosimeters come into contact with the artificial rainwater while allowing the water to run off the dosimeters, preventing it from remaining on them for an extended period. The lower half of the sample holders consisted of six milled holes with a diameter of 5 cm, designed to hold three granophyre and three gabbro samples each (Fig. 4.4). One granophyre and one gabbro sample in each sample group were positioned at an angle of 30°, while all other samples were placed horizontally, in order to evaluate the correlation between the dip of the rock surface and the observed weathering effects. Additionally two glass dosimeters from each type were placed above the whole weathering setup to monitor the influence of the atmospheric conditions.

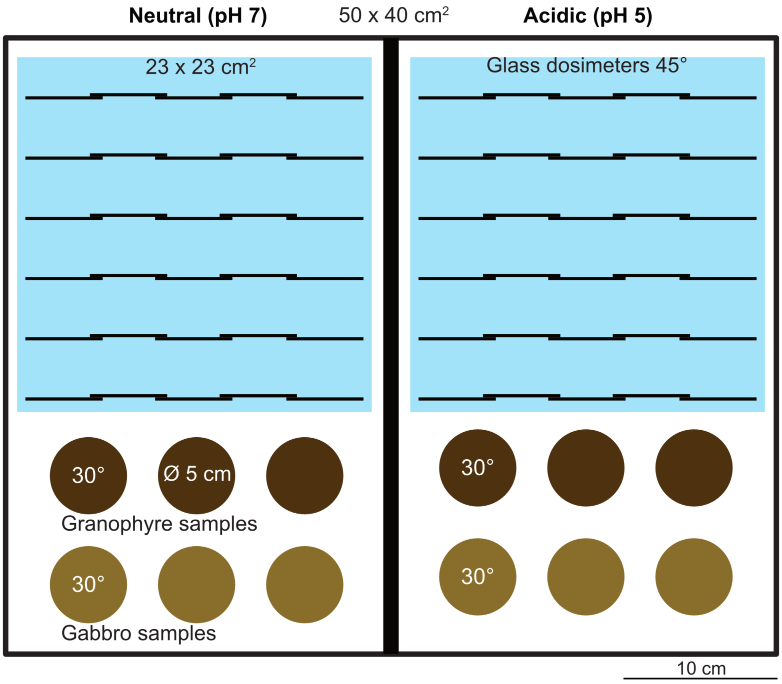

Figure 4.4: Scheme of the sample positions inside the climate chamber with the two separated sample groups, each consisting of six rock samples and thirty glass dosimeters. Two rock samples in each group were placed in the chamber with an angle of 30°, the other rock discs were placed horizontally. All glass dosimeters were placed with an angle of 45° and the used slide frames were slightly overlapping to make optimum use of the limited space available.

4.1.3 Sample preparation

4.1.3.1 Rock samples

Two separated groups of rock samples from Murujuga (Chapter 3.1.1) were used for the climate chamber experiment, with each group consisting of three granophyre and three gabbro samples. The rock samples were cut into discs with a diameter of 5 cm using a core drill at the Institute for Geosciences of the University of Bonn. This diameter was chosen, because the measurement area of the chroma meter used is also 5 cm in diameter (Chapter 2.1). After drilling, the cores were cut with a small tablesaw to create discs as thin and as flat as possible. Both, the drill and tablesaw, were cooled with tab water, resulting in all samples being exposed to tab water and rinsed once before starting the simulated weathering process. To prevent contamination, the samples intended for DNA sampling were not cut, but brought to size using a hammer and chisel (Chapter 2.7). The rock samples were afterwards coated with Araldite® resin (Huntsman, 2004) on all sides except on the top, which retained the intact rock varnish. This coating ensured that only material from the rock varnish was weathered, while protecting the underlying rock and the freshly cut sides. The resin used is UV stable and insoluble by acids (Huntsman, 2004). It was also ensured that two discs were cut from each larger rock sample to allow placement of samples from the same source in each experimental group, given the heterogeneity of the larger rock samples and their varnish (see Chapter 3.1.1).

4.1.3.2 Glass dosimeters

Three different types of glass dosimeters were melted in larger blocks by the Fraunhofer ISC at their site in Bronnbach, Germany and afterwards cut into thin slices, each approximately 2.5 x 3.5 cm^2 in size. After cutting, the glass panes were fire-polished and UV stable adhesive tape was applied on both sides. A 1 x 1 cm^2 window was cut into the adhesive tape on both sides, slightly extended on the front side towards the bottom to allow the artificial rainwater to run off the samples. This 1 cm^2 area was measured with Fourier-transform infrared spectroscopy (FT-IR) and imaged by optical microscopy. For easier handling the glass panes were all placed and secured in slide frames. After each time step, a set of six glass dosimeters was removed from the climate chamber and sent to the Fraunhofer ISC. The dosimeters were packed together with a bag of silica gel and shipped via express delivery to ensure that they arrived within 24 hours of removal from the chamber. Upon arrival, the dosimeters were stored in a desiccator for another 24 hours before being measured by FT-IR.

4.1.3.3 Artificial rainwater compositions

For the weathering experiment, two types of artificial rainwater were used. In 2006, numerous rainwater samples were collected and analysed on Murujuga. These samples were not collected near industrial facilities on Murujuga, but the mean measured pH was around 5, ranging between 4.5 and 7.5 (Gillett, 2006). Recent pH measurements from Murujuga also range around 5 with some values being even lower (MacLeod & Fish, 2021; MRAMP, 2023). In the 1960s, the rainwater pH on Murujuga was estimated to have been between 7.0 and 7.2 (Bednarik, 2002). Based on this, the pH of the artificial rainwaters used was adjusted to 5.0 and 7.0 (± 0.1), respectively.

For the artificial rainwater demineralised water with a conductivity of < 2 µS/cm was used. The slightly acidic artificial rainwater with a pH of 5 (± 0.1) additionally consisted of a stock solution that contained a mixture of 1.2 parts of concentrated HNO_3 and 1 part of concentrated H_2SO_4. This stock solution was prepared by mixing 900 ml of demineralised water, 10.8 ml of HNO_3 and 9 ml of H_2SO_4. The neutral artificial rainwater, with a pH of 7 (± 0.1), was prepared by adding NaOH to the demineralised water. For this, a stock solution of 900 ml demineralised water and 4.5 g of NaOH was used. The artificial rainwater for irrigating the two sample groups in the climate chamber was prepared in separate 20-litre containers by adding a calculated amount of stock solution to reach the desired pH. The pH was checked both after preparation and before each rainfall event using a pH meter. In total, 477.5 litres of each type of artificial rainwater were produced during the experiment, using 3.17 ml of the acidic and 47.79 ml of the neutral stock solution.

The average pH throughout the experiment was 4.99 (± 0.01) for the acidic artificial rainwater and 7.05 (± 0.01) for the neutral artificial rainwater. The climate chamber lab had an ambient temperature between 25 °C in winter an 31 °C in summer due to the exhaust heat of the climate chamber. The water temperature of the artificial rainwater matched the ambient temperature.

Blank samples of both types of artificial rainwater were analysed using inductively coupled optical emission spectroscopy (ICP-OES; Chapter 2.4). Mean values were calculated from these six samples (three from the acidic & three from the neutral artificial rainwater). The accuracy and precision are detailed in Chapter 2.4. Most elements, such as P, Mn, Fe, and Mg, were found only at very low concentrations (less than 10 ppb), as expected. The acidic artificial rainwater contained higher levels of S compared to the neutral water, attributable to the addition of H_2SO_4, while the neutral rainwater exhibited approximately ten times higher Na concentrations due to the addition of NaOH (Tab. 4.3). The concentrations of K and Ca, as well as Na in the acidic water and S in the neutral water were above or around 100 ppb (Tab. 4.3). This might be due to the relatively high concentrations of these elements in the tap water, which was demineralised using a single cartridge for water desalination rather than a Milli-Q® system. Additionally, the high Si content in the blanks could be a result of contamination from silicon components within the ICP-OES, such as the torch.

Table 4.3: Mean composition of the used artificial rainwater obtained from the ICP-OES measurements of the blank samples taken during the climate chamber experiment. For some elements the concentration were rounded to 10 ppb because the original data was given as ppm with only two digits.

Elements (ppb)	P	S	Mn	Fe	Mg	Si	Ca	Na	K
acidic (pH 5)	3.5	140	0.2	7.3	8.0	270	160	130	130
neutral (pH 7)	1.6	100	0.1	6.3	5.0	170	100	1210	120

4.2 Results

4.2.1 Rock varnish

4.2.1.1 Colour changes over time

Colour measurements were conducted throughout the climate chamber experiment. The colour change was calculated by comparing the measurements taken during and after the experiment with the initial measurement, which served as a reference value (see Chapter 2.1).

The mean ΔE of all weathered rock samples, divided into the two groups with different rainwater compositions, shows a significant difference in colour change. As expected, the ΔE after the first two time periods, totalling 15 days, already revealed changes of 1.63 ± 0.04 for samples weathered with rainwater at pH 5 and 1.30 ± 0.04 for the group with a pH of 7. Thereafter, the rate of change slowed down for both groups (Fig. 4.5). For the neutral group (pH 7), the mean ΔE values remained around 1.5 for the rest of the experiment. In contrast, the ΔE of the group weathered with acidic rainwater (pH 5) continued to increase steadily, reaching a maximum of 2.98 ± 0.04 after 360 days of weathering. It is notable that both groups exhibited a peak followed by a slight decrease after 90 days, which was the only period simulating solely the rainy season. The slight decrease observed after 120 days occurred following a period simulating only the dry season. All subsequent periods included both dry and rainy seasons (Fig. 4.5).

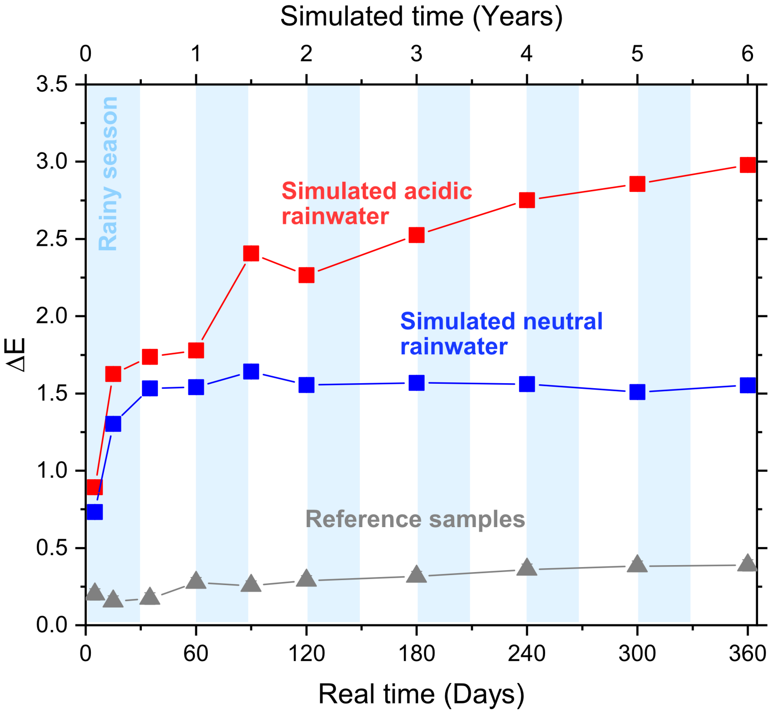

Figure 4.5: Average ΔE values of all rock samples that were weathered in the climate chamber as a function of weathering time, along with the reference samples that were not weathered. The weathered samples are divided into two groups: those exposed to artificial rainwater with a pH of 5 (red) and those with a pH of 7 (blue). Error bars (95 %) are smaller than the symbol size. The blue-shaded areas indicate the simulated rainy season with the highest number of simulated rainfall events, representing the period from January to June (Tab. 1.2).

Reference samples stored under dry and controlled conditions showed a maximum mean ΔE of 0.39 ± 0.04 after 360 days. The ΔE of the reference samples appeared to increase over time. When examining the individual ΔE values for each of the four reference samples, it is noticeable that the values fluctuated throughout the experiment, with only the mean value showing a roughly linear increase. This pattern is also visible in Fig. 4.6, which displays the granophyre and gabbro reference samples separately.

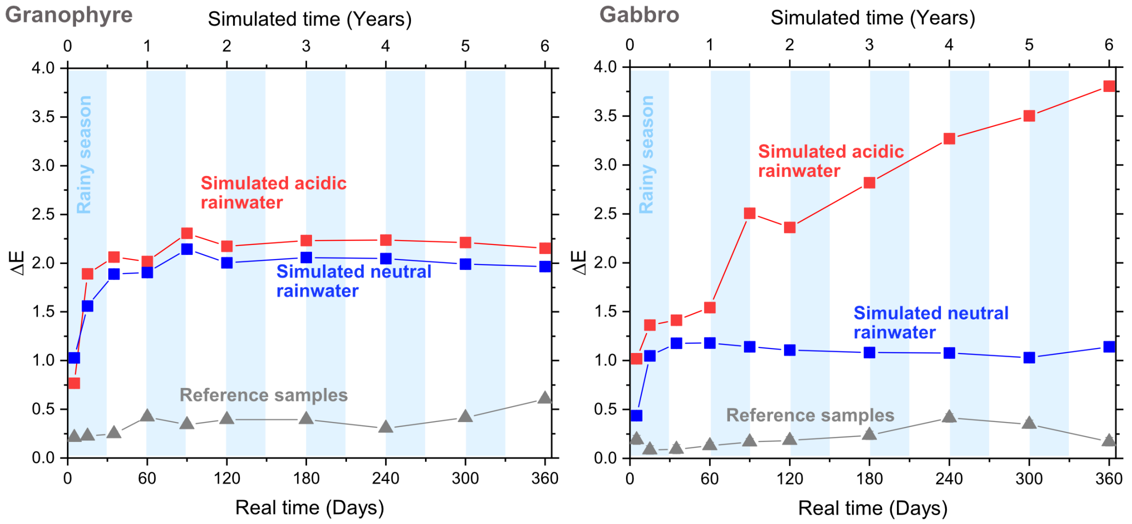

Figure 4.6: Average ΔE values of the granophyre (left) and gabbro (right) samples weathered with artificial rainwater at a pH of 5 (red) and 7 (blue) as a function of weathering time. Error bars (95 %) are smaller than the symbol size. The blue-shaded areas indicate the simulated rainy season with the highest number of simulated rainfall events, representing the period from January to June (Tab. 1.2).

When the mean ΔE was calculated separately for the granophyre and gabbro samples, further divided into the two rainwater composition groups, it became evident that the entire increase in ΔE for the group irrigated with acidic rainwater (pH 5), as shown in Fig. 4.5, originated from the gabbro samples (Fig. 4.6). These samples displayed an even larger disparity between the two groups, with a ΔE of 3.80 ± 0.04 for the samples weathered under acidic conditions (pH 5) compared to a ΔE of 1.14 ± 0.03 for the neutral group (pH 7; Fig. 4.6). Again, it was notable that the ΔE did not change significantly after the first 15 days of weathering. The development of ΔE values for the two granophyre sample groups followed a similar pattern after the initial 35-day period. Both granophyre groups exhibited a higher ΔE of around 2 after 35 days compared to the gabbro samples, which then remained roughly constant. The difference between the two granophyre groups after 35 days was 0.17 and stayed within this range until the end, with values between 0.11 and 0.22 (Fig. 4.6). It is noteworthy that, as previously mentioned, the ΔE values for both granophyre groups increased until 90 days and then decreased once after the 120 day measurement before remaining constant for the rest of the experiment. The 90 and 120 day periods were the only two periods simulating solely the wet or dry season, respectively. This effect was even more pronounced for the gabbro samples weathered with acidic rainwater at pH 5, where the mean ΔE increased from 1.54 ± 0.04 after 60 days to 2.51 ± 0.04 after 90 days and decreased slightly after 120 days before constantly increasing again for the rest of the experiment. Conversely, the gabbro samples weathered with neutral rainwater at pH 7 did not exhibit any significant changes after 90 and 120 days compared to earlier measurements.

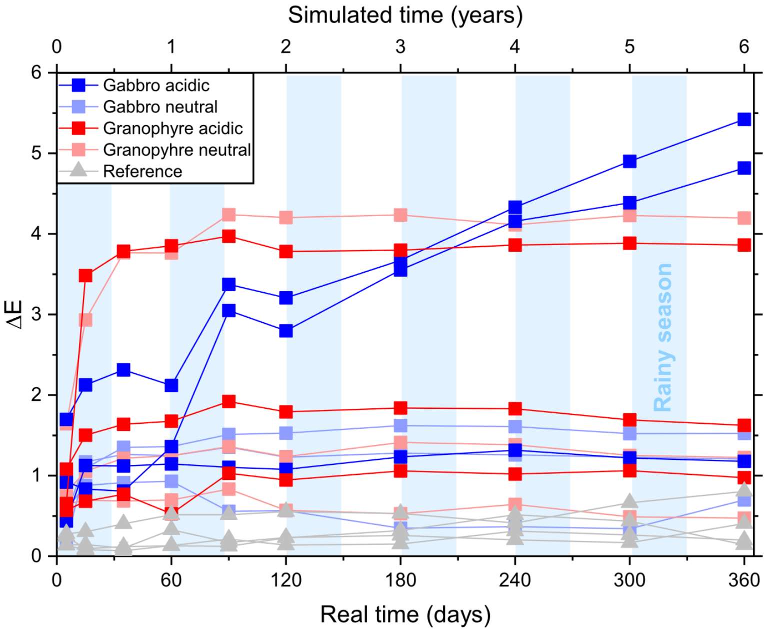

Figure 4.7: ΔE values of the granophyre an gabbro samples as a function of weathering time. Error bars (95 %) are smaller than the symbol size. The blue-shaded areas indicate the simulated rainy season with the highest number of simulated rainfall events, representing the period from January to June (Tab. 1.2).

The differences between the single samples, as well as within the sample groups, were quite high in three out of four groups. It was noticeable that, as shown in Fig. 4.6, only the gabbro samples weathered under acidic conditions exhibited a continuous colour change. This was due to the change of two out of three samples within this group (Fig. 4.7). It was also noticeable that one granophyre sample weathered under acidic and one weathered under neutral conditions had significantly higher ΔE values than the other samples in their group but did not change significantly after 35 days of weathering. Most of the other rock samples weathered in the climate chamber had ΔE values between 1 and 1.5 after the initial 35 days of weathering and did not change significantly thereafter. One gabbro and one granophyre sample stood out with significantly lower ΔE values, in the same range as the reference samples (Fig. 4.7). The ΔE values of the individual samples at each time step are given in Tab. A1 in the appendix and the whole dataset can be found in the digital supplementary material.

It was also noticeable that, while the mean ΔE compared to the initially measured colour before the start of the weathering experiment did not change significantly for most of the samples, a measurable colour change occurred from step to step. When the ΔE was calculated by comparing the most recent measurement with the preceding one, instead of the initial measurement, it became evident that a continuous change in colour occurred in all sample groups throughout the experiment. Furthermore, it was observed that the step-to-step changes over the course of the experiment got smaller in the different sample groups, except for the gabbro samples weathered under acidic conditions. In this group, the ΔE in comparison to the initial measurements continued to increase over time. The continuous change from step to step, without further increase in the ΔE when compared to the initial measurement, in the other three sample groups can be attributed to small but consistent fluctuations in the ΔE across all samples within this groups. These fluctuations caused slightly smaller or larger ΔE values in comparison to the initial measurement at each step, which were not reflected in the mean values. This occurred because the samples within each group exhibited changes in different directions at each step, leading to a smoothing effect in the mean values.

The sum of the step-to-step changes was greater than the overall ΔE for all samples, but the differences between these values varied significantly depending on the samples. This was particularly apparent for the reference samples, where the step-to-step changes often exceeded the absolute ΔE. This indicated that the colour of the reference samples fluctuated around the initial value but did not move significantly away from it. For some other samples, the extent of change from step-to-step compared to the absolute ΔE was conspicuously high, particularly for one gabbro and one granophyre sample weathered under neutral conditions that had low absolute ΔE values. For these two samples (NA2 & NR2), the absolute ΔE was only 0.70 ± 0.04 and 0.47 ± 0.04 at the end of the experiment (Tab. 4.4), respectively, while the sum of the step-to-step changes was 3.85 and 2.31, respectively. The step-to-step changes of all samples are given in Tab. A2 in the appendix.

As aforementioned, the granophyre and gabbro samples were cut from different rock pieces with various types of varnish, even on the same rock type. Consequently, the samples for the climate chamber experiment were always prepared as pairs from the same rock piece, with one sample from each pair placed in each group to ensure comparability (Chapter 3.1.1). When comparing these sample pairs, it was noticeable that the differences between pairs of the same rock type were considerable. For instance, granophyre sample pairs had a ΔE ranging from < 1 to approximately 4, while the difference between the two samples within one pair, which were weathered with different artificial rainwater types, reached a maximum of 1.15 (Tab. 4.4). Additionally, it was notable that, for the granophyre pair with the greatest colour change (SR1 & NR1), the sample weathered with neutral rainwater exhibited a slightly larger ΔE than the one weathered with acidic rainwater (Tab. 4.4).

Among the gabbro pairs, only two showed significant differences between the two groups weathered under different conditions. The third pair (SA3 & NA3) had the smallest ΔE, with values around 1.2 for both the acidic and neutral sides and a difference of only -0.03 ± 0.03, which is zero within the error. This pair, cut from the gabbro, featured a smoother and darker surface than the other two pairs (see Chapter 3.1.1). Consequently, all the difference between the acidic and neutral sample groups shown in Fig. 4.6 arises from only two of the three gabbro sample pairs, which display significant variations between the groups, with ΔE differences of 3.90 and 4.12. These two pairs were cut from gabbro samples with a porous, uneven, relatively bright surface that appears less metallic (see Chapter 3.1.1).

Similarly, the granophyre pair with the greatest difference in ΔE between the sample weathered with acidic and neutral rainwater (SR3 & NR2) also had a brighter and less metallic appearance compared to the other granophyre samples. The total difference was 1.15 and the absolute ΔE value of the sample weathered with acidic rainwater was more than three times larger than of the sample weathered under neutral conditions (Tab. 4.4). The highest ΔE values within the granophyre samples were observed in the pair with the most porous surface (SR1 & NR1), featuring visible deep holes and a relatively dark colour (see Chapter 3.1.1). The ΔE values of 3.86 ± 0.05 and 4.20 ± 0.04 after 360 days were quite high. However, most of this colour change occurred within the first 35 days of weathering, after which there was minimal additional change (Fig. 4.7). This was also true for the granophyre pair with the greatest difference in colour change, as aforementioned.

Table 4.4: Comparison of the ΔE values of the used pairs of rock samples after 360 days of artificial weathering with acidic (pH 5) and neutral (pH 7) artificial rainwater. The error (95 %) is given for all values.

Rock type	**Sample names**	**Acidic (ΔE)**	**±**	**Neutral (ΔE)**	**±**	**Difference**	**±**
Granophyre	**SR1 & NR1**	3.86	0.05	4.20	0.04	-0.34	0.04
	SR2 & NR3	0.97	0.03	1.23	0.04	-0.25	0.03
	SR3 & NR2	1.62	0.03	0.47	0.04	1.15	0.03
Gabbro	**SA1 & NA1**	5.42	0.03	1.52	0.02	3.90	0.03
	SA2 & NA2	4.82	0.06	0.70	0.04	4.12	0.05
	SA3 & NA3	1.18	0.02	1.20	0.03	-0.03	0.03

One sample from each rock type in both groups was placed in the climate chamber at a 30° angle to examine the correlation between rock surface dip and observed weathering effects (see Chapter 4.1.2). The samples chosen for this positioning were all those with ‘1’ in their sample name (see Chapter 3.1.1). In both the acidic and neutral sample groups, these angled samples had the highest ΔE values. It is unclear whether this result was due to their angled positioning or due to their surface characteristics, as the variations between rock samples are substantial, even within the same rock type. However, the gabbro pairs numbered ‘1’ and ‘2’ were cut from the same rock piece, thus having comparable surface conditions. Notably, the colour change of the angled neutral-side sample is more than twice that of the non-angled sample weathered with neutral rainwater (pH 7), with a ΔE of 1.52 ± 0.02 compared to 0.70 ± 0.04 (Tab. 4.4). For the two samples from the same gabbro piece weathered under acidic conditions, the difference is smaller, but the sample angled at 30° still shows a greater colour change, with a ΔE of 5.42 ± 0.03, compared to 4.82 ± 0.06 for the non-angled sample (Tab. 4.4).

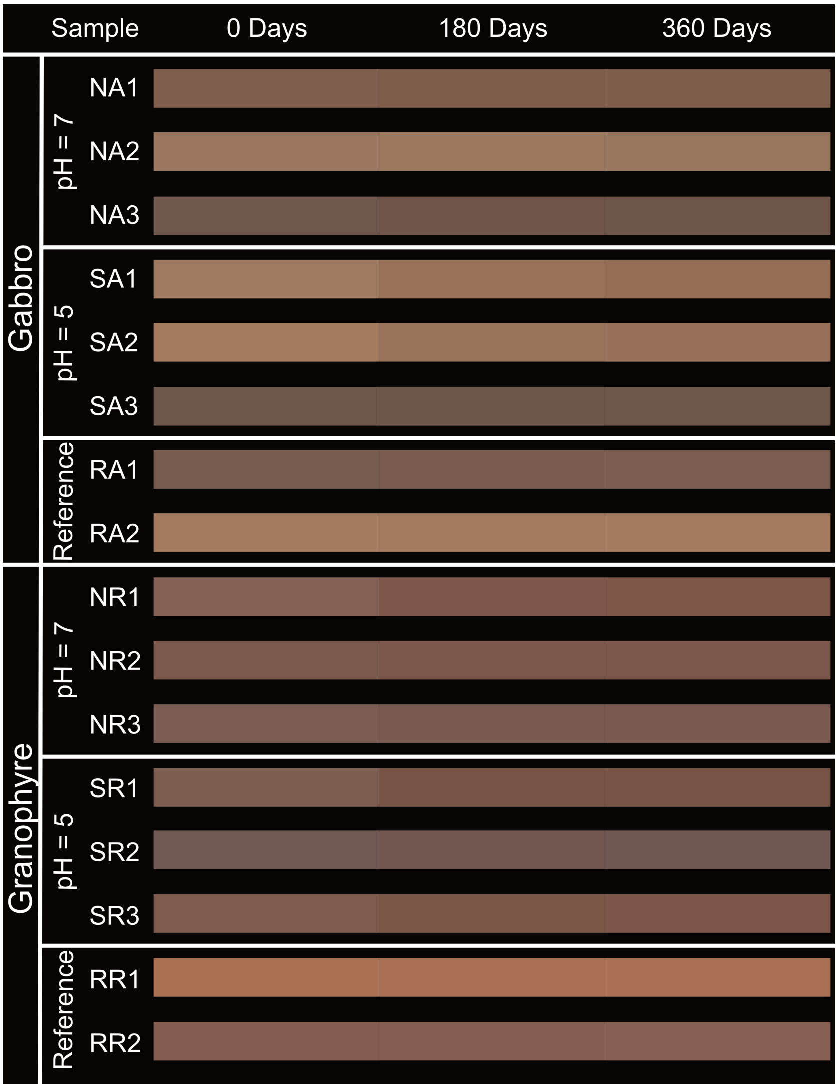

Figure 4.8: Measured colours of the used rock samples before, after, and 180 days into the artificial weathering experiment.

The colour changes are not only represented by ΔE values, but are also of a magnitude that is visible to the human eye. Since the measured area is covering the whole sample, the measured colour accurately reflects the mean colour of the sample surfaces (Chapter 2.1). The colours varied from sample to sample, as shown in the image of the used samples (Fig. 3.1), with colours ranging from nearly orange to dark brown tones. In most samples, a noticeable colour change occurred between the measurements taken before the experiment and those taken after 180 days of weathering ($\Delta E > 1$). Most of this change took place within the first 15 to 35 days (Fig. 4.6). During the latter half of the experiment, only samples SA1 and SA2 showed any additional visible change compared to their measured colour after 180 days of weathering. It was also notable that the colour of the four reference samples remained visually unchanged over the 360-day period (Fig. 4.8). Over the course of the experiment, the colour of all samples darkened, with the samples exhibiting the most substantial visible and measured colour change (SR1, NR1, SA1 & SA2) shifting from a light brown to a medium brown tone.

The colour change ΔE is influenced by changes in brightness, L*, as well as in the chromatic components a* and b* (Chapter 2.1). As shown in Fig. 4.8, the samples darkened throughout the weathering experiment. This negative change in L* is also apparent in the calculated ΔL* values for the samples analysed. The granophyre samples reached a mean ΔL* of -1.5 to -1.7 after an initial drop over the first 35 days, with no significant differences between the sample groups weathered with different types of artificial rainwater (Fig. 4.9), closely resembling the ΔE values in Fig. 4.6. By contrast, for the gabbro samples, the ΔL* values were even lower in the group weathered with acidic artificial rainwater (pH 5), reaching a minimum mean value of -3.25 ± 0.2 after 360 days. Samples weathered with neutral rainwater (pH 7) showed no significant change after the initial drop within the first 15 days (Fig. 4.9). This progression of ΔL* values aligns with the overall observed colour changes ΔE.

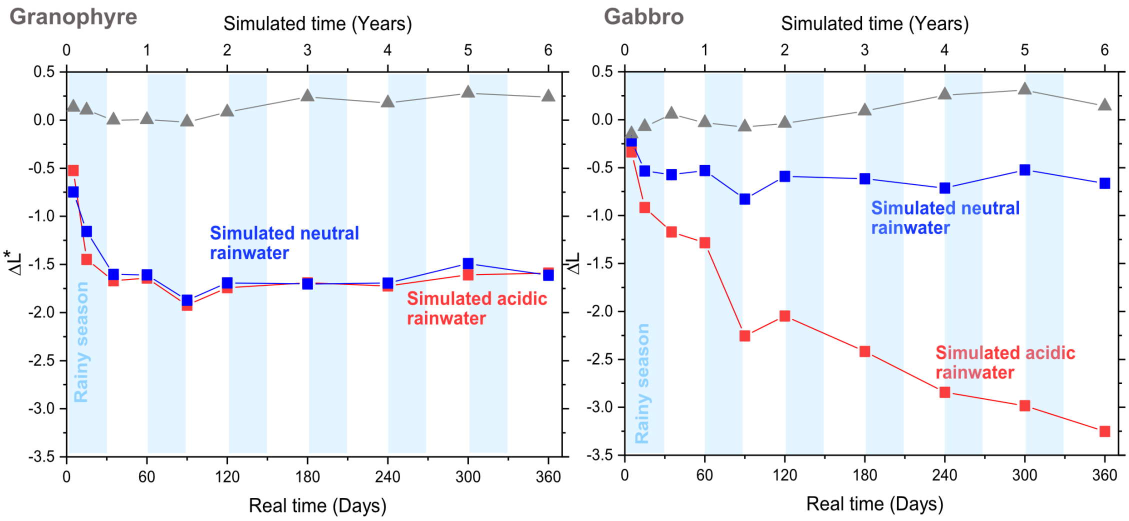

Figure 4.9: Average ΔL* values of the granophyre (left) and gabbro (right) samples weathered with artificial rainwater at pH values of 5 (red) and 7 (blue) as a function of time. Error bars (95 %) are smaller than the symbol size. The blue-shaded areas indicate the simulated rainy season with the highest number of simulated rainfall events, representing the period from January to June (Tab. 1.2).

Since ΔL*, Δa*, and Δb* values contribute equally to the calculated colour change ΔE (Chapter 2.1), it was straightforward to assess which component most influenced the overall ΔE. Here, the primary contribution arises from changes in brightness L* for the samples measured. For instance, the gabbro samples weathered with acidic artificial rainwater reached a mean maximum ΔE of 3.80 ± 0.04, while the mean ΔL* for this group was -3.25 ± 0.02. In contrast, Δa* was only 0.88 ± 0.01, and Δb* was -0.53 ± 0.01 for this group. The same applies across other sample groups and weathering periods. The highest Δa* value of only 1.76 ± 0.01 was recorded on a gabbro sample weathered under acidic conditions (SA1), and the highest Δb* value on a granophyre sample weathered under neutral conditions (NR1) at 2.37 ± 0.03, while both samples had much higher ΔL* values of -5.12 ± 0.01 and -3.14 ± 0.01, respectively.

The development of the Δa* and Δb* values throughout the weathering experiment was similar to those of the ΔE and ΔL* values. The mean values for the reference samples remained consistently close to zero, while the granophyre and gabbro samples showed rapid change over the first 15 to 35 days. Subsequently, the granophyre samples in both groups, one weathered under acidic and one under neutral conditions, showed no significant further change, with overall mean Δa* values for both groups in the range of approximately 0.5 to 0.8. The Δb* values of the granophyre samples were higher, ranging from 0.8 to 1 for the group weathered with neutral artificial rainwater (pH 7) and from 1 to 1.4 for the group weathered with acidic artificial rainwater (pH 5). The Δa* values for the two different groups of gabbro samples also followed the trend of the ΔE and ΔL* values, with a continuous increase after the initial 15 to 35 days for the group weathered with acidic rainwater, while the other group did not significantly change after this initial period. The development of Δb* values for the group weathered with neutral artificial rainwater was similar, with no further significant change after reaching values of approximately 0.7 within the first 15 days. By contrast, the gabbro samples weathered with acidic artificial rainwater (pH 5) reached their maximum Δb* after 5 days, then began a steady decrease after 35 days, reaching -0.53 ± 0.01 by the end of the experiment. As before, the reference samples remained close to zero for all measurements.

In summary, the most important observations were that (1) the colour of all samples changed significantly over the first 15 days of weathering, reaching mean ΔE values of 1 to 2, (2) the change thereafter nearly halted in all sample groups, except for the group of gabbro samples weathered under acidic conditions (Fig. 4.6), (3) the main part of the colour change was due to a shift in the brightness of the samples, represented by the L* value (Fig. 4.9), (4) the differences within the sample groups were considerable and often larger than the differences between the sample groups (Tab. 4.4), (5) the colour change on some samples was substantial enough to be easily visible to the naked eye (Fig. 4.8), and most important (6) the colour change was overall larger in the sample groups weathered under slightly acidic (pH 5) conditions compared to the samples weathered under neutral (pH 7) conditions. The individual ΔE, ΔL*, Δa*, and Δb* values of all samples measured at the end of the experiment are also shown in Tab. 4.6.

4.2.1.2 Textural and morphological changes over time

High-resolution optical images

High-resolution optical images were taken before and after the weathering experiment, as well as after 180 days of weathering, and were analysed to identify visible surface changes as a result of weathering. For this, the two images captured before and after the experiment were superimposed, with one image converted to a negative (Chapter 2.6). This method facilitated easier identification of changes, though it did not permit quantitative analysis.

All reference samples, stored under controlled conditions outside the climate chamber throughout the duration of the experiment, showed no significant surface changes over larger areas, as indicated by other analytical methods, such as colour measurements. On one sample, however, a small piece of rock at the edge, approximately 0.5 mm in diameter, had chipped off, while in another, a similarly sized flat piece chipped off in the centre. The latter piece detached directly in the area measured with p-XRF, potentially due to physical force applied by the measuring head on the sample surface. It is possible that the other piece on the edge was also chipped off due to physical force while handling the samples. Therefore it unfortunately is possible that pieces of rock that chipped off from the samples weathered in the climate chamber were not solely removed by the applied weathering, but by physical force while handling the samples.

The gabbro samples weathered under neutral conditions exhibited diverse changes. In the first sample (NA1), only a few small areas (each < 1 mm) showed changes, and no larger fragments detached. However, the second sample displayed more notable differences. The superimposed images revealed that larger areas had altered over the course of the experiment (Fig. 4.10; NA2). The lighter areas darkened and the surface structures changed with lighter, orange coloured parts partially being washed away or dissolved and the darker, sometimes black, underlying layers being revealed. The changes on this sample (NA2) are neither as pronounced nor as intense as those observed on the corresponding gabbro samples weathered under acidic conditions (Fig. 4.11; SA1 & SA2). Overall, the affected area spans nearly half of the sample, although the individual changed spots within this area were relatively small, measuring around 1 mm or less, but numerous. Estimating the total proportion of the sample that changed was not feasible. Most changes appear to have occurred during the first half of the experiment, as the images from 180 to 360 days display fewer changes compared to the images taken before the experiment and after 180 days (Fig. 4.10a & b). Conversely, some areas appeared brighter after 180 days and appeared to darken again after 360 days (Fig. 4.10b). The measured colour change ΔE on the sample with significant surface changes (NA2) was only 0.70, the smallest value within its sample group (Tab. 4.4). This sample's colour changes were not only much lower than those of two of the gabbro samples weathered under acidic conditions, which exhibited comparable visual changes, but the ΔE values also fluctuated significantly, reaching a maximum of 0.93 after 60 days and a minimum of 0.34 after 300 days. This fluctuation fits the observed colour variation, where certain areas brightened initially and then darkened again at specific spots, as described above.

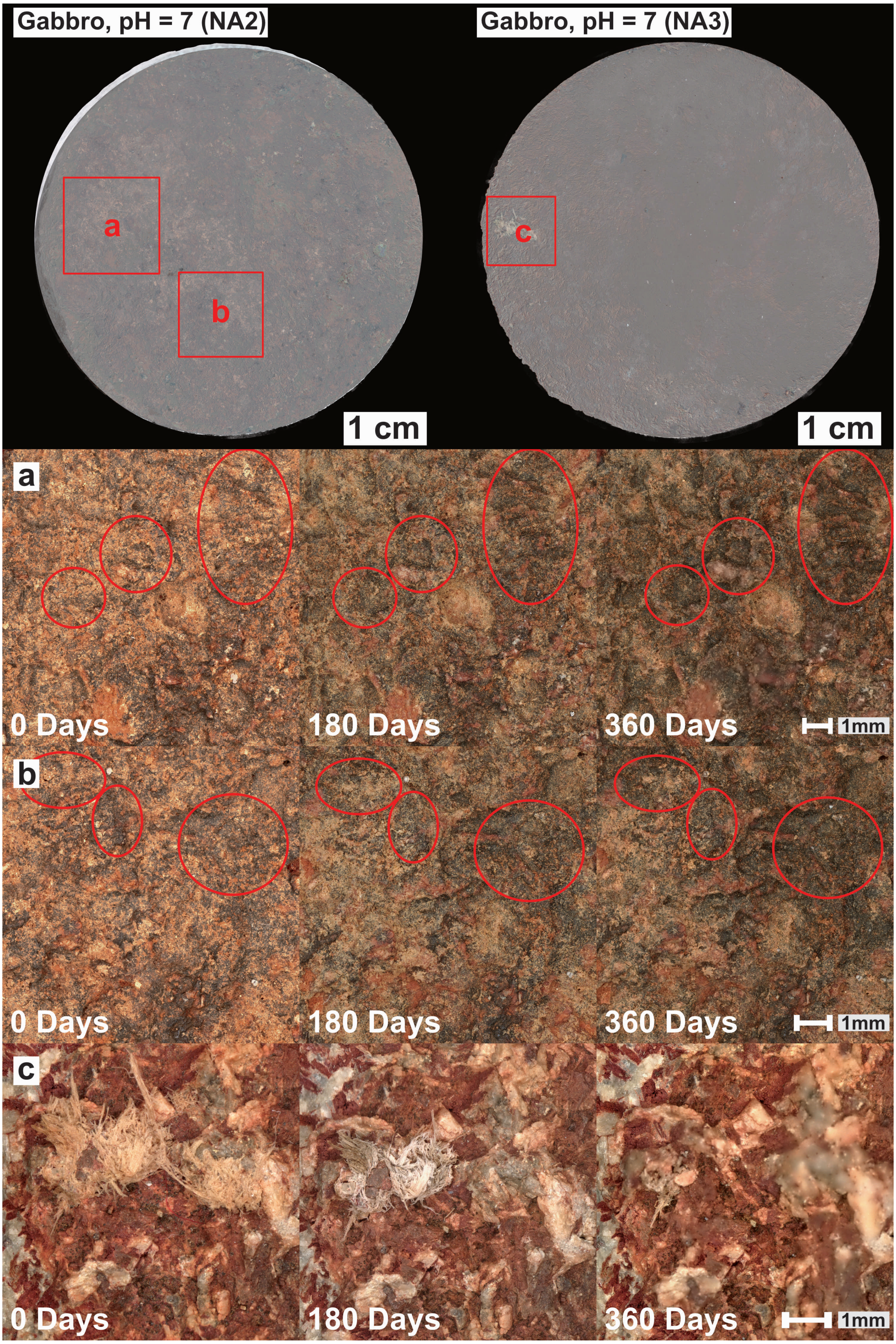

Figure 4.10: Optical images of the surface of two gabbro samples. In the first sample (a & b) over the course of the experiment, some orange material disappeared, exposing the darker areas underneath. On the second sample (c) organic fibres on the surface were washed away or dissolved during the experiment. The grey images in the top section present the full images of the samples, with negative and normal (50 % transparency) images superimposed for comparison.

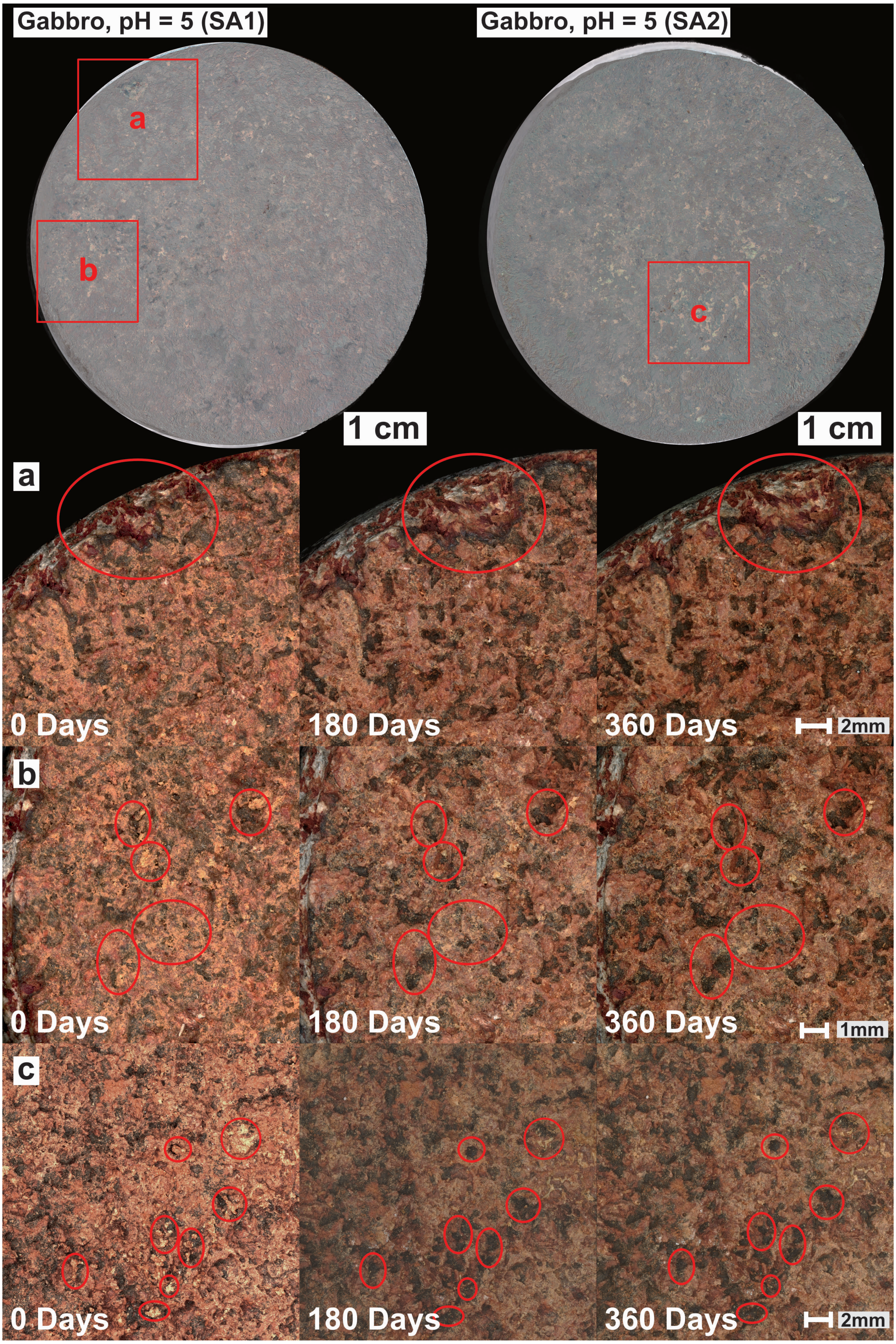

Figure 4.11: Optical images of the surface of two granophyre samples weathered under acidic conditions. On one sample (a) some material chipped off and on both samples (b & c) significant amounts of material were washed away or dissolved over the course of the experiment. The grey images in the top section display the full sample images, with superimposed negative and normal (50 % transparency) pictures, enhancing visibility of these changes.

In the third sample of this group (NA3), no changes to the rock surface itself were observed. However, a larger (2–3 mm) piece of material resembling organic fibres was gradually washed away or dissolved over the course of the weathering experiment (Fig. 4.10c). Raman spectroscopy, conducted after the end of the weathering experiment, confirmed that the fibre remnants were of organic origin.

Two of the gabbro samples weathered under acidic conditions changed significantly (SA1 & SA2), while on the third sample (SA3), only some organic fibres were visibly lost over the course of the experiment, similar to one gabbro sample weathered under neutral conditions (NA3), but over a smaller area (Fig. 4.10c). Additionally, a very small piece of material with a diameter of < 0.5 mm was chipped off. This sample also had the darkest and densest surface compared to the other two gabbro samples weathered under acidic conditions, which exhibited an orange-brown hue with small visible darker patterns and an overall porous surface structure (Fig. 3.1; SA1 to SA3).

The other two samples (SA1 & SA2) underwent significant change over nearly the entire surface area, similar to one of the gabbro samples weathered under neutral conditions (Fig. 4.10a & b). In one of these two samples, a larger piece of rock also chipped off near the edge during the first half of the experiment. No cracks were visible at the beginning of the experiment, and the piece was relatively large, approximately 2 x 2 mm^2 in size (Fig. 4.11a). The observed changes were spread across the entire area, individually small but numerous. The changes are visible in the superimposed images of both samples as small, light yellow to orange spots dispersed across most of the sample surface (Fig. 4.11; SA1 & SA2). At each of these spots, some of the orange material covering the sample surface, which comprised the majority of the sample, was dissolved, washed away, or chipped off over the course of the experiment, exposing the underlying layer. This layer appeared darker, nearly black, at most spots. Although each area of change was small, the large number of affected spots led to a substantial overall alteration of the surface (Fig. 4.11b & c). This correlated with the measured colour changes on both samples, which exhibited the highest ΔE values within their sample group and significantly higher values compared to the samples weathered under neutral conditions (Fig. 4.4). The material loss may have been due to dissolution upon contact with the artificial rainwater used, it may have chipped off due to physical strain, or was subsequently washed away.

All three granophyre samples weathered under neutral conditions displayed different surface changes compared to the gabbro samples under similar conditions. The changes were primarily limited to smaller areas on two samples. The Araldite® resin used to protect the sides of the samples against weathering became less shiny, more brittle, and brighter over the course of the experiment, likely due to prolonged UV exposure, despite being labelled UV-stable (Huntsman, 2004). These changes, visible in the superimposed images (Fig. 4.12; NR2), were not considered as part of the surface changes as they did not affect the rock surface directly, though they might have influenced colour measurements. On one granophyre sample, a piece near the edge chipped off (Fig. 4.12a). This chipped off piece, greater than 1 mm, originally displayed a visible crack on the surface before the experiment. After 180 days, this crack was still visible, but at the end of the experiment, the piece detached, with a new crack forming, which looked like the next piece of material could chip off soon (Fig. 4.12a). Another sample (NR3) showed a yellow coating over portions of the surface at the start of the experiment, which largely vanished by the 180-day mark. By the end of the experiment, only small remnants of this coating remained (Fig. 4.12b), which were identified as lepidocrocite by Raman spectroscopy using the RRUFF database (Lafuente et al., 2015). The yellow coating initially covered less than 10 spots, each approximately 1 mm or smaller.

Two granophyre samples (SR1 & NR1), which were cut out of the same piece of granophyre but weathered under different conditions, stand out due to their rough surface with very fine structures and an overall dark colour compared to the other granophyre samples as described in Chapter 3.1.1. Both samples showed considerable changes over large areas regardless of weathering conditions, although the specific changes differed depending on the weathering conditions. Sample NR1, weathered under neutral conditions, had a predominantly dark surface with red, black, and orange patterned areas before the experiment (Fig. 3.1; NR1). During weathering, the orange areas on the sample were dissolved or washed away, with black regions gradually becoming visible underneath the orange patches (Fig. 4.13a). This change was prominent over an area of approximately 2.0 x 2.5 cm^2, as well as in smaller areas elsewhere on the sample. These changes appear as orange areas in the superimposed images of the sample (Fig. 4.13; NR1). Red and black areas remained mostly unchanged. It remains unclear whether the change resulted from dissolution or physical weathering of the orange material, exposing underlying black areas.

The other granophyre sample, which was weathered under acidic conditions (SR1), had more dark areas and fewer red patches compared to NR1, weathered under neutral conditions, despite originating from the same piece of granophyre. Fine orange structures were also visible on the sample surface (Figs. 3.1 & 4.13b). During weathering, parts of these orange structures disappeared within the first 180 days, with additional but minor changes observed afterwards (Fig. 4.13b). A yellow mineral grain on the surface also disappeared in the first 180 days, with no trace remaining after the end of the experiment, making it impossible to identify the mineral phase. Additionally, a fine-grained, white layer, resembling secondary minerals, which were identified as albite (Chapter 3.1.3.2), was visible on SR1's surface (Fig. 4.13c) and progressively disappeared, mostly within the first 180 days (Fig. 4.13b & c). Whether this layer was dissolved or washed away remains unknown. The disappearance of the albite grains affected a broad surface area, visible as light blue are in SR1's superimposed images (Fig. 4.13; SR1). Both granophyre samples displayed the most significant colour changes among their respective groups, as reflected in their high ΔE values (Tab. 4.4).

In contrast, the other two granophyre samples weathered under acidic conditions showed minimal changes (SR2 & SR3). No extensive surface differences were observed, apart from one chipped off piece similar to that shown in Fig. 4.12a. This sample had a visible crack before the experiment and a piece, measuring about 2 x 1 mm^2, detached during the first half of the experiment. On the other sample a larger piece of material chipped off in the middle of the sample over the course of the experiment.

Overall, it was observed that small fragments chipped off from a large number of the rock samples, primarily along the edges. Since this phenomenon was also observed in some of the reference samples that were not weathered, it can not be ruled out that some of this chipping resulted from sample handling during measurements or transportation. Additionally, the edges of the samples were subjected to considerable physical forces during the sample preparation with a core drill, potentially causing crack formation and material loosening. Some samples also exhibited partial varnish removal along the edges during cutting (Fig. 4.11a). The most notable changes other than chipped off material included (1) the widespread removal of orange material, which exposed the underlying, darker portions of the sample (Figs. 4.11b, 4.11c & 4.13a), (2) the disappearance of white fine-grained material that was identified as albite and had accumulated in holes and crevices, also exposing the underlying varnish (Fig. 4.13c), (3) the dissolution or washing away of individual mineral grains and thin layers of lepidocrocite (Figs. 4.12b & 4.13b), and (4) the removal of organic fibres from the surface over the course of the weathering experiment (Fig. 4.10c). In summary, it can be said that the changes observed on the samples weathered under slightly acidic (pH 5) conditions were more pronounced than on the samples subjected to artificial rainwater with pH 7. This is especially true for the gabbro samples weathered under different conditions, where the largest overall changes were observed.

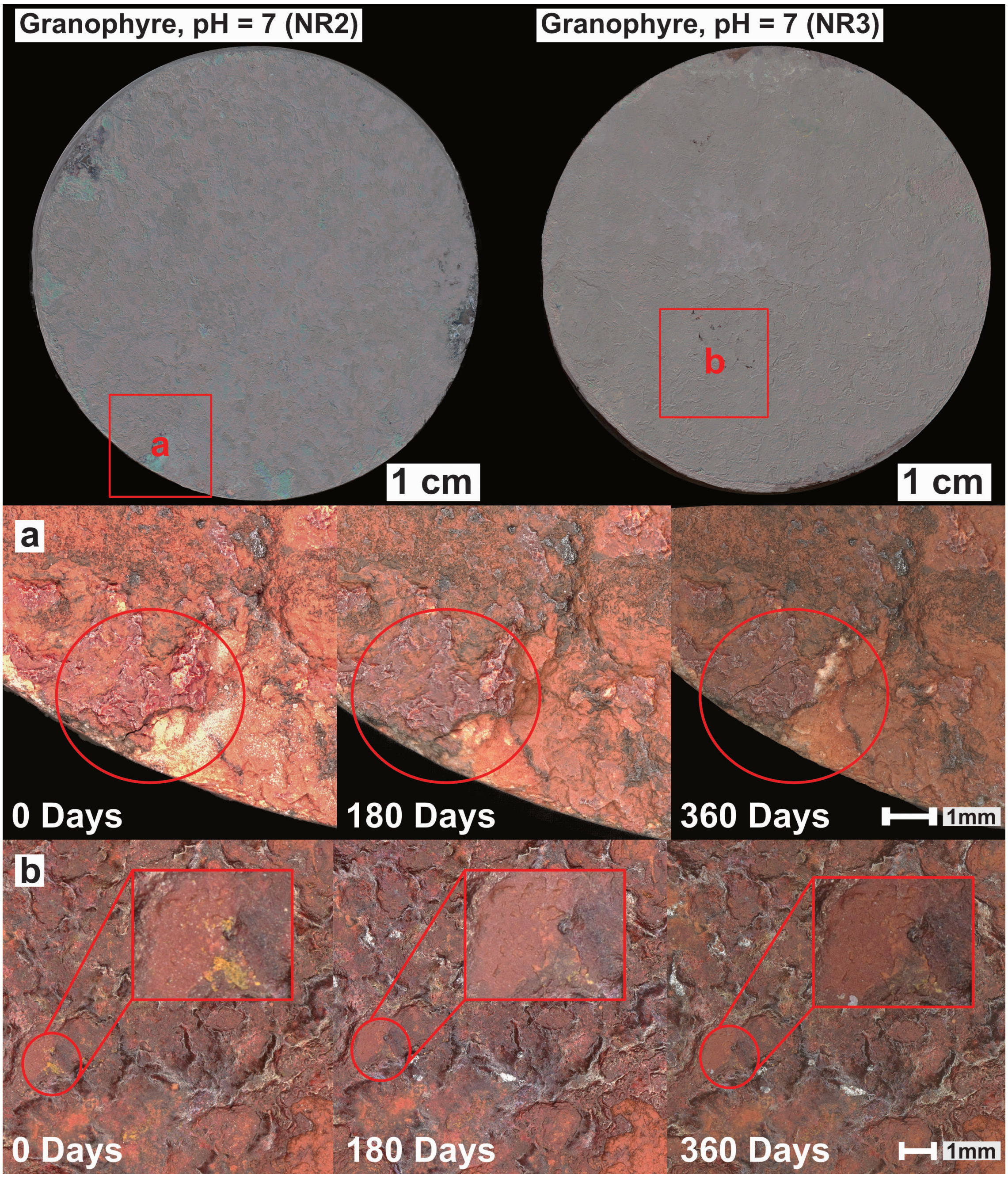

Figure 4.12: Optical images of the surface of two granophyre samples weathered under neutral conditions. In (a) one area, some material chipped off, while on another sample (b) a lepidocrocite layer gradually disappeared over the course of the experiment on multiple small spots. The grey images in the top section display the full sample images, with superimposed negative and normal (50 % transparency) pictures, enhancing visibility of these changes.

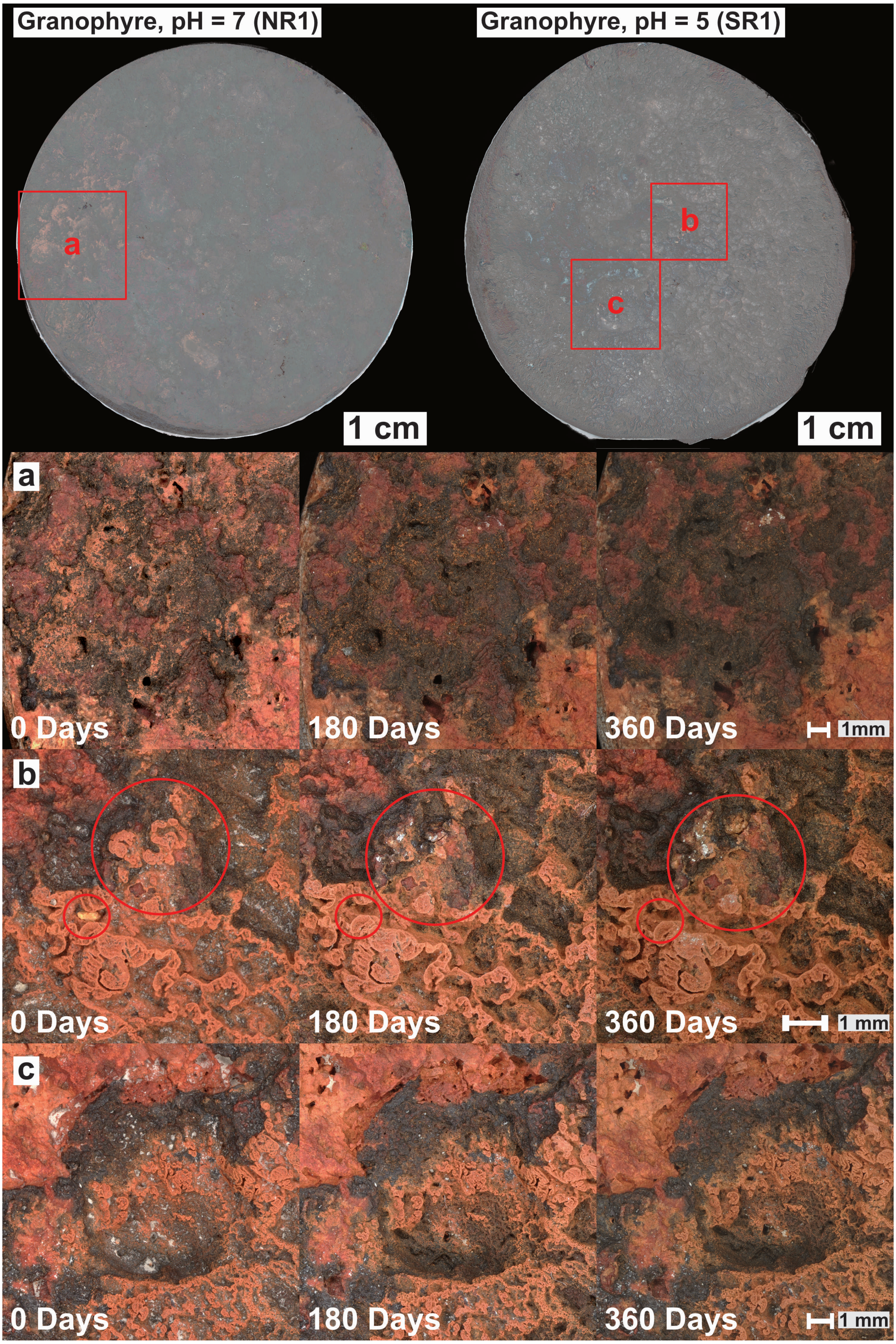

Figure 4.13: Optical images of the surface of two granophyre samples. The colour of the neutral sample (a) has significantly changed over a large area, with (b) some material chipping off and (b & c) being washed away or dissolved. The grey images in the top section display the full sample images, with superimposed negative and normal (50 % transparency) pictures, enhancing visibility of these changes.

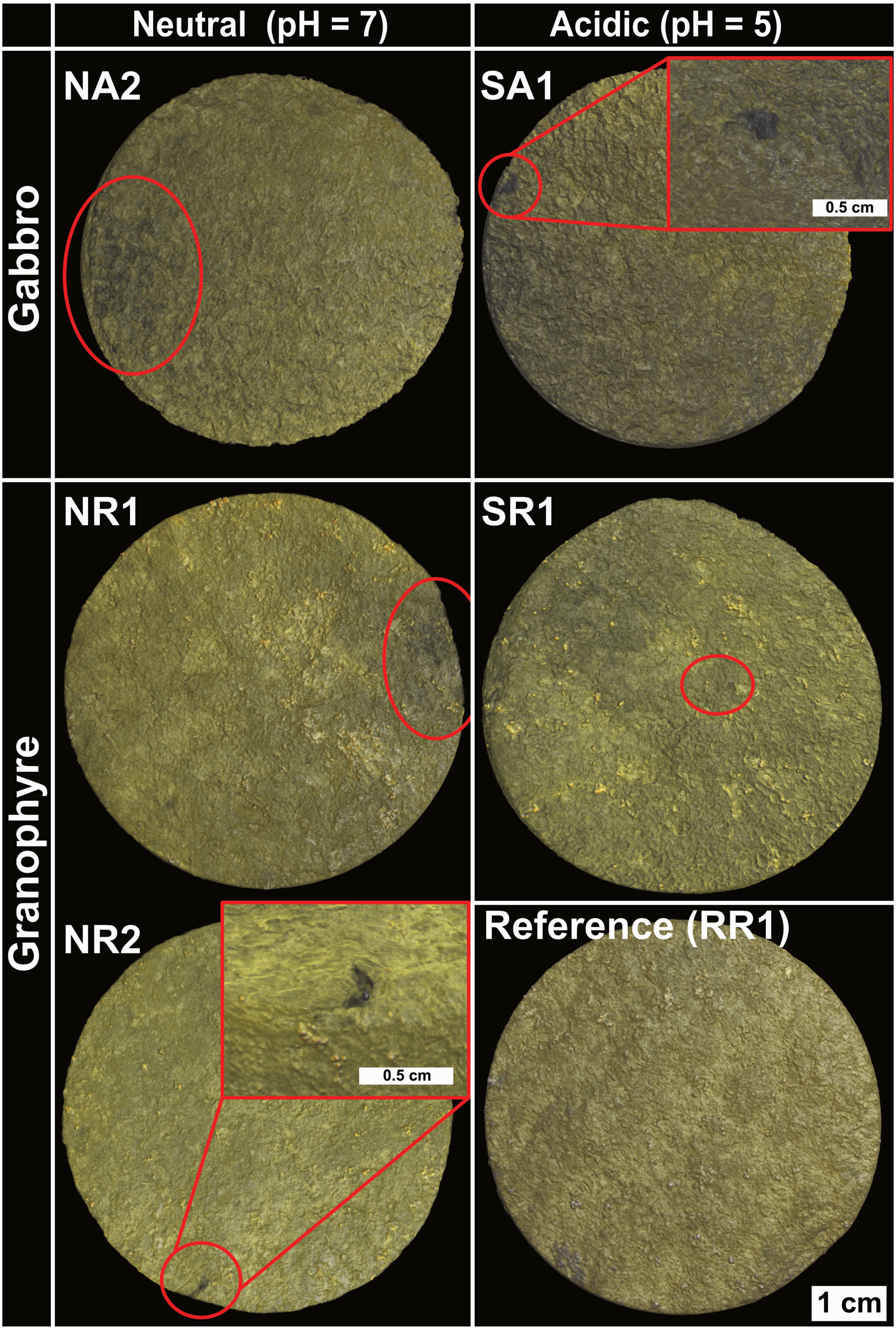

Figure 4.14: Superimposed μ-CT scans taken before an after the weathering experiment of several rock samples. Areas with visible changes were marked with red circles. The reference sample shown (RR1) exhibited no changes. The enhanced views of the material loss were taken from a different viewing direction.

µ-CT scans

Additionally to the high-resolution optical images, all samples were scanned before and after the weathering experiment using µ-CT to visualise changes on the sample surfaces in the resulting 3D scans. The µ-CT device used had a significantly lower resolution (voxel size = 38 µm) than the µ-CT used in previous research (Neumann, 2021). However, the higher-resolution device could not be utilised due to the larger size of the samples. The resulting scans were superimposed to highlight surface changes. For better comparison, the scans taken prior to the weathering experiment were displayed with a greyscale colour scheme, while those taken post-experiment were displayed in amber. With this setting, all material that disappeared during the experiment appeared in grey and could be easily identified.

The µ-CT scans of the reference samples did not show any visible changes in the superimposed scans (Fig. 4.14; RR1). Although high-resolution optical images revealed some material loss from one of the reference samples, these changes could not be identified in the µ-CT scans. This was likely due to the lower resolution of the scans and the small scale of the changes. On two samples weathered in the climate chamber, material loss from chipping was visible in the superimposed µ-CT scans (Fig. 4.14; NR2 & SA1). These changes coincided with observations from the high-resolution optical images (Figs. 4.11a & 4.12a). Additionally, grey areas indicating material loss were visible in two granophyre samples weathered under different conditions(NA2 & SA1), where the lower halves of these samples appeared more greyish compared to the rest of the µ-CT scans (Fig. 4.14; NA2 & SA1). These significant surface changes were consistent with observations made from the high-resolution optical images (Figs. 4.10 & 4.11).

The fact that these changes were visible in the µ-CT scans, despite a resolution of only 38 µm per voxel, indicated that (1) material was lost rather than just the colour or chemistry of the surface had changed and (2) the changes were substantial, involving a thicker part of the uppermost layer of the samples and not only a few µm. Conversely, some changes observed in the high-resolution optical images were not evident in the µ-CT scans. For instance, structural changes in granophyre sample SR1, visible in the high-resolution optical images (Fig. 4.13b), were not detected in the µ-CT scans (Fig. 4.14; SR1), despite the known locations of these changes. Another granophyre sample, NR1, showed significant changes in the high-resolution optical images that were not found in the µ-CT scans, however, another area, seemingly unaffected in the high-resolution optical images, appeared to have changed in the µ-CT scans (Fig. 4.14; NR1).

Samples not shown in Fig. 4.14 exhibited no visible changes in the superimposed µ-CT scans. Notably, some sample colours differed due to varying densities and adjustments in greyscale thresholds during analysis. Two sets of scans could not be analysed, and two other sets displayed unrealistically large changes. The superimposition of these latter scans required excessive computation time, suggesting software-related errors that produced incorrect results. Only the largest surface holes (e.g. in sample

NR1) were discernible in the μ-CT scans. Most surface roughness, pores, and cracks observed in the high-resolution optical images were undetectable in the μ-CT scans, due to the low resolution. Consequently, the μ-CT scans appeared smoother than the actual surfaces, making them less suitable for detailed analysis. This limitation also hindered reliable quantification of surface changes, pore space, or crack volumes. Moreover, the calculated sample volumes were inconsistent, with all samples showing approximately 1.3 % less volume after the experiment. This was unrealistic given the different amount of visible material loss in high-resolution optical image observations and the differences in the measured weight loss.

Overall the μ-CT scans did not deliver as many insights on the surface changes of the samples as expected, which was mainly due to the lower resolution compared with the optical images and the μ-CT device used in a previous study, where the μ-CT scans delivered better results (Neumann, 2021). Nevertheless, the μ-CT scans were useful to confirm the most significant changes observed in the optical images and to confirm that the observed changes were not due to a change of colour and rather due to the loss of material.

4.2.1.3 Weight changes over time

All rock samples were weighed prior to the climate chamber experiment, after 180 days, and at the end of the experiment after 360 days of weathering. All 16 samples weathered in the climate chamber exhibited weight loss. After 180 days, the weight lost already accounted for approximately 60 to 85 % of the total loss over the experiment, indicating a deceleration in weight reduction over time. The granophyre samples exposed to neutral rainwater (pH 7) lost more weight than those exposed to acidic rainwater (pH 5; Tab. 4.5). Conversely, gabbro samples weathered with acidic rainwater lost more weight than those in the neutral rainwater group. Among all groups, the gabbro samples exposed to acidic rainwater showed the greatest average total loss of -0.0302 g per sample after 360 days (Tab. 4.5). The reference samples, in contrast, exhibited slight weight gains. This increase was unlikely to reflect actual changes, given the controlled storage conditions in a closed container, making a dust deposition while storage unlikely. A more plausible explanation is a calibration drift in the weighing scale over the more than a year-long measurement period.

Notably, samples with the most substantial surface changes also experienced the greatest weight loss. Gabbro samples SA1, SA2, and NA2, which exhibited significant surface alterations, lost -0.0460, -0.0398, and -0.0379 g, respectively. Samples SR1 and NR1 also showed significant surface changes, with NR1 losing -0.0259 g, the highest loss among the granophyre samples. However, SR1 was an exception, losing only -0.0094 g, which was less than some granophyre samples showing less visible surface changes.

Overall, weight changes were minimal relative to the initial total weights of 45 to 70 g per sample. It is important to recall that weathering only affected the uppermost layer of the top surface, because all other surfaces were sealed with Araldite® resin (Chapter 4.1.3). The weight loss of the individual samples measured at the end of the experiment is given in Tab. 4.6.

Table 4.5: Mean weight loss of the different sample groups that were weighed before the experiment, after 180 days into the experiment, and after 360 days at the end of the experiment. The error for all measurements is ± 0.0002 g.

Samples	**Mean change of weight (g)**	
	180 days	**360 days**
Granophyre neutral	-0.0118	-0.0187
Gabbro neutral	-0.0158	-0.0203
Granophyre acidic	-0.0086	-0.0098
Gabbro acidic	-0.0226	-0.0302
Granophyre reference	0.0040	0.0075
Gabbro reference	0.0032	0.0047

4.2.1.4 Chemical surface changes over time

The chemical changes were expressed for different elements as relative change Δ_{el} (%) to facilitate comparison between results. The calculations compared measurements taken after each time step to the initial measurements recorded prior to the start of the weathering experiment, which both were normalized to 100 % to correct errors due to different distances between the samples and the measuring head (see Chapter 2.2.2).

Before discussing the chemical surface changes of the samples weathered in the climate chamber, the results of the reference samples have to be examined. For these samples the p-XRF measurements varied significantly throughout the weathering experiment. It was assumed that the reference samples did not undergo significant changes during storage. This assumption was supported by the stable colour measurements of the reference samples and the fact, that no major changes on the surfaces of the reference samples were visible in the high-resolution optical images (see Chapters 4.2.1.1 & 4.2.1.2). Therefore, this variability suggested that the p-XRF results were influenced by external factors such as room temperature, humidity, and air pressure during the measurements. The mean relative change in key measured elements across all reference samples generally exhibited consistent trends for each set of measurements. Exceptions included the MnO and SO_3 measurements in the gabbro and granophyre samples, as well as the TiO_2 measurements in the granophyre reference samples, where the measured changes fluctuated over the course of the experiment (MnO) or increased or decreased by higher values than the other elements (Fig. 4.15; SO_3 & TiO_2). The relative changes of the other measured elements ranged between ± 5 to 7.5 % for the gabbro and granophyre samples as shown in Fig. 4.15. For the granophyre samples it was noticeable that the Al_2O_3 and P_2O_5 concentrations increased consistently after the 180-day measurement, reaching the highest positive values.

Due to the measured changes in the reference samples, the mean values of the gabbro and granophyre reference samples were subtracted from the measured mean values of the corresponding samples weathered in the climate chamber. The resulting corrected relative change for the different elements is given as $\Delta_{\text{el}}^{\text{corr}}$ in %. The margins of error were calculated within a 95 % confidence interval.

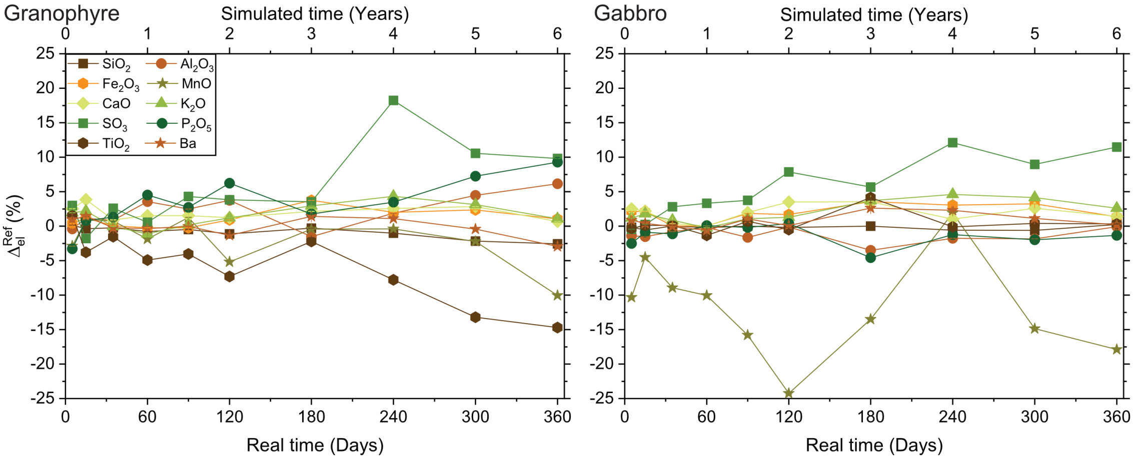

Figure 4.15: Relative chemical changes of the reference sample surfaces of the granophyre (left) and gabbro (right), which were stored throughout the experiment and measured alongside the weathered samples, are displayed as relative percentage changes (Δ_{el}) compared to the initial measurements. Individual error bars (95 %) are smaller than the symbol size.

The average relative change of the main components SiO_2, Al_2O_3, and Fe_2O_3 was comparably low throughout the experiment across all sample groups, ranging within $\Delta_{\text{el}}^{\text{corr}} = \pm 6$ %, as shown in Fig. 4.16. While the changes in the granophyre sample groups were higher for SiO_2 towards the end of the weathering experiment, the changes in Al_2O_3 were more pronounced in the gabbro samples during the same period. The differences between acidic and neutral weathering conditions were noticeable and in most cases, the samples weathered under acidic conditions exhibited greater changes than those under neutral conditions for the same type of rock. The change of the Fe_2O_3 contents was mostly negative and exhibited more fluctuations compared to the changes in SiO_2 and Al_2O_3 contents. No clear differentiation between the four sample groups was possible, and the measured relative changes at the end of the experiment were comparable for all sample groups (Fig. 4.16c). Since all these elements were major components with a content of > 10 wt. %, even relatively small percentage changes correspond to substantial absolute changes.

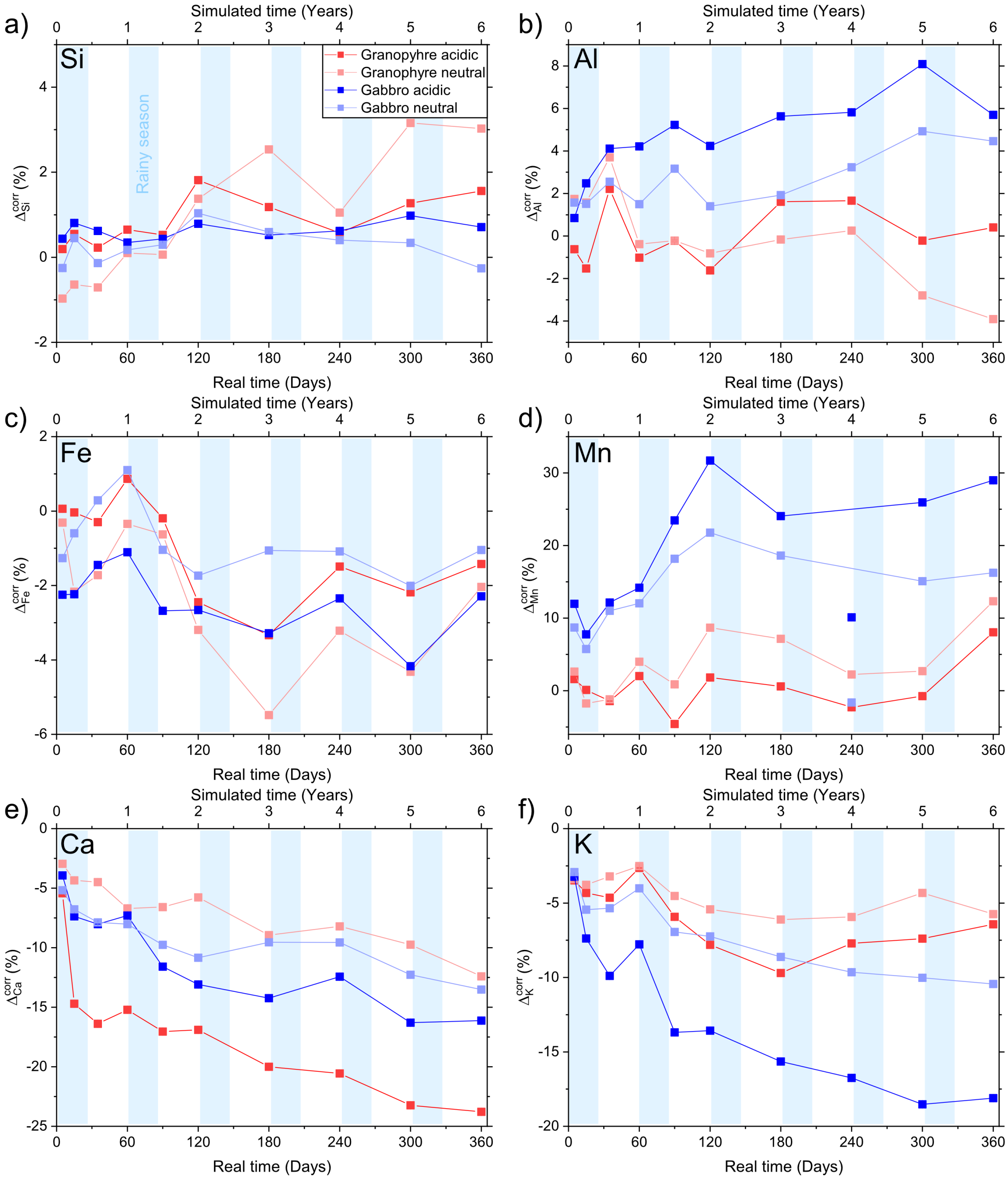

Figure 4.16: Mean relative chemical changes of the granophyre (red) and gabbro (blue) samples as a function of time , weathered under neutral (lighter shades) and acidic (darker shades) conditions. The values represent the relative change $\Delta_{\mathrm{el}}^{\mathrm{corr}}$, corrected by subtracting the average changes of the corresponding reference samples for different element oxides: (a) SiO_2, (b) Al_2O_3, (c) Fe_2O_3, (d) MnO, (e) CaO, and (f) K_2O. Error bars (95 %) are smaller than the symbol size. The blue-shaded areas indicate the simulated rainy season with the highest number of simulated rainfall events, representing the period from January to June (Tab. 1.2).

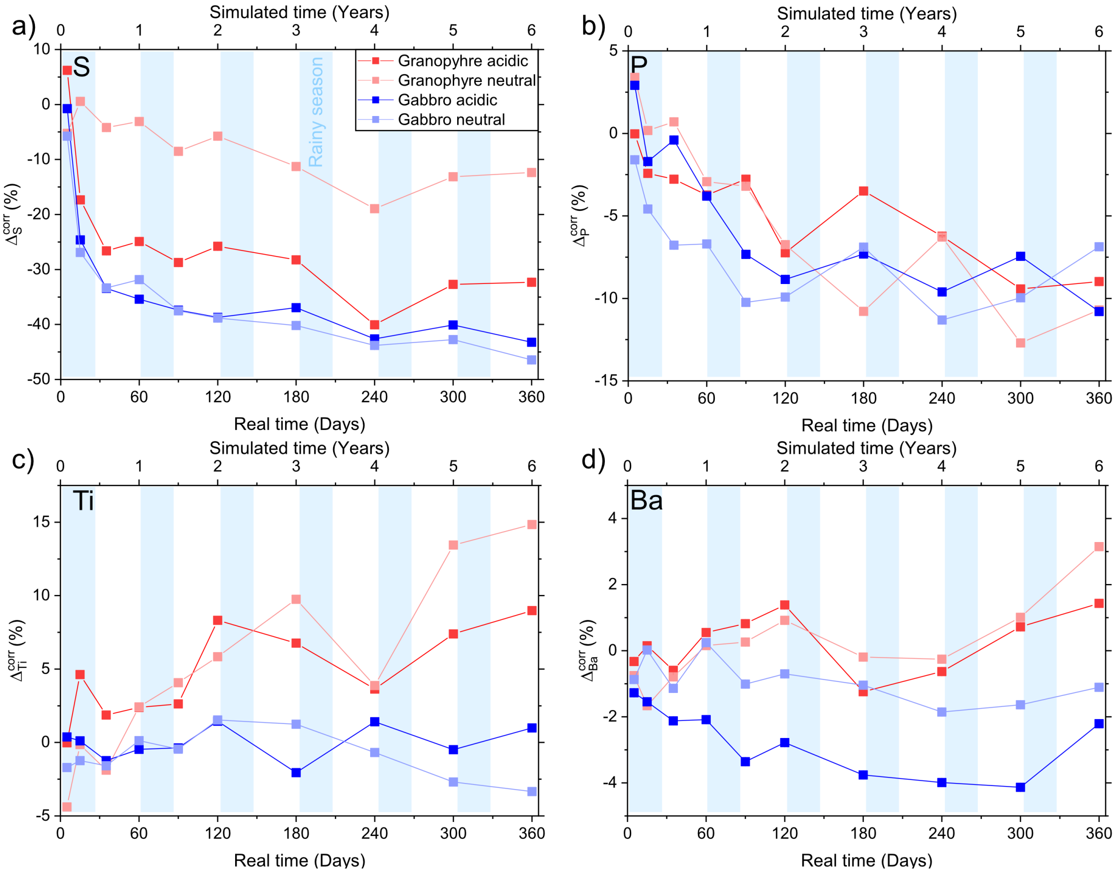

Figure 4.17: Mean relative chemical changes of the granophyre (red) and gabbro (blue) samples as a function of time, weathered under neutral (lighter shades) and acidic (darker shades). The values represent the relative change Δ_{el}^{corr}, corrected by subtracting the average changes of the corresponding reference samples for different element oxides: (a) SO_3, (b) P_2O_5, (c) TiO_2, and (d) Ba. Error bars (95 %) are smaller than the symbol size. The blue-shaded areas indicate the simulated rainy season with the highest number of simulated rainfall events, representing the period from January to June (Tab. 1.2). The TiO_2 measurements of one granophyre sample weathered under neutral conditions were excluded from the calculation due to TiO_2 contents below the detection limit.

While changes in the SiO_2 content of individual samples were similar across all samples, three individual gabbro samples weathered under different conditions (NA2, SA1 & SA2) exhibited significantly higher Al_2O_3 changes of up to 12 %. These three samples contributed to the higher average changes in the gabbro groups and also exhibited the most pronounced surface alterations within this groups (see Chapter 4.2.1.2). One granophyre sample weathered under neutral conditions (NR1) stood out due to its high Fe_2O_3 changes of up to -9 %, explaining the pronounced negative changes in this sample group (Fig. 4.16c).

The MnO content displayed greater variability than the other elements (Fig. 4.16). Changes in the granophyre samples were relatively minor, peaking at 12 % at the end of the experiment, whereas the gabbro samples exhibited $\Delta^{\text{corr}}_{\text{Mn}}$ values as high as 30 % after 120 days in the acidic group. A slight increasing trend was observed over time for the gabbro samples, although the 240-day measurements deviated from this pattern. Since the 240-day reference sample data also deviated from the overall trend (Fig. 4.15), these data points were excluded. Similar to the Al_2O_3 changes, the three samples with the highest MnO changes were the gabbro samples NA2, SA1, and SA2.

As shown in Figs. 4.16 and 4.17, the CaO, K_2O, SO_3, and P_2O_5 contents of the samples changed in similar patterns, but with different intensities depending on the element and sample group. For all four elements, a more or less pronounced decrease over the first 15 to 35 days was observed in most sample groups, followed by a slower but steady decline for the rest of the experiment. The smallest relative changes were observed for P_2O_5, with maximum values of -20 % in one granophyre sample weathered under acidic conditions (SR1). Again, the gabbro samples NA2, SA1, and SA2 stood out, exhibiting notable P_2O_5 decreases of -12 to -20 %.

These three gabbro samples also exhibited some of the highest changes in SO_3 and K_2O content, with values up to -64 and -24 %, respectively. Overall, the changes of the SO_3 content were the largest among the four elements, with average values reaching up to -46 % by the end of the experiment. Individual variability was particularly high in the granophyre groups and, for instance, sample SR1 (acidic conditions) showed an initial decrease of -45 % after 15 days and a change of -73 % by the experiment's conclusion.

The CaO and K_2O contents changed by average values of up to -24 and -18 %, respectively, with some individual samples standing out. One gabbro sample weathered under neutral conditions (NA2) exhibited the largest individual CaO change of -23 %. For the changes of the K_2O content, besides the aforementioned gabbro samples, two granophyre samples (SR1 & NR3) weathered under different conditions stood out within their groups, with values of up to -11 and -8 %, respectively.

The differences between the four sample groups were relatively minor for the changes of the P_2O_5 content (Fig. 4.17b). However, for the other three elements, it was evident that samples weathered under acidic conditions exhibited higher relative changes (Fig. 4.16e & f), with one exception: the changes in SO_3 content in gabbro samples weathered under neutral conditions were comparable to those in gabbro samples weathered under acidic conditions (Fig. 4.17a).

Changes in TiO_2 concentration exhibited differences between the granophyre and gabbro samples. The gabbro samples showed only minor changes with no significant differences between weathering conditions and no observable trends over time. In contrast, the granophyre samples demonstrated more significant changes (Fig. 4.17c). Due to the high fluctuations of the TiO_2 concentrations of the granophyre reference samples most of the calculated change at the end for the granophyre is due to the correction with the measured values of the reference samples and therefore is questionable. Results from granophyre sample NR1 were excluded as the TiO_2 concentration was below the p-XRF detection limit.

Trace elements Cr, Sr, and Ba also demonstrated variable changes. For Cr, the changes ranged from 4 to -28 % but showed no consistent trends. Measurements for granophyre sample NR1 were excluded due to concentrations falling below detection limits. Changes in Sr were smaller, ranging from 2 to -8 %, with no samples displaying conspicuous deviations within any group. The relative Ba concentration changes were minor and in a similar range as for SiO_2. The changes fluctuated slightly between positive and negative values in most sample groups, with an increase observed in the final measurement at 360 days (Fig. 4.17d).

Unlike for the colour measurements, no conspicuous irregularities in elemental changes correlated with periods of varying simulated irrigation as after 90 days where only the wet season was simulated and after 120 days, where only the dry season was simulated. However, variability within sample groups was significant, likely due to inhomogeneous varnish compositions. This was consistent with observations of colour and morphological changes (Tab. 4.4). Certain samples, including gabbro samples NA2, SA1, and SA2, as well as granophyre samples SR1 and NR1, consistently stood out within their groups. Without correcting for reference sample data, fluctuations, particularly in MnO values, would have been more pronounced. The differences between the individual samples at the end of the experiment are shown in Fig. 4.18 and are given in Tab. 4.6. Additionally, the whole dataset including all individual measurements taken at each time step is given in the digital supplementary material.

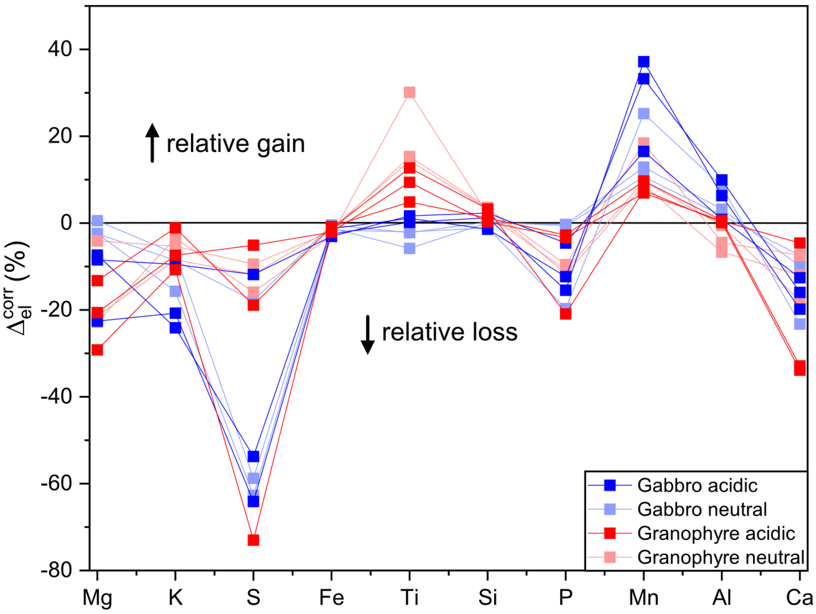

Figure 4.18: Corrected changes of the element concentrations of all samples at the end of the weathering experiment. Error bars (95 %) are smaller than the symbol size.

In summary, p-XRF measurements revealed substantial variability in the elemental changes. Unlike in the results of other analytical methods, the reference samples displayed significant changes during storage, which were attributed to varying measurement conditions rather than real surface changes. Subtracting reference sample results and normalising all measurements to 100 % improved the data but did not eliminate all fluctuations. The extent of changes varied by element. Major components, including SiO_2, Fe_2O_3, and Al_2O_3, showed relatively minor changes, mostly below 5 %. In contrast, MnO exhibited significantly higher changes, particularly in gabbro samples. Changes in other elements with lower overall concentrations, such as Ca, K, S, P, and Ti, were also more pronounced. Rapid initial changes were observed in some elements, such as Ca, K, S, and P, within the first 15 to 35 days for certain groups. Trace element concentrations remained relatively stable across most samples. Overall it was noticeable that the measured changes in the sample groups weathered under slightly acidic conditions were more pronounced for most of the measured elements than the observed changes in the sample groups weathered under neutral conditions. Compared to other analytical methods the differences for some of the elements were significantly smaller between the different simulated weathering conditions, e.g. for P or Fe.

Table 4.6: Complete data obtained at the end of the weathering experiment. The errors are given in the digital supplement.

			Colour Changes				Chemical comp (wt. %; Cr, Sr & Ba in ppm)															
		Sample	**ΔE**	**ΔL^***	**Δa^***	**Δb^***	**Cr**	**Sr**	**Ba**	**MgO**	**K_2O**	**SO_3**	**Fe_2O_3**	**TiO_2**	**SiO_2**	**P_2O_5**	**MnO**	**Al_2O_3**	**CaO**	**Fe/Mn**	**Weight loss (g)**	**Surface changes***
Gabbro	**neutral**	**NA1**	1.52	-0.75	0.55	1.21	587	214	461	4.19	1.27	0.21	20.76	1.28	49.43	0.60	0.74	16.97	4.54	25.48	-0.0082	3
		NA2	0.70	-0.58	0.23	-0.31	471	160	446	3.51	1.62	0.23	20.81	1.39	48.69	0.63	4.54	16.13	2.44	4.14	-0.0379	4
		NA3	1.20	-0.66	0.25	0.97	376	206	444	3.28	1.28	0.25	22.70	1.48	45.44	1.23	3.04	18.57	2.75	6.75	-0.0147	2
	acidic	**SA1**	5.42	-5.12	1.76	-0.36	627	155	512	3.33	1.39	0.19	19.56	1.41	54.00	0.31	1.78	15.01	3.03	9.92	-0.0460	5
		SA2	4.82	-4.22	0.51	-2.26	622	170	500	2.84	1.30	0.21	19.95	1.92	53.47	0.33	2.22	14.51	3.26	8.13	-0.0398	4
		SA3	1.18	-0.41	0.37	1.04	430	200	439	3.36	1.38	0.16	22.35	1.37	44.40	0.86	5.24	18.32	2.57	3.85	-0.0048	2
Granophyre	**neutral**	**NR1**	4.20	-3.36	1.37	2.11	<d.l.	1811	1106	2.15	2.15	0.24	16.16	<d.l.	53.31	1.46	3.96	19.71	1.00	3.68	-0.0259	4
		NR2	0.47	-0.46	0.07	0.06	211	1824	673	2.36	1.13	0.41	24.97	1.22	42.69	3.07	6.06	17.17	0.92	3.72	-0.0117	2
		NR3	1.23	-1.01	0.47	0.50	870	2652	617	2.32	0.74	1.11	41.85	1.19	31.95	4.61	0.16	14.99	1.07	239.37	-0.0186	2
	acidic	**SR1**	3.86	-2.97	1.05	2.23	100	877	621	2.31	1.17	0.45	19.58	1.08	50.42	1.26	3.86	18.74	1.13	4.59	-0.0094	4
		SR2	0.97	-0.73	0.13	0.63	1343	2960	735	1.80	0.42	2.21	41.26	1.30	30.04	7.27	0.08	13.92	1.69	492.94	-0.0198	2
		SR3	1.62	-1.07	0.52	1.10	150	314	524	2.47	1.31	0.18	26.03	1.74	46.73	1.20	5.30	14.45	0.59	4.44	-0.0002	3
			Chemical changes (Δ_{el}^{corr} %)											**Element concentrations rainwater samples (ppb)**								
		Sample	**MgO**	**K_2O**	**SO_3**	**Fe_2O_3**	**TiO_2**	**SiO_2**	**P_2O_5**	**MnO**	**Al_2O_3**	**CaO**	**P**	**S**	**Mn**	**Fe**	**Mg**	**Si**	**Ca**	**Sr**	**Na**	**K**
Gabbro	**neutral**	**NA1**	-2.46	-8.56	-17.89	-0.43	-2.22	0.24	-0.63	10.67	1.74	-7.41	1.87	16.88	6.31	10.20	34.89	51.94	135.53	0.66	95.38	116.26
		NA2	-2.37	-15.69	-62.67	-1.57	-2.01	-1.08	-19.70	25.21	8.47	-23.28	14.31	31.79	12.86	45.73	53.50	110.20	228.01	0.84	110.20	216.95
		NA3	0.55	-7.06	-58.78	-1.14	-5.80	0.06	-0.30	12.88	3.17	-9.86	5.08	46.66	12.56	11.67	31.34	65.51	215.16	0.59	87.07	133.66
	acidic	**SA1**	-22.60	-20.73	-64.08	-2.53	0.21	1.21	-15.46	37.19	6.30	-19.79	8.73	19.96	12.54	30.05	50.54	119.19	164.56	1.01	40.73	114.30
		SA2	-7.33	-24.10	-53.76	-1.26	1.11	-1.40	-12.31	33.28	9.95	-15.98	11.89	22.67	9.45	28.45	41.32	90.32	237.78	0.90	52.02	169.93
		SA3	-8.50	-9.50	-11.86	-3.07	1.65	2.32	-4.62	16.48	0.84	-12.60	9.62	11.55	14.66	7.85	36.18	46.69	54.72	0.82	76.75	71.30
Granophyre	**neutral**	**NR1**	-22.84	-3.42	-15.89	-2.90	30.14	2.10	-10.84	9.69	-0.54	-17.85	4.35	82.05	4.60	7.33	29.88	127.79	217.30	0.44	163.81	104.97
		NR2	-4.14	-5.32	-9.42	-1.93	15.36	3.64	-11.72	8.79	-6.72	-11.94	2.09	16.94	44.76	3.87	6.90	477.85	112.61	0.23	56.94	70.32
		NR3	-21.46	-8.48	-11.79	-1.28	14.34	3.35	-9.55	18.47	-4.47	-7.41	3.62	22.14	9.39	8.01	15.06	64.51	95.50	0.32	67.38	41.20
	acidic	**SR1**	-29.19	-10.72	-73.03	-1.37	12.72	3.26	-20.92	7.54	0.15	-33.87	7.02	20.57	5.33	2.31	18.52	52.62	113.85	0.25	108.70	21.92
		SR2	-20.63	-7.45	-5.07	-2.07	9.39	0.25	-3.29	6.92	0.47	-4.60	4.37	-4.24	19.60	3.31	5.61	204.41	99.80	0.24	28.37	53.49
		SR3	-13.27	-1.10	-18.87	-0.83	4.85	1.17	-2.74	9.71	0.61	-32.87	3.02	-2.07	37.09	8.11	12.36	206.61	15.90	0.36	56.32	24.47

*ordinal-scaled (see Chapter 4.2.5); < d.l.: concentration below detection limit

4.2.1.5 Change of the microbial community composition over time

Alpha Diversity

The alpha diversity of microbial communities, measured using the Shannon (Shannon, 1948) and Simpson (Simpson, 1949) indices, revealed significant differences between treatments and rock types, highlighting the influence of environmental conditions on community richness and evenness (Fig. 4.19). The gabbro samples demonstrated a marked variability in diversity across treatments, with significantly higher diversity under neutral conditions compared to acidic conditions or samples taken before the experiment (day 0). These differences were supported by ANOVA results ($F = 24.26$, $p < 0.001$), with pairwise comparisons showing significant increases in diversity from acidic conditions to neutral conditions (Tukey HSD (Tukey, 1949), $p < 0.05$; Tab. A3). Notably, neutral treatments appeared to support a more even distribution of taxa, potentially due to the less stressful environment promoting the growth of multiple microbial groups.

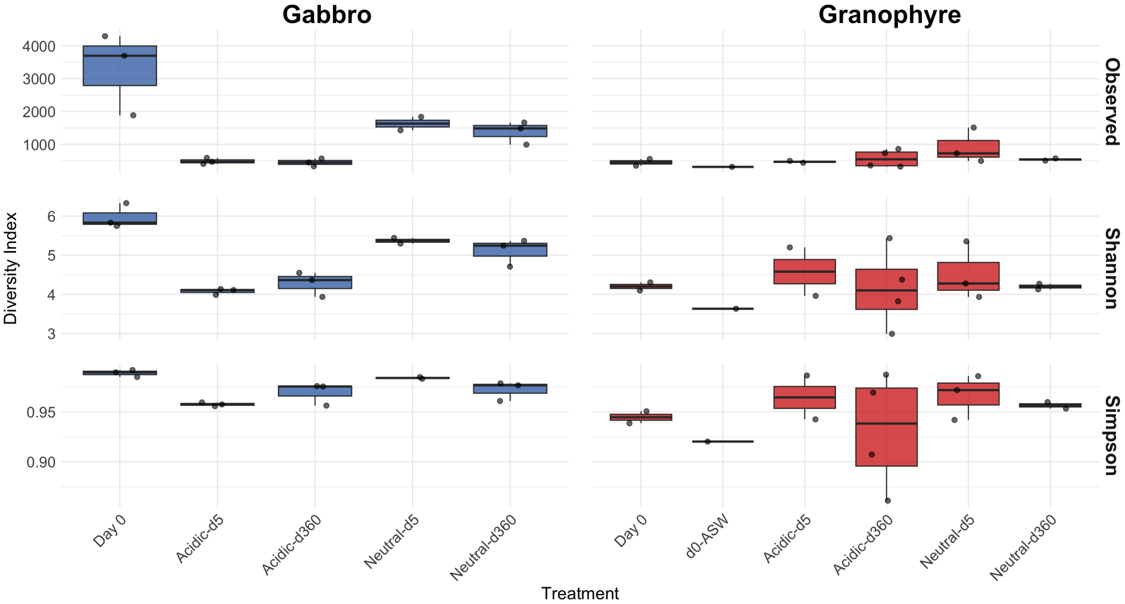

Figure 4.19: Alpha diversity (Shannon & Simpson indices) of microbial communities by treatment and rock type. The gabbro samples showed significant differences between treatments, while the granophyre samples remained stable. The sample d0-ASW is the sample that was sawed with a table saw and was therefore potentially exposed to contaminants through the used tap water. The other samples were taken before the start of the weathering (Day 0), after 5 days (d5), and after the weathering experiment (d360) and were weathered at pH 5 (Acidic) and pH 7 (Neutral).

In contrast, granophyre samples displayed a more stable alpha diversity profile, with no significant differences observed between treatments (ANOVA, $p = 0.916$; Tukey HSD, $p > 0.9$; Tab. A4). The lack of substantial variation suggests that microbial communities on this rock type were less affected by environmental stressors such as pH fluctuations. This stability might be attributed to the different varnish composition or structural properties of the rock surface, which could buffer against changes in microbial community structure.

The Kruskal-Wallis test (Kruskal & Wallis, 1952) further confirmed the trends observed on gabbro samples, with significant differences in diversity across treatments ($p = 0.021$). However, no significant differences were observed on granophyre samples ($p = 0.832$), supporting the hypothesis of its microbial community's resilience to environmental changes.

Beta Diversity

Beta diversity analysis, assessed through principal coordinate analysis (PCoA) based on Bray-Curtis dissimilarities (Bray & Curtis, 1957), revealed clear differences in microbial community composition between rock types and treatments (Fig. 4.20). Gabbro communities exhibited distinct clustering by treatment, with samples weathered under acidic conditions forming a separate cluster from those weathered under neutral conditions and samples taken before the start of the experiment (day 0). This separation highlights the significant influence of pH on microbial community composition, likely reflecting shifts in the relative abundance of acid-tolerant and pH-sensitive taxa. Neutral conditions on gabbro samples supported a broader range of taxa, contributing to the distinct clustering observed in the ordination space.

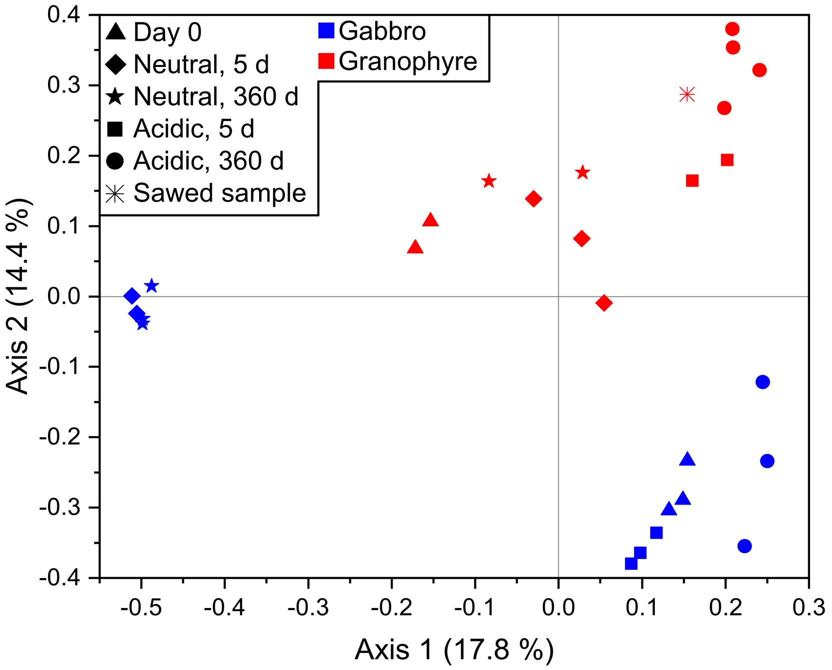

Figure 4.20: Beta diversity visualized through PCoA based on Bray-Curtis dissimilarities. Distinct clustering was observed for gabbro communities by treatment, while the granophyre samples showed overlapping clusters, indicating greater stability.

Samples taken from the granophyre, on the other hand, exhibited tighter clustering with substantial overlap between treatments. This suggests that the granophyre microbial communities were more homogeneous and less influenced by environmental factors such as pH or duration of the applied simulated weathering. The stability observed on the granophyre may be linked to its more stable mineralogical properties, which could provide a consistent microhabitat for microbial colonization.

Statistical analysis using PERMANOVA confirmed the significant effect of treatment ($p < 0.01$) and rock type ($p < 0.01$) on beta diversity, with gabbro samples showing greater variability in community composition across treatments compared to granophyre samples. Pairwise comparisons indicated that acidic treatments of gabbro samples differed significantly from neutral and day 0 samples, further emphasizing the impact of pH on microbial community structure.

Heatmap of Taxonomic Composition

The heatmap of genus-level relative abundance (Fig. 4.21) provides a detailed overview of microbial community composition across treatments and rock types, revealing notable differences between gabbro and granophyre samples. The gabbro samples exhibited a dynamic and variable microbial profile, with genera such as *Rubrobacter* and *Geodermatophilus* dominating under acidic conditions due to their resilience to low pH and desiccation stress. These taxa play significant roles in mineral weathering and biogeochemical cycling, particularly in extreme environments. Neutral conditions on gabbro samples supported a more diverse microbial community, with increased relative abundances of *Bacillus* and *Cyanobacteria*, indicative of enhanced primary production and nutrient cycling activities. Samples collected on day 0 displayed a simpler community structure, reflecting the initial colonisation state of the rock surface. In contrast, granophyre samples showed a more uniform microbial composition across treatments, with dominant taxa such as *Proteobacteria* and *Actinobacteriota* consistently present, regardless of environmental conditions. These taxa likely serve as core members of the granophyre samples microbial ecosystem, contributing to its stability and resilience. Under neutral conditions, slight increases in *Firmicutes* and *Deinococcota* were observed, taxa commonly associated with biogeochemical cycling and stress resistance. Overall, the microbial communities on the granophyre remained relatively stable, suggesting that its varnish properties may provide a consistent microhabitat, buffering against environmental perturbations. These observations highlight the distinct ecological responses of gabbro and granophyre surfaces to varying environmental conditions, particularly the strong influence of pH on microbial community structure and function on gabbro surface samples.

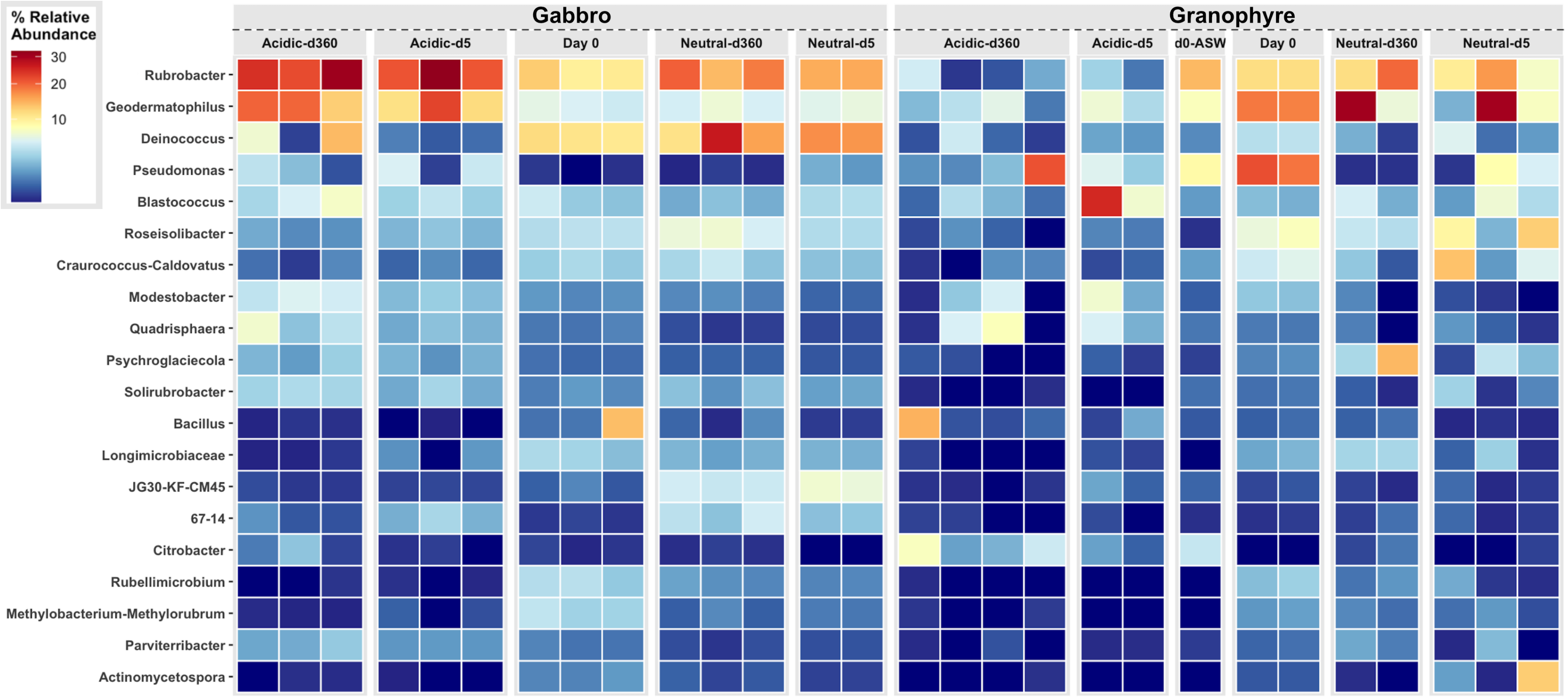

Figure 4.21: Heatmap of genus-level relative abundance across treatments and rock types. The gabbro samples exhibited greater taxonomic variability, while the community composition of the granophyre samples remained stable. The sample d0-ASW is the sample that was sawed with a table saw and was therefore potentially exposed to contaminants through the used tap water. The other samples were taken before the start of the weathering (Day 0), after 5 days (d5), and after the weathering experiment (d360) and were weathered at pH 5 (Acidic) and pH 7 (Neutral).

4.2.2 Glass dosimeters

4.2.2.1 Changes of the water content over time

Three different types of glass dosimeters were prepared by the Fraunhofer ISC for the weathering experiment in the climate chamber. Additional dosimeters were used to measure the impact of the atmospheric conditions in the chamber and were placed above the weathering setup (see Chapter 4.1.2). As reference samples, glass dosimeters were placed alongside the reference rock samples in a laboratory with controlled temperature and humidity, without any simulated weathering. The water content of the glass dosimeters was measured using FT-IR (Chapter 2.10). The vulnerability to alteration depends on the composition of the glass dosimeters (Chapter 3.2).

M3 glass dosimeters

The least vulnerable glass type, M3, was expected to show the smallest alteration over time. This was confirmed by the measured water contents of the weathered dosimeters. The change in water content is expressed as ΔE_{IR}, calculated using the intensity of the OH absorption band at 3300 cm^{-1} within the infrared spectrum (Chapter 2.10). For the M3 glass type, the measured ΔE_{IR} values ranged from 0.002 after 5 days of weathering, which was equal to the estimated standard error for all FT-IR measurements, to a maximum of 0.043 after 360 days. This maximum was observed in the samples weathered under acidic conditions (pH 5).

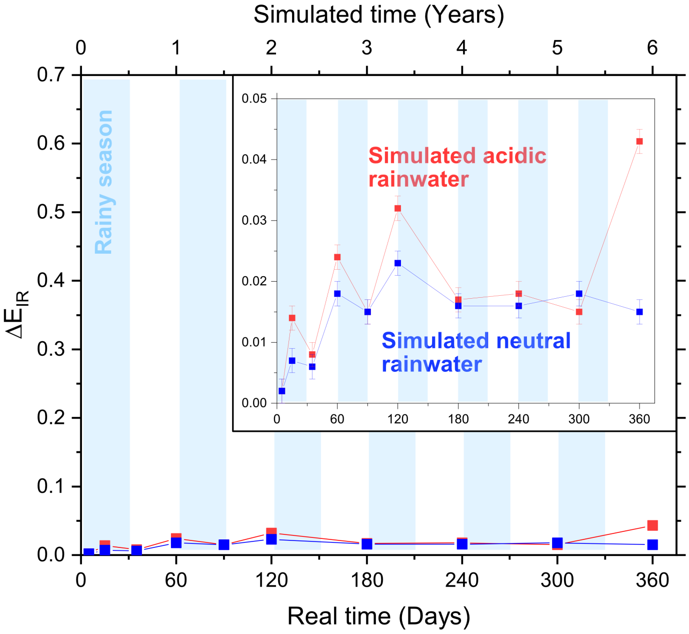

Figure 4.22: ΔE_{IR} of the glass dosimeters M3 as a function of time. The blue-shaded areas indicate the simulated rainy season with the highest number of simulated rainfall events, representing the period from January to June (Tab. 1.2).

Overall, the fluctuations in ΔE_{IR} values were substantial. No clear trend was observed following an initial increase in water content, nor was there a significant difference between the two groups weathered under different conditions, except for the final measurement after 360 days (Fig. 4.22). At this time, the ΔE_{IR} for the dosimeters weathered under acidic conditions was 0.043, indicating an increase compared to the measurement after 300 days ($\Delta E_{IR} = 0.015$). In contrast, the dosimeters weathered under neutral conditions (pH 7) exhibited a ΔE_{IR} of 0.015 after 360 days, remaining within the same range as the measurements taken earlier within this group.

M5 glass dosimeters

Glass type M5 displayed a nearly constant increase in water content over the course of the experiment. Fig. 4.23 shows that the ΔE_{IR} after only 5 days of weathering was already 0.012, which was as high as one of the measurements for the M3 type after 360 days of weathering. The increase in ΔE_{IR} for the M5 type progressed relatively slowly during the first half of the weathering period, reaching values of 0.074 and 0.056 after 180 days. The difference between the two groups weathered with different types of artificial rainwater was small, but the ΔE_{IR} values for the dosimeters weathered under acidic conditions were slightly higher than those of the other group, indicating greater alteration.

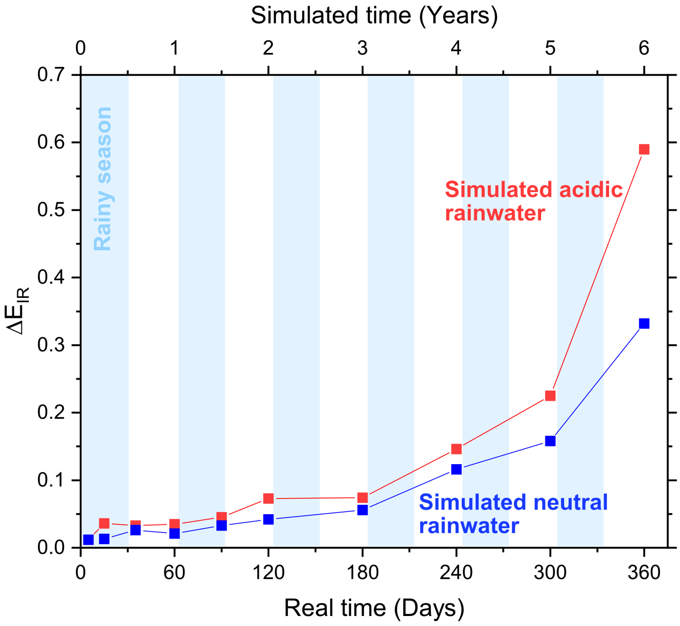

Figure 4.23: ΔE_{IR} of the glass dosimeters M5 as a function of time. The estimated standard error of 0.002 is to small to be visible in the Figure. The blue-shaded areas indicate the simulated rainy season with the highest number of simulated rainfall events, representing the period from January to June (Tab. 1.2).

The ΔE_{IR} values increased at an accelerating rate during the second half of the weathering experiment, reaching their maximum after 360 days, with a ΔE_{IR} of 0.590 for the dosimeter weathered under acidic conditions and 0.332 for the dosimeter weathered under neutral conditions (Fig. 4.23). It was also noteworthy that the difference between the two groups exposed to different conditions increased significantly during the second half of the experiment. The development of ΔE_{IR} for both groups appeared to grow exponentially.

MI glass dosimeters

Glass type MI is also highly vulnerable to alteration and exhibited a much higher ΔE_{IR} compared to glass type M3. The development of the water content, as represented by ΔE_{IR}, was similar to that of glass type M5, as shown in Figs. 4.23 and 4.24. During the first half of the weathering experiment, the ΔE_{IR} increased slowly, and the difference between the two sample groups was smaller, with the dosimeters weathered using neutral artificial rainwater displaying higher water contents at certain points.

The ΔE_{IR} increased more rapidly during the second half of the weathering experiment, as observed for glass type M5, although the difference between the two sample groups remained smaller. Only the final measurement, taken after 360 days, revealed a significant difference between the two dosimeters, with a ΔE_{IR} of 0.595 for the dosimeter weathered with acidic rainwater, compared to 0.353 for the dosimeter weathered under neutral conditions. As for type M5, the development of ΔE_{IR}, and consequently the water content, appeared to exhibit exponential growth.

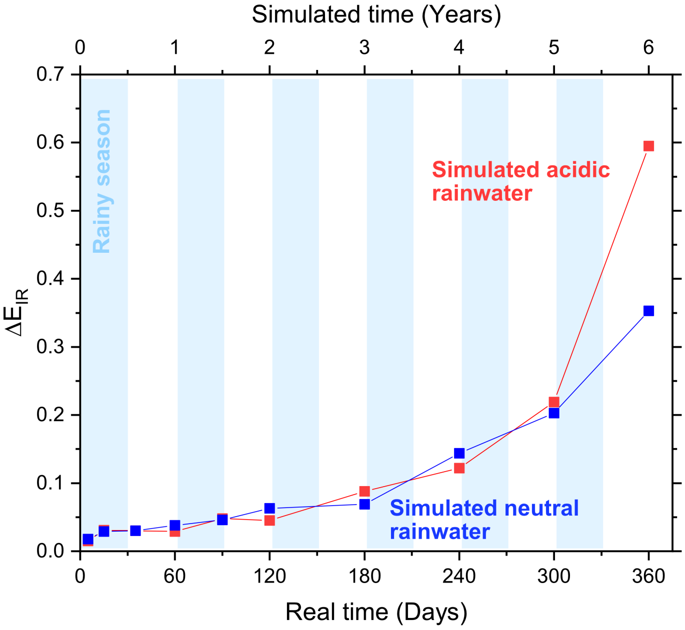

Figure 4.24: ΔE_{IR} of the glass dosimeters MI as a function of time. The estimated standard error of 0.002 is to small to be visible in the Figure. The blue-shaded areas indicate the simulated rainy season with the highest number of simulated rainfall events, representing the period from January to June (Tab. 1.2).

Glass dosimeter reference samples

One glass dosimeter of each type was placed alongside the rock reference samples to monitor the storage conditions. The ΔE_{IR} of these dosimeters ranged from 0.008 for glass type M3 to 0.018 for type MI after 180 days, and from 0.024 for M3 to 0.027 for MI after 360 days. Compared to the ΔE_{IR} of the dosimeters weathered in the climate chamber, the values for the more vulnerable types, M5 and MI, were very low. For these types, the ΔE_{IR} values of the dosimeters weathered in the chamber for just 15 days were within the same range as those of the reference dosimeters after 360 days.

In contrast, the ΔE_{IR} values for the least vulnerable type, M3, were relatively high, even exceeding the ΔE_{IR} of the M3 dosimeters weathered in the climate chamber under controlled conditions after 360 days. The same trend was observed for the M3 dosimeters placed above the experimental setup to monitor alteration caused by the atmospheric conditions in the climate chamber. For both M3 dosimeters, the ΔE_{IR} values, at 0.112 and 0.133, were significantly higher than those for all M3 dosimeters weathered in the climate chamber, which had a maximum ΔE_{IR} of 0.043. It was also notable that the ΔE_{IR} after 180 days represented approximately one-third of the final ΔE_{IR} measured after 360 days. These values were even more comparable for the reference dosimeters, as they were returned to the same location after measurement, unlike the dosimeters from the chamber, which were not reintroduced after being measured.

The MI and M5 dosimeters placed above the climate chamber setup to monitor alteration caused by atmospheric conditions exhibited a ΔE_{IR} of only 0.019 to 0.029 after 180 days, which was similar to the range measured for the reference dosimeters of these glass types. However, after 360 days of weathering, the ΔE_{IR} increased sharply to values between 0.157 and 0.207, much higher than those of the reference dosimeters. This rapid increase in ΔE_{IR} during the second half of the experiment was consistent with observations for the M3 dosimeters placed above the climate chamber setup, as well as for the M5 and MI dosimeters weathered inside the chamber. The ΔE_{IR} values of the M5 and MI dosimeters placed above the setup were comparable to the ΔE_{IR} values measured for the weathered dosimeters after 240 to 300 days (Figs. 4.23 & 4.24).

4.2.2.2 Surface textural and morphological changes over time

The morphological changes of the glass dosimeters were analysed using images taken with an optical microscope (Chapter 2.6). These images visualised the alteration on the glass surface. Over the course of the weathering experiment the dosimeters, which had been fire-polished prior to the experiment, began to exhibit small cracks in the surface alteration layers (SALs). These layers formed as a result of aqueous corrosion of the glass surface (Geisler et al., 2019). The number of cracks increased over time, and by the end of the experiment, when the highest ΔE_{IR} values were recorded, these cracks had started to interconnect in some cases (Fig. 4.25b). It is assumed that the cracks formed over the repeated cycles of dry and wet conditions.

The cracks allow water to penetrate deeper into the SALs, leading to a higher water content in these layers and, consequently, an increased ΔE_{IR}. Additionally, some crystals formed on the surface of the glass dosimeters, appearing as darker spots with relief in the images. Overall, the ΔE_{IR} values correlated well with the visible alterations on the glass surface, as demonstrated in Fig. 4.25. The first visible cracks appeared on glass types MI and M5 after 90 to 120 days and their numbers continued to grow throughout the experiment. Glass type M3, the most stable type used, did not exhibit any cracks over the entire duration of the experiment.

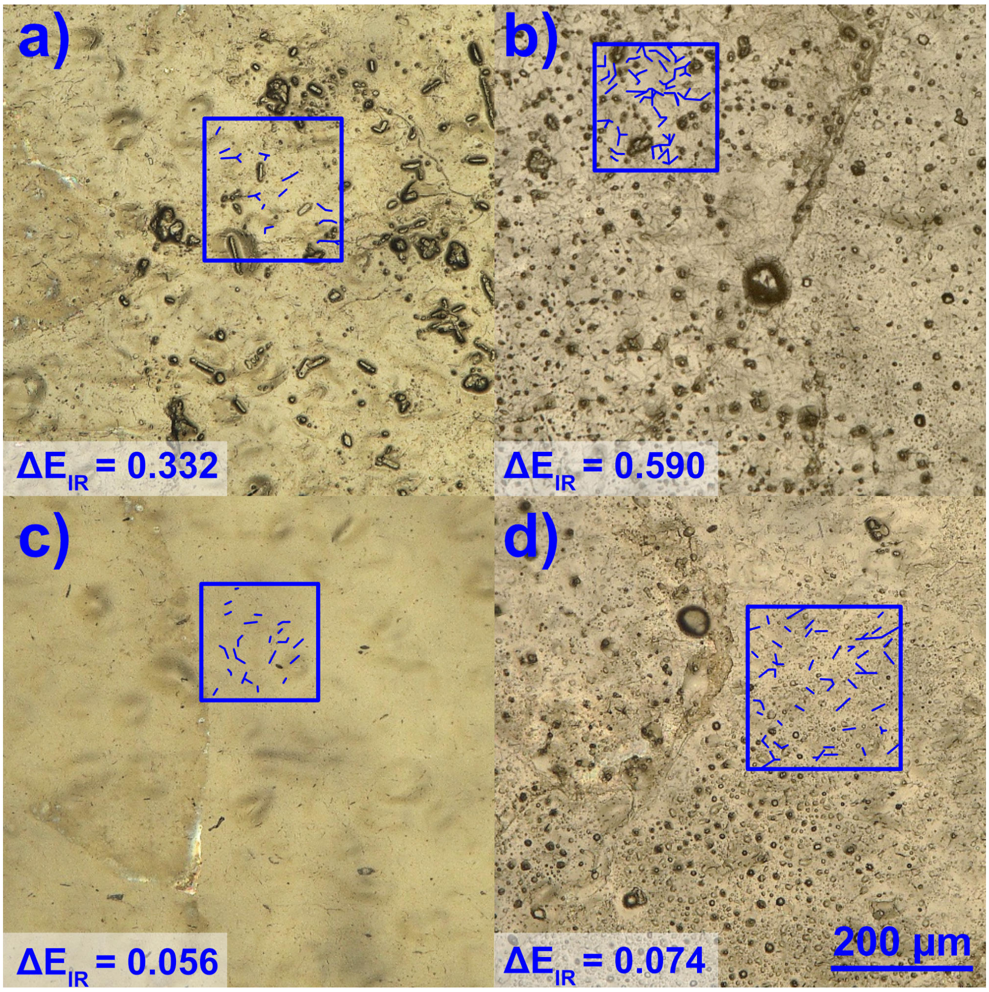

Figure 4.25: Optical images of four different glass dosimeters from glass type M5. The glass dosimeters were weathered for 360 days under (a) neutral and (b) acidic conditions, as well as for 180 days under (c) neutral and (d) acidic conditions. The cracks that occurred on the surface alteration layers are visible on all pictures in different quantities and were highlighted in blue in a small cut out of each picture. The pictures were taken with 300x magnification.

The differences between the glass samples weathered under neutral and acidic conditions were also apparent in the surface images. For glass type M5, significantly more cracks were visible after 180 and 360 days of weathering under acidic conditions. After 360 days, on the samples exposed to acidic conditions, these cracks had interconnected multiple times (Fig. 4.25a & b). A similar pattern was observed in the dosimeters made from glass type MI.

4.2.3 Artificial rainwater composition after distinct rainfall events

Over the course of the weathering experiment, samples of the artificial rainwater that flowed over the rock samples were collected at three different occasions during the second half of the experiment (Fig. 4.2). These water samples were subsequently analysed using ICP-OES (Chapter 2.4). At each occasion, 14 samples were taken in two consecutive simulated rainfall events over two days. Seven of the samples were taken from the acidic side and seven from the neutral weathering side, with each set of seven containing one blank reference sample. This procedure resulted in a total of 42 samples (3 occasions × 14 samples). From each of the four different sample groups, which consisted of three rock samples each, a total of nine water samples per group were collected.

As with the results obtained with other methods, the variability within the sample groups led to some outliers. Nonetheless, significant differences were observed between the two rock types and between samples weathered under different conditions for most of the analysed elements (Fig. 4.26). The element concentrations of the blank samples, collected alongside water samples exposed to the rock varnish, were subtracted from the corresponding water samples. This resulted in negative values for certain elements, particularly K, Na, and Ca, which are present in normal tap water at higher concentrations and therefore the blank samples had relatively high concentrations of these elements (Tab. 4.3). The elevated baseline concentrations in the demineralised water used to prepare the artificial rainwater rendered the evaluation of these elements unreliable. For instance, more than half of the measured K concentrations in the samples were slightly lower than those in the stock solution but within the range of error (95 %). For other elements, especially Mn the concentrations in the reference samples were significantly lower than in the water samples that were in contact with the rock samples (Fig. 4.26). Also if the concentrations of the reference samples in many cases were partly in the same range as the water samples that were in contact with the rock samples, the subtraction of the concentrations of the corresponding reference sample yielded reliable results fro all elements except the ones mentioned above (K, Na & Ca). None of the measured element concentrations were below the detection limit.

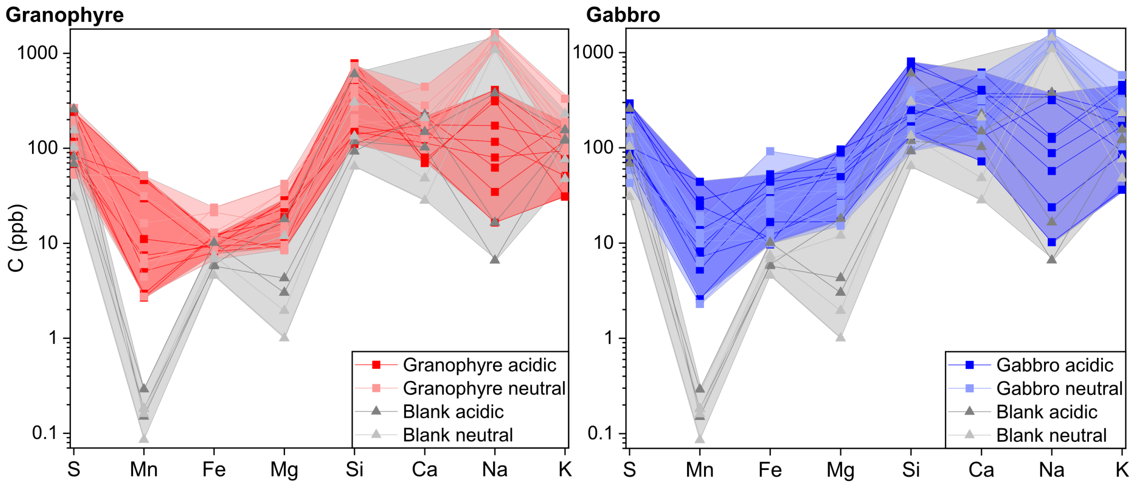

Figure 4.26: Spiderplot of element concentrations in the collected artificial rainwater samples that were in contact with granophyre (left) and gabbro (right) samples compared with the blank samples.

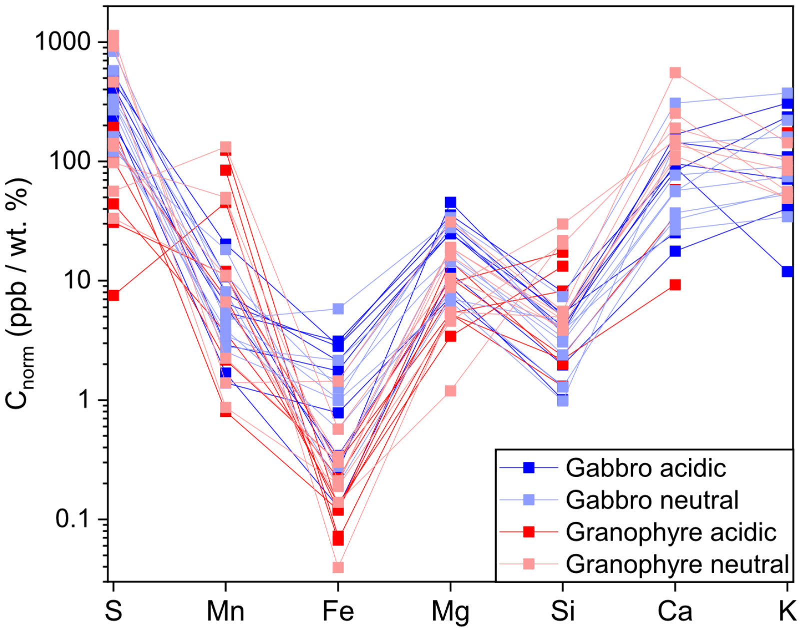

Figure 4.27: Normalised element concentrations (i.e., element concentration in solution divided by their measured concentration on the varnish surface) in the collected artificial rainwater samples that were in contact with granophyre and gabbro samples. Negative values after the blank subtraction were excluded and therefore from some elements the number of shown samples is significantly lower than for others.

A normalisation of the element concentrations in the water samples, after blank subtraction, to the element content on the surface of the corresponding samples measured by p-XRF (Tab. 3.1) did not yield results that facilitated a clearer distinction between the different sample groups, nor was the range of the results significantly reduced. This indicates that there was no strong correlation between the amount of material dissolved in the rainwater that had been in contact with the rock surfaces and the element concentrations measured on the corresponding surfaces (Fig. 4.27). This is further discussed in Chapter 5.3.2.2.

On average, the Si and Mg concentrations in the water samples at pH 5 were higher for the gabbro samples compared to those at pH 7, while for the granophyre samples, it was the other way around (Fig. 4.28a & b). The amount of Si dissolved in water in contact with the granophyre samples was approximately twice as high as for the gabbro samples, while the Mg content was three to four times higher in water samples exposed to the gabbro surfaces compared to those exposed to the granophyre.

The Fe concentrations were consistently higher for the gabbro samples compared to the granophyre, with no significant differences observed between the pH levels. However, a notable outlier was evident in the pH 7 group (Fig. 4.28c). The range of Fe concentrations for the granophyre samples was much smaller than that for the gabbro samples. Interestingly, the highest Fe concentrations (approximately 30 ppb) were associated with water samples from the gabbro rocks SA1 and SA2, which also exhibited the highest colour change values (Tab. 4.4) and were weathered under acidic conditions. In the pH 7 group, the highest Fe concentration (46 ppb) was measured in water from gabbro rock NA2, which had the lowest ΔE within its group. As aforementioned, these three gabbro samples experienced a high weight loss and high changes on the surface as evident in the high-resolution optical images (see Chapter 4.2.1.2; Tab. 4.6). Not only were the Fe, but also the Mg contents in the water samples that were in contact with these three gabbro rocks the highest among all samples (Tab. 4.6). For the granophyre rocks, Fe concentrations were significantly lower and the measured concentrations higher at pH 7 (Fig. 4.28c).

The differences in Mn concentrations between water rinsed over the granophyre and gabbro samples were more pronounced at pH 7 than at pH 5. Thus, at pH 5, Mn concentrations were higher for the gabbro samples and lower for the granophyre samples when compared to the pH 7 results, similar to the trends observed for Si and Fe (Fig. 4.28d). The highest overall Mn concentrations were measured in the artificial rainwater that was in contact with the granophyre samples NR2 and SR3, which were cut out of the same piece of granophyre (Tab. 4.6).

For both rock types, the S concentrations were higher in the group weathered at pH 7 compared to the group at pH 5. Outliers were observed in the gabbro group at pH 7, and the overall range of S concentrations was larger for both rock types at this pH. For both pH values, P concentrations were higher for the gabbro samples. Large ranges within the sample groups led to outliers in three of the four groups (Fig. 4.28f).

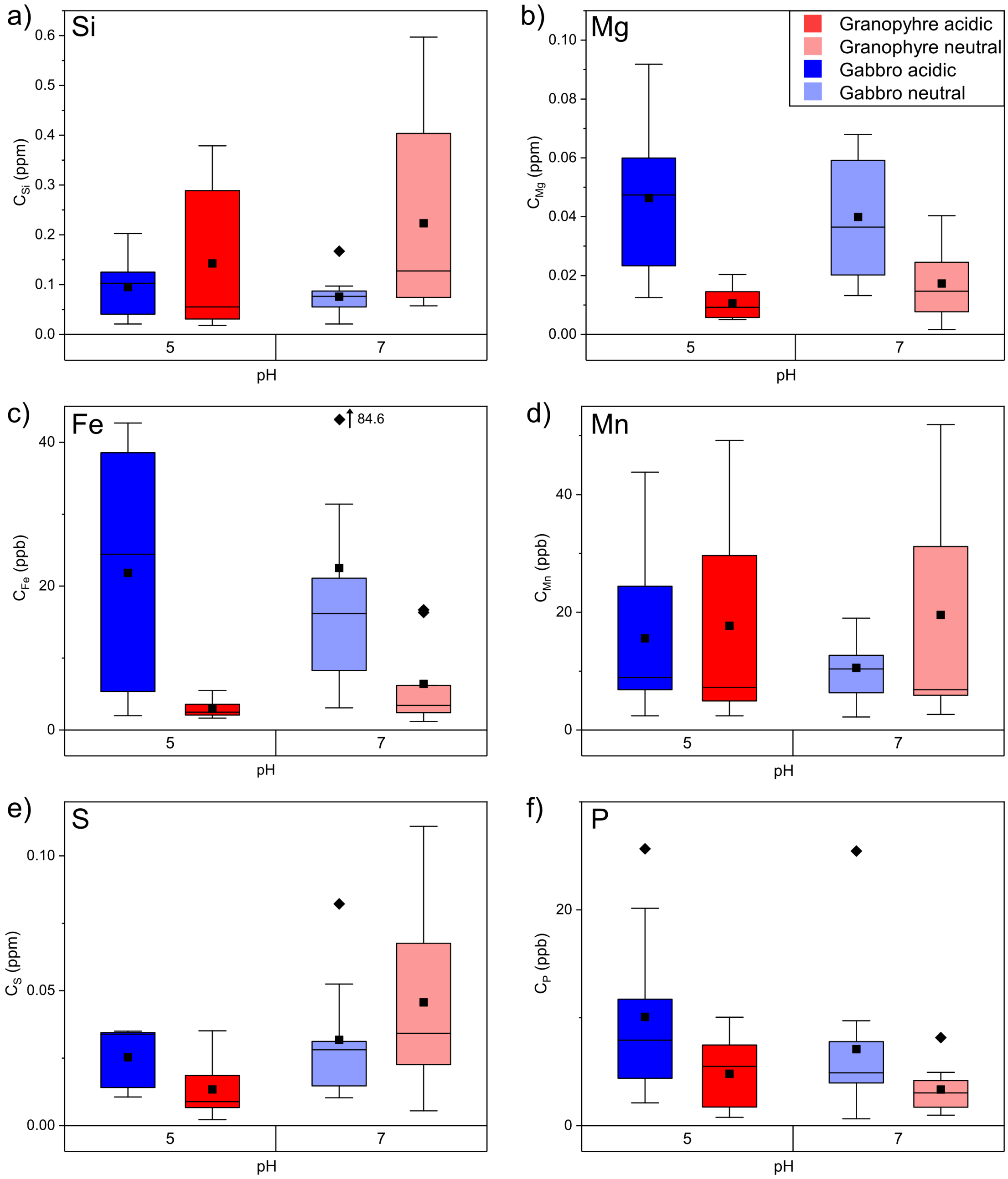

Figure 4.28: Mean element concentrations of (a) Si, (b) Mg, (c) Fe, (d) Mn, (e) S, and (f) P in the collected artificial rainwater samples after blank correction presented in the following manner: The results for water rinsed over the granophyre (red) and gabbro (blue) samples are shown for different weathering conditions, with pH 5 represented by a stronger colour and pH 7 by a lighter colour. The coloured boxes represent the range encompassing half of the results, while the whiskers indicate the range within 1.5 times the interquartile range (IQR). The line within the box displays the median value, and the black square marks the mean. All outliers are shown as black diamonds.

Other elements measured were excluded from the evaluation due to contamination of the blank samples, which resulted in multiple negative values (K, Ca & Na), concentrations near the detection limit (Li), or poor accuracy (Ba). In general, no clear trend was observed in terms of higher concentrations in the water samples with pH 5 or pH 7. In fact, for four out of six elements (P, Mn, Mg & Si) evaluated, the concentrations were higher at pH 5 for the gabbro samples. On the other hand, for four out of six elements (S, Fe, Mg & Si) for the granophyre samples, the concentrations were higher at pH 7. Most element concentrations were in the low ppb range, with Si showing the highest absolute concentrations. Mn and Fe are key components of the varnish, which partly consists of Fe- and Mn-oxides, and for both elements, the measured concentrations greatly exceeded those found in the blank samples, indicating that material was dissolved. Overall, the six blank samples collected alongside the other water samples had mean concentrations of only 0.2 ppb Mn, 6.8 ppb Fe, 2.5 ppb P, and 0.001 ppm Mg. The concentrations of Si and S were higher in the blanks, at 0.2 and 0.1 ppm, respectively. The S content in the blanks with pH 5 was higher slightly higher compared to blanks with pH 7, due to the use of a stock solution containing H_2SO_4 for the preparation of the artificial rainwater at pH 5 (Chapter 4.1.3.3). Additionally, the concentrations of P, Si, and Mg in the blank samples with pH 5 were roughly twice as high as in the blank samples with pH 7 (Tab. 4.3). The whole dataset is given in the digital supplementary material.

A comparison of the Mn and Fe contents in the artificial rainwater samples showed that the mean concentrations of both elements were within the same range for the gabbro samples, at approximately 10 to 22 ppb. For the granophyre samples, the Mn content was similar to that of the gabbro samples, whereas the Fe content was significantly lower, with values of only 2.9 and 6.4 ppb, depending on the weathering conditions (Fig. 4.28c). When the measured concentrations for the individual samples were normalised to the Fe_2O_3 and MnO content of the corresponding rock samples, and the values for Fe and Mn were compared, it was noticeable that the Mn dissolution rates were significantly higher relative to the MnO content than the Fe dissolution rates relative to the Fe_2O_3 content. The range was highly dependent on individual samples, varying from values < 1, indicating a lower normalised dissolution of Mn compared to Fe, to values > 1000 for some of the granophyre samples. When outliers with values > 500 were excluded, the mean ratio of normalised Mn to Fe dissolution rates was approximately 60 for the granophyre samples and 12 for the gabbro samples.

To investigate the effect of the surface angle on the weathering of the rock varnish, one rock sample from each of the four sample groups was positioned at a 30° angle (Chapter 4.1.2). However, due to the large variability in the results (Fig. 4.28) and the inhomogeneity of the varnish surface within the same rock sample groups, it was not possible to reliably determine whether the samples angled at 30° led to different amounts of dissolved material compared to the horizontally placed samples in the chamber.

4.2.4 Residue after the climate chamber experiment

Over the course of the weathering experiment, residual material accumulated at the bottom of the two glass tanks, which were used to collect the excess rainwater. After each simulated rainfall event, most of the water was removed from the tanks by an external pump (see Chapter 4.1.1), but a small amount of water remained in the tanks and evaporated. It was expected that the residue was a mixture of material that had been washed away and material that was dissolved in the artificial rainwater and subsequently re-precipitated in the glass tanks. The residue was first detached from the bottom of the tank using acetone and then collected and dried in small ceramic containers. The material was then heated in an oven to ensure that all organic material, such as parts of the silicone used in the tanks, present in the collected material, was combusted. After this, the material was weighed and analysed using p-XRF, as well as XRD. The p-XRF measurements were normalised to 100 %, to make them comparable to the p-XRF results of the rock samples.

The residue was visible in both glass tanks, especially in the tank used for the samples weathered under acidic conditions. In this tank, the residue had a brown-reddish colour, while the residue in the other tank was much brighter and less noticeable. After extraction and heating, a total of 0.0641 g of residue was recovered from the acidic side of the tank and 0.0433 g from the neutral side.

According to the p-XRF measurements, the main component of both residue samples was SiO_2, with 70.73 ± 1.44 wt. % in the sample from the acidic side and 71.22 ± 0.70 wt. % in the sample from the neutral side (Tab. 4.7). Other major components were Al and Fe, while elements such as Ca, Mg, P, and Mn, which are known to be present in the samples varnish (Tab. 3.1), were relatively depleted, with concentrations of less than 1.5 wt. % (Tab. 4.7). The S concentration in the residue was very high, with 0.99 ± 0.04 and 0.90 ± 0.02 wt. %, compared to the measured concentrations in the bulk rock and rock varnish (Tabs. 1.1, 3.1 & 4.7). Overall, the results of the p-XRF measurements from the residue on the neutral side showed lower concentrations of nearly all elements and especially a higher SiO_2 content.

Table 4.7: Composition of the residue in the glass tanks after the climate chamber experiment. The error (95 %) is given for all elements.

Element (as oxide)	**SiO_2**	**Al_2O_3**	**Fe_2O_3**	**MnO**	**MgO**	**CaO**	**K_2O**	**TiO_2**	**P_2O_5**	**SO_3**
Acidic side (wt. %)	70.73	14.03	9.10	0.19	1.30	1.23	0.58	1.38	0.46	0.99
Error (wt. %)	1.44	0.75	0.65	0.01	0.39	0.08	0.05	0.03	0.04	0.04
Neutral side (wt. %)	71.22	14.13	7.63	0.44	1.49	1.46	0.46	1.72	0.56	0.90
Error (wt. %)	0.70	0.73	0.67	0.03	0.41	0.03	0.03	0.03	0.03	0.02

The XRD measurements of the residual material did show that it was mostly composed of quartz, albite, and hematite. Also smaller amounts of diopside and cristobalite were found, as well as some pyrite in the residue from the acidic side

(Figs. A7 & A8). Except for the minor components these phases were all found in the varnish (see Chapter 3.1.3).

4.2.5 Cross correlations: Statistical data analysis

4.2.5.1 Rock varnish

Correlations at the end of the experiment

The observed changes on the surface of the samples could not be quantified but were categorised based on visible differences in the high-resolution optical images taken before and after the weathering experiment, as well as after 180 days of weathering. The μ-CT scans were also utilised to evaluate surface changes. However, the results were less reliable than anticipated and the resolution was significantly lower compared to the optical high-resolution optical images (see Chapter 4.2.1.2). To examine a potential correlation between the surface changes and other parameters, the observed changes were summarised, considering the following: (1) pieces that chipped off and their size, (2) changes across a wider area of the samples with individual small features, (3) organic fibres on the surface that disappeared over time but were not part of the actual rock varnish, and (4) other changes observed only on individual samples, such as the disappearance of lepidocrocite on one sample. Based on these four parameters, each sample was assigned to a category ranging from 0 (no visible changes) to 5 (major changes, including chipped off pieces).

Table 4.8: Categorised observed changes and colour change ΔE after the end of the weathering experiment of all samples weathered in the climate chamber.

		Sample	Observed changes	Category	ΔE
Gabbro	ref	**RA1**	none	0	0.20
		RA2	small piece chipped off on the edge	1	0.14
	neutral	**NA1**	minor changes on small areas spread over the surface	3	1.52
		NA2	major changes over a wide area of the surface	4	0.70
		NA3	organic fibre attached to the surface was washed away over a larger area	2	1.20
	acidic	**SA1**	larger piece of material chipped off on the edge, major changes over a wide area of the surface	5	5.42
		SA2	major changes over a wide area of the surface	4	4.82
		SA3	small piece chipped off in the middle, organic fibre attached to the surface was washed away over a small area	2	1.18
Granophyre	ref	**RR1**	small piece chipped off in the middle	1	0.80
		RR2	none	0	0.40
	neutral	**NR1**	major changes over a wide area of the surface	4	4.20
		NR2	larger piece of material chipped off on the edge	2	0.47
		NR3	thin layer of lepidocrocite vanished from the surface on multiple, small spots	2	1.23
	acidic	**SR1**	major changes over a wide area of the surface	4	3.86
		SR2	larger piece of material chipped off on the edge	2	0.97
		SR3	larger pieces of material chipped off in the middle	3	1.62

The results of this categorisation and the corresponding colour changes of all samples are presented in Tab. 4.8. All reference samples exhibited no significant changes, apart from some chipped-off material, and were therefore categorised as 0 or 1. In contrast, all samples weathered in the climate chamber were categorised between 2 and 5 (Tab. 4.8). It should be noted that the chosen categories were designed only to provide an indication of the relative extent of surface changes compared to other samples and were not intended to reflect a quantitative measure of surface alteration.

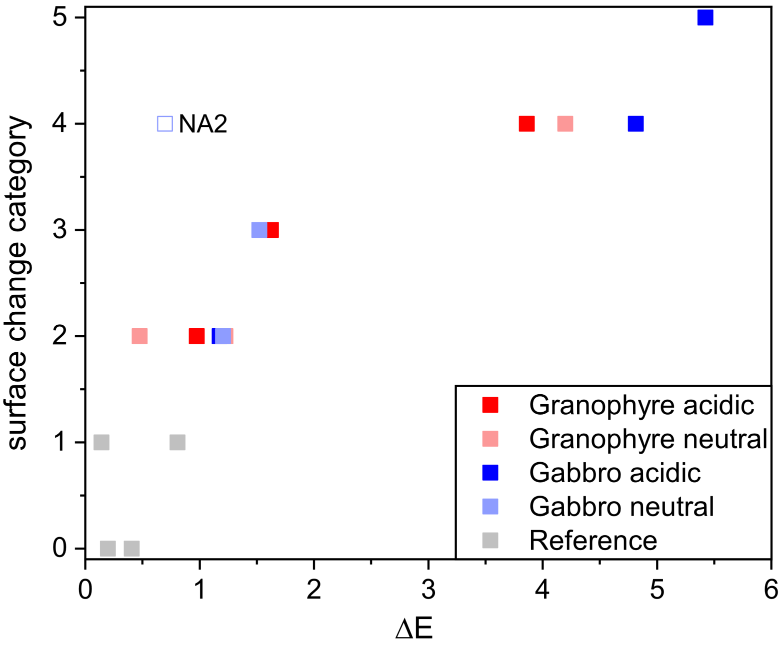

Figure 4.29: Correlation between ordinal-scaled visible changes (Tab. 4.8) and the colour change measured at the end of the weathering experiment. The gabbro sample NA2 is highlighted with an empty square as an outlier. Error bars (95 %) are smaller than the symbol size.

The comparison between the categorised, ordinal-scaled, surface changes and the measured colour change ΔE revealed a positive correlation between the two parameters as shown in Fig. 4.29. This suggests that the observed changes on the sample surfaces were linked to the measured colour change, which is reasonable given that most of the surface alterations were associated with changes in surface colour, as seen in the high-resolution optical images in Chapter 4.2.1.2. An exception was noted for one gabbro reference sample (RA2) and one gabbro sample weathered under neutral conditions (NA2). A piece of material chipped off the reference sample, resulting in its categorisation as 1, yet the measured colour change was the smallest among all reference samples, with a ΔE of only 0.14 after 360 days of weathering. Gabbro sample NA2 exhibited significant surface changes, as shown in Fig. 4.10, but its measured ΔE was only 0.70, the lowest among all gabbro samples. The surface changes observed on NA2 were comparable to those on other gabbro samples weathered under acidic conditions, where the measured ΔE was much higher. In the high-resolution optical images, the colour change on sample NA2 appeared less pronounced than on other samples (Figs. 4.10 & 4.11), which might partially explain the low measured ΔE.

The colour change ΔE also correlated with the weight loss measured at the end of the weathering experiment, but the correlation coefficient for these two parameters was only $R^2 = 0.31$. Sample NA2 again stood out, exhibiting a high weight loss and a comparatively low ΔE value (Fig. 4.30). The weight loss was consistent with the observed surface changes on sample NA2, further indicating that the colour of this sample changed differently compared to the other samples. Excluding NA2 from the calculation of the correlation improved the coefficient significantly, to $R^2 = 0.67$. Notably, all reference samples showed an apparent positive weight change, likely due to calibration drift in the weighing scale over the year-long measurement period (see Chapter 4.2.1.2). The relationship between the colour change ΔE and weight loss appeared to follow a linear trend, as illustrated in Fig. 4.30. This trend indicated a weight loss of 0.008 ± 0.001 g per one ΔE for a surface area of approximately 20 cm^2.

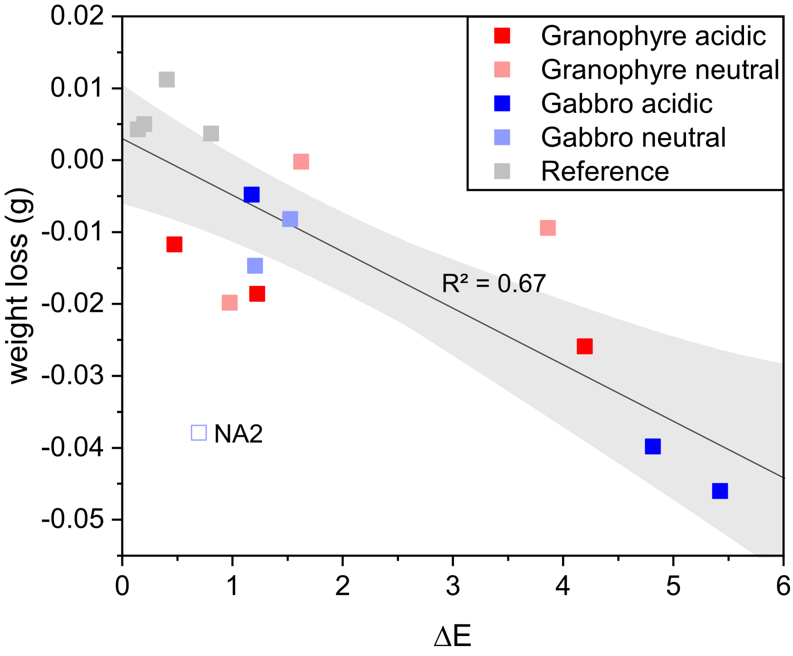

Figure 4.30: Correlation of weight loss and colour change measured at the end of the weathering experiment. The gabbro sample NA2 is highlighted with an empty square as an outlier and was excluded from the calculated linear trend, which is depicted as a red-blue line. Error bars (95 %) are smaller than the symbol size.

The weight loss, the ΔE values, and the observed surface changes were all based on results at the end of the experiment and did not account for the development of these parameters over time. The samples were also weighed after 180 days of weathering, and the calculated weight loss at that time correlated with the measured ΔE after

180 days, with $R^2 = 0.31$ when sample NA2 was included and $R_2 = 0.56$ when it was excluded.

The μ-CT scans could not be analysed quantitatively and therefore, the results from these scans could not be correlated with other parameters measured during the experiment. Instead, the scans were used solely to confirm the observed changes on the sample surfaces, as identified using the high-resolution optical images.

The colour change ΔE, calculated using changes in brightness (ΔL*) and chromatic components (Δa* & Δb*), showed a strong correlation with ΔL* (R = -0.99) and with Δa* (R = 0.85), while the correlation with Δb* was much weaker (R = -0.17). This indicates that the primary component driving the colour change ΔE was the change in brightness (ΔL*) on the sample surfaces. This result aligns with earlier observations discussed in Chapter 4.2.1.1 during the analysis of the colour measurement data. The contribution of Δa* to the overall ΔE values was also significant, particularly when compared to Δb*, which had little impact due to its small magnitude relative to ΔL* and Δa* (see Chapter 4.2.1.1).

The initial chemical composition of the samples revealed linear inter element correlations among the concentrations of Cr, Sr, SO_3, Fe_2O_3, and P_2O_5, with R values mostly > 0.85. The high correlations were mainly driven by two granophyre samples weathered under different conditions (SR2 & NR3) that exhibited extraordinary high concentrations of these elements (see Chapter 3.1.3.1; Tab. 3.1). Excluding these two samples reduces the correlation coefficients to way smaller R values for most of the element correlations. The same goes for the apparent correlations between the Fe-Mn ratios calculated and the content of SO_3 (R = 0.99), Fe_2O_3 (R = 0.86), and P_2O_5 (R = 0.93), which were also mainly due to the two samples with high concentrations of these elements and extraordinary high Fe-Mn ratios of > 100.

Previous studies reported negative correlations between MnO and SiO_2 or Al_2O_3, along with a positive correlation between MnO and BaO content, but no correlation between MnO and Fe_2O_3 concentrations (Xu et al., 2019). Another study identified a positive correlation only between Mn and Ba, without significant correlations for other elements such as Fe, Si, and Al (Goldsmith et al., 2014). In the present study, MnO concentrations did not correlate with other elemental concentrations measured before the weathering experiment. The correlation coefficient between MnO and Ba was R = 0.0051, contradicting previous findings. This discrepancy may be due to the low MnO concentrations in the present samples, with mean values around 3 wt. % and a maximum of only 9.10 wt. % (Tab. 3.1), compared to mean and maximum values exceeding 10 wt. % in other studies (Goldsmith et al., 2014; Xu et al., 2019).

The percentage changes at the end of the experiment and the initial elemental concentrations of the same element correlated significantly only for Sr and TiO_2. A negative correlation (R = -0.78) was observed between the initial Sr concentrations and the concentration change $\Delta_{\mathrm{Sr}}^{\mathrm{corr}}$ (%), indicating that higher initial Sr concentrations corresponded to larger negative percentage changes. For TiO_2, a negative correlation (R =

-0.80) was primarily due to one sample with a TiO_2 concentration below the detection limit, resulting in an exaggerated percentage change. Excluding this sample reduced the correlation coefficient to -0.48, suggesting no genuine correlation. All percentage changes were corrected using the reference samples, as described in Chapter 4.2.1.4. Consequently, only the 12 samples weathered in the climate chamber were included for comparisons and the reference sample stored under controlled conditions were excluded.

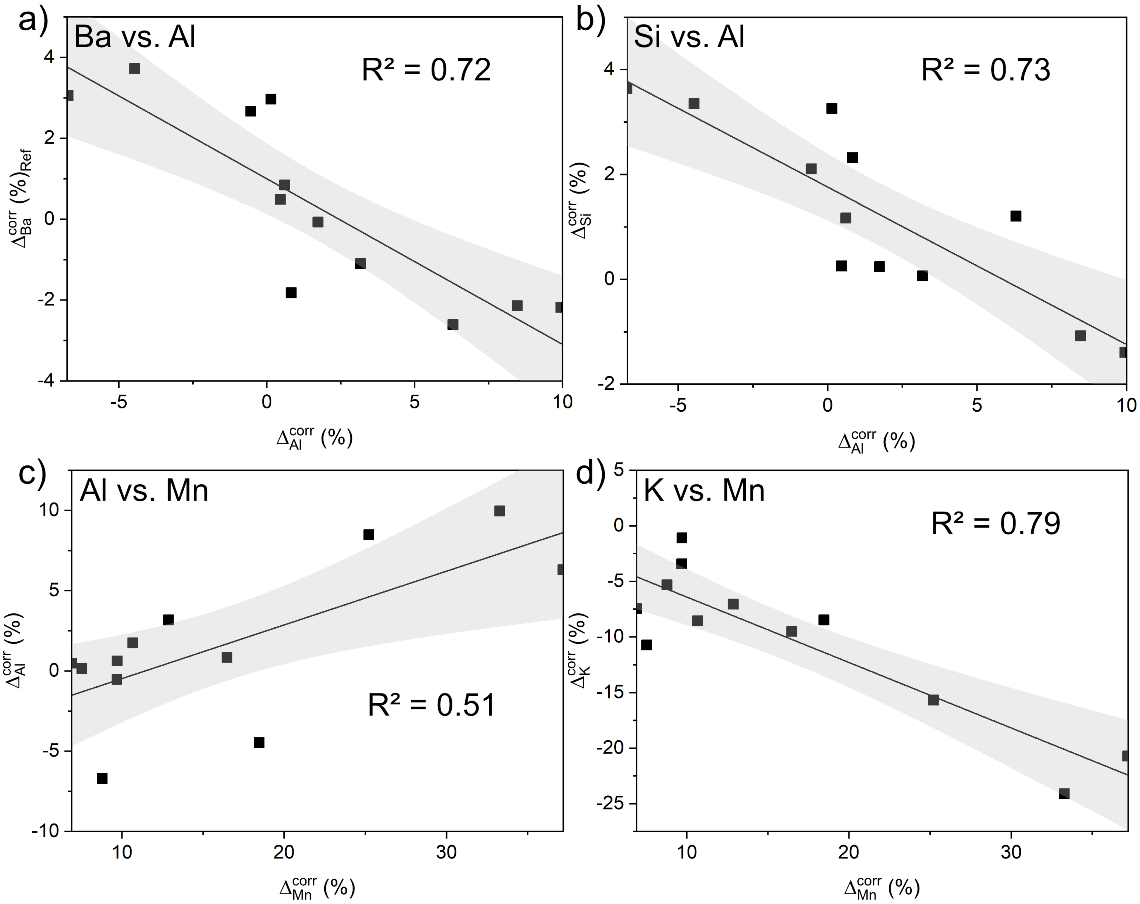

Figure 4.31: Inter element correlations of the surface concentration changes at the end of the experiment. The confidence bands and error bars are presented within a 95 % confidence interval. The error bars are smaller than the symbol size.

Only three correlations between percentage changes of elemental concentrations at the end of the experiment with $R^2 > 0.7$ were observed. For the changes of the MnO and K_2O concentrations, a negative correlation was observed, indicating that a higher percentage increase of MnO on the sample surfaces corresponded to a higher loss of K_2O. Here, one sample with a small change in the MnO content stood out due to relatively high changes in the K_2O concentrations (Fig. 4.31d). The changes in the Al_2O_3 and Ba concentrations were also negatively correlated, indicating that a high positive change in the Al_2O_3 concentrations corresponded to a negative change in the Ba content on the surface (Fig. 4.31a). The change in the Al_2O_3 content was also negatively correlated with the change in SiO_2, indicating that a greater loss of SiO_2 coincided with an increase in the Al_2O_3 concentration (Fig. 4.31b).

The change in the Al_2O_3 content was also positively correlated with the change in the MnO content, with a smaller R^2 than the aforementioned correlations. Here, two granophyre samples weathered under neutral conditions stood out with highly negative changes in the Al_2O_3 content. The results for the other samples indicated that an increase in the MnO content corresponded to an increase in the Al_2O_3 content (Fig. 4.31c). The changes in the Ba and SiO_2 contents were also correlated, with $R^2 = 0.58$.

The mean elemental concentrations in the artificial rainwater, which was in contact with the rock samples and analysed using ICP-OES (Chapter 2.4), were compared with each other and other parameters measured at the end of the weathering experiment. A correlation was found between Mn and Si, as well as between Mg and Sr, in the water samples. The Mn and Si correlation ($R = 0.87$) was influenced by two outliers. Excluding these reduced the correlation coefficient to only 0.51. Interestingly, these two outlier granophyre samples (NR2 & SR3) were the samples with the lowest measured MnO content on the surface, but had the highest Mn concentrations in the artificial rainwater samples that were in contact with the samples. The Mg and Sr correlation was stronger ($R = 0.94$), suggesting that higher Mg concentrations corresponded to higher Sr concentrations in the water.

From a total of 1,935 correlation coefficients calculated for the combinations of 45 parameters only 21 with $R > 0.85$ were found. Some of them were not discussed as it was assumed that there is no genuine connection between these parameters as for example the correlation between the relative change of the Ba concentration on the samples and the concentration of Sr in the water samples which correlated with $R = -0.89$. All data and correlation matrices are provided in the digital supplementary material.

Correlations over time

The only parameters measured at each time step of the experiment were the colour change, ΔE, and the changes in surface element concentrations (Fig. 4.2), as well as the calculated change of the Fe-Mn ratio and the changes on the glass dosimeters (Chapter 4.2.5.2). Consequently, only the correlations between these parameters could be assessed over the duration of the experiment. To simplify the analysis, the mean changes of the four different sample groups were used instead of the results from the 12 individual samples.

The number of correlating parameters was highly dependent on the sample group. For example, in the gabbro group weathered under acidic conditions, 18 out of 135 correlations had a correlation coefficient with $R > 0.85$, while in the group of gabbro samples weathered under neutral conditions it were only four. Notably, in none of the sample groups did the change in MnO concentration over time correlate with any other parameter with $R > 0.85$.

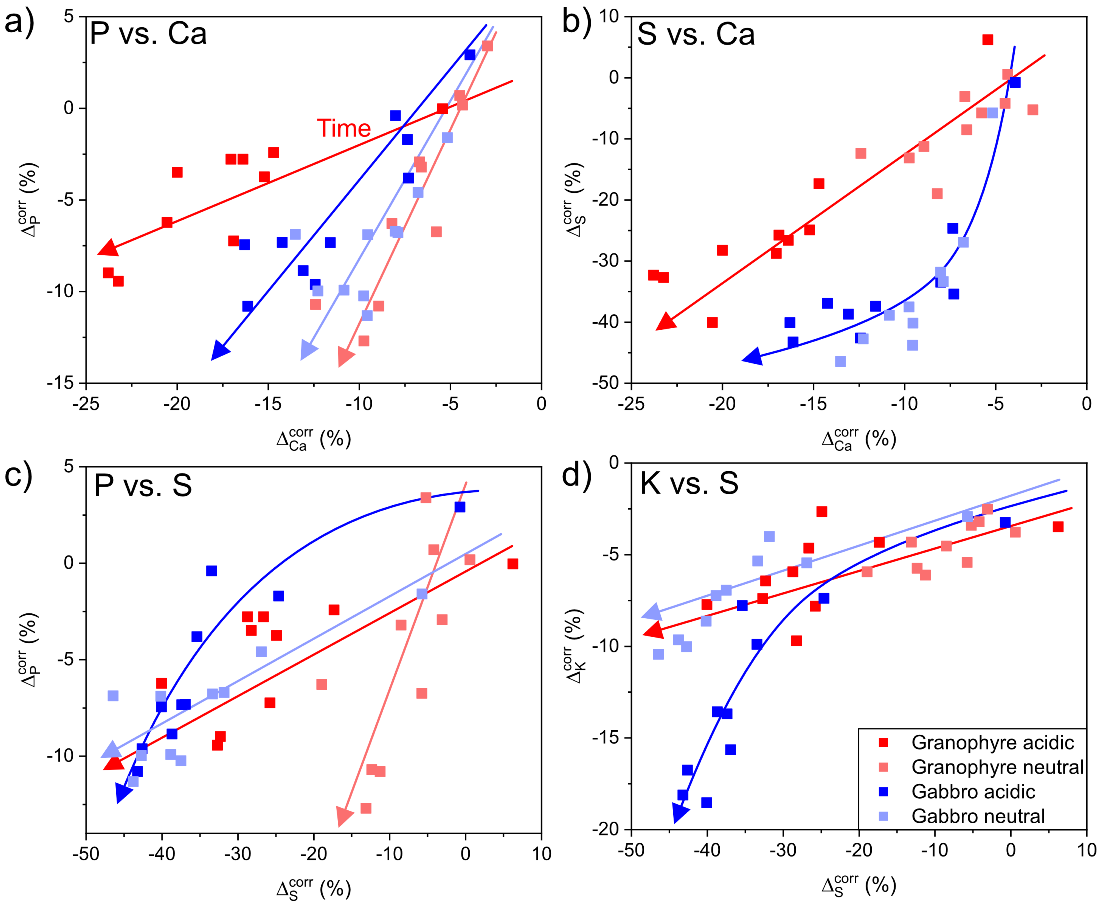

Figure 4.32: Inter element correlations of the surface concentration changes over the course of the experiment, divided into the four different sample groups. All lines are provided as guides to the eye only, indicating potential trends over the experiment's duration, with arrowheads pointing towards the end of the experiment. Where only one line is shown, it represents both sample groups of the same rock type, with granophyre shown in red and gabbro in blue. Error bars (95 %) are smaller than the symbol size.

The colour change ΔE correlated with the changes of the Al_2O_3, CaO, K_2O, and P_2O_5 concentrations, with $R > 0.85$ for the gabbro samples weathered under acidic conditions. However, this correlation was not observed in all other sample groups. This discrepancy arose due to the consistent colour change observed exclusively in this sample group. Similarly, some other parameters showed correlations only within one or two sample groups. The only correlations with $R > 0.85$ across all sample groups were between glass dosimeters, as explained in Chapter 4.2.2. There were correlations with $R > 0.75$ in most of the sample groups between the percentage changes of different elements.

These correlations could be observed among the elements that decreased relatively consistently over the course of the experiment, namely SO_3, P_2O_5, K_2O, and CaO. The highest correlation coefficients were found between CaO and P_2O_5, as well as SO_3, with correlation coefficients ranging from 0.71 to 0.91. For CaO and P_2O_5, the developments over time varied significantly between the sample groups. Notably, the samples weathered under acidic conditions exhibited the highest changes in CaO content, while changes in P_2O_5 content were relatively uniform across all sample groups. This variation led to different ratios between the changes in CaO and P_2O_5 (Fig. 4.32a). For the correlation between CaO and SO_3, the changes in SO_3 content also depended on the weathering conditions. Consequently, the development of both elements showed a similar ratio within each rock type, regardless of the weathering conditions. For the gabbro samples, the initial measurements had a different ratio between the changes, resulting in a curved trend (Fig. 4.32b).

The correlations between SO_3 and P_2O_5, as well as between SO_3 and K_2O, were less pronounced for the granophyre samples, with R values ranging only from 0.57 to 0.72. In contrast, the R values for the gabbro samples ranged from 0.82 to 0.86. In both cases, three out of four sample groups followed a similar trend, while the fourth group deviated significantly. For SO_3 and P_2O_5, the granophyre group weathered under neutral conditions showed a much lower change in SO_3 content than the other groups. This discrepancy led to significant differences in the ratios between the elements (Fig. 4.32c). For the correlation between SO_3 and K_2O changes, the gabbro samples weathered under acidic conditions were exceptional, exhibiting significantly higher changes in K_2O content (Fig. 4.32d). The probable trend again formed a curve due to the low changes in SO_3 observed during the initial measurements.

Correlations of the Fe-Mn ratio

The Fe-Mn ratio on the sample surfaces was also examined due to its potential correlation with other parameters. For gabbro samples, weight loss and colour change, ΔE, correlated with changes in the Fe-Mn ratio measured at the end of the experiment. Two gabbro samples weathered under neutral conditions exhibited increased Fe-Mn ratios alongside minimal weight loss. In contrast, the third gabbro sample displayed a decreased Fe-Mn ratio paired with substantially greater weight loss. A similar pattern was observed in samples weathered under acidic conditions. Here, one sample showed only a slight decrease in the Fe-Mn ratio with negligible weight loss, while the other two exhibited decreases of approximately 15 % in the Fe-Mn ratio and significantly higher weight loss (Fig. 4.33a). A comparable correlation was observed between the colour change and the Fe-Mn ratio, with the greatest colour changes coinciding with the largest decreases in the Fe-Mn ratio. The gabbro sample NA2, which was weathered under neutral conditions, again, formed an exception, where the measured colour change did not align with surface changes (Fig. 4.33b). For gabbro samples, the correlation coefficients were $R = 0.90$ (weight loss) and $R = 0.94$ (ΔE). In contrast, for granophyre samples, the Fe-Mn ratio showed weaker correlations with $R = 0.34$ for the weight loss and $R = 0.14$ for the colour change ΔE. This indicated no significant correlation for these samples. Moreover, the overall changes in the Fe-Mn ratio were smaller and exhibited less variation than in the gabbro samples. The absence of a correlation for granophyre samples is evident in Fig. 4.33, but it is also noticeable that most measurements are in close range to a possible trend of the development of both parameters for the gabbro samples.

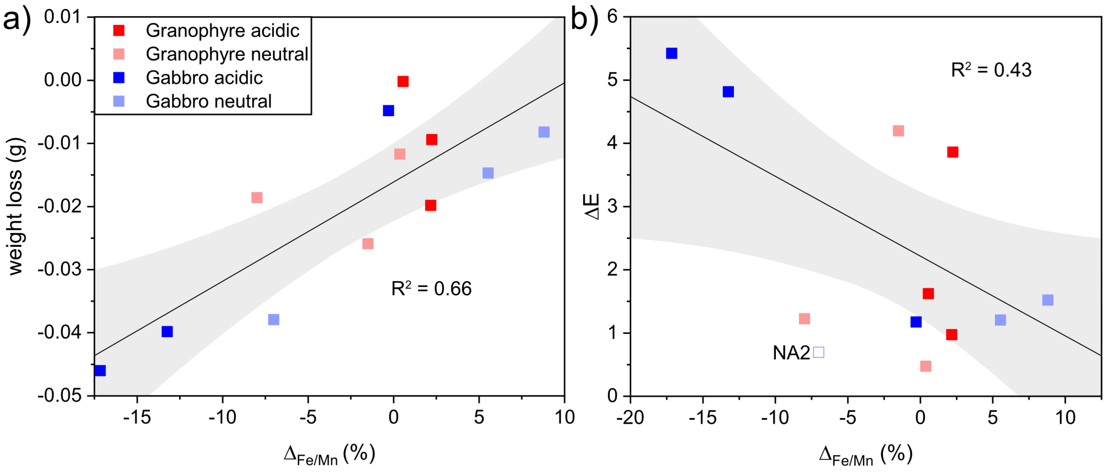

Figure 4.33: Correlation of the Fe-Mn ratio on the surface with (a) the weight loss and (b) colour change at the end of the experiment. Gabbro sample NA2 is highlighted in (b) as it stands out again, consistent with Figs. 4.29 and 4.30, and was excluded from consideration when assessing a potential trend. The confidence bands and error bars are presented within a 95 % confidence interval. The error bars are smaller than the symbol size.

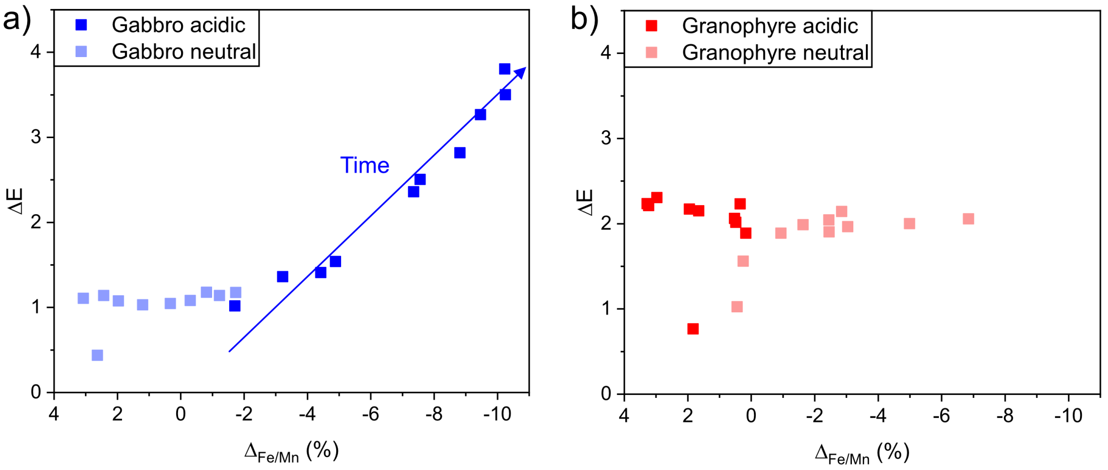

Figure 4.34: Correlation of the mean Fe-Mn ratio with the mean colour change over the duration of the experiment for (a) gabbro and (b) granophyre sample groups. The line serves as a visual guide to represent the time axis and indicate a potential trend. Error bars (95 %) are smaller than the symbol size.

Fe-Mn ratios measured after the end of the experiment correlated strongly with Cr (R = 0.90), SO_3 (R = 0.99), and P_2O_5 (R = 0.96) concentrations measured on the sample surfaces. However, this was largely influenced by two granophyre samples (SR2 & NR3) with very low Mn contents, resulting in ratios > 100. These samples, which also had extraordinary high Cr, SO_3, and P_2O_5 concentrations, significantly reduced the correlation coefficients when excluded.

A comparison of the mean changes in colour and the Fe-Mn ratio over the course of the experiment revealed a correlation only for gabbro samples weathered under acidic conditions. In this group, a decreasing Fe-Mn ratio coincided with an increasing ΔE, with $R = 0.98$ (Fig. 4.34a). No such correlation was found in the other three groups. In these groups, the Fe-Mn ratio exhibited strong fluctuations over time, while colour changes occurred predominantly in the first one or two time steps and remained largely unchanged thereafter. The correlation coefficients for these three groups were < 0.70.

No other significant correlations between the change in the Fe-Mn ratio and other parameters were identified. Overall, the correlation matrix for the parameters measured at the end of the experiment on individual rock samples, as well as the matrices for the mean values of the different sample groups over the duration of the experiment, showed many possible correlations with $R > 0.85$ or higher. However, most of these correlations were either found only within a single sample group or were influenced by outliers, as described above, and were thus not further analysed. All data and correlation matrices are provided in the digital supplementary material.

Principal component analysis (PCA)

A PCA was conducted with the results obtained after the end of the experiment (Abdi & Williams, 2010), using Origin (OriginLab Corporation, 2018). Initially, the PCA included 45 different parameters per sample, which resulted in cluttered outcomes. Consequently, the number of parameters was reduced to 12. Here, the parameters with the highest sum of their coefficients in principal components 1 (PC1) and 2 (PC2) were chosen. Using these 12 parameters, 75.40 % of the variance among the samples could be described using only PC1 and PC2, which had eigenvalues of 6.32 and 2.72, respectively. Notably, the only parameter connected to Mn among the 12 was the Fe-Mn ratio. The surface concentrations of Fe_2O_3 were also included.

The gabbro and granophyre samples were not clearly separated from each other and the differences within the sample groups were often greater than those between samples from different groups. Overall, it was noticeable that pairs of samples cut from the same rocks shared more similarities than the sample groups as a whole. Granophyre samples NR3 and SR2, which were cut from the same piece of rock, formed two outlying samples that stood out due to their high SO_3, Fe_2O_3, Cr, and P_2O_5 contents, leading to high PC1 values. These samples were also characterised by low SiO_2 and K_2O contents, as well as relatively high negative changes in Sr content on the surface. The other two pairs of granophyre samples were closer together but still showed significant differences. Samples NR1 and SR1 exhibited the highest ΔE among the granophyre samples and very low Cr concentrations compared to the other samples. These two samples also displayed high surface changes, which could not be incorporated into the PCA (see Chapter 4.2.1.2). They also stood out due to high changes in TiO_2 concentration on the surface, particularly NR1, which showed around 30 % change. This partly explained the high PC2 value of sample NR1 compared to SR1, as well as the closer proximity of SR1 to SR3 (Fig. 4.35). The last pair of granophyre samples (NR2 & SR3) was not characterised by any outstanding parameters when compared to the other samples. Overall, the values of most parameters included in the PCA were close to the mean values of all samples, making it relatively difficult to clearly separate them from the others based on individual parameters.

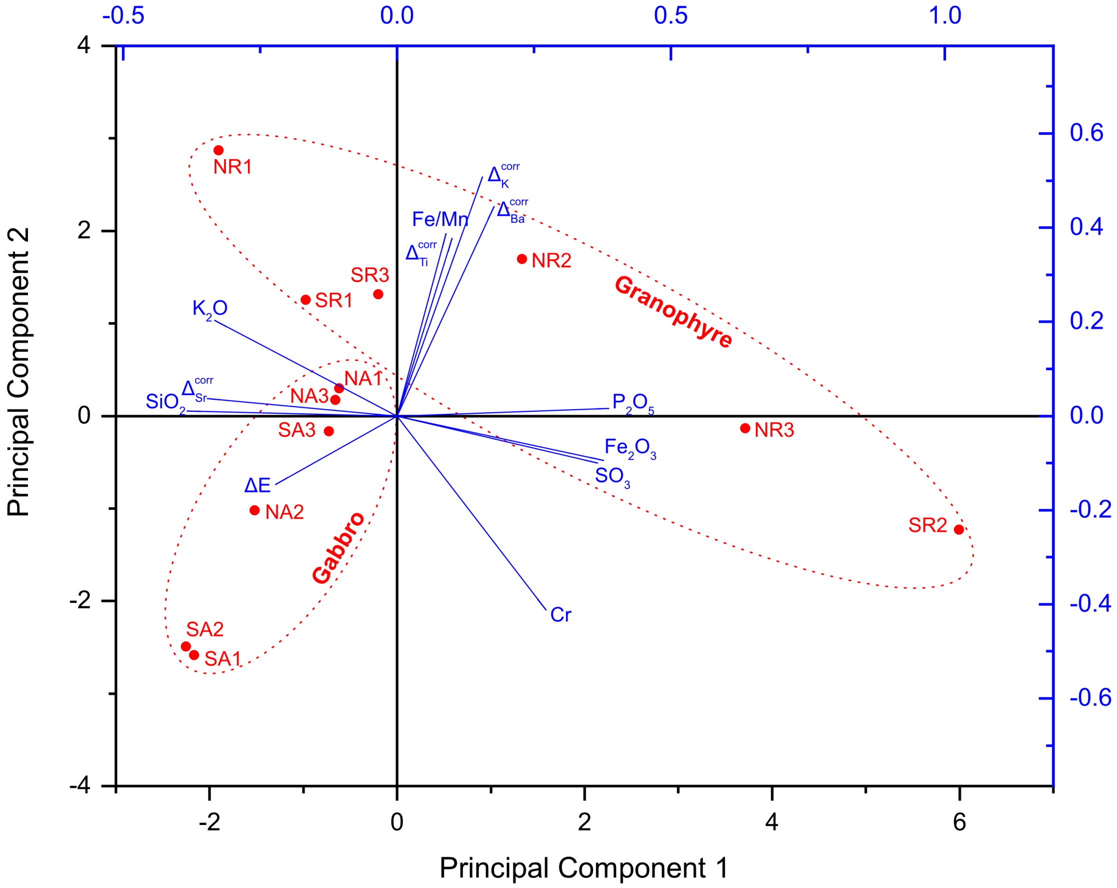

Figure 4.35: Principal component analysis (PCA) of the results acquired after the end of the weathering experiment. The number of parameters was reduced and only those with the highest contributions to PC1 and PC2 are displayed. These include the colour change ΔE, the measured concentrations of various elements such as Cr, the percentage changes in element concentrations compared to pre-weathering measurements (e.g. Δ_{Ba}^{corr}), and the Fe-Mn ratio. All used rock samples are shown as red dots.

Two gabbro samples weathered under acidic conditions (SA1 & SA2) stood out due to their high ΔE values, which were the highest among all samples (Fig. 4.4), as well as due to their high changes in K_2O concentration and low changes in TiO_2 concentration during the experiment. These two samples also exhibited very large surface changes, which could not be included in the PCA. The same applied to the gabbro sample NA2, weathered under neutral conditions, which was in relatively close proximity to samples SA1 and SA2. It mainly differed from these two samples due to a very low ΔE value. This group of three samples also stood out in comparison to others due to their high positive relative change in MnO concentration on the surface and the highly positive change in Al_2O_3 concentration. The MnO change also led to a relatively high negative change in the Fe-Mn ratio. All of these parameters were not included in the PCA due to their low coefficients for PC1 and PC2.

The other three gabbro samples were the closest to each other and had overall very low values for PC1 and PC2. Similar to the granophyre samples NR2 and SR3, no individual parameters of these samples stood out, and for most parameters, the values were close to the mean values of all samples.

For the gabbro samples, the PCA revealed distinct differences between samples that showed high surface changes in the high-resolution optical images and those with significantly fewer changes observed, with a clear separation between these groups. There was no systematic separation between samples weathered under neutral and acidic conditions, as one sample weathered under acidic conditions was closely grouped with two samples weathered under neutral conditions. Variations within the groups were also observed, likely due to inhomogeneous surface conditions and compositions among the sample pairs. Conversely, the granophyre samples were primarily grouped based on the original rock pieces from which they were cut, resulting in closer proximity between sample pairs regardless of the weathering conditions for most of the samples. Overall, the differences among the granophyre samples were much greater than those observed among the gabbro samples, as expected, given the substantially different types of rock varnish present on the granophyre sample surfaces (see Chapter 3.1).

As noted above, the parameters related to Mn and Fe, which are essential components of rock varnish (see Chapter 1.4), were mostly excluded from the principal component analysis (PCA) due to their low coefficients in PC1 and PC2. A separate PCA was conducted using only the parameters associated with Mn and Fe, along with colour change and weight loss (Fig. A9). In this analysis samples SA1, SA2, and NA2 formed a distinct group, primarily characterised by the colour change ΔE, the positive $\Delta_{\mathrm{el}}^{\mathrm{corr}}$ (%) changes in MnO and Fe_2O_3, negative weight loss, a negative change in the Fe-Mn ratio at the end of the experiment, and high Fe concentrations in the analysed artificial rainwater that had been in contact with the samples.

Granophyre samples SR2 and NR3 were also grouped together and stood out due to their high Fe_2O_3 content and low MnO content, which resulted in an exceptionally high Fe-Mn ratio. The remaining samples formed a broader group with a wider range in comparison to the PCA shown in Fig. 4.35, distinctly separated from the other two groups. The other samples were in relative close proximity to each other with no distinct separation between the granophyre or gabbro samples, as well as not distinct separation of samples weathered under neutral or acidic conditions.

4.2.5.2 Glass dosimeters

The three types of glass dosimeters weathered in the climate chamber were used to quantify the simulated weathering and to compare the two simulated conditions to each other, as well as to compare the weathering of the rock samples to a known standard. Therefore, a comparison of the alteration of the glass dosimeters, determined by the water content and expressed as ΔE_{IR}, with the measured parameters of the rock samples was of great interest.

The vulnerability to alteration of the glass dosimeters depended on their composition. The correlation of the measured ΔE_{IR} values for the three glass dosimeters demonstrated that some of the dosimeter types underwent different alterations. While types MI and M5 exhibited similar changes, with nearly identical values after each time step and within each sample group ($R^2 = 0.99$), glass type M3 altered in a different manner, showing no clear trend (see Chapter 4.2.2) and no significant correlation with the other glass types MI and M5 ($R < 0.75$). The comparison of glass types MI and M5 indicated that the ΔE_{IR} values were smaller in the neutral group. However, the ratio between the two glass types remained consistent under both conditions and was close to one (Fig. 4.36).

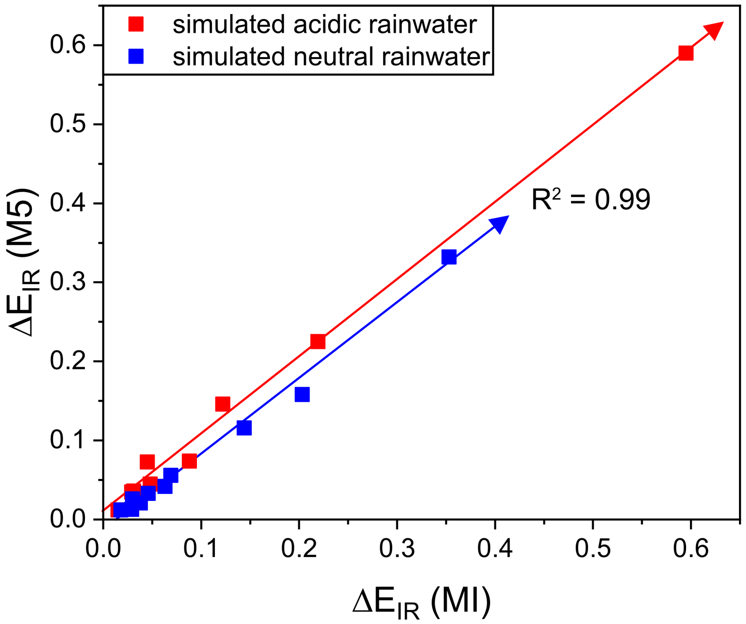

Figure 4.36: Correlation of ΔE_{IR} values of the glass types MI and M5 weathered under acidic (red) and neutral (blue) conditions. The blue and red lines show the linear trends of the correlations over time with the arrowhead indicating the trend over time. Error bars (95 %) are smaller than the symbol size.

Significant correlations between the alteration of the glass dosimeters and the parameters measured on the rock samples could not be identified. Only the parameters measured at the same time steps as the removal of the glass dosimeters from the climate chamber were analysed. These were the measured colour change and the changes in the chemical composition of the sample surfaces. Most parameters acquired from the rock samples exhibited, if any significant changes occurred, rapid and substantial changes during the first two to three time steps, corresponding to a total of 15 to 35 days of weathering. Thereafter, the rate of change slowed considerably, or no further significant changes were observed (Figs. 4.6, 4.16 & 4.17).

In contrast, the rate of change in glass dosimeters MI and M5 was initially slow but appeared to increase exponentially towards the end (Figs. 4.23 & 4.24). This opposing trend between the glass dosimeters and the rock samples created difficulties in comparing these parameters, resulting in very low correlation coefficients. In such comparisons, either the apparent exponential growth of the ΔE_{IR} of the glass dosimeters dominated, while the parameters measured on the rock samples exhibited rapid changes early on and slower changes later on, or the rock sample parameters ceased to change significantly after the initial phase, leading to even poorer correlations. For instance, the colour change ΔE of the gabbro samples weathered with two different types of artificial rainwater shows this issue. Both rock sample groups exhibited an initial rapid change in ΔE, followed by a slower yet steady rate of change in the acidic group (Fig. 4.37a) or no significant changes after the initial period in the neutral group (Fig. 4.37b).

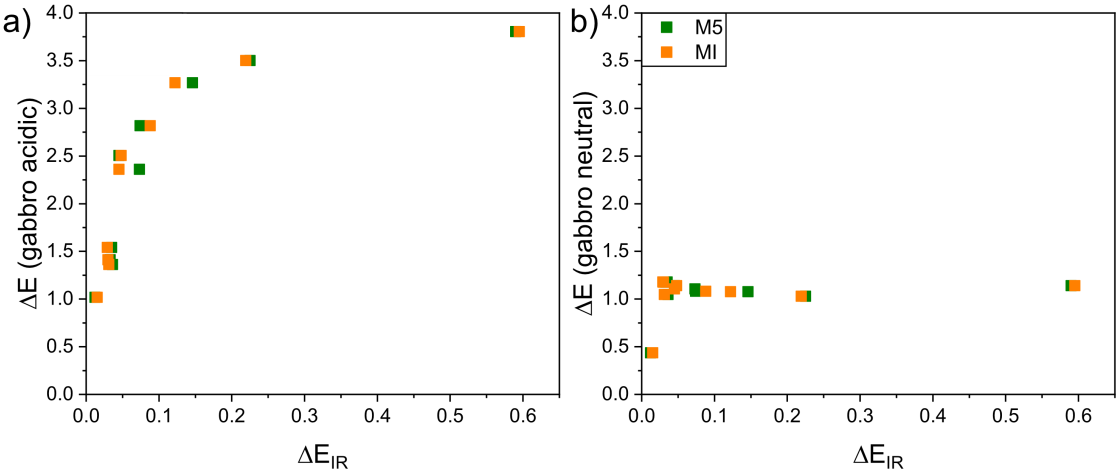

Figure 4.37: Colour change ΔE of the gabbro samples weathered under (a) acidic and (b) neutral conditions as function of ΔE_{IR} of the glass types MI and M5. Error bars (95 %) are smaller than the symbol size.

Glass type M3 did not exhibit changes following a consistent trend and the overall measured changes were an order of magnitude lower than those for the other glass types, resulting in a relatively high margin of error. The correlations observed between the M3 dosimeters and the parameters measured on the rock samples were mainly attributable to the behaviour of the M3 dosimeters. These initially exhibited an increase in ΔE_{IR} over the first 120 days of weathering, followed by a plateau for the rest of the experiment, except for the final measurement under acidic conditions

(Fig. 4.22). This development, characterised by an initial increase and subsequent stagnation, was also observed in some parameters measured on the rock samples as aforementioned, leading to relatively high apparent correlation coefficients.

The lack of further increase in ΔE_{IR} for the M3 dosimeters, contrary to expectations, is believed to result from their low vulnerability to alteration. Typically, stagnation of ΔE_{IR} indicates that the maximum level of surface alteration has been reached. However, this was not the case for the M3 dosimeters, as it is known that the ΔE_{IR} of this glass type can reach significantly higher values. Additionally, the observed structures on the glass surface showed almost no visible alteration (see Chapter 4.2.2.2). Consequently, the results for this glass type were considered unrealistic and were excluded from statistical analyses, despite some correlations being observed.

4.3 Discussion of the climate chamber experiment

4.3.1 Setup and methods

Experimental setup and procedure

The climate chamber experiment was carried out as planned, with no major issues arising during its course. The total experiment lasted one week longer than initially planned due to necessary maintenance, which led to two extended pauses halfway through the experiment (at 180 days of weathering). These pauses, totalling 30 days, did not cause any significant irregularities in the data acquired after 240 days, compared to the data recorded after 180 days of weathering. This was true for both the glass dosimeters and the rock samples in the chamber. The extended interval between measurement points was also not evident in the reference sample data, except for one MnO measurement on the gabbro reference samples, which was excluded in the data analysis (see Figs. 4.6 & 4.15). This demonstrated that storage under controlled conditions had little to no impact on the weathering of the rock samples and glass dosimeters. This conclusion was further supported by the low ΔE_{IR} values measured on the glass dosimeters stored as reference dosimeters (see Chapter 4.2.2) and the minimal colour change ΔE measured on the reference samples (Fig. 4.6).

The experimental setup run without major complications. All components of the additional setup installed in the climate chamber, including the Ultra Vitalux® lamps, irrigation pumps, suction pump, time switches, and nozzles, operated throughout the experiment without critical failures. Although the suction pump failed once, it was promptly replaced with a spare pump kept on hand for such incidents. The air pump maintaining the artificial rainwater in equilibrium with atmospheric CO_2, to ensure a consistent pH, also functioned reliably, maintaining the pH within the target range of 5 ± 0.1 and 7 ± 0.1. The pH variability was even lower than the target error of ± 0.1 on average (see Chapter 4.1.3.3). Other simulated parameters remained within the known error ranges of the used climate chamber, which was recalibrated after approximately 220 days of simulated weathering to ensure consistent conditions throughout. The artificial rainwater was not externally heated or cooled, matching the ambient temperature of the climate chamber laboratory, which ranged from a maximum of 31 °C in summer to a minimum of 25 °C in winter. The experiment started in April and was finished in June of the following year, meaning that simulated years 3 and 4 coincided with winter, during which the artificial rainwater was at its coolest temperatures.

As mentioned in Chapter 4.1.2 some plastic parts of the used setup got significantly darker over the course of the experiment, which likely was due to the high dose of simulated solar radiation including UV-light. The oil used for cooling during drilling and milling, as well as the acidic rainwater are two possible reasons for the darkening that was observed more intense on the side with simulated acidic conditions as already discussed in Chapter 4.1.2.

Analytical methods

The colour measurements were completed without significant issues. The measurement procedure, which involved a high number of measurements, achieved an error of only ± 0.01 to ± 0.03 for L*, a*, and b*, resulting in a propagated margin of error (95 %) for ΔE of only ± 0.02 to ± 0.05. This was approximately an order of magnitude lower than the errors reported in the most recent MRAMP report, where standard deviations of 0.28 for L*, 0.21 for a*, and 0.19 for b* were observed, leading to a maximum ΔE of 1.1 in a test comparing 20 consecutive measurements on the same surface (MRAMP, 2023). Previous studies also reported less precise measurements, with ΔE values reaching up to 4.0 for repeated measurements on identical spots (Lau et al., 2007, 2010; Markley et al., 2015). These findings highlight the importance of a reliable measurement setup, capable of consistently measuring the same surface area, maintaining a fixed angle, and minimising shading effects caused by the chroma meter's light source on uneven sample surfaces.

The use of a self-written programme for the p-XRF measurements, calibrated with granophyre and gabbro samples, yielded good results with realistic absolute compositions for most of the tested rock samples. However, the Fe_2O_3 content for two of the samples exceeded the calibration range. Consequently, it was estimated that the Fe_2O_3 values were overestimated, as the total sum of the measured elements exceeded 100 %, requiring the normalisation of all absolute values to 100 %. While a factory-calibrated programme would have avoided this issue, as shown in previous work (Neumann, 2021), it might have resulted in shifted absolute concentrations for some elements due to the lack of calibration with the specific sample compositions. Another notable issue was the high measured variability in the reference samples over the course of the experiment. These changes are believed to have been caused by external factors, such as temperature and humidity, as discussed in Chapter 4.2.1.4. It was additionally observed that the total sums varied from measurement to measurement for the different samples, which was likely due to slightly different distances between the measurement head and the sample surfaces. These fluctuations could be corrected by normalising all individual measurements to 100 %. Although a factory-calibrated programme could have mitigated some of these problems, the corrected results still yielded reliable data, showing clear trends for certain elements and overall good reproducibility. In particular, the gabbro samples exhibited relatively small changes in the reference samples, with nearly all elements showing variations of less than 5% (Fig. 4.15).

The relatively small measurement area, with a diameter of approximately 1 cm, restricted the analysis to a limited section of each sample. While these measurements provided reliable data for the relative change in surface composition, they did not represent the composition of the entire, highly heterogeneous sample surfaces, unlike the colour measurements. As a result, additional measurements were required to characterise the compositions of distinguishable areas with varying structures and colours. However, it was not possible to monitor changes in these individual areas over time (see Chapter 3.1.3.1). Measuring more spots on different parts of the samples could have improved representativeness but would have required longer intervals between weathering phases, as the p-XRF measurements were time-consuming, taking approximately 30 minutes per sample per spot. The calculation of Fe-Mn ratios, which are known to be important, also relied on single-spot measurements. Additional measurements revealed that the Fe-Mn ratios varied depending on the measurement spot and the surface colour indicating different varnish types (see Chapter 3.1.3.1).

The high-resolution optical images captured at the Westerwald campus of Hochschule Koblenz allowed for visualisation of surface changes on a small scale and comparison of these changes over the course of the experiment. With a pixel size of 3 to 4 µm, small details were discernible, enabling the analysis of microstructures on the surface. However, variations in ambient lighting and the lack of manual exposure settings for the samples during imaging caused colour inconsistencies between image sets, complicating direct comparisons. Some images had to be retaken due to overexposure, and although exposure adjustments were partially possible in post-processing, it was not consistently feasible to accurately visualise colour changes in the samples. Consequently, quantifying the observed surface changes based on these images was impossible. The pixel size was small but unfortunately not small enough to distinguish every mineral grain from each other, as high-resolution optical images taken with the optical microscope in the used Raman spectroscope show, where small individual grains with sizes < 3 µm are visible (see Chapter 3.1.3; Fig. A3).

Additionally, capturing a greater number of images per sample at more time points would have been beneficial. This would have allowed for a more precise determination of when surface changes occurred, especially during the critical early phases of the experiment. Significant changes were observed with other methods as early as 15 or 35 days. Therefore, another set of images during these intervals would have helped to identify which changes occurred almost immediately and which developed over time. Nevertheless, the images provided far better results than initially expected and served as an excellent supplementary source of information for understanding surface changes. These insights were missing in previous related research (Neumann, 2021).

Unfortunately, the µ-CT scans of the samples did not provide the expected level of detail. With a resolution of only 38 µm per voxel, the scans were considerably less detailed than the high-resolution optical images and, consequently, offered limited new insights. Most surface changes were more easily observed in the high-resolution optical images. A µ-CT with higher resolution, similar to the one used in previous work (Neumann, 2021), might have produced better results. However, no such scanner was available that could accommodate the size of the rock samples used in the climate chamber. As a result, the evaluation of the µ-CT scans was mostly restricted to confirming changes already identified in the high-resolution optical images.

All other methods employed during the experiment delivered results with the expected quality without any significant issues arising during the measurements. It would have been particularly interesting to collect samples of the artificial rainwater during the initial simulated weathering events, during which rapid changes were observed in most of the samples. Analysing the element concentrations in the water at the start of the experiment, and comparing them with those from the artificial rainwater samples collected toward the end, could have provided valuable insights into whether the element concentrations in the used artificial rainwater were initially higher.

Weathering acceleration

The simulated weathering was accelerated by a factor of six, allowing the simulation of six daily cycles within a 24-hour period. This acceleration was chosen to simulate a sufficiently long timeframe to observe significant changes using the applied analytical methods on both the rock samples and the glass dosimeters. Accelerated weathering experiments often involve conditions that deviate significantly from natural environments, such as setting pollutant concentrations far higher than those observed in nature (Unterwurzacher & Mirwald, 2008). For example, studies on rock varnish alteration on Murujuga subjected samples to unrealistic pollutant levels over short periods or immersed parts of the varnish in aqueous solutions with varying pollutants and pH values to examine alterations under different conditions (Lau et al., 2007; Ramanaidou et al., 2017).

In studies involving other rocks unrelated to Murujuga, more parameters such as solar radiation, temperature fluctuations, and rainfall were simulated to create more realistic conditions, although the time component was still extremely accelerated (Labus & Bochen, 2012). As not all chemical and physical processes can be accelerated to the same extend, excessively high acceleration rates can yield unrealistic results, often leading to calculated weathering rates that exceed those observed under natural conditions (Crewdson, 2008; Sitzia et al., 2021). Therefore, it was critical to choose an acceleration rate that produced measurable changes over the experiment's duration (equivalent to 12 months in real time) without being too extreme, which could potentially yield unrealistic results.

Some studies, for instance, simulated daily cycles within only 40 minutes (Sitzia et al., 2021), a rate that would have approached the limits of the climate chamber's capabilities. In this study, a sixfold acceleration was chosen as it balanced the chamber's capabilities with the need for realistic conditions. This rate allowed the simulation of months and years in multiples of 24 hours and limited maximum heating and cooling rates to approximately 9 °C per hour, which is reasonably close to observed natural rates. Furthermore, this setup allowed the simulation of solar radiation exposure on Murujuga without causing unrealistically high temperatures on the sample surfaces. The pH range was selected to reflect conditions already observed on Murujuga, ensuring that pH-related weathering effects remained realistic. However, to explore potential scenarios at lower pH levels, irrigation experiments included pH levels as low as 3.

Consequently, the results are expected to approximate naturally occurring varnish degradation under controlled, accelerated conditions in a climate chamber. It is acknowledged, however, that the chemical and physical weathering processes differ from those in nature due to the acceleration, which must be considered when interpreting the data. For example, the high amount of simulated rainfall over short periods may have influenced surface processes differently compared to natural conditions. Extreme rainfall events are hypothesised to reset surface acidity by washing away deposited pollutants (MacLeod & Fish, 2021). In this case, the simulated conditions might have resulted in less acidic surfaces than those in nature, potentially reducing degradation rates. On the other hand, factors such as the higher intensity of simulated solar radiation or the faster heating and cooling cycles might have introduced greater physical stress, potentially accelerating degradation compared to natural conditions.

When combined with the glass dosimeters from Fraunhofer ISC, the simulated weathering results can potentially be compared to natural conditions on Murujuga. This would require a future study placing glass dosimeters of the same compositions on Murujuga to compare the changes observed in natural conditions with those from the climate chamber experiment. Such a comparison could also enable extrapolation of the changes observed in artificially weathered rock samples to natural conditions. To achieve this, it was critical to keep all simulated parameters as close as possible to the conditions measured on Murujuga, with only the time component being accelerated.

However, the climate chamber's limitations meant it was not possible to simulate atmospheric conditions, as well as dust and pollutant deposition on rock surfaces in a dry state, which naturally occurs on Murujuga (MacLeod & Fish, 2021; Smith et al., 2022). Consequently, pollutant components and the surface pH of the rocks were influenced solely by the simulated rainfall events. During the simulated dry season, when no rainfall events occurred, pollutants were not introduced into the system, resulting in identical weathering conditions for both sample groups. This may have reduced the acceleration of weathering in samples subjected to acidic conditions. The lower rate of colour change observed in the rocks during the simulated dry season, compared to the high rate of colour change during the simulated wet season, supports this interpretation.

4.3.2 Results

4.3.2.1 Weathering of the varnish

Colour, chemical, and morphological changes during the initial period
Due to the low margin of error and the high sensitivity of the colour measurements, it was possible to reliably track the development of changes on the weathered samples. It was expected that the colour would change relatively quickly during the initial irrigation experiments, which is why the first measurements were conducted after 5 days of weathering, followed by a second set of measurements after another 10 days. A rapid change in colour over a short period at the beginning of an artificial weathering experiment had also been observed in a previous study (Neumann et al., 2022). This rapid colour change is believed to result mainly from secondary minerals on the sample surfaces that were washed away during the initial simulated rainfall events. For example, fine-grained white mineral grains, identified as albite, were visible on one granophyre sample in high-resolution optical images taken before the experiment began, but these grains had nearly entirely disappeared in images captured after 180 days (Fig. 4.13c).

It must be noted that all samples had been in contact with water during cutting, as the used saw and drill were water-cooled. Following cutting, all samples were rinsed with demineralised water to remove the residual mixture of water and sawdust from the surfaces. This implies that (1) changes observed during the first two or three measurement steps could not have been caused by residues from the sawing and drilling process, as they had already been removed and (2) the changes during these initial time periods were due to material that was either very loose or highly sensitive to dissolution. Such material was washed away or dissolved during the simulated rainfall but had not been entirely removed during the sawing and rinsing processes. Here, it has to be noted, that the duration of the simulated rainfall was significantly longer as the rinsing process and the amount of water that was in contact with the samples therefore was much higher. It is possible that some secondary minerals were already washed away during the rinsing of the samples, as well as dust on the surface, before the start of the experiment and before the initial measurements.

The extent of the initial colour change across the samples after just 15 days was relatively high and varied significantly depending on the individual sample, with values ranging from a ΔE of only 0.68 to 3.48. The highest change was measured on a granophyre sample weathered under acidic conditions (SR1), where the fine-grained white albite aggregates had been visible prior to the start of the experiment. The mean ΔE values of the gabbro and granophyre samples weathered under acidic conditions were slightly higher after 15 days compared to those weathered under neutral conditions (Fig. 4.6). However, a comparison of sample pairs cut from the same rock pieces revealed that, for some pairs, the samples weathered under acidic conditions exhibited higher ΔE values, whereas for other pairs, the opposite was observed.

The only additional data collected after this initial 15-day period were p-XRF measurements. Significant changes occurred during this period, and for some elements, changes occurred at a similarly rapid rate as the colour changes. The elements S, P, Ca, and K exhibited fast changes for most of the sample groups (Figs. 4.16 & 4.17). This suggests that the material washed away, dissolved, or altered during the early stages was enriched in these four elements relative to the rest of the surface. For both rock types, various correlations were observed between the decreases in these four elements (Fig. 4.32). This suggests that the elements might have been bound within the same minerals at the surface, leading to a simultaneous decrease in their concentrations when this material was dissolved or washed away. However, since no phases containing all four of these elements were identified in the mineral composition of the varnish (Chapter 3.1.3.2), this explanation appears unlikely for all elements, which is further supported by the differing ratios of elemental changes depending on the sample group and rock type.

For the granophyre sample SR1, weathered under acidic conditions, where most of the albite grains disappeared during the first half of the experiment, the SO_3 content on the surface decreased by -46.74 ± 0.03 % after the first 15 days of weathering, and the CaO content decreased by -12.95 ± 0.02 %. Given the high amount of emitted SO_x on Murujuga (Department of the Environment and Energy, 2023), it seems likely that a portion of the S content on the surface was bound in mineral phases that were not part of the rock varnish but instead originated from the deposition of emitted SO_x (Garland, 1977; Smith et al., 2022). The correlation between the relative changes of the SO_3 and CaO, as well as the SO_3 and K_2O (Fig. 4.32) content measured on the sample surfaces suggests that some of the deposited SO_x has been bound on the surface as small gypsum ($CaSO_4 \bullet 2H_2O$) or arcanite (K_2SO_4) crystals, which were subsequently washed away or dissolved by the simulated rainfall during the first days of weathering. As no Na could be measured with the used p-XRF the content on the surface is unknown, but the EDX measurements proved that Na can be found on the varnish and is enriched in the outermost layers of the varnish (Fig. A4). Therefore it is also possible that the S was bound in minerals that contain Na like glauberite ($Na_2Ca(SO_4)_2$) or thénaridte (Na_2SO_4). Nevertheless, on the surface of sample SR1 only albite crystals were identified by Raman spectroscopy in addition to the components found on all samples (Figs. A1 & A2) and no gypsum or other S-bearing phases were found. The same goes for the other analysed samples.

Taking into account the overall relatively low SO_3 content on the samples with only 0.45 wt. % at the beginning of the experiment for sample SR1, these S-bearing phases were likely too small to be visible in the high-resolution optical images or under the optical microscope of the used Raman spectrometer and were easily washed away or dissolved. It is also possible that the S was bound together with organic material that was subsequently washed away. As no S-bearing phases could be identified by any of the used techniques it remains unknown how parts of the S were bound on the surface. The S remaining after the initial decrease is believed to have been bound in the varnish layers, where the outermost parts were slightly enriched in S, as element distribution maps show (Chapter 3.1.3.2), and were therefore harder to dissolve or wash away. This explains the rapid initial decrease in SO_3 concentrations, followed by a much slower decrease over the remainder of the experiment. It was also observed that the total reduction of SO_3 on the surface varied between 0.02 and 0.33 wt. %, with most values clustering around 0.1 wt. %, even on the samples with the highest overall SO_3 contents. Sample SR1 showed the highest absolute change in SO_3 content.

It is known that bird droppings can increase the acidity on the surface of rocks and it has been reported that bird droppings on Murujuga rocks could also play a role in the alteration of the rock surface (Bednarik, 1979, 2002; Duffy et al., 2017). These droppings are known to contain high amounts of P (Duffy et al., 2017), which is brought onto the rock surfaces and can later infiltrate in the varnish along cracks and the porosity, as shown by the elemental distribution maps of some parts of the rock varnish (Chapter 3.1.3.2). It is therefore possible that small amounts of remaining bird droppings were present on the surface of the samples before the start of the weathering experiment. These remains were likely washed away at the beginning of the experiment, explaining the rapid initial decrease in P_2O_5 content on some samples, while the P bound in the varnish layers was more stable, explaining the initial decrease followed by slower changes, as for the S content.

Parts of the Ca on the surface that were not bound in gypsum or other crystals, if there have been some, may have been bound in calcite crystals, which are known to be found on the surfaces of Murujuga rocks (Neumann, 2021), but were also not identified on the samples used in this study. It is unlikely that the calcite was dissolved during this short period of weathering. Rather, it was likely washed away, as small calcite grains are known to withstand longer periods of artificial weathering, as shown in a previous study (Neumann, 2021).

No phases containing high amounts of K were found on the sample surfaces and the differences in the decrease of K_2O contents were considerable. The highest changes were measured on two gabbro samples weathered under acidic conditions (SA1 & SA2), as well as on a single gabbro sample weathered under neutral conditions (NA2), which were also the only samples showing a high initial decrease in K_2O concentrations. The phase or phases on the surface that contained high amounts of K, which were dissolved or washed away, leading to this rapid decrease, remain unknown.

It is suggested that extreme rainfall events wash away the phases which are deposited on the surface of the rocks on Murujuga due to the NO_x and SO_x emissions. This is believed to reset the pH of the rock surface (MacLeod & Fish, 2021). Whether this leads to a true reset of the pH on the surface, or, especially after light rainfall events, instead causes even more acidic conditions on the surface due to the mixing of acidic dust with water, creating an acidic solution, is disputed (Smith et al., 2022). Either way, the simulated rainfall during the first 15 days, which involved a total of 163 mm of simulated precipitation (equivalent to the mean rainfall in January, February & March on Murujuga), is comparable to a major rainfall event due to the high amount of precipitation in a short period of time. Therefore, it is likely that the dust, if there was some remaining after sawing and rinsing the samples, was washed away rather than remaining on the surface and mixing with the water to create more acidic surface conditions. This is supported by the significant decrease in S concentrations on the sample surfaces (Fig. 4.17a), as well as by the fact that the brief contact with water during sawing and the subsequent cleaning of the samples was not sufficient to remove all of the secondary minerals on the surface. It is possible that the aforementioned mixing of acidic dust with water occurred during the sawing and washing stages before the start of the experiment, and that this mixture partly remained on the surface after the samples dried. Unlike real conditions on Murujuga, where dust deposition occurs during dry periods, no dust deposition was simulated in the climate chamber. Therefore, S was only potentially brought onto the samples that were weathered under acidic conditions by the H_2SO_4 added to the artificial rainwater (Chapter 4.1.3.3).

Due to the lack of additional data acquired after the initial 15 days of weathering, it is not possible to determine in greater detail what exactly occurred on the sample surfaces during this period. It is also not possible to ascertain how much of the observed changes in the high-resolution optical images taken after 180 days of weathering occurred during this initial phase. However, it can be stated with certainty that the changes in other parameters were also more pronounced during the first half of the experiment, as evidenced by the weight loss of the samples and the changes observed in the high-resolution optical images (see Chapter 4.2.1.2) making it likely that the weight-loss and visible changes in the initial period have also been more pronounced than over the remainder of the weathering experiment.

Subsequent changes as weathering progresses

After the initial phase with rapid surface changes discussed earlier, the further colour changes measured on the rock samples were relatively small, except for the gabbro samples weathered under neutral conditions (Fig. 4.6). The changes in the surface chemistry, which were also measured continuously, did not stagnate for all measured elements as the colour changes did, and continuous changes were recorded for some elements, not just for the sample group where colour changes were measured continuously (Figs. 4.16 & 4.17). This indicates that changes were still occurring on the surface of all samples, regardless of the rock type or weathering conditions. The observed changes in the high-resolution optical images, as well as the weight loss observed in the second half of the experiment, further support this (see Chapter 4.2.1.2). Notably, the MnO concentrations measured on the gabbro samples, which increased rapidly between 60 and 120 days of weathering, as well as the observed decrease in Fe_2O_3 content on the granophyre samples, were conspicuous (Fig. 4.16). The Ca, K, P, and S contents of all samples continued to decrease throughout the experiment, though at a lower rate than at the beginning. Together with the ongoing changes observed in the high-resolution optical images, this suggests the continuous alteration of the surface, which did not result in a significant colour change for most of the samples. This was also confirmed when analysing the step-to-step changes in colour, where the measured L*, a*, and b* values were compared with the values from the previous measurement cycle, rather than the initial values, to calculate the colour change ΔE (Tab. A2). In some cases, the changes between two measurement periods were quite large, as described in Chapter 4.2.1.1, especially for two samples weathered under neutral conditions, one made up of gabbro and one made up of granophyre (NA2 & NR2), with low absolute ΔE values at the end of the experiment.

It can therefore be concluded that all samples, regardless of rock type or weathering conditions, continued to change continuously throughout the entire experiment and not only during the first two to three time steps, as the comparison of the mean measured ΔE values of the different sample groups would suggest. It is also clear that the changes varied between the different sample groups, and therefore between the weathering conditions, as shown by the colour measurements of the gabbro samples weathered under acidic conditions, the p-XRF data, and the observed changes in the high-resolution optical images.

Over the wet season, simulated between 60 and 90 days of weathering, the ΔE of al sample groups increased more rapidly compared to the dry season before (days 30 to 60), except for the gabbro samples weathered under neutral conditions. This increase in ΔE values was followed by a decrease after 120 days (Fig. 4.6). The period between 60 and 90 days was the only period that exclusively simulated the wet season, while the period following was the only period that exclusively simulated the dry season. This suggests that the colour change was more pronounced during the rainy season, while during the dry season the colour change diminished, making the difference in comparison to the initial colour smaller again. This is likely due to the fact that, during the rainy season, pollutants were introduced into the system through the artificial rainwater, leading to increased alteration during this period. It is also possible that some secondary minerals or other material highly sensitive to alteration remained on some of the samples, which were not entirely washed away during the first wet season, causing another relatively fast increase in ΔE values at the start of the second rainy season. The observed slower colour change at the end of the first wet season, even if some secondary minerals were left, might be due to the smaller total precipitation in the second half of the wet season compared to the first half (Tab. 1.2). A slight decrease in ΔE values was also observed during the first dry season, between 35 and 60 days of weathering, which is consistent with the observations made during the second dry season (Fig. 4.6). The reason why the colours of the samples changed in a way during the dry season that they became less different from the initial measurements, as shown by the decreasing ΔE, is not known. The simultaneously measured changes in the elemental surface compositions showed no similar trend depending on the wet and dry seasons for most sample groups and elements and, unfortunately, there were no additional measurements at these time points that could provide further insights into the processes that occurred.

One of the main concerns regarding the potential endangerment of the petroglyphs is that surface alteration leads to changes in the colour of the varnish, which becomes progressively brighter over time and that this may be accelerated by anthropogenic pollution. This would result in a reduced contrast between the dark varnish layer and the underlying brighter layer exposed when petroglyphs are carved into the rock varnish (Bednarik, 2002; Mulvaney, 2009; Black et al., 2017b). It is known that the darkest parts of the varnish contain more Mn (see Chapter 3.1.3.2) and that the dissolution of Mn, triggered by changing pH values on the surface, can cause a colour change in the varnish (MacLeod & Fish, 2021). On all samples weathered in the climate chamber, the brightness, measured by the ΔL^* value of the measured colour, decreased over the course of the experiment. This darkening, which is visible in the colours of the samples due to the high ΔL^* values (Fig. 4.8), stands in contrast to the suspected "bleaching" (Bednarik, 2002, p. 36) of the rock samples due to weathering effects. The decrease in brightness primarily occurred during the first 15 to 35 days of weathering and may therefore be attributed to the initial changes discussed earlier. Only on the gabbro samples weathered under acidic conditions did the brightness continue to decrease significantly throughout the entire experiment.

Aside from the colour change, which occurred throughout most of the experiment, the chemical changes observed vary significantly and the overall complex trends are difficult to interpret. These variations were largely due to the different developments observed across the sample groups, depending on the elements analysed. While the trends in colour change across the four sample groups were found to largely depend on the weathering conditions, the trends in chemical compositions were more dependent on the rock type hosting the varnish for most of the measured elements.

As described above, the concentrations of Ca, K, S, and P on the sample surfaces changed continuously throughout the experiment. With the exception of the K content, where the group of gabbro samples weathered under acidic conditions stands out, as it is the case for the measured colour changes. The trends for the other three elements are similar across all groups, showing a constant decrease with varying intensities. While the observed changes in these elements are noteworthy and potential explanations have already been discussed, the developments in the concentrations of the primary components of rock varnish, Al, Fe, and Mn, are of greater interest (Chapter 1.4).

The Al content exhibited only small changes, however, given the high initial Al concentrations on the samples, even these small relative changes corresponded to a relatively large total amount. In this context, the group of gabbro samples once again stood out, as it did for the trends in the Mn content. For both Al and Mn, the observed changes were positive throughout the experiment. Combined with the colour changes, surface alterations, and weight loss, this suggests that these samples experienced the most significant transformations. Additionally, since no Al or Mn were introduced into the system or onto the sample surfaces, the increases cannot be attributed to deposition of new material, but are instead likely due to the uncovering of underlying layers containing higher concentrations of these elements compared to the outermost layers measured at the start of the experiment. A similar trend was observed for the gabbro samples weathered under neutral conditions. Here too, the Mn and Al content increased over the course of the experiment and also if taking into account the lower ΔE values and less observed changes on most of the samples in the high-resolution optical images, as well as less weight loss compared to the samples weathered under acidic conditions, this positive change can only be explained by the uncovering of underlying material with higher Al and Mn contents.

In contrast, no significant increases in Mn or Al content were observed for the granophyre samples. Instead, the Si concentrations in both granophyre groups increased slightly over the course of the experiment. As also no Si was introduced into the system, this suggests that material with a higher Si content was uncovered as the overlying layers were dissolved or washed away, or the decreased content of other elements led to a relative increase of the measured Si content.

A comparison of the relative changes in element concentrations at the end of the experiment revealed correlations between the changes in Mn and Al, as well as between Mn and K (Fig. 4.31). These correlations, along with the observed trends in the element concentrations, suggest that material containing K and Si was dissolved while underlying layers, richer in Mn and Al, were exposed. Paired with the observed colour changes, it can be deduced that this underlying material was darker, which is supported by some of the changes visible in the high-resolution optical images, particularly for samples with the greatest increases in Mn concentrations, which were gabbro samples weathered under different conditions (Figs. 4.10 & 4.11; SA1, SA2 & NA2).

Observed changes on the individual samples

Due to the varying types of varnish on the sample surfaces and the significant differences between the samples, even within the same sample groups, it was necessary to study the characteristics of samples with similar surfaces and types of varnish, which primarily were the sample pairs cut out of the same pieces of rock. This approach aims to understand the alteration processes on the different surfaces and the resulting variability within the same sample groups, as observed with all analytical methods applied. The PCA demonstrated that most samples were better categorised by the rock pieces from which they were cut and the rock type, rather than by the weathering conditions (Fig. 4.35). Consequently, comparing the sample pairs originating from the same rock pieces proved highly valuable.

The gabbro samples SA1, SA2, NA1, and NA2 were all cut from the same piece of rock. Sample NA1 weathered under neutral conditions, stood out due to its distinct surface structure and colour, despite originating from the same piece of gabbro (see

Chapter 3.1.1). Consequently, its composition and characteristics, as well as the observed changes, differed significantly from those of the other three samples as shown in Tab. 4.9. This again highlights the pronounced inhomogeneity of rock surfaces on Murujuga. The other three samples in this group were distinguishable from the remaining rock samples by various parameters (Tab. 4.9).

Although gabbro samples SA1, SA2, and NA2 shared many similar conditions, and the observed changes were comparable for most parameters, the measured colour change clearly distinguished the sample weathered under neutral conditions (NA2) from the two samples weathered under acidic conditions. Step-to-step analysis revealed that sample NA2 experienced consistent colour changes, which, at certain intervals, were even larger than those of samples SA1 and SA2 (Tab. A2). However, the overall colour change for sample NA2 remained less pronounced when compared to its initial measurements. For most rock samples, the majority of the colour change ΔE resulted from variations in brightness, expressed as ΔL^*. In the case of gabbro sample NA2, the change in brightness ΔL^* was only -0.58 at the end of the experiment, which is a minor value compared to other samples. Conversely, the changes in the other two colour components, Δa^* and Δb^*, fell within a range comparable to other rock samples. High-resolution optical images revealed that, on all of the three samples, the brighter surface areas were partly removed, exposing darker regions beneath. The absence of significant darkening on sample NA2 can only be explained by a concurrent brightening of the sample's brighter areas during the weathering experiment, effectively compensating for the darker regions that were uncovered.

The surface of the three samples was notably uneven and porous compared to the other gabbro samples (see Chapter 3.1.1). Beneath the brighter uppermost layer of varnish, a more compact and darker layer was visible (Figs. 4.10 & 4.11). Under high magnification, it became evident that both surface layers were not composed of a single phase but rather consisted of the same distinct phases. These phases, varying in colour from darker to lighter, were present in different proportions, resulting in an overall darker or lighter appearance (Fig. A3) and varying densities of colour. The darker, nearly black regions of the varnish were found to contain higher concentrations of Mn, predominantly in the form of birnessite, whereas the lighter regions contained less Mn, with their colour primarily attributed to hematite.

The observed changes suggest that, on the three gabbro samples weathered under neutral (NA2) and acidic (SA1 & SA2) conditions, the brighter, more porous surface areas, composed mainly of hematite and kaolinite, were dissolved and / or washed away during the experiment. These areas, due to their larger surface area because of their high porosity, were more susceptible to alteration. Additionally loose or loosened particles were likely washed away during the experiment as a result of physical weathering effects induced by temperature and humidity fluctuations combined with rapid heating during simulated solar radiation. The presence of chemical weathering leading to the dissolution of hematite was supported by the

Table 4.9: Summary of the conspicuous changes on the different rock sample pairs.

	Samples		**Colour change (ΔE)**	**Chemical changes & composition**	**Morphological changes**	**Weight loss**	**Element concentrations in rainwater samples**	**Comments**
	Acidic	**Neutral**						
Gabbro		**NA1***	1.52	Low MnO content compared to other samples from the same piece	Few changes in small areas < 1 mm.	low	No conspicuous results	Significantly different surface compared to other samples from the same piece
	SA1* **SA2**	**NA2**	NA2 $= 0.70$, SA1 & SA2 around 5	Strong K_2O, SO_3, and CaO decrease, Al_2O_3 and MnO increase	Removal of brown to red varnish on large areas, uncovering of black varnish underneath	very high on all samples	High Fe and Mg content	All samples had a very uneven and porous surface and displayed the overall largest changes.
	SA3	**NA3**	Around 1.2 on both	Relatively high MnO content	Chipped off piece in the middle of SA3	low	No conspicuous results	No significant differences between acidic and neutral sample, organic material on the surface
Granophyre	**SR1**	**NR1**	Very high, around 4	Strong CaO and SO_3 decrease on SR1, high MgO loss on both	Albite grains disappeared on sample SR1, uncovering of black varnish as on some gabbro samples	high on NR1, low on SR1	No conspicuous results	Very inhomogeneous and porous varnish with different colours ranging from orange to black
	SR2	**NR3**	Around 1 on both	High Sr, Cr, Fe_2O_3, and P_2O_5 content, nearly no MnO	Material chipped off on both pieces. Lepidocrocite removed from NR3	relatively high	No conspicuous results	Very dense and even surface, metallic lustre. No larger changes observed but high weight loss
	SR3	**NR2**	NR2 $= 0.47$, SR3 $= 1.62$	Highest MnO content with small increase over time	Only material chipped off on both pieces	low	High Si and Mn content	No black varnish areas but high MnO content

*Samples NA1, NA2, SA1 & SA2 were cut from the same piece of rock but sample NA1 differed significantly and was therefore no included with the other samples in the same row high Fe content in the artificial rainwater samples that had been in contact with these three gabbro samples. The underlying darker layers, which were subsequently exposed, contained more Mn-oxides, mainly birnessite, reflected by an increased relative Mn content at the surface. It can also be deduced that these darker layers contained more kaolinite, explaining the higher Al_2O_3 contents. As the SiO_2 content was not increased this indicates that the removed layers contained some excess SiO_2 that was not bound in kaolinite.

The lower K_2O and significantly decreased SO_3 and CaO contents of the varnish surfaces indicate that the removed brighter layer contained higher concentrations of these components compared to the underlying darker layer, or secondary minerals on top of the varnish layers were washed away and were mostly composed of this elements. The relatively low colour change observed in gabbro sample NA2, weathered under neutral conditions, can be attributed to several factors. Firstly, the overall weight loss was slightly smaller than in the other samples and the high-resolution optical images qualitatively revealed less extensive changes. Additionally, smaller changes in the MnO and K_2O surface concentrations suggest that the overall alterations were less pronounced under neutral conditions. The comparable increase of the Al_2O_3 content on sample NA2, as observed in the samples SA1 and SA2, weathered under acidic conditions, indicates that more kaolinite was exposed on the surface. The bright colour of kaolinite may have compensated the darker colour of the Mn-oxide-rich areas, contributing to the smaller overall colour change. The reason for the relatively high Mg concentrations in the artificial rainwater samples remains unclear, as no phases containing significant amounts of Mg were identified on the surface, and the observed changes in MgO concentrations on the samples varied significantly.

The observed correlations between the changes in the Fe-Mn ratio, weight loss, and colour change, as described in Chapter 4.2.5 (Fig. 4.33), were primarily driven by the aforementioned gabbro samples. In these samples, the Fe-Mn ratio decreased due to the exposure of Mn-rich layers, which became visible as the uppermost layer of the varnish was removed. This removal not only reduced the weight but also has contributed to the colour changes observed in most of the samples over time.

The third pair of gabbro samples exhibited relatively small changes over the course of the experiment (Tab. 4.9). The overall lower degree of change in these samples can be attributed to their less porous, darker surfaces, characterised by relatively high MnO content, indicating a greater proportion of Mn-oxides, mainly birnessite. This composition appeared to render the samples less susceptible to chemical alteration. Notably, in the sample weathered under acidic conditions, a piece of rock chipped off from the middle of the sample and some parts of the samples looked like material had chipped off prior to the start of the weathering experiment (Fig. 3.1). This suggests that the harder, denser surface may be prone to physical weathering effects, where larger sections of the surface are more likely to flake off under physical stress in combination with chemical weathering making areas of the samples more vulnerable (e.g. along cracks).

Since all three pairs of granophyre samples were cut from different pieces of rock, the differences between these pairs were more pronounced than those observed among the gabbro samples. One pair of granophyre samples (NR3 & SR2) stood out the most due to several parameters and especially the chemical composition of the varnish (Tab. 4.9). The slightly higher colour change in the sample weathered under neutral conditions (NR3) could be explained by the presence of surface patches where a lepidocrocite layer was observed. This layer was largely dissolved over the course of the weathering experiment (Fig. 4.12). Both samples featured a dense and even surface with a metallic lustre and brown appearance, believed to consist primarily of hematite. In small areas, a brighter and more orange varnish with a less dense and metallic lustre was identified, likely containing a mixture of hematite and kaolinite.

Due to their dense structure, which reduces pore space and therefore reduces the surface area compared to other samples, both samples were expected to be relatively resistant to chemical weathering effects. This resistance likely accounts for the minor surface changes observed, regardless of the weathering conditions. However, it was noticeable that parts of both samples chipped off, a phenomenon also observed on gabbro samples with dense and compact surface varnish layers, as aforementioned. The percentage changes and element concentrations in the rainwater samples that interacted with these granophyre samples were comparably low, further supporting the conclusion that these samples were relatively resistant to the applied weathering conditions. The primary evidence of weathering was the removal of most of the lepidocrocite layer during the experiment, as observed in the high-resolution optical images (Fig. 4.12). Due to the high overall Fe_2O_3 content in these samples, the removal of the relatively small amounts of lepidocrocite was not detectable in the measured Fe_2O_3 concentration changes on the surface of sample NR3. It is important to note that lepidocrocite removal occurred under neutral weathering conditions at pH 7. However, no lepidocrocite was detected on any of the samples weathered under acidic conditions, precluding a comparison of the weathering effects on lepidocrocite under different conditions.

The second pair of granophyre samples that stood out due to their high colour change were samples NR1 and SR1, weathered under different conditions (Tab. 4.9). Most of the colour change occurred during the first 35 days of weathering, after which both samples stabilised at a ΔE of around 3.7, with minimal variation throughout the rest of the experiment. This trend was also observed in most other rock samples, as aforementioned. Both samples had highly uneven and porous surfaces with some larger holes visible with the naked eye. Notably, they were the only samples on which orange, red, and black varnish was found. The orange varnish, in particular, displayed very fine structures.

Although the uncovering of darker material, containing more birnessite, was observed on these samples, there was no significant change in the measured MnO content on the surface, unlike for the gabbro samples as discussed earlier. The MnO content was relatively high on both samples in comparison to the other rock samples. However, the p-XRF measurements were taken only at a single spot in the centre of each sample. Unlike on the gabbro samples described earlier, the observed changes on these samples did not occur in the area where the p-XRF measurements were performed, which likely explains why the relative surface changes were not reflected in the p-XRF results. This limitation, measuring only a small area of the sample, highlights a common issue with p-XRF measurements that were limited to a small spot tat cannot be considered representative of the entire surface of the varnish, as discussed earlier.

The differences between NR1 and SR1 were more pronounced than those observed in other sample pairs (Tab. 4.9). It was surprising that the measured weight loss of the acidic sample remained low despite strong visible changes in the high-resolution optical images, including the loss of nearly all of the white, fine-grained phase that was found to be mainly albite. This could be explained by the limited presence of this material, as it appeared only in a few spots. Furthermore, the observed changes in the red and orange varnish were more widespread on the sample weathered under neutral conditions, potentially leading to greater weight loss during the experiment. This suggests that (1) the amount of material washed away or dissolved was larger in the neutral sample, and (2) the orange varnish had different properties in the two samples. Otherwise, it would be difficult to explain why the orange material dissolved at pH 7 but not at pH 5, especially as the removal of orange parts of the varnish was observed for some of the gabbro samples at pH 5.

The third pair of granophyre samples (NR2 & SR3) exhibited a red to brown surface and was distinguished by the highest measured MnO contents on the surfaces at the beginning of the experiment, despite the absence of large dark or black areas typically associated with higher birnessite concentrations and therefore high MnO contents. Additionally, the Si and Mn content in the rainwater samples in contact with these rocks was notably high compared to other samples (Tab. 4.6). The visible and colour changes on both samples were relatively minor. Only a small amount of material chipped off on both samples, and no substantial surface changes were observed across larger areas (Tab. 4.9).

Despite the high Mn concentrations in the water samples, the MnO content on the rock surfaces also increased over time, consistent with the trends observed in all other rock samples. Other measured parameters did not display any particularly notable or distinctive trends for these samples. What is particularly intriguing is that these samples had such high MnO contents on their surfaces despite the absence of visibly large black varnish areas. This suggests that Mn can also be incorporated into other types of varnish, broadening the understanding of how Mn may be distributed and bound in surface coatings. The increase of the measured MnO content on the surface in combination with the high Mn content in the water samples, again suggests that material was dissolved or washed away uncovering layers that contained more Mn. In contrast to other samples, this process was not identifiable in the high-resolution optical images of these two samples.

Change of the microbial community composition over time

The microbial communities inhabiting rock varnishes have been scarcely studied, particularly in the context of how varying environmental conditions, such as pH, influence their dynamics. This study aimed to fill that gap by investigating microbial communities associated with two distinct rock types - gabbro and granophyre - under different pH treatments. It was found that both rock types exhibited significant shifts in microbial composition under acidic (pH 5) versus neutral (pH 7) conditions, highlighting the critical role of pH in shaping microbial dynamics and biogeochemical processes.

The gabbro samples exhibited greater microbial diversity and more pronounced shifts under acidic treatments, with significant increases in genera such as *Rubrobacter* and *Geodermatophilus*, which are known for their resilience to low pH and oxidative stress. These genera are often associated with the cycling of metals like Fe and Mn, a process crucial for rock varnish formation. The ability of these taxa to facilitate the dissolution of primary minerals and promote biomineralization aligns with findings from other studies on rock varnish, such as Krinsley et al. (2017), which identified similar microbial species involved in Mn-Fe enrichment in rock varnish samples. This reinforces the notion that acidophilic microbes play a key role in the biogeochemical cycling of Fe and Mn, facilitating the deposition of these metals in the varnish layer. However, *Geodermatophilus*, for example, has been reported in other studies as Mn(II)-oxidizing bacterial detected in desert rock varnish (Hungate et al., 1987; Carmichael et al., 2015). These findings parallel observations in uranium-rich environments, where similar taxa contribute to mineral transformations under extreme conditions (Sanyal et al., 2024).

Deinococcus, detected in this study, is well-known for its remarkable resilience to extreme environmental conditions, including desiccation, radiation, and oxidative stress (Daly, 2009). Its presence under acidic treatments in gabbro samples underscores its adaptive capabilities and potential role in biogeochemical cycling, particularly Mn oxidation. As highlighted in previous studies, *Deinococcus spp.* are not only involved in oxidative stress resistance, but also actively participate in Mn cycling by promoting the oxidation of Mn(II) to Mn(IV), a process critical for the stabilization of rock surfaces and the formation of Mn-oxides (Tebo et al., 2005; Sun et al., 2010; Carmichael et al., 2015; Santos et al., 2019). These capabilities align with findings from environmental studies that demonstrate the involvement of *Deinococcus* in mineral transformation and biomineralization under stress conditions, further emphasizing its ecological significance in rock varnish ecosystems.

On the other hand, the granophyre varnish showed a more stable microbial community across all treatments. The dominance of *Proteobacteria* and *Actinobacteriota* in these samples is consistent with their known resilience in nutrient-limited environments and their role in organic matter degradation and nutrient cycling. The microbial stability observed in the granophyre samples could reflect its more resistant surface composition, which was not as easily altered by the simulated weathering as the gabbro sample surfaces. The presence of these core taxa suggests that microbial ecosystems on the granophyre samples may be less impacted by environmental changes, allowing these microbes to maintain their roles in fundamental processes such as nitrogen cycling and organic carbon decomposition.

In both rock types, rare but potentially significant taxa were observed. While not dominant in terms of abundance, microbes such as *Firmicutes* and *Chloroflexi*, detected in the granophyre samples weathered under neutral conditions, could play important roles in anaerobic processes. These genera have been implicated in anaerobic photosynthesis and organic matter degradation, processes that contribute to altering local microenvironments, such as pH and oxygen gradients. This, in turn, could facilitate the precipitation of minerals, including Mn- and Fe-oxides, thus playing a key role in the stabilization of rock surfaces.

The microbial dynamics observed in this study underscore the complex interplay between microbial taxa, environmental conditions, and varnish, as well as host rock composition. While abundant genera, such as *Rubrobacter* and *Geodermatophilus*, are likely the primary drivers of metal cycling and biomineralization under acidic conditions, the presence of rare taxa is not without significance. These microorganisms, although not dominant in abundance, contribute unique metabolic functions that can alter microenvironments and drive critical biogeochemical cycles. It is known that even low-abundance microbes can play essential roles in rock biomineralization and metal oxidation processes (Karačić et al., 2022).

Environmental factors such as pH and oxygen availability were found to be key drivers of microbial community composition and functioning. Acidic conditions not only reduce microbial diversity, but also enriched the activity of stress-resistant and metal-cycling taxa, leading to enhanced biomineralization processes. In contrast, neutral conditions supported a more diverse microbial community with a broader range of metabolic capabilities. Genera such as *Cyanobacteria* and *Bacillus*, which were more abundant under neutral conditions, are known for their roles in primary production and organic matter decomposition. However, some *Bacillus* strains are capable of Mn(II) oxidation (Carmichael et al., 2015). Their increased presence indicates that neutral conditions promote key metabolic activities such as photosynthesis, organic carbon cycling, and potentially Mn oxidation, which collectively contribute to stabilizing microbial communities and influencing the chemical properties of rock surfaces.

Observed correlations between measured parameters

The statistical analysis of the changes in elemental concentrations across all samples at the end of the experiment revealed various correlations (Fig. 4.31). While previous studies identified a positive correlation between changes in Al_2O_3 and SiO_2 (Neumann, 2021), the data from this study suggested a negative correlation. Both elements in the varnish are primarily associated with kaolinite, which would typically lead to a positive correlation, as the dissolution of kaolinite would lead to a proportional loss of both elements. In this study, the increasing Al_2O_3 content on the sample surfaces might be explained by an overproportional loss of other components, aside from kaolinite, caused by weathering. This would result in a relatively elevated Al_2O_3 content on the surface. The absence of a corresponding increase in SiO_2 concentration suggests an overproportional loss of phases containing predominantly SiO_2, with little to no Al_2O_3, as for example small quartz crystals.

The positive correlation between higher Al_2O_3 and MnO contents may be attributed to uncovered areas containing more birnessite and kaolinite compared to the originally measured surface, as discussed earlier for certain gabbro samples with significant surface changes (SA1, SA2 & NA2). In these cases, the correlation was largely driven by these three samples, which exhibited substantial positive changes in the concentrations of both elements. Conversely, the negative correlations observed between MnO and K_2O, as well as between Ba and Al_2O_3, might indicate that minerals in the uncovered areas, which were richer in MnO and Al_2O_3, contained lower amounts of Ba and K_2O than the material that was dissolved or washed away.

The residue collected from the two used glass tanks after the weathering experiment showed statistically indistinguishable chemical compositions. However, the colours of the residues differed significantly. The residues confirmed material loss due to physical weathering on both sides. Notably, higher levels of sulphur than those observed on the rock varnish were detected, confirming the significant sulphur loss measured using p-XRF. Furthermore, relatively high amounts of SiO_2 in the residual material, exceeding the contents measured on the rock surfaces, were conspicuous. The depletion of MnO in the residue compared to the surface composition and the relatively high Mn concentration in the artificial rainwater samples were also noteworthy. The Mn and Fe concentrations in the water samples from the neutral and acidic sides were nearly identical, while the Fe concentration in the residue was at least 20 times higher. This finding, along with the high SiO_2 content, is evidence that parts of the residue were not re-precipitated but instead consisted of small rock fragments removed by physical weathering processes. The Si, Al, and Fe in these fragments were likely bound in small quartz, kaolinite, and haematite crystals that had been washed away. On the other hand this also indicates that the Mn-bearing phases, mostly birnessite, were more likely to be dissolved than washed away, explaining the Mn depletion in the residue that is therefore believed to be mainly formed of small crystals that were washed away rather than of re-precipitated material.

Overall, it was observed that the rougher the surface of the samples was, the greater the observed changes, regardless of the rock type, were. For granophyre and gabbro samples, darker, nearly black areas of the varnish, which are rich in Mn, primarily bound as birnessite, were often found beneath lighter red to brown varnish. The lighter varnish, believed to consist mainly of haematite and kaolinite, therefore primarily contained Fe, Al, and Si, with lower Mn concentrations than the darker varnish. These observations were supported by p-XRF measurements of red, orange, and black varnish areas (Tab. 3.2). The transition to an overall darker colour in samples with the most significant colour change was largely attributed to the uncovering of darker underlying varnish layers, as observed for both the granophyre and gabbro varnish samples. However, it was not possible to determine whether the darker varnish layers were also dissolved or became thinner during the weathering experiment. This limitation was due to the insufficient resolution of the used imaging techniques, which are unable to detect changes at a nm scale. Among other factors, the gabbro samples were more likely to have a varnish with higher pore space which was less dense and therefore the gabbro samples experienced more changes compared to the granophyre samples. It was observed overall that the changes of the colour, sample surface structures, surface chemistry, and sample weight were larger in the sample groups weathered under slightly acidic conditions (pH 5) compared to the sample groups weathered under neutral conditions (pH 7). For some of the measured parameters, there were exceptions, e.g. the weight loss of one of the granophyre pairs (SR1 & NR1), where the sample weathered under neutral conditions experienced a significantly higher loss of weight.

4.3.2.2 Artificial rainwater samples

It was evident that significant amounts of Mn, Fe, and other elements were dissolved from all samples, regardless of the weathering conditions. This conclusion is further supported by the analyses of the artificial rainwater samples. The amount of dissolved material did not correlate with the initial concentrations of the corresponding elements on the sample surfaces or with the relative changes observed during the experiment. This finding suggests that the dissolved quantity is not directly dependent on the available amount of each element. Instead, it appeared to depend on factors such as how the elements were bound to the surface and the porosity of the surface, which influences the surface area in contact with the artificial rainwater. The concentrations of various elements in the collected rainwater samples varied significantly between samples.

As mentioned earlier, the highest concentrations of Fe were measured in the rainwater from gabbro samples weathered under neutral and acidic conditions, which also exhibited the most pronounced surface changes over time (SA1, SA2 & NA2). This finding indicated that the haematite of these sample surfaces continuously dissolved. Smaller amounts of Fe were detected in the rainwater from all other samples, demonstrating that haematite dissolution occurred across all samples with every rainwater exposure, even though to a much lesser extent. This trend applied to all other elements as well.

The S and P concentrations in the rainwater samples were relatively low, even though the surface concentrations of both elements decreased significantly across all samples. Most of this change occurred during the first half of the experiment, whereas water samples were only collected during the second half. It can be speculated that the S and P concentrations in the rainwater in the initial stages of the experiment, especially at the beginning, were considerably higher. The differences in the overall dissolution behaviour between the two rock types were more pronounced than the differences between the two rainwater types with pH 5 and pH 7. This was particularly evident for Fe, with mean concentrations of approximately 20 ppb in the gabbro samples and around 3 ppb in the granophyre samples. These findings indicated that, within the tested pH range, surface properties related to the rock type were more influential in the dissolution process than the rainwater pH. It is assumed that the rougher and more porous surfaces of the gabbro samples contributed to the increased dissolution of certain elements. Only Si and Mn showed notable deviations. This was mainly due to two granophyre samples (NR2 & SR3), which exhibited very high Mn and Si contents in the collected rainwater samples. These two samples also had rougher and more porous surfaces, further supporting the role of surface texture in dissolution processes.

The comparison of Mn and Fe concentrations in the rainwater samples, normalised to the Fe_2O_3 and MnO contents on the rock sample surfaces, revealed that the normalised Mn concentrations were significantly higher. This was particularly evident in the granophyre samples, where the mean normalised Mn to Fe concentration ratio was approximately 60. This finding indicated that Mn was more mobile and dissolved faster than Fe on the sample surfaces, consistent with observations made by other researchers in previous studies (Goldsmith et al., 2014; MacLeod & Fish, 2021). The solubility of different elements and the implications of these results are further examined in Chapter 5.3.2.2.

4.3.2.3 Glass dosimeters

The glass dosimeters were placed in the climate chamber to serve as reference material, enabling a comparison of the simulated weathering effects and ensuring an examination of the simulated atmospheric conditions and storage conditions of the reference samples. Three different types of glass were used, each with varying vulnerability to alteration, resulting in distinct developments in the measured ΔE_{IR} values. The two more vulnerable glass types, MI and M5, exhibited similar trends with minor differences between the two weathering conditions. In contrast, the least vulnerable type, M3, displayed minimal surface changes, with ΔE_{IR} values an order of magnitude lower than those of the other samples (see Chapter 4.2.2). The slow initial increase in ΔE_{IR}, followed by a rapid increase towards the end of the experiment, complicated the comparison and correlation of results from the MI and M5 dosimeters (see Chapter 4.2.5.2). Nevertheless, except for type M3, the glass dosimeters proved useful for evaluating differences between simulated weathering conditions and for potential long-term studies comparing simulated conditions with those on Murujuga.

For glass type M5, lower ΔE_{IR} values were consistently observed under neutral weathering conditions throughout the experiment. In contrast, the differences between the two weathering conditions were smaller for glass type MI, becoming significant only in the final measurement taken after 360 days. This indicates that the simulated acidic conditions overall caused greater alteration of the glass samples. Before the experiment, it was anticipated that one or both of the more vulnerable glass types might reach their maximum measurable ΔE_{IR} values during the experiment, leading to the inclusion of the less vulnerable M3 type. However, none of the dosimeters reached their maximum ΔE_{IR} values, indicating that the simulated alteration was less intense than expected. Additionally, the difference between the acidic and neutral conditions was smaller than anticipated, despite the use of rainwater with pH 5 and pH 7.

The glass dosimeters stored in a laboratory under controlled conditions alongside the rock reference samples were not subjected to simulated weathering and altered only to a very small extent compared to the dosimeters weathered in the climate chamber. This was expected and supports the observation that the rock reference samples also did not change significantly while stored. The dosimeters used to monitor the atmospheric conditions in the climate chamber above the experimental setup had ΔE_{IR} values in a range between the weathered dosimeters and the stored reference dosimeters (except for glass type M3), indicating that the atmosphere in the chamber contributed only to a minor proportion of the observed alteration on the samples weathered in the experimental setup under different conditions.

The results from the glass dosimeters are highly significant for future research, as they offer the potential to assess weathering conditions across various locations on Murujuga and compare these field results with simulated weathering in the climate chamber. This would allow: (1) an evaluation of environmental condition differences on Murujuga, (2) insights into whether weathering rates are influenced by proximity to industrial sites, and (3) extrapolation of the changes observed in the climate chamber experiment to real-world conditions.

To achieve these objectives, a large number of glass dosimeters would need to be deployed at various locations on Murujuga, at differing distances from industrial complexes. Additionally, dosimeters should be placed in locations with similar weather and climate conditions to Murujuga but without the potential impact of industrial pollutants. Such an approach would enable the assessment of pollutant effects on the dosimeters and, by extension, on rock surfaces under real-world conditions.

5 Irrigation experiments

5.1 Experimental approach

5.1.1 Experimental procedure

The irrigation experiments were conducted alongside the climate chamber experiment. Six rock cubes were placed in the experimental setup (see next Section) into Teflon© containers, and a seventh Teflon© container was placed in the centre as a blank sample (Fig. 5.1). The samples were irrigated with artificial rainwaters with a decreasing pH starting at 8.0 (± 0.1). For each pH, two experiments were performed: half of the rock cubes were positioned at an angle of 30°, while the other half were placed horizontally. In the second experiment, the orientations of the angled and horizontal cubes were switched. Prior to the experiments and after each set of two experiments at the same pH, all cubes were analysed with a chroma meter and p-XRF to monitor any potential changes of the colour and chemical surface composition. The artificial rainwater that was in contact with the rock varnish was collected in the Teflon© containers (Fig. 2.4), along with the blank samples of the artificial rainwater. The Teflon© containers were cleaned in the same manner as those used for the climate chamber experiment. All artificial rainwater samples were than analysed using ICP-OES. In total, 12 experiments were conducted with artificial rainwaters with a pH of 8.0, 7.0, 6.0, 5.0, 4.0, and 3.0 (± 0.1) leading to 84 water samples, including 12 blanks.

Before the experiments, the 5-litre canister containing the artificial rainwater was stored in an oven set to 32 °C to warm up the water. After taking the canister out, ambient air was pumped into the artificial rainwater to reach an equilibrium with the CO_2 in the air ensuring a constant pH value. The pH was then checked again prior to the start of irrigation. The rock cubes were also kept in the same oven to maintain a surface temperature of 30 °C at the beginning of each experiment. This temperature was consistently maintained using the installed infrared lamps and monitored with an infrared thermometer. Irrigation lasted for 10 minutes to fill up the Teflon© containers, after which the collected water was stored in cleaned plastic tubes. The artificial rainwater had a temperature between 30.3 and 31.1 °C prior to the start of the irrigation. After being pumped through the setup the water temperature decreased by around 1 °C.

5.1.2 Experimental setup

A pre-existing setup, modified from a previous study, was reused for these experiments (Neumann et al., 2022). This setup consisted of an acrylic glass structure featuring a newly built holder for the Teflon© containers in the center, along with two nozzles connected to a pump and two 40 W infrared lamps positioned above. Additionally, an infrared thermometer was installed above one of the samples to monitor the surface temperature (Fig. 5.1). Both nozzles were connected to an external pump and a 5-litre canister containing the artificial rainwater. The entire setup, excluding the pump and canister, was placed within a larger plastic container to collect any excess artificial rainwater. Unlike the climate chamber experiments, the nozzles in this setup nebulised the water, creating very small droplets similar to those produced in earlier experiments (Neumann et al., 2022).

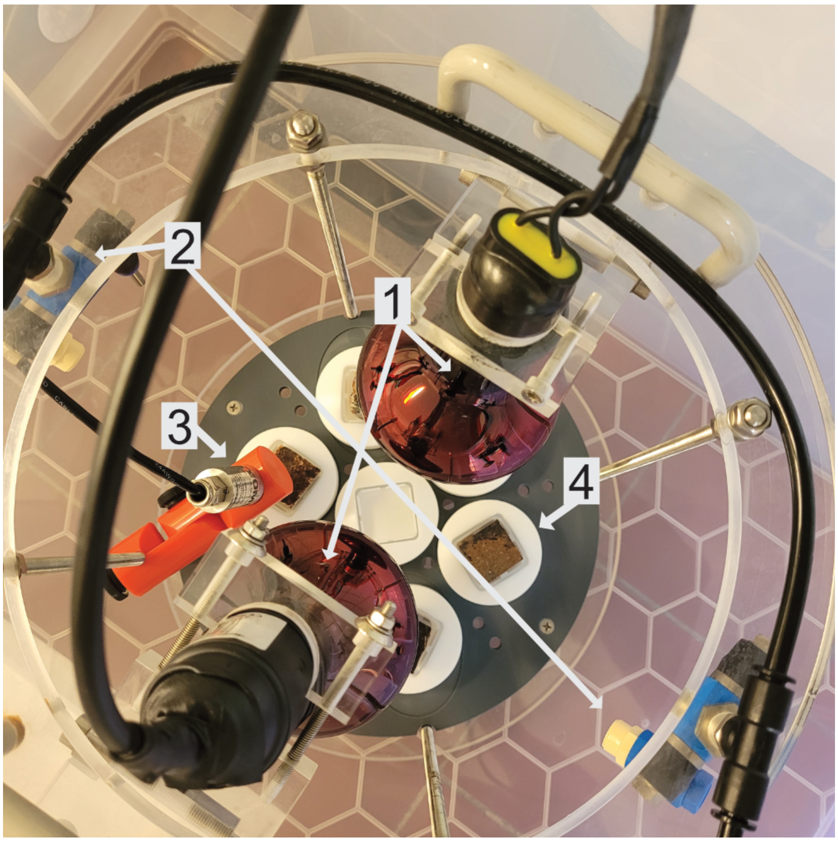

Figure 5.1: Experimental setup for the irrigation experiments. The setup consists of (1) two infrared lamps with a power of 40 W each, (2) two nozzles for irrigation, (3) an infrared thermometer to control the sample surface temperature, (4) the small Teflon© containers for artificial rainwater collection.

5.1.3 Sample preparation

5.1.3.1 Rock samples

For the irrigation experiments smaller cubes with an edge length of 2 x 2 cm^2 and a height between 1.5 and 2 cm were cut out of the remaining material from a previous study (Chapter 3.1.1). The used rocks were collected in 2019 on Murujuga and were cut using the same water-cooled tablesaw as for the other samples used in the climate chamber experiment (Chapter 4.1.3). A total of six cubes, three from granophyre and three from gabbro samples, were cut (Fig. 3.2). The cubes were also coated with Araldite® resin (Huntsman, 2004) on all sides except the varnish as the samples used in the climate chamber experiment (Chapter 4.1.3).

5.1.3.2 Artificial rainwater compositions

For the irrigation experiments, the same stock solutions as those used in the climate chamber experiment were utilised. One of these two stock solutions contained HNO_3 and H_2SO_4 to lower the pH of the demineralised water used as base for the artificial rainwater and the other stock solution contained NaOH to increase the pH of the artificial rainwater, as described in Chapter 4.1.3.3.

Artificial rainwaters with pH values of 8.0, 7.0, 6.0, 5.0, 4.0, and 3.0 (± 0.1) were prepared using demineralised water and the stock solutions. The water was stored in a 5-litre tank and the pH was checked again before each of the experiments to ensure that the pH did not change over the time.

5.2 Results

5.2.1 Colour changes

The colour of the varnish on the six rock cubes was measured prior to the irrigation experiments and after each set of two experiments conducted with the same pH, as described in Chapter 2.1. Due to the size of the rock cubes, which was smaller than the measured area of the chroma meter, slight variations in the positioning of the samples led to apparent colour changes, with ΔE values > 1, which were deemed unrealistically high due to the significantly lower changes calculated from all other measurements. Consequently, two measurements, one from a granophyre sample and one from a gabbro sample, were excluded from the presented data.

Fig. 5.2 shows the colour change that was calculated relative to the data acquired before the start of the irrigation experiments. Notably, the mean colour change ΔE of the gabbro samples was highest after the first set of irrigation experiments, where artificial rainwater with pH 8 was used. Subsequently, ΔE consistently decreased, indicating that the colour gradually returned closer to its original state. The colour of the granophyre cubes remained relatively constant, with ΔE values between 0.2 and 0.3 throughout the experiments (Fig. 5.2). The contribution to ΔE primarily arose from changes in ΔL*, which decreased on five out of six cubes after the first experiments, except for one gabbro cube (II). Thereafter, the brightness began to increase again, approaching a neutral or even positive ΔL*. The only exception was one granophyre cube (V), which exhibited a consistently decreasing brightness (Fig. 5.2). The two excluded measurements are also shown in Fig. 5.2, illustrating that including these values would significantly alter the mean ΔE and ΔL* values.

The Δa* and Δb* values were reasonably small for most samples, with mean Δa* values ranging from -0.02 to 0.04, largely within the errors. Only gabbro cube II exhibited significantly greater changes. The mean Δb* values displayed slightly more variation, ranging from -0.03 to 0.10. Again, gabbro cube II showed more substantial changes.

Overall, the colour changes were relatively minor and the margins of error were significantly larger compared to the results from the climate chamber experiment (see Chapter 4.2.1.1). The larger margins of error were attributed to slight differences in the positioning of the samples during each measurement, as the samples covered only about 20 % of the measured area. This led to the assumption that the actual colour change of the cubes might be approximately five times greater than the measured results, as well as the associated margins of error. It was also noticeable that, as observed in the climate chamber experiment, the colour of the gabbro cubes changed more than that of the granophyre cubes. The whole dataset can be found in the digital supplementary material.

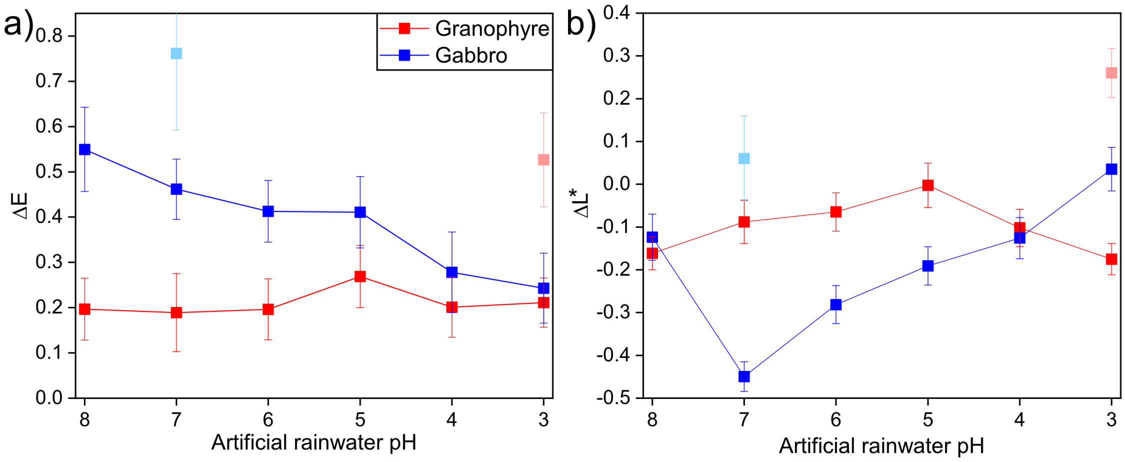

Figure 5.2: Calculated (a) mean colour change ΔE and (b) change in brightness ΔL* for the granophyre (red) and gabbro (blue) cubes as a function of pH, which reflects the course of the irrigation experiments. The colour was measured after each set of irrigation experiments at the same pH, starting at pH 8 and progressively decreasing to pH 3, with a total of 12 irrigation experiments conducted on each cube. One measurement after pH 7 from the gabbro and one after pH 3 from the granophyre was excluded from the calculations. The mean values, including these two measurements, are shown in lighter blue and red in both graphs.

5.2.2 Chemical surface changes

The chemical composition of the varnish on the six rock cubes was measured using p-XRF at the LVR Museum in Bonn, as described in Chapter 2.2.2. The change in chemical composition was calculated as Δ_{el} (%), representing the relative percentage change compared to the first set of measurements taken before the irrigation experiments. The Mg values varied considerably and were often recorded as zero due to their low concentration. This may be attributed to the fact that Mg is the lightest element detectable by the device, making accurate measurement challenging.

The mean Si and P concentrations of the granophyre cubes did not change significantly, with maximum values < 1 % over the course of all irrigation experiments. The gabbro cubes exhibited slightly larger negative changes in Si concentrations after the initial experiments at pH 8, with no further changes observed during subsequent irrigation experiments. In contrast, the P concentrations of the gabbro cubes increased after experiments conducted at pH 5 and below, ultimately reaching slightly positive values (Figs. 5.3 & 5.4).

As shown in Fig. 5.3, the mean Al concentration of the varnish exhibited small variations throughout the experiments, with slightly larger negative changes than those observed for Si and P following the initial irrigation experiments at pH 8, accompanied by some fluctuations over time. As with Si and P, the gabbro samples showed larger changes than the granophyre samples. No individual cubes displayed significant deviations from the overall mean values.

The measured Fe, Mn, and K concentrations followed a similar pattern, showing slightly positive changes after the initial experiments at pH 8, with larger changes observed on the gabbro cubes. For the granophyre cubes, the relative changes approached zero and eventually turned negative over the course of the experiment. Overall, the fluctuations and changes were relatively minor for all three elements. For Ca, however, the fluctuations were more pronounced, with mean changes on the gabbro varnish ranging from 1.1 to 5.3 % and values ranging between -2.5 and 6.3 % on the granophyre varnish, without any discernible trend for both types of rock except the change of the Mn content of the granophyre samples that seemed to exhibit a slightly negative trend over the course of the experiments (Fig. 5.3).

The S concentrations exhibited notable changes. After weathering at pH 8, mean decreases of approximately -30 % for granophyre and -10 % for gabbro were observed. This reduction in S concentrations increased until weathering at pH 5. At pH 3 and 4, the concentrations increased again, resulting in higher S contents after the pH 3 experiments than at the start of the irrigation experiments (Fig. 5.4a). The stock solution used to prepare the artificial rainwaters at pH < 6 contained H_2SO_4 (see Chapter 5.1.3.2). Consequently, the S content in the rainwaters increased significantly at pH 3 and 4, reaching concentrations of up to 10.22 ± 0.18 ppm (see Chapter 5.2.3). This increase in S content likely caused an accumulation of S on the rock cubes, leading to elevated surface concentrations after irrigation with pH 4 and 3.

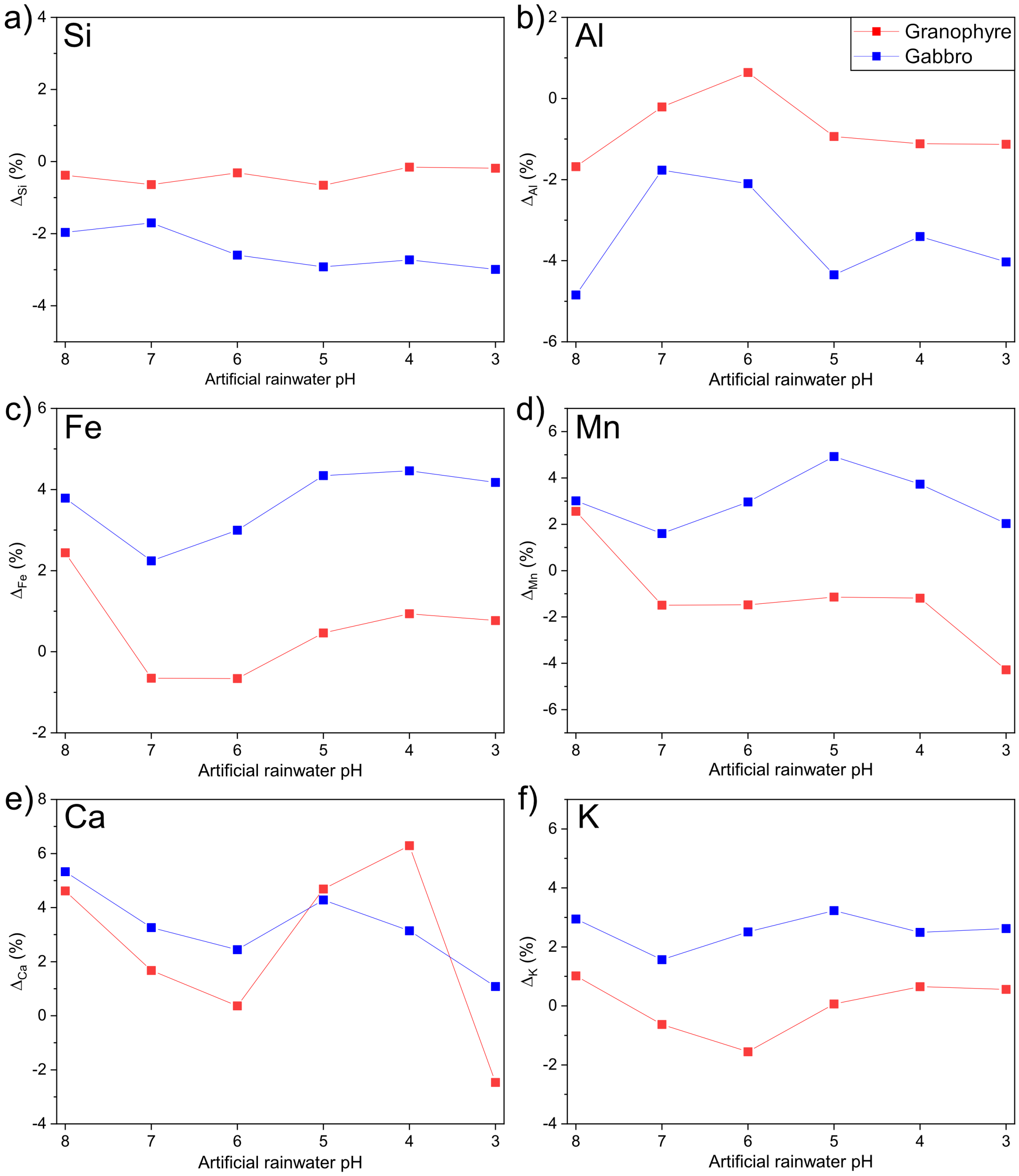

Figure 5.3: Mean chemical changes of the granophyre (red) and gabbro (blue) cubes as a function of pH, which reflects the course of the irrigation experiments, presented as Δ_{el} for (a) Si, (b) Al, (c) Fe, (d) Mn, (e) Ca, and (f) K. The measurements were conducted after each set of two irrigation experiments, with a decreasing pH starting at 8. The Δ_{el} represents the relative percentage change compared to the first set of measurements, taken before the irrigation experiments began. Error bars (95 %) are smaller than the symbol size.

Overall, the changes of the samples used for the irrigation experiment were smaller than the observed changes on the rock samples used in the climate chamber experiment (Chapter 4.2.1.4) and did not exceed $\Delta_{\mathrm{el}} \pm 5$ %, except for Ca and S. Additionally, the fluctuations of the measurements were lower, except for the Ca results. There were no clear trends visible for most of the elements, but noticeable differences between the gabbro and granophyre samples, with consistently lower changes measured on the granophyre samples than on the gabbro samples, except for the S content. This findings are consistent with the observed larger changes on the gabbro sample surfaces in the climate chamber experiment. The differences between the samples of the same rock type were significantly smaller than for the samples used in the climate chamber experiment. The whole dataset is provided in the digital supplementary material.

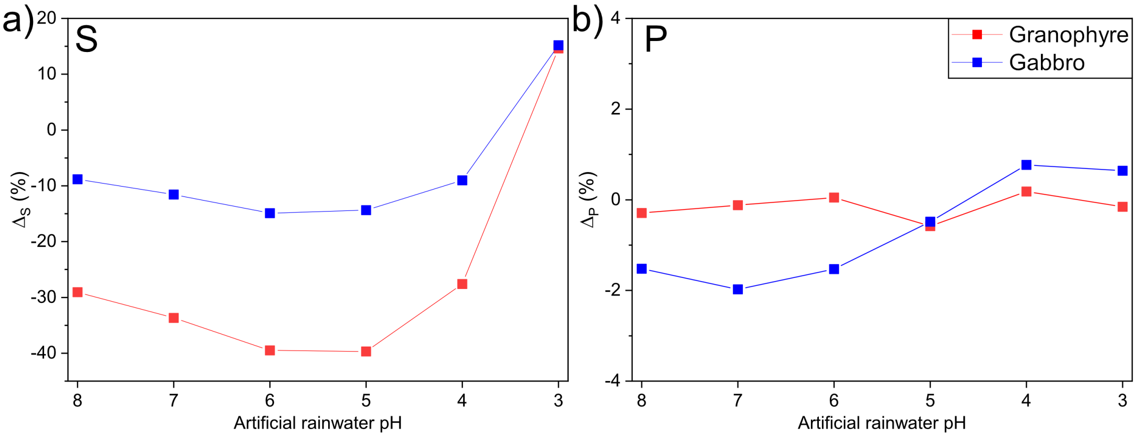

Figure 5.4: Mean chemical changes of the granophyre (red) and gabbro (blue) cubes as a function of pH, which reflects the course of the irrigation experiments, presented as Δ_{el} for (a) S and (b) P. The measurements were conducted after each set of two irrigation experiments, with a decreasing pH starting at 8. The Δ_{el} represents the relative percentage change compared to the first set of measurements, taken before the irrigation experiments began. Error bars (95 %) are smaller than the symbol size.

5.2.3 pH dependence of dissolution

The concentrations of different elements in the artificial rainwater samples, collected during the irrigation experiments, were examined using ICP-OES (Chapter 2.4). For each pH value, starting at 8, a total of two experiments was conducted, and per experiment, seven samples, including one blank, were collected. With a total of 84 samples, it was possible to determine the pH dependence of the dissolution of different elements, evaluate the differences between the two rock types used, and assess the impact of the angle of the sample surface. The concentrations measured in the artificial rainwater rinsed over the rock samples were corrected by subtracting the corresponding blank sample concentrations to account for possible contamination and accurately examine the actual dissolved material (Chapter 2.4).

The average concentrations measured during the first irrigation experiment at pH 8 were four to 20 times higher for all measured elements, except for Mn, compared to those observed in the second irrigation experiment conducted with the same artificial rainwater at pH 8. For all subsequent irrigation experiments, the measured concentrations for experiments conducted at the same pH were within the same range. This observation suggests that some secondary minerals and / or other material was washed off the sample surfaces during the first experiment at pH 8. This likely resulted in the contamination of the water samples with small fragments of material, which subsequently dissolved in the artificial rainwater while stored. The rainwater was stabilised with concentrated HNO_3 while the samples were stored between the experiment and the measurements. The significant initial changes in colour and chemical composition observed after the experiments at pH 8, which in many cases exceeded the changes observed over the remainder of the experiment, as mentioned previously, also support the assumption that more material was removed from the surface during the first of the two experiments at pH 8.

For these reasons, it was assumed that the measured concentrations in the first experiment did not represent the amount of material dissolved while the rainwater was in contact with the rock surfaces. Consequently, the results from the first experiment were excluded from the box plots in Figs. 5.5 and 5.6, although they are shown as individual symbols.

The solubility of Si minerals in aqueous solutions is well understood and known to increase at pH 8 and above (Iler, 1979; House & Orr, 1992). This was not reflected in the irrigation experiment results. For pH values between 3 and 7, Si concentrations ranged between 0.01 and 0.04 ppm, with slightly higher values for the gabbro samples. At pH 8, the concentrations were only significantly higher in the first of two experiments, which was excluded due to suspiciously high concentrations (Fig. 5.5a). For pH 3 and 4, the concentrations were slightly elevated in the gabbro samples compared to pH 5 to 7, indicating slightly increased dissolution under acidic conditions.

For the Mg and Na concentrations in the rainwater, similar trends were observed, with very similar concentrations for all pH values. However, unlike for Si, the concentrations for Mg and Na increased stronger towards acidic conditions at pH 4 and 3 in the water samples that were in contact with gabbro rocks (Fig. 5.6). At all pH levels, the concentrations of Mg and Na in the water samples that were in contact with the gabbro samples, were higher compared to those in water samples in contact with granophyre rock samples. The Ca concentrations followed a comparable trend, with the highest concentrations measured at pH 3. However, a stronger increase in Ca concentrations under acidic conditions was observed for water samples in contact with both types of rock compared to Si, Mg, and Na. Similar to the other elements mentioned, the concentrations in the water samples in contact with gabbro rocks were higher than those in contact with granophyre samples (Fig. 5.5e).

As shown in Fig. 5.5, the Al and K concentrations followed a similar trend, with the highest element concentrations for the gabbro samples measured under acidic conditions, particularly at pH 3. Additionally, no increase in concentrations at pH 8 was observed, except for the results from the first experiment at pH 8,

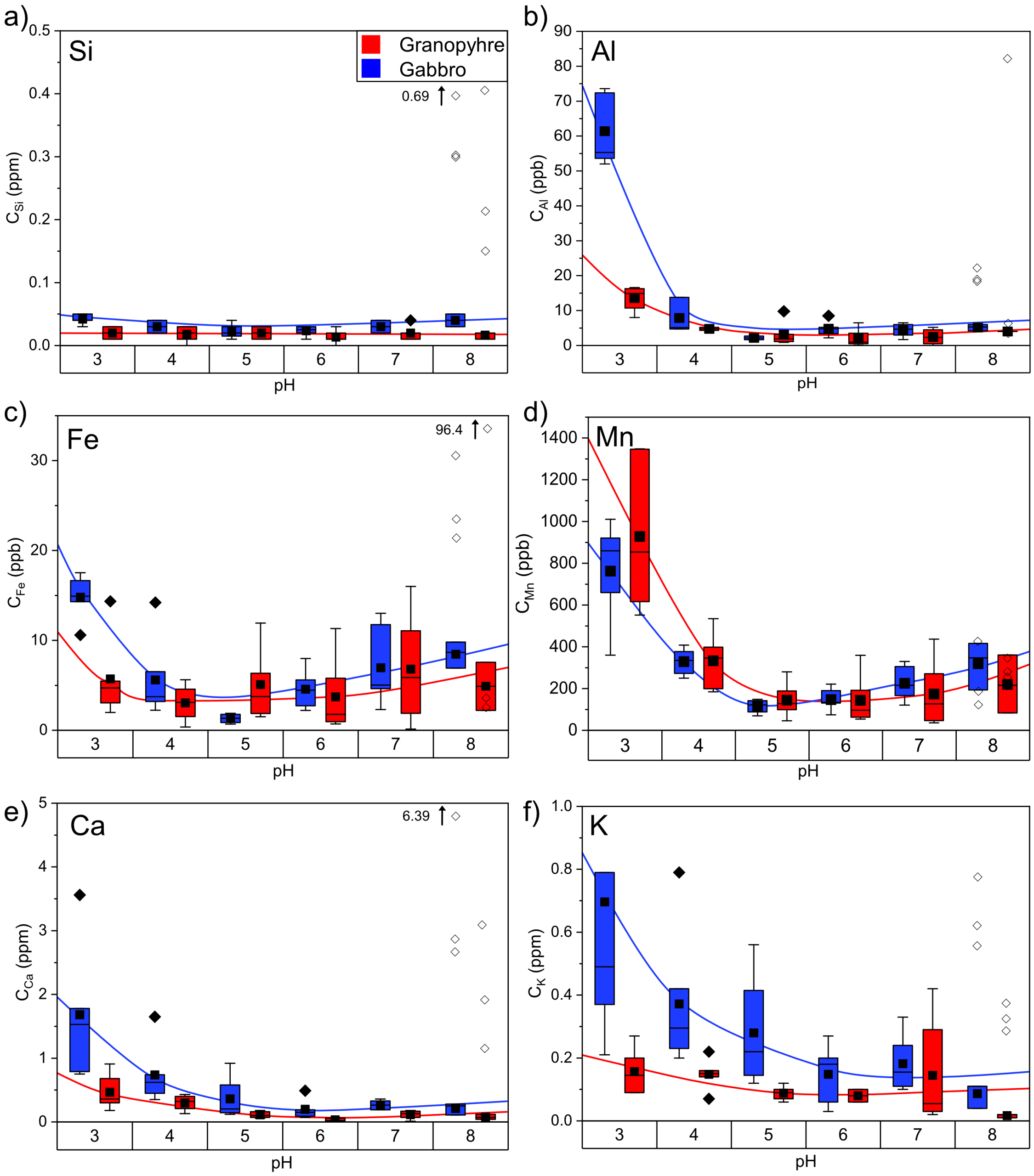

Figure 5.5: Box plots of the pH dependence and element concentrations in the artificial rainwater samples after subtracting the concentrations of the corresponding blank samples collected from the irrigation experiments for (a) Si, (b) Al, (c) Fe, (d) Mn, (e) Ca, and (f) K. The coloured boxes represent the interquartile range (IQR), which includes 50 % of the results, while the whiskers extend to the range within 1.5 times the IQR. The line within each box indicates the median, while the black square denotes the mean. The outliers included in the calculations are displayed as filled black diamonds, while the results from the first experiment at pH 8 are shown as empty black diamonds. The red and blue lines serve as guides to the eye, illustrating possible trends in the data.

which were excluded. For both elements, the differences between the granophyre and gabbro samples were pronounced. The concentrations in the granophyre samples were lower and the changes in concentration depending on the pH were much smaller.

Due to the importance of Fe- and Mn-oxides in the varnish, the concentrations of these two elements were of particular interest. For both elements, a significant increase in concentrations was measured under acidic conditions at pH 3 and for Mn already at pH 4, while the lowest concentrations were observed at pH 5 to 6. The increase in concentrations towards alkaline conditions at pH 8 was more pronounced for Fe and Mn than for other elements. Mn was also the only element where the concentrations measured in the first experiment at pH 8 were in a comparable range as in the second experiment (Fig. 5.5c & d). For Fe, the concentrations in the gabbro samples were higher, except at pH 5. Conversely, for Mn, the granophyre samples exhibited higher concentrations at pH 5 and below. The highest Mn concentrations, exceeding 1000 ppb, were unexpected and beyond the calibration range, necessitating re-measurements of some samples. These re-measurements confirmed the high concentrations.

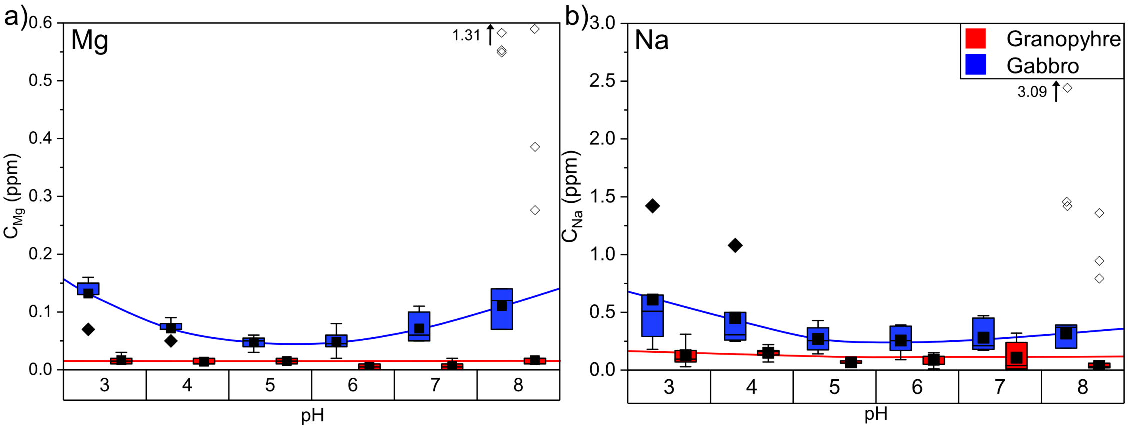

Figure 5.6: Box plots of the pH dependence and element concentrations in the artificial rainwater samples collected during the irrigation experiments for (a) Mg and (b) Na. The coloured boxes represent the interquartile range (IQR), which includes 50 % of the results, while the whiskers extend to the range within 1.5 times the IQR. The line within each box indicates the median, while the black square denotes the mean. The outliers included in the calculations are displayed as filled black diamonds, while the results from the first experiment at pH 8 are shown as empty black diamonds. The red and blue lines serve as guides to the eye, illustrating possible trends in the data.

Measurements of S concentrations were excluded from the evaluation because the blank concentrations were elevated due to the use of a stock solution containing H_2SO_4 to produce the artificial rainwater with pH values of 3 to 5. Consequently, the S concentration in the blank samples was 1.09 ± 0.02 ppm at pH 4 and 10.22 ± 0.18 ppm at pH 3. The measured S concentrations in the samples that were in contact with the rock varnish were only slightly higher or, in some cases, even lower than the blank concentrations, resulting in negative values. The differences were within the margin of error (95 %), except for two individual values. Similarly, P concentrations were here excluded due to low accuracy and poor precision. Additionally, the P concentration in the blank samples increased with lower pH values, exceeding 50 ppb at pH 3. In contrast, for other elements, the concentrations in the blank samples were low relative to those in the samples that were in contact with the rock varnish. Furthermore, the blank concentrations remained relatively constant throughout the irrigation experiments, despite changes in pH. The whole dataset including all measurements is given in the digital supplementary material.

Overall, it was observed that the lowest concentrations of all elements were measured at pH 5 and 6 or above. For some elements, such as Si, Mg, and Na there was only a little to no increase over the whole pH range tested. However, for most of the analysed elements, concentrations increased towards lower pH values, sometimes drastically, as seen for Mn, K, and Al. Only for Fe and Mn, as well as for the Mg content of the gabbro samples, an increase of the measured concentrations was observed at pH 7 and 8. Without excluding the first of the two pH 8 experiments the concentrations would seem to have increased significantly at pH 8 for all shown elements except Mn, which is visible in Figs. 5.5 and 5.6, where the results of the first experiment are plotted, but were excluded from the box plots and estimated trends.

For all elements, except Mn at low pH values, the concentrations were significantly higher in the water samples that had been in contact with the gabbro compared to those in contact with the granophyre. The observed concentrations partly followed the characteristic U- or V-shaped trend, commonly observed when dissolution rates or solubility are plotted as a function of pH (Appelo & Postma, 2004). It was also noted that the range and number of outliers were greater for the gabbro samples compared to the granophyre.

Fig. 5.7 shows the concentrations of Fe and Mn normalised to the measured Fe and Mn contents on the surface of the corresponding rock cubes for the tested pH levels. This analysis revealed that the normalised Mn concentrations were significantly higher than the normalised Fe concentrations, regardless of the pH level or rock type. The lowest ratios were observed at pH 8 and pH 7, with values of at least 10 and 7, respectively, on one of the granophyre samples. The mean values ranged from > 100 to nearly 1000. While the Mn/Fe ratios on the granophyre samples appeared to increase with decreasing pH levels, the gabbro samples displayed maximum mean values at pH 5. The range of concentrations at each pH level and for each rock type was relatively large across all groups, with significantly greater variability observed for the granophyre samples. This variability persisted even after excluding outliers with ratios exceeding 2000 from the calculated mean values and the box plots (Fig. 5.7).

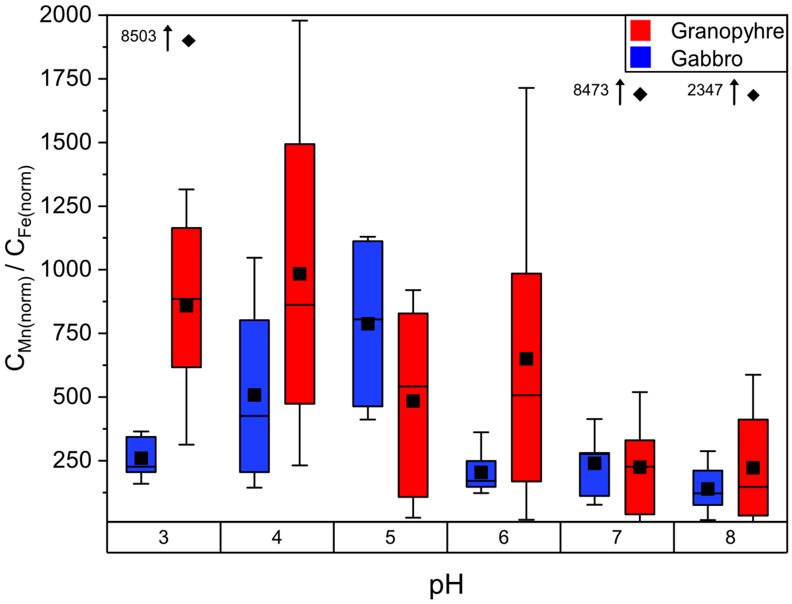

Figure 5.7: Ratio of the normalised concentration of Mn and Fe in the artificial rainwater samples of the granophyre and gabbro cubes for the tested pH levels, showing the much higher normalised Mn dissolution compared to Fe. All outliers were excluded from the shown box plots.

To investigate the effect of the surface angle on the concentrations of various elements in the collected water samples, all samples were irrigated twice under identical pH conditions but with the surface oriented at either 30° or 0° (horizontal) in separate experiments. Consequently, half of the water samples collected were in contact with a rock varnish surface angled at 30° (Chapters 2.4 & 5.1.1). For this analysis the data from the first experiment at pH 8 was also excluded due to the aforementioned reasons.

The comparison of the measured concentrations for ten elements, based on surface angle, revealed small but consistent differences. Overall, it was observed that the range of results from samples with a 30° angle was smaller compared to the horizontally placed samples. This may be attributed to the fact that none of the cubes had perfectly flat surfaces. When positioned horizontally, water likely followed different flow patterns across the inhomogeneous surfaces, leading to varying durations of water contact with the surface. These variations potentially resulted in a broader spread of element concentrations. In contrast, at a 30° angle, although the surfaces remained uneven, the steeper orientation caused water to run off more quickly, reducing the contact time and yielding more uniform results.

A large number of outliers towards higher concentrations are visible in Fig. 5.8. This is likely due to the inclusion of results from all irrigation experiments with varying pH values. High concentrations were only measured at pH 3 (Figs. 5.5 & 5.6), resulting in a larger number of samples with lower concentrations at pH values ranging from 4 to 8.

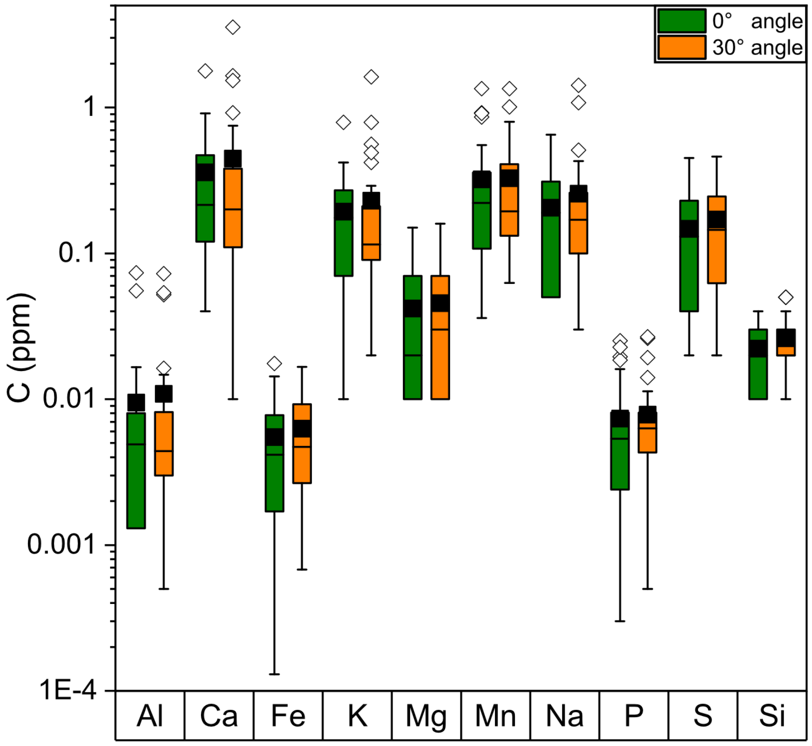

Figure 5.8: Element concentrations in the artificial rainwater samples collected during the irrigation experiments depending on the surface angle. The results for each element and angle are presented to illustrate the overall differences between the two surface angles tested. The coloured boxes represent the interquartile range (IQR), which includes 50 % of the results, while the whiskers extend to the range within 1.5 times the IQR. The line within each box indicates the median, while the black square denotes the mean. Extreme values that were identified as outliers are displayed as diamonds. The data of the first experiment at pH 8 was excluded.

Given the variability in the absolute concentrations measured, percentage differences between the two groups per element were analysed to permit comparability. For all elements the average measured concentrations were higher at an angle of 30° with most values being between 10 and 20 % larger at this angle. Only for Mn, P, and Mg the concentration differences were < 10 % (Fig. 5.8). These results indicate that measured concentrations were slightly increased when the surface was inclined at 30°.

5.2.4 Cross correlations: Statistical data analysis

The results of the irrigation experiments were also analysed for potential correlations between the various parameters. Of particular interest was whether the dissolution of material on the surface during the experiments correlated with the development of the corresponding element concentrations on the sample surface, as well as whether the initial element concentrations on the different samples were linked to the quantity of material dissolved in the artificial rainwater that had been in contact with the rock samples. Due to the smaller number of samples, compared to the weathering experiments in the climate chamber, it was more challenging to determine whether apparent correlations were genuine or coincidental.

Similar to the weathering experiment, the measured parameters for all samples at the end of the experiment, as well as the mean values of the measured parameters for the gabbro and granophyre samples over the duration of the experiment, were analysed for potential correlations. Here, time was not recorded chronologically but instead represented by pH steps, starting from the highest pH (8) and decreasing to the lowest artificial rainwater pH (3) used for the irrigation experiments. For the analysis of the changes over the course of the experiments, the colour change, the percentage change in the concentrations of various elements, and the total sum of element concentrations in the artificial rainwater samples were examined. Due to the pH dependence of dissolution, which caused significantly different concentrations at each step with different pH values, it was unsuitable to use the measured concentrations from the artificial rainwater at each step directly. Instead, the cumulative sum of all previous steps was calculated to determine whether the total quantity of the concentrations of a given element influenced the colour or the respective element concentration on the sample surface. Consequently, the summed concentrations increased at each experimental step. For the calculated sums the measured concentrations from the first experiment at pH 8 were again excluded due to suspiciously high values, as described in Chapter 5.2.3.

Correlations over time

Due to the observed similar trends for most of the elements (see Chapter 5.2.3), the summation of the concentrations resulted in similar trends in the calculated sums of the different elements, leading to high correlation coefficients in the correlation matrices. These correlations were attributed to the pH dependence and calculation methodology rather than intrinsic relationships, and thus, correlations between the sums of different element concentrations were excluded from the analysis of the correlation matrices.

The correlation matrices were evaluated for correlations in the matrices of both rock types, as in the data for the weathering experiment. After excluding correlations between the summed concentrations of elements in the artificial rainwater samples, very few correlations remained. None of the element concentration sums showed significant correlations with other parameters for either rock type, with $R > 0.85$. For the granophyre samples, a negative correlation was observed between the percentage change in Mn concentration and the sums of Mn, P, and Fe concentrations in the artificial rainwater samples, with correlation coefficients of -0.81, -0.90, and -0.85, respectively. Considering the high Mn concentrations in the artificial rainwater samples (Fig. 5.5d), it was reasonable that the Mn concentration on the sample surfaces decreased as more Mn was dissolved. However, this correlation was not found for the gabbro samples, where the correlation coefficient between the Mn sum in rainwater and the Mn concentration change on the surface was only -0.14. Here, it has to be taken into account, that the amount of Mn dissolved in rainwater from the gabbro samples was comparably high to that from the granophyre samples (Fig. 5.5d). For the colour change and the element sums for the gabbro samples also high correlation coefficients were found. This was mainly due to the constant decrease of the colour change on the gabbro samples, similar to the constant increase of the element concentration sums, but was not observed for the granophyre samples.

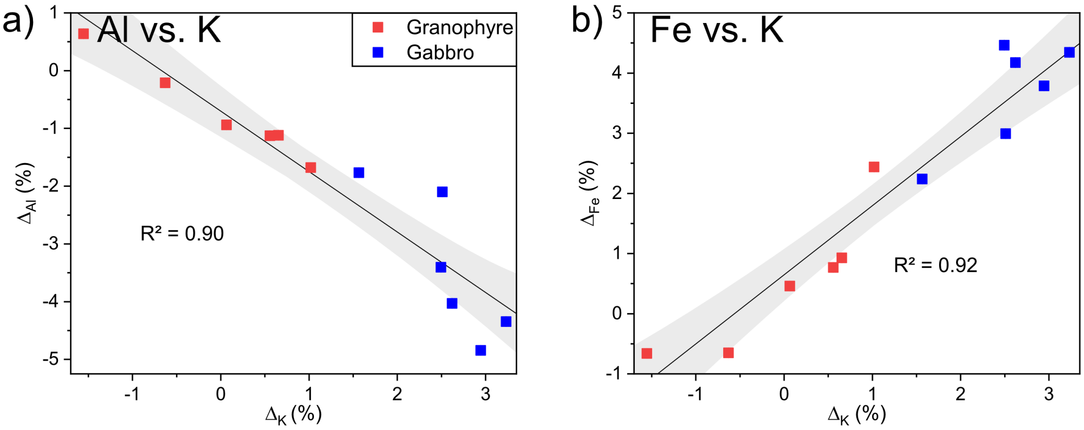

Figure 5.9: Correlation between the percentage change in K concentration and the changes in (a) Al and (b) Fe concentrations on the surface of the rock samples used in the irrigation experiments. No clear trend was observed over the course of the irrigation experiments, making it impossible to depict a development over the decreasing pH values. The confidence bands and error bars are presented within a 95 % confidence interval. The error bars are smaller than the symbol size.

Changes in K concentration correlated with changes in Al and Fe concentrations for both rock types, with correlation coefficients of $R^2 = 0.90$ and $R^2 = 0.92$, respectively. Positive changes in Al concentrations on the surface were associated with negative changes in K concentrations for both rock types. The gabbro samples exhibited larger negative changes in Al concentrations, accompanied by greater positive changes in K concentrations, compared to the granophyre samples. However, the trend appeared consistent for both rock types (Fig. 5.9a). There was no systematic progression over the course of the experiments towards higher or lower concentrations, as the values fluctuated seemingly randomly between measurements and the overall values were relatively small. Similarly, Fe concentration changes were positively correlated with K concentration changes, indicating that higher positive changes in Fe concentrations corresponded to higher positive changes in K concentrations for both rock types. Again, the values for gabbro samples were larger than those for granophyre samples, but the parameter ratios were consistent, yielding similar potential trends for both rock types (Fig. 5.9b). No systematic trend over the course of the experiments was observed in this case either. These correlations also led to relatively high correlation coefficients for changes in Al and Fe concentrations.

Other correlations were observed only for one of the two rock types and were therefore not analysed further. All data and correlation matrices are available in the digital supplementary material.

Correlations at the end of the experiments

The comparison of various parameters measured after the final irrigation experiment revealed some correlations. Specifically, the measured element concentrations, the changes in these concentrations, the sum of the concentrations per element in the corresponding artificial rainwater samples, and the colour change (ΔE) were compared.

Particular attention was given to correlations among parameters associated with the same element to explore potential relationships between the sum of element concentrations in the artificial rainwater samples, the initial element concentrations, and changes in these concentrations on the rock samples. Due to the inclusion of 28 different parameters, approximately 750 correlations were examined, resulting in a high number of correlations with $R > 0.85$. Consequently, some correlations could not be analysed in detail. However, all data and correlation matrices are provided in the digital supplementary material.

The colour change (ΔE) is an important parameter and was found to correlate with various other parameters in the climate chamber experiments. In the irrigation experiments, however, ΔE only correlated with the percentage change in K concentrations on the samples, with $R > 0.85$. This limited correlation may be due to the smaller magnitude of colour changes observed during these experiments compared to those measured on samples weathered in the climate chamber, as well as very similar ΔE values for all of the used samples with a range only between 0.18 and 0.30, which is quite small compared to the differences of other parameters and the colour changes measured on the samples weathered in the climate chamber experiment.

The sum of some element concentrations in the collected water samples correlated with the initial element concentrations measured on the sample surfaces for the corresponding element. For Al, a negative correlation ($R = -0.86$) suggested a trend of higher total Al concentrations in the artificial rainwater samples when the Al content on the samples was lower. In this case, gabbro samples exhibited lower Al concentrations compared to granophyre samples but had higher sums of Al concentrations in the rainwater samples (Fig. 5.10a). However, this trend was unclear due to the small sample size (six rock samples) and substantial variability between individual samples. A similar negative correlation ($R = -0.98$) was observed between the sums of Si concentrations in the rainwater samples and the initial Si concentrations on the rock surfaces. This indicated that higher Si concentrations in the rainwater samples corresponded to lower Si contents on the sample surfaces (Fig. 5.10d). The differences in Si content on the samples (25–65 wt. %) were relatively high compared to other elements shown in Fig. 5.10, whereas the overall sums of Si concentrations were low, with a maximum of around 0.35 ppm, despite Si being the primary component of the rock samples.

A positive correlation (R = 0.77) was found between the sum of S concentrations in the rainwater samples and the initial S concentration on the rock surfaces. The total S content on the samples was relatively low (< 0.25 wt. %), resulting in larger errors, whereas other elements presented in Fig. 5.10 had concentrations of at least 1 wt. %. The difference between gabbro and granophyre samples was considerable, with gabbro samples showing higher S contents and higher sums of S concentrations in the rainwater (Fig. 5.10c). For Mn, the correlation coefficient was the same as for S, with a small spread among five of the six data points with one sample being a bit of the probable trend, as also observed for S. This positive correlation indicated higher Mn concentrations in the rainwater samples when the Mn concentrations on the corresponding rock samples were higher (Fig. 5.10b). Here, the values and range for the gabbro and granophyre samples was similar.

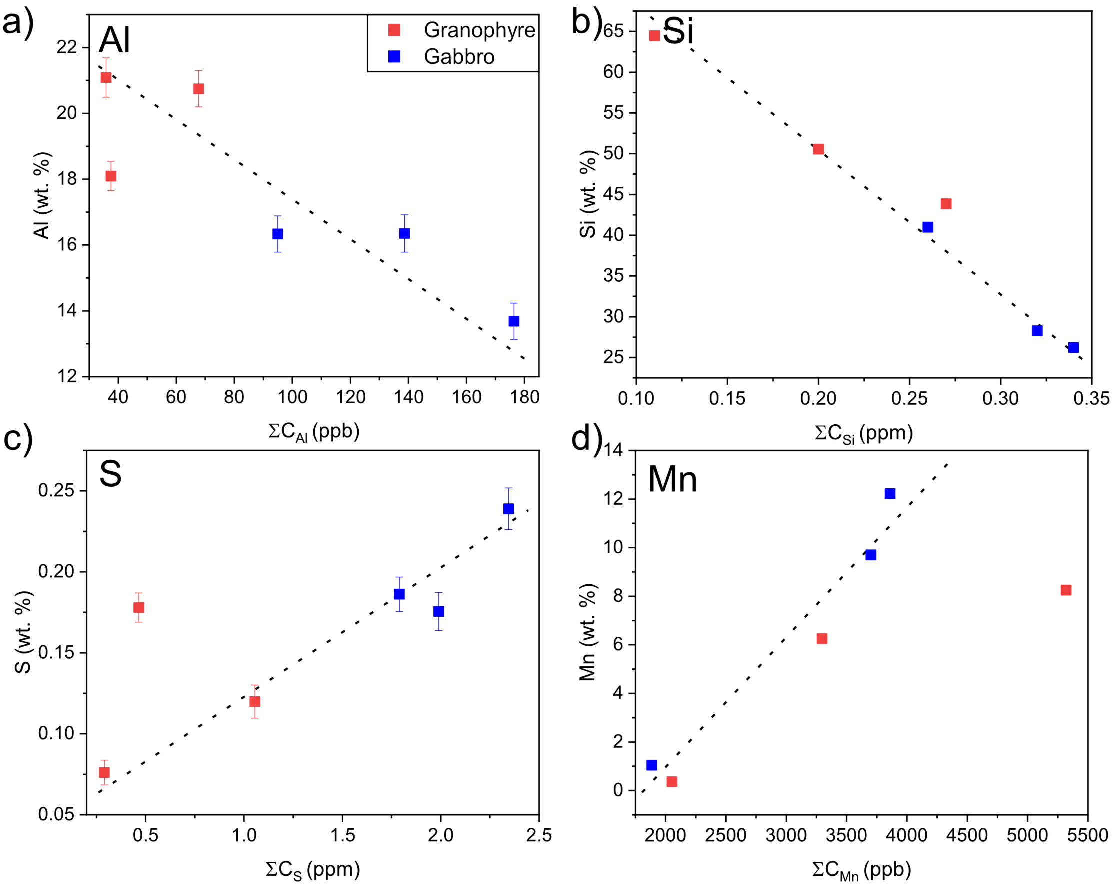

Figure 5.10: Correlation of the initial element concentrations for different elements as a function of the corresponding sums of dissolved material for (a) Al, (b) Mn, (c) S, and (d) Si. The dotted lines in the Figure serve as guides to the eye to highlight potential trends. Error bars (95 %) for some elements are smaller than the symbol size. The measured concentrations from the first experiment at pH 8 were excluded for the calculations.

These correlations between the sums of element concentrations in the rainwater samples and the element content measured on the sample surfaces were generally weak, with a relatively large spread, except for Si. Notably, for Al and S, the two rock types exhibited significantly different values but appeared to follow the same overall trend, with comparable ratios of the two parameters. Due to the small sample size the validity of the probable trends depicted in Fig. 5.10 remains uncertain.

A correlation was observed between the change in Fe content on the sample surfaces and the initial Fe content on the samples. This positive correlation (R = 0.88) indicated that higher initial Fe contents resulted in a greater percentage increase of the Fe content on the surface. A distinction between the two sample groups was apparent, with gabbro samples displaying overall higher Fe contents on their surfaces (Fig. 5.11a). Similar correlations were identified for percentage changes in Al and Si contents on the surface and their respective initial concentrations, with R = 0.83 for Al and R = 0.79 for Si. The observed decrease in Al and Si contents on the sample surfaces suggested that higher initial Al contents, as measured on the granophyre samples, led to smaller percentage decreases in Al content. A comparable trend was observed for percentage Si content changes, where granophyre samples exhibited higher initial Si contents, resulting in smaller percentage decreases of the Si contents compared to the gabbro samples. In one granophyre sample, the Si content on the surface even increased.

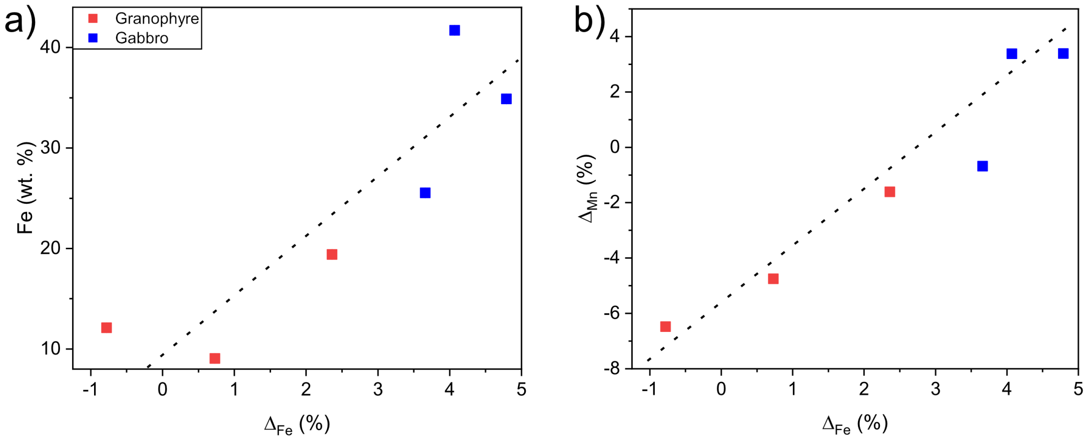

Figure 5.11: Correlation of (a) the initial Fe concentrations and (b) the percentage changes of the Mn concentrations as a function of the percentage changes of the initial Fe concentrations. The dotted lines serve as guides to the eye to highlight potential trends. Error bars (95 %) are smaller than the symbol size.

The change in Fe content also correlated with the change in Mn content on the surface, showing a strong positive correlation (R = 0.96). Higher changes in Mn content appeared to correspond with higher changes in Fe content. For gabbro samples, both Mn and Fe contents increased, whereas for granophyre samples, the Mn content decreased by up to more than 6 %, while the Fe content decreased by less than 1 % in only one sample, while for the other two samples there was still a small increase of the Fe content (Fig. 5.11b). Additionally, the percentage change in Mn concentrations on the surface correlated negatively with the change in Al concentrations ($R = -0.92$) and the change of Mg ($R = -0.89$) and Si ($R = -0.90$) concentrations.

Numerous other correlations ($R > 0.85$) were identified, many of which were between different elements and various parameters (e.g. the percentage S content on the surface and the sum of Al concentrations in the rainwater samples, with $R = 0.92$). Not all of these correlations were examined in detail, as they were mostly between different elements and different types of parameters where a genuine correlation seemed unlikely and the chance for coincidental correlations is relatively high, due to the low number of samples analysed. However, all data and correlation matrices are available in the digital supplementary material.

Principal component analysis (PCA)
As for the results from the weathering experiment, a PCA (Abdi & Williams, 2010) was performed. Due to the high number of 28 parameters, the results appeared cluttered, and the number of parameters was reduced to 10. These parameters were selected based on their high coefficients in PC1 and PC2. The selected parameters included the colour change ΔE, measured concentrations of Al, P, and Mn, percentage changes in element concentrations (Si, K & Ca) compared to pre-weathering measurements, and the sum of the concentrations of Mn, Fe, and S in the collected artificial rainwater samples. PC1 and PC2 accounted for 84.30 % of the variance in the chosen parameters, with eigenvalues of 5.17 and 3.25, respectively.

The PCA results revealed a separation between the granophyre and gabbro samples. Two granophyre samples were characterised by negative PC1 and positive PC2 values, while the third granophyre sample exhibited a negative PC2 value but remained closer to the other granophyre samples than to the gabbro samples. Among the gabbro samples, samples I and III were primarily described by a positive PC1 value and a PC2 value close to zero, whereas sample II was almost exclusively defined by a strongly negative PC2 value (Fig. 5.12).

Gabbro samples I and III were positioned in relative proximity, influenced by their high sums of S and Fe in the artificial rainwater samples, a pronounced change in the K concentrations on two of the samples, elevated ΔE values, and significant negative changes in Si concentrations on the surface. Gabbro sample II, with lower values for these parameters, was positioned further away. Sample II also exhibited lower sums of Mn and Fe in the rainwater samples, a lower overall Mn content, and a small negative percentage change in Mn concentration, in contrast to the positive changes in Mn content observed in samples I and III.

Granophyre samples IV and VI were characterised by high Al and P contents, relatively high sums of Mn in the artificial rainwater samples (notably sample VI), substantial negative changes in Ca concentrations, and higher Mn contents compared to sample V. Sample V was separated from the other granophyre samples due to its high positive change in Ca concentration, low Mn content on the surface, and low sums of Mn concentrations in the rainwater samples.

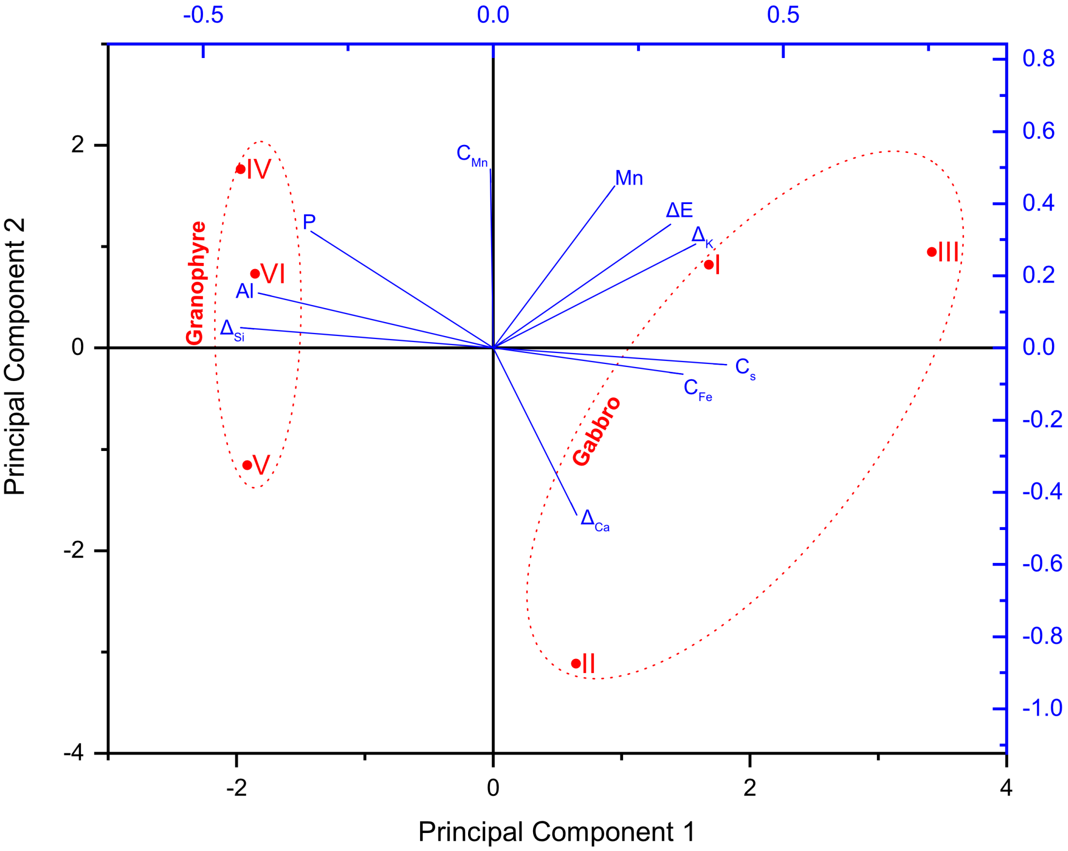

Figure 5.12: Principal component analysis (PCA) of the results obtained at the conclusion of the irrigation experiments. The analysis focused on a reduced number of parameters, retaining only those with the highest contributions to PC1 and PC2. These parameters include the colour change (ΔE), measured concentrations of specific elements such as Mn, percentage changes in element concentrations compared to pre-weathering values (e.g. Δ_{Si}), and the sum of the concentrations of Mn, Fe, and S in the collected artificial rainwater samples (e.g. C_{Mn}). The six rock samples are presented as red dots, with gabbro (I-III) and granophyre samples (IV-VI).

A PCA focusing solely on Mn, Fe, and the colour change (ΔE) was also performed (Fig. A10), as for the results of the weathering experiment. In this analysis, gabbro samples I and III were even closer together, primarily described by the changes in Mn and Fe contents on the surface, as well as the Fe content. The third gabbro sample and all granophyre samples were distributed across a wider range, showing no clear proximity to each other or to gabbro samples I and III. This spread reflected a high degree of variability among these samples, indicating difficulty in distinctly separating gabbro and granophyre samples using PCA, apart from gabbro samples I and III, which had relatively similar parameters.

These results partly contrasted with the PCA outcomes from the weathering experiment, where all gabbro samples exhibited relative proximity to one another and were distinctly separated from the granophyre samples. It should be noted that the parameters utilised in the two PCAs were almost entirely different.

5.3 Discussion of the irrigation experiments

5.3.1 Setup and methods

The experimental setup for the irrigation experiments functioned without any issues. The pH of the artificial rainwater was verified prior to each irrigation session, and no deviations greater than 0.05 from the target pH value were observed throughout the entire series of experiments. Similarly, the water and sample temperatures remained within the target range of 30 °C, with a tolerance of ± 1 °C. Consequently, it is expected that any variations in the measured element concentrations were attributable solely to the differing pH levels of the rainwater, rather than unintended irregularities in other experimental parameters. Due to the type of nozzles used in this setup, the simulated raindrops were significantly smaller, and the water pressure considerably higher, compared to the climate chamber experiment.

For the colour measurements, the same device and measurement procedure as in the climate chamber experiment were employed. However, the smaller size of the rock cubes used in this study, covering only approximately 20 % of the measured area, introduced challenges. The resulting colour measurements did not represent an average of the actual sample colours, as a substantial portion of the measured area included the white background, specifically, the Teflon© plate used in the setup. This resulted in a higher margin of error, as even minor adjustments in the sample positioning on the Teflon© plate caused significant measurement variability.

Two measurements from different cubes were excluded from the calculated mean values because the resulting ΔE values were deemed excessively high, which was likely due to misplacement of the cubes during measurement. Unfortunately, these misplacements were only identified after the measurements were completed, making it impossible to repeat them and obtain corrected values. The smaller sample size also contributed to an increased margin of error, approximately ± 0.1, which was higher than that observed in the climate chamber experiment. In that experiment, the rock samples were sized to match the measured area, minimising measurement errors. For future studies, always using samples of the same size as the measured area would significantly reduce measurement variability and improve accuracy and reproducibility.

The p-XRF measurements for the irrigation experiment had to be conducted using a different device than the one used for the rock samples weathered in the climate chamber. Consequently, the absolute values obtained were not directly comparable.

To address this, the rock cubes from the irrigation experiment were also measured using the same p-XRF device employed for the climate chamber samples once, ensuring comparable results for the surface composition, as presented in Tab. 3.1. Nevertheless, the relative changes in the elemental composition on the surfaces remained as reliable as those observed in the climate chamber experiment. Consistency was maintained by measuring the same spot on the samples for each analysis, as was done for the climate chamber experiment. The overall changes observed were relatively minor, with maximum values remaining below ± 5 %, except for the change of the S content.

Considering the ICP-OES measurements it is noted here that, due to significantly higher Mn concentrations in some samples compared to those from the climate chamber, several concentrations exceeded the calibration range, necessitating remeasurement. These re-measurements confirmed the initial results and the mean values of both sets of measurements were subsequently used. For S, the concentrations in the artificial rainwater adjusted to pH 4 and 3 were notably high, due to the H_2SO_4 used in the stock solution for pH adjustment. As a result, the blank samples exhibited elevated S concentrations, rendering it impossible to accurately determine the amount of S dissolved in the samples at pH 3.

In the first set of artificial rainwater samples collected after the initial irrigation experiment at pH 8, the element concentrations were significantly elevated compared to those in the second experiment conducted at the same pH, as previously described in Chapter 5.2.3. It was therefore assumed that some secondary minerals remained on the surface and were subsequently washed away, even though the samples had been rinsed prior to the start of the first experiment. This observation explained the pronounced colour and chemical changes observed after the first set of experiments at pH 8. The ICP-OES results from the first experiment were consequently excluded from the overall data analysis. To prevent such an issue, it would have been necessary to rinse the samples more thoroughly or to perform an initial irrigation cycle with demineralised water without collecting water samples. On Murujuga, a rainwater pH of 8 has not been observed, either in the present or in the past. Therefore, the results obtained at pH 8 were less important compared to those for lower pH values.

5.3.2 Results

5.3.2.1 Rock varnish samples

The surfaces of the rock samples used in the irrigation experiment appeared more uniform than those of the samples used in the climate chamber experiment, with the varnish being relatively homogeneous, particularly on the gabbro samples (Fig. 3.2). Nevertheless, the chemical compositions measured on these samples varied significantly, with Mn contents ranging from 0.26 to 9.10 wt. %. In combination with the homogeneous appearance of the varnish, this suggested that the varnish thickness varied considerably among the samples, potentially allowing for differing contributions from the underlying weathered rind in the chemical composition measurements using the p-XRF.

The colour and p-XRF measurements revealed that the weathering-induced changes on these samples were less pronounced than those observed in the climate chamber experiment, which was expected due to the significantly lower weathering time. The most significant colour differences were detected after the initial irrigation experiments, with these differences diminishing over time and reaching their lowest values after the final experiments at pH 3. This trend indicates a high rate of change at the beginning of the experiments due to some secondary minerals that were washed away, similar to the pattern observed in the climate chamber experiment. This assumption is supported by the high measured element concentrations in the water samples of the first experiment conducted at pH 8. By the end, the measurements were within the range of the reference samples stored under controlled conditions. Notably, the granophyre samples exhibited colour changes only at the first measurement, remaining stable throughout the subsequent experiments, mirroring the behaviour of the samples weathered in the climate chamber. The measured ΔL^* values were consistently negative, aligning with the results of the climate chamber experiments.

The chemical changes observed for most elements and sample groups were also the highest after the initial set of experiments conducted at pH 8. An exception was the Si content in the granophyre samples, which showed only minimal changes (Fig. 5.3a). Particularly notable was the sharp decrease in S content following the initial irrigation experiments, a trend also observed in the climate chamber experiment. It was hypothesised that SO_x emitted by industrial complexes on Murujuga was deposited on the rock surfaces in an unknown form (see Chapter 4.3.2.1). As the surface mineralogy of these samples was not examined, it remains unclear which S-bearing mineral phases were present and subsequently removed during the first experiment at pH 8. The sum of the dissolved S in the rainwater samples correlated with the measured amount of S on the surface area measured before the start of the irrigation experiments, indicating that more S on the surface led to more S being dissolved in the rainwater and / or more S-bearing phases being washed away (Fig. 5.10).

In combination with the colour measurements, it can be assumed that, as in the climate chamber experiment, the rock samples underwent significant changes during the first two sets of experiments at pH 8, each with 10 minutes of simulated rainfall. The ICP-OES data indicates that most of this changes have happened during the first of the two experiments. These changes are thought to have appeared primarily due to secondary minerals being washed away or dissolved, despite the samples being rinsed with demineralised water before the experiments to remove sawing dust from the surface. This initial rinsing apparently did not remove all secondary minerals, as also observed in the climate chamber experiment. Here, it has to be noted again that the simulated irrigation was significantly longer than the rinsing process and the amount of water in contact with the rock varnish was therefore much higher.

Similar to the rock samples used in the climate chamber experiment, the samples used for the irrigation experiment exhibited significant changes after the initial phase as described above. A correlation was observed between the change in K concentration and the changes in Fe and Al content measured on the surface over the course of the experiments (Fig. 5.9). Although the correlation coefficients were relatively high, they do not appear to reflect a genuine trend, as there was no consistent increase or decrease over the course of the experiments. This, also considering the low range of changes (approximately 5 %), appears more plausible than a genuine correlation of these parameters.

At the end of the experiment, the results from different samples revealed a correlation between the Fe content on the surface and the change in Fe content, suggesting that higher initial Fe contents led to greater relative changes. However, this correlation was primarily driven by the two gabbro samples, for which significantly higher Fe contents and changes were observed. When analysed separately, the two rock types, with only three data points per group, did not exhibit strong individual correlations. A similar observation was made for the relative changes in Mn and Fe concentrations, which also appeared to be correlated. In this case, the higher correlation coefficient was largely due to the initial increase of the Fe and Mn content on the gabbro samples (Fig. 5.3).

The PCA of the samples used in the irrigation experiments revealed that, similar to the samples weathered in the climate chamber experiments, it was possible to distinguish the two rock types from each other using different parameters. However, the differences between the samples of the same rock type were still relatively large (Fig. 5.12).

5.3.2.2 Artificial rainwater samples

The irrigation experiments allowed for the examination of a broader pH range (3 to 8) than the climate chamber experiment, which was limited to testing two pH values. This wider range enabled a more comprehensive investigation of how varying pH levels influenced the dissolution rate of intact rock varnish from Murujuga. A key finding was that, irrespective of the artificial rainwater's pH within the chosen range, measurable amounts of material consistently dissolved in contact with the rainwater, even after only brief contact with the rock surfaces. This observation aligns with the findings of a previous study, where artificial rainwater with a pH of 4.8 was rinsed over Murujuga rock samples (Neumann et al., 2022), as well as with the findings from the analysed rainwater samples from the climate chamber experiment. The concentrations of dissolved elements varied significantly depending on both the pH of the rainwater and the type of rock.

To ensure accuracy, the element concentrations in the rainwater samples were calculated by subtracting the concentrations measured in corresponding blank samples.

This approach eliminated potential contamination from the artificial rainwater or the plastic tubes used during the experiments, even though the tubes were cleaned beforehand. Thus, the concentrations presented in Chapter 5.2.3 are solely attributed to the dissolution of components from the rock varnish. The experimental design ensured that only the varnish layer and not the underlying host rock came into contact with the rainwater. This was achieved by coating the cut sides of the cubes with Araldite® resin, which is stable under the simulated conditions and does not contain any of the measured elements.

The overall concentrations of the measured elements in the rainwater samples were relatively low, remaining well below the maximum solubility limits for these elements at the tested pH levels and water temperature. For instance, the solubility of Mn in aqueous solutions at pH 7 is approximately 1000 ppb at room temperature (Hem, 1963), with solubility increasing under more acidic or alkaline conditions, following a characteristic U- or V-shaped curve (Appelo & Postma, 2004). However, the measured Mn concentrations at pH 7 were significantly lower, with mean values around 200 ppb. Even at pH 3, where higher concentrations were recorded, most samples exhibited Mn concentrations below 1000 ppb (Fig. 5.5d). Similarly, for Si, whose solubility increases at higher pH levels (House & Orr, 1992), the maximum solubility at room temperature is about 150 ppm in the pH range between 3 and 8 (Iler, 1979), whereas maximum measured concentrations remained below 1 ppm across all pH values. The solubility of Fe at the tested pH values is also much higher than the concentrations measured in the rainwater samples (Furcas et al., 2022).

These findings suggest that the concentrations in the rainwater samples were not restricted by the maximum solubility of the elements in aqueous solutions. Instead, the limiting factors are believed to have been the dissolution and alteration rates of the minerals under the given experimental conditions. Dissolution rates are known to increase under both acidic and alkaline conditions, as observed for elements such as Fe and Mn (Schwertmann, 1991; Martin, 2005). This explains the higher concentrations measured at pH 3 and 4 for most elements, as well as slightly higher concentrations at pH 8 for some elements. The results indicate that the amount of material dissolved was primarily constrained by these dissolution rates and thus by the limited contact time between the artificial rainwater and the sample surfaces.

Contrary to this assumption, the varying angles of the sample surfaces, which resulted in longer or shorter contact times between the water samples and the varnish surface, did not significantly impact the element concentrations in the rainwater samples, as illustrated in Fig. 5.8. The angle of 30° was selected to facilitate comparison with the climate chamber experiments, where samples were weathered at the same angle. It was initially assumed that steeper surface angles would lead to lower element concentrations in the rainwater samples due to faster runoff and reduced contact time between the artificial rainwater and the varnish surface. While measurable differences were observed, as described in Chapter 5.2.3, these differences were inconsistent across different elements, making it impossible to deduce a clear influence of the surface angle on the amount of material dissolved. Nevertheless, it is reasonable to assume that significantly longer contact times between the artificial rainwater and the rock varnish would result in higher element concentrations in the water samples, as suggested by previous studies (Ramanaidou et al., 2017).

For most elements, particularly Si, as well as Al, Ca, K, and Na, the element concentrations did not increase at pH 8 (Figs. 5.5 & 5.6), when excluding the results of the first experiment at pH 8 which were thought to be unreliable and mainly due to secondary minerals and dust that was washed off and not due to higher dissolution, as described earlier and in Chapter 5.2.3. Only for Fe, Mn, and Mg the concentrations increase at pH 8. Under acidic conditions (pH 3 & 4) significantly higher concentrations were measured for all elements, except for Si. Under the environmental conditions observed on Murujuga, where pH values ranged from 4.4 to 5.2 in 2019 (MacLeod & Fish, 2021) and from slightly above 4 to around 6 in 2022 and 2023 (MRAMP, 2023), the changes observed at pH 8 are less relevant. However, the increase in dissolution rates and element concentrations between pH 5 and 4 could have significant implications. Due to the missing increase towards higher pH for most of the elements, the characteristic U- and V-shaped curves often observed when plotting mineral dissolution rates or solubility against pH (Appelo & Postma, 2004) were only observed for some elements like Fe and Mn.

Mineral dissolution reactions

The most important elements in the rock varnish are Si, Al, Fe, and Mn due to the main mineral components identified in the varnish, which are hematite (Fe_2O_3), kaolinite ($Al_2Si_2O_5(OH)_4$), and birnessite ($(Na,Ca)(Mn^{4+},Mn^{3+})_2O_4 \bullet 1.5H_2O$) as described in Chapter 3.1.3.2.

For Si, as one of the main components of the varnish, concentrations exceeded 0.05 ppm for all pH values test, with no observable significant increase at lower or higher pH levels. The absence of an increase in the measured concentrations, and consequently in the dissolution rate, suggests that a potential shift in the rainwater pH on Murujuga towards more acidic conditions would not affect the amount of Si dissolved from the varnish surface. Interestingly, it was observed that the total amount of dissolved Si over the course of the irrigation experiments was negatively correlated with the Si content measured on the sample surface. This suggested that more Si was dissolved when the overall Si content on the samples was lower. This finding is counterintuitive, as one would expect higher Si availability to lead to more dissolved material and therefore to higher element concentrations in the analysed rainwater samples. However, given the small sample size of six samples from two different rock types, it is possible that this observed relationship is not genuine. This interpretation is further supported by the absence of any correlation between surface Si content and dissolved Si amounts in the samples weathered in the climate chamber experiment.

The amount of dissolved Si was slightly higher in the water samples in contact with gabbro rocks during the irrigation experiments, whereas the reverse was true for the samples from the climate chamber experiment. Notably, the amount of Si dissolved in the climate chamber water samples was significantly higher for both rock types, with mean concentrations exceeding 0.1 ppm at pH 5 and 7.

The Al concentrations in the water samples were significantly lower, with values below 10 ppb at pH 5 to 8. However, concentrations increased at pH 4 and 3, reaching values above 50 ppb for the gabbro samples at pH 3. This increase at lower pH levels is relevant for assessing how a potential decrease in the rainwater pH on Murujuga might impact varnish dissolution. Similar to Si, a negative correlation was observed between the total amount of dissolved Al and the initial Al content on the sample surface. However, this correlation was even weaker, and when the two rock types were analysed separately, no correlation was found. This suggests that, as for Si, there may be no genuine relationship between these two parameters.

Si and Al were primarily bound in the varnish within kaolinite ($\mathrm{Al_2Si_2O_5(OH)_4}$), while Si also occurred in smaller quartz crystals. Therefore, understanding the pH dependent dissolution of kaolinite is critical for interpreting the measured concentrations. Under acidic conditions, the dissolution reaction of kaolinite leads to the production of silicic acid and is represented as follows (Cama et al., 2002):

$$Al_2Si_2O_5(OH)_4 + 6H^+ \longrightarrow 2Al^{3+} + 2H_4SiO_4 + H_2O$$

It is well established that the initial dissolution rate of kaolinite in undersaturated solutions is significantly higher than in solutions nearing saturation. Consequently, it takes a considerable amount of time for a solution to reach saturation (Polzer & Hem, 1965). Cama et al. (2002) demonstrated that for the dissolution reaction, the rate increases both as pH decreases and as temperature rises in acidic solutions far from saturation. This applies to the artificial rainwater used in the experiments as well as to natural rainwater on Murujuga. The observed dissolution rates range at 25 °C from $10^{-14.2}$ mol/m^{2}s at pH 5 to $10^{-13.6}$ mol/m^{2}s at pH 3 and at 50 °C from 10^{-14} mol/m^{2}s at pH 5 to $10^{-12.6}$ mol/m^{2}s at pH 3 (Cama et al., 2002). Therefore, it can be assumed that the pH dependent dissolution rates on Murujuga fall within this range, given ambient temperatures mostly around 30 °C and rock surface temperatures occasionally exceeding 50 °C due to solar radiation.

Furthermore, the dissolution of kaolinite is known to be incongruent, resulting in a slightly higher release of Si than Al (Yang & Steefel, 2008). This is basically in agreement with the higher Si concentrations compared to Al in the varnish. At pH 4, the Al concentration was approximately three times higher than at pH 5, consistent with the dissolution rates proposed by Cama et al. (2002), which are about 3.5 times higher between these pH levels at both 25 and 50 °C. At pH 3, the Al concentrations in the artificial rainwater samples were around 15 times higher than at pH 5, aligning with the proposed dissolution rates for kaolinite, which are approximately 6 to 30 times greater at pH 3 compared to pH 5, depending on the temperature (Cama et al., 2002).

It can therefore be concluded that kaolinite within the rock varnish dissolves under mildly acidic conditions at relatively slow rates that increase significantly as pH decreases. A reduction in the rainwater pH would consequently increase the amount of kaolinite dissolved in the varnish during each rainfall event, although the overall quantities remain small, as indicated by the low Al concentrations in the rainwater samples. The much higher concentrations of Si at pH > 3 cannot solely be attributed to the incongruent dissolution of kaolinite. This suggests that additional Si-containing material must also be dissolving. Moreover, the missing increase in Si concentrations at lower pH levels (< 4) was unexpected, as similar proportional increases would be anticipated if the dissolution of kaolinite was the sole source. The reasons for this discrepancy remain unclear. It has to be noted that even these small amounts of dissolved material can influence the physical weathering observed.

The Fe was primarily bound in hematite on the surface. The concentration curve for Fe indicated higher dissolution rates of hematite under acidic conditions and a slight decrease under alkaline conditions. However, a significant increase in Fe concentrations in the rainwater samples was observed only at pH 3 for the gabbro samples. The pronounced differences in the concentrations of the rainwater samples that had been in contact with gabbro and granophyre suggested that a greater amount of hematite had been dissolved from the gabbro samples. Overall, the Fe concentrations, with mean values ranging from < 4 ppb at pH 5 to around 15 ppb at pH 5, were significantly lower than those of the rainwater samples collected during the climate chamber experiment, where the mean Fe concentrations at pH 5 were approximately 15 ppb. For both groups of samples, it was notable that the Fe concentrations exhibited more outliers compared to Si, Al, and Mn concentrations, and the overall range of results was significantly greater than that of some other elements, especially at pH 6 to 8 (Fig. 5.5).

Hematite, along with lepidocrocite, which was identified on the surface of one rock sample weathered in the climate chamber, are known to be among the more stable Fe-oxide-phases (Schwertmann, 1991; Furcas et al., 2022). Hematite, an Fe(III)-oxide (Fe_2O_3), was observed to undergo partial hydration when in contact with water, forming goethite-like (FeOOH) molecules (Jang et al., 2007; Zhang et al., 2021). This hydration step is essential for the dissolution of hematite in aqueous solutions, as the two known dissolution mechanisms, excluding organic material, rely on the presence of FeOOH. These two mechanisms are either proton-promoted (1) or reductive (2) (Schwertmann, 1991; Martin, 2005):

$$(1)\ FeOOH + 3H^+ \longrightarrow Fe^{3+}(aq) + 2H_2O$$

$$(2)\ FeOOH + e^- + 3H^+ \longrightarrow Fe^{2+}(aq) + 2H_2O$$

In both cases, dissolution under acidic conditions relied on the presence of H^+ ions, leading to higher dissolution rates at lower pH values (Schwertmann, 1991; Martin, 2005). The Pourbaix diagram for Fe species shows a stability field for Fe^{3+}(aq) at pH < 3 and for Fe^{2+}(aq) at pH < 8 as shown in Fig. 5.13b (Pourbaix, 1974; Martin, 2005; Black et al., 2017b). The calculated dissolution rates for FeOOH at 25°C begin to increase at pH < 6 and are higher for the reductive reaction, as this involves Fe^{2+}(aq), which is more stable at higher pH values (Martin, 2005).

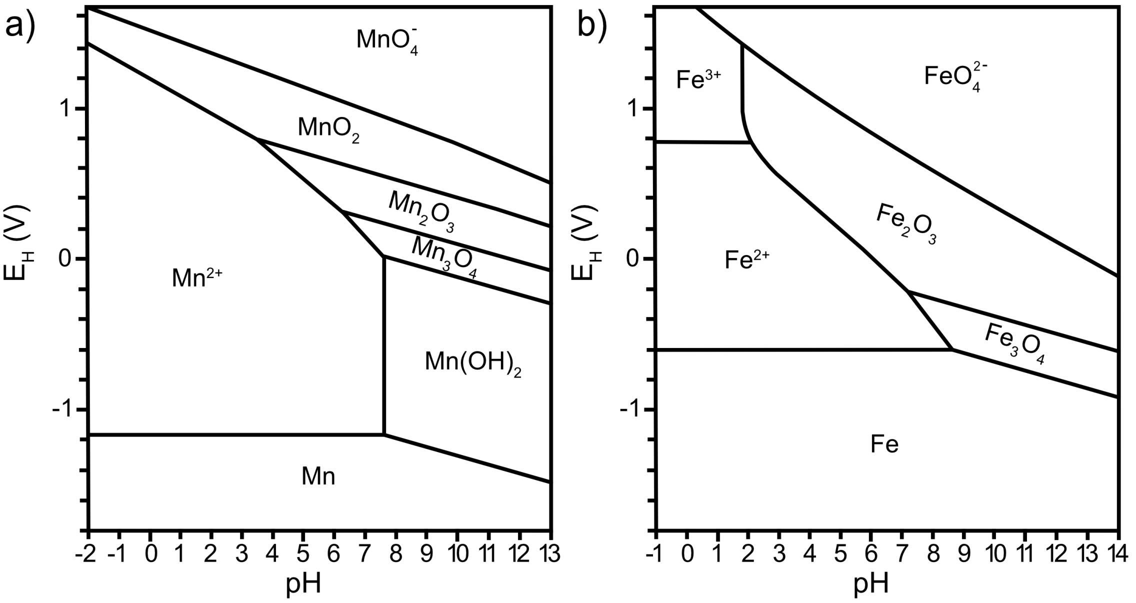

Figure 5.13: E_H-pH diagrams for (a) Mn and (b) Fe showing the possible stability fields of different Fe- and Mn-phases in an aquaeous system at 25 °C and 1 atm depending on the pH and the redox potential. The figures were adapted and simplified form Pourbaix (1974).

As the Fe dissolution rates in the irrigation experiments started to increase significantly at pH < 4, it can be assumed that the dominant reaction was proton-promoted, resulting in mostly Fe^{3+}(aq) ions in the rainwater samples. These ions are stable only at pH values below 4. This reaction was slower, as mentioned previously, which explains the low concentrations of Fe in the dissolution. The calculated dissolution rates were in a similar range to those for kaolinite (Cama et al., 2002; Martin, 2005), aligning with the concentrations of Al and Fe in the rainwater samples, which were of a similar order of magnitude.

This hypothesised dissolution process requires the presence of water and the dissolution rates increased significantly when the pH level dropped below 4. The present-day pH on Murujuga is still known to be significantly higher (MacLeod & Fish, 2021; MRAMP, 2023). Therefore, it could be inferred that the dissolution of hematite remains comparatively low on Murujuga, as was observed for the samples used in the climate chamber and irrigation experiments.

The observed slight increase in Fe solubility at pH 8 is not further discussed, as such pH values have not been observed on Murujuga regularly, either in the present or in the past. It is noteworthy that the lowest Fe concentrations were not observed near neutral conditions, as might have been expected due to the low H^+ ion concentrations in such conditions, but at pH 5 for the gabbro samples and between 4 and 6 for the granophyre samples. This finding corresponded to the observed concentrations in the water samples from the climate chamber experiment, where no significant difference between pH 5 and 7 was evident.

The Mn was primarily bound in birnessite crystals, although small amounts of todorokite were also identified, as shown in Chapter 3.1.3.2. The Mn concentrations measured in the irrigation experiments were lowest at pH 5, similar to the trend observed for Fe concentrations. With most values ranging between 100 and 150 ppb at pH 5, these concentrations were nearly ten times higher than those in the water samples collected during the climate chamber experiment. At pH 7, the concentrations were more than ten times higher than in the climate chamber experiment, reaching approximately 200 ppb, while the samples from the climate chamber experiment had values around 16 ppb, as previously mentioned.

Due to the broader range of pH values compared to the climate chamber experiment, significant variations in Mn concentrations were observed during the irrigation experiments. Under alkaline conditions, a gradual increase in Mn concentrations was noted, with values around 250 ppb at pH 8. Conversely, under acidic conditions, Mn concentrations rose sharply for pH values below 5, reaching mean concentrations of 330 ppb at pH 4 and 850 ppb at pH 3. This indicated that the dissolution rates of Mn-containing minerals, primarily birnessite, increased substantially at lower pH levels. The total amount of dissolved Mn was positively correlated with the measured Mn content on the surface, suggesting that higher surface Mn contents led to more dissolved material (Fig. 5.10).

Birnessite is a Mn(III,IV)-oxide with the formula $(Na,Ca)(Mn^{4+},Mn^{3+})_2O_4 \bullet 1.5H_2O$, containing both Mn^{3+} and Mn^{4+} ions (Martin, 2005) in its complex structure. Todorokite is also a Mn(III,IV)-oxide with the formula $(Ca,Na,K)(Mn^{4+},Mn^{3+})_6O_{12} \bullet nH_2O$. Both of these Mn-oxide-phases have the nominal formula MnO_2 and, along with hydrated Mn-oxide ($Mn^{3+}OOH$), can dissolve in aqueous solutions under slightly acidic conditions via a reductive reaction (Martin, 2005; MacLeod & Fish, 2021):

$$MnO_2 + 2e^- + 4H^+ \longrightarrow Mn^{2+}(aq) + 2H_2O$$

$$MnOOH + e^- + 3H^+ \longrightarrow Mn^{2+}(aq) + 2H_2O$$

The Pourbaix diagram for Mn species (Fig. 5.13a) indicates that Mn_3O_4 is the least stable phase at lower pH values and is theoretically stable at pH > 7 (Pourbaix, 1974; Black et al., 2017b; Smith et al., 2022), although some sources suggest stability only at pH > 9 (Martin, 2005), which could explain the absence of Mn_3O_4-phases in the analysed rock varnish, other as stated by MacLeod and Fish (2021). Experimental studies demonstrated that a transformation between Mn_3O_4 and MnOOH occurred already at pH values between 8 and 8.5 (Lefkowitz et al., 2013). At slightly lower pH values, between 7 and 7.5, a transformation of MnOOH to MnO_2 was observed (Lefkowitz et al., 2013). This observation is consistent with predictions from another study (Martin, 2005). At lower pH values, the reductive dissolution of MnO_2 to Mn^{2+} in aqueous solutions is accelerated, along with the dissolution of other Mn-phases, due to the increased concentration of H^+ ions (Martin, 2005). The abundance of different Mn-phases and their highly pH dependent dissolution rates result in narrow stability windows, rendering Mn-phases particularly susceptible to pH changes. It is therefore assumed that even minor pH fluctuations can significantly alter Mn precipitation and dissolution dynamics (MacLeod & Fish, 2021).

At higher pH values, the precipitation of Mn-phases is favoured (MacLeod & Fish, 2021). Conversely, at lower pH values, it is hypothesised that not only does the structure of the oxides change (Lefkowitz et al., 2013), but also portions of Mn dissolve into Mn^{2+} ions in aqueous solution (Black et al., 2017b; MacLeod & Fish, 2021). While the dissolution rates for birnessite and todorokite are not well established, the dissolution rate for hydrated Mn-oxide (MnOOH) has been calculated to be in the order of 10^{-7} to 10^{-6} mol/m^{2}s at pH 4 (Martin, 2005). This rate is several orders of magnitude higher than the dissolution rates calculated for kaolinite and Fe-oxide-phases discussed earlier, which is consistent with the substantially higher Mn concentrations in the water samples.

Not only were the absolute Mn concentrations in the rainwater samples significantly higher than the Al and Fe concentrations, but the relative dissolution rates were also elevated when the amounts of Fe and Mn in the rainwater samples were normalised to the Fe and Mn content on the corresponding rock samples (Figs. 4.27 & 5.7). Data from the irrigation experiments revealed that the normalised concentration of Mn at pH 7 and 8 was approximately 250 times higher than that of Fe. This ratio increased towards lower pH values, reaching up to 1000 times higher concentrations for the granophyre samples at pH 4 and approximately 750 times higher concentrations for the gabbro samples at pH 5. The normalised Mn to Fe concentration ratio decreased at pH 3 due to the increased dissolution of Fe, as aforementioned.

These comparably rapid dissolution rates of various Mn-phases, which further accelerate at lower pH values, indicate that a decrease in the pH of rainwater on Murujuga results in an enhanced alteration of Mn-oxides, which are a critical component of the rock varnish. Studies have shown that birnessite sheets begin to degrade at pH < 7 (Lefkowitz et al., 2013). The present-day pH on Murujuga is known to be below 5 in many instances (MacLeod & Fish, 2021; MRAMP, 2023), leading to the conclusion that Mn dissolution is already significantly accelerated under these conditions. This is supported by the observed Mn concentrations in artificial rainwater samples (Fig. 5.5), the known dissolution reactions, the Pourbaix diagram for Mn (Pourbaix, 1974; Martin, 2005; Lefkowitz et al., 2013; Black et al., 2017b; Smith et al., 2022), and the estimated dissolution rates presented in Chapter 6.1.

It has been proposed that rock varnish cannot form in areas where rainwater has a pH < 5.6 (Bednarik, 2009). Although, it is plausible that the formation of new Mn-oxide minerals is inhibited at this pH, the precise pH threshold at which Mn-phases are exclusively dissolved and no formation of new Mn minerals occurs, remains disputed, with various thresholds proposed (Bednarik, 2009; Lefkowitz et al., 2013; Goldsmith et al., 2014; MacLeod & Fish, 2021; Smith et al., 2022). Nonetheless, it can be definitively stated that at all tested pH values, significant Mn dissolution occurred, with dissolution rates increasing under more acidic conditions ($pH < 5$).

These findings, along with the observed concentrations of Al, Fe, and Si across all tested pH values, contradict the results of a previous study, which stated that significant dissolution of Al, Mn, and Fe begins only at pH 3 or below (Ramanaidou et al., 2017). It is likely that the earlier study did not detect these elements at higher pH values due to the large volume of solutions used (100 ml) and relatively high detection limits (Chapter 1.1; Ramanaidou et al., 2017). As mentioned in Chapter 1.1, contrary to the assertions of Ramanaidou et al. (2017), the dissolution of critical varnish components such as Mn-oxides does not necessarily result in the destruction of the entire varnish. It is possible that even if some material is dissolved, the varnish regrowth rate could be equal to or greater than the dissolution rates.

For Mn, Fe, and several other elements measured, the lowest concentrations were observed at pH 5 to 6, whereas the lowest concentrations would typically be expected near neutral conditions around pH 7 (Appelo & Postma, 2004; Martin, 2005). The demineralised water used in the experiments had a pH of approximately 5.5 if no stock solution was added. To prepare artificial rainwater at pH 6 to 8, NaOH was added (Chapter 5.1.3.2). For acidic rainwater with pH 3 to 5, HNO_3 and H_2SO_4 were used, as these acids reflect the known NO_x and SO_x emissions on Murujuga, which can lead to the precipitation of N- and S-bearing phases on the rock surface, thereby lowering the pH (MacLeod & Fish, 2021; Smith et al., 2022). No Na was added to the artificial rainwater at $pH < 5$, although higher Na concentrations are likely in Murujuga's rainwater due to the site's proximity to the ocean and the influence of aerosols and sea spray.

For nearly all elements measured, the concentrations began to increase at a $pH < 5$. This suggests that a reduction in the pH of rainwater on Murujuga to values below 5 could represent a critical threshold at which alteration rates significantly accelerate. In the climate chamber experiment, a pH of 5 was selected to simulate conditions that are not only observed on Murujuga in certain instances, but are also prevalent under many circumstances. This choice made the obtained data more robust, ensuring that the simulated conditions could not be dismissed as excessively extreme. Conversely, slightly lower pH values would likely have resulted in more pronounced differences between the two sample groups, as indicated by the pH dependence of dissolution rates.

It is notable that the overall element concentrations in the rainwater at pH 5 and 7 from the climate chamber experiment and the irrigation experiments varied significantly depending on the measured elements (as previously discussed for Si, Fe & Mn). Ambient conditions in both types of experiments were similar, with rock surface temperatures of approximately 30 °C and the same artificial rainwater used. Moreover, the stock solutions employed to adjust the pH of the artificial rainwater were identical for both experiments, as was the demineralised water used as the base for its preparation.

However, significant differences were observed in the composition and surface structure of the rock samples, even within the sample groups of the individual experiments. Some samples from the climate chamber experiment are characterised by varnish structures and surface chemical compositions that are similar to those of the rock samples used in the irrigation experiments. Consequently, it was reasonable to expect comparable results. The only notable difference between the experiments was the type of nozzles used for irrigation. In the climate chamber experiment, nozzles producing larger drops were employed, whereas in the irrigation experiments, the nozzles nebulised the water, creating very small droplets. It is therefore assumed that these differences in irrigation methods account for the observed variations in concentrations, as all other parameters were either similar or comparable.

6 Discussion

The experimental setup, analytical methods, and results of the long-term weathering experiment and the irrigation experiments that were conducted were already discussed in Chapters 4.3 and 5.3, respectively.

In Chapter 4.3, it was examined how the different samples weathered in the climate chamber changed over the course of the experiment and how these changes depended on the weathering conditions, particularly the host rock and varnish types of the individual samples. In the following it is shown how the observed different types of varnish behaved, how vulnerable they are to alteration and how they can be characterised, as well as which other components were present on the sample surfaces (Chapter 6.2).

The processes of mineral dissolution and the pH dependence of dissolution rates were discussed in Chapter 5.3, alongside the differences between the two host rock types. Combined with the analysed varnish composition and mineralogy described in Chapter 3.1.3, it is possible to estimate pH dependent dissolution rates for a model varnish, which are presented in the following section.

6.1 Prediction of natural varnish dissolution rates

The amount of dissolved Fe and Mn at different pH levels (Chapter 5.2.3), in combination with the varnish composition from quantitative EMP data (Chapter 3.1.3.2) and the annual precipitation on Murujuga, were used to estimate an order of magnitude for the varnish dissolution rates as a function of pH. For this estimation, a model varnish area with the mean composition derived from the ESM measurements and a size of 1 x 1 cm^2 with a thickness of 1 μm was assumed. This varnish was considered to be composed of 11.1 wt. % Fe, 11.7 wt. % Si, 10.1 wt. % Al, and 9.6 wt. % Mn, along with minor amounts of other elements. This composition is based on the quantitative EMP data of black varnish samples from rocks collected on Murujuga in 2022. The data that is fully given in the digital supplementary material.

To calculate the density of the varnish, the estimated chemical composition was converted into a mineralogical composition. Only the three primary components kaolinite, hematite, and birnessite were considered relevant. This approach yielded an approximate composition of 55 vol. % kaolinite (48 wt. %), 9 vol. % hematite (16 wt. %), and 19 vol. % birnessite (19 wt. %). The remaining 17 vol. % likely are other phases and were excluded from the density calculation. The estimated density of the varnish was 3.00 g/cm^3, considering a density of 2.63 g/cm^3 for kaolinite, 5.26

g/cm^3 for hematite, and 3.00 g/cm^3 for birnessite. Consequently, the model varnish with dimensions of 1 x 1 cm^2 and 1 µm thickness was calculated to have a weight of 3 mg, containing 0.28 mg of Mn and 0.33 mg of Fe.

Based on an annual precipitation of approximately 297 mm on Murujuga (Australian Government, Bureau of Meteorology, 2023), 29.7 ml of rainwater per year would flow over the model varnish surface area of 1 cm^2. By incorporating the different element concentrations measured in the artificial rainwater samples, it is possible to estimate the annual dissolution of Mn and Fe as a function of pH and, consequently, the time required to dissolve the hematite and birnessite contained in a 1 µm thick layer of the model varnish. The results of this ballpark estimates are presented in Tab. 6.1.

The lower Mn and higher Fe concentrations observed in the rainwater samples from the climate chamber experiment resulted in much lower estimated dissolution rates for Mn and slightly higher rates for Fe. Particularly, the high Mn concentrations in the irrigation experiment samples indicate high dissolution rates, so that a varnish layer of 1 µm thickness potentially would dissolve in less than 10 years. A key observation was that dissolution rates for Fe and Mn were the lowest at pH values between 5 and 6, while a decrease of the pH to values below 5 caused a significant increase in dissolution rates. This finding suggests that the currently observable pH levels on Murujuga (MacLeod & Fish, 2021; MRAMP, 2023) are sufficiently low to substantially accelerate rock varnish alteration.

As previously noted, Mn and Fe concentrations at pH 7 in the irrigation experiments were slightly elevated, though the calculated rates were still lower than those under more acidic conditions. As no pH values > 7 were observed on Murujuga, the results for pH 8 were not further taken into account.

The calculated dissolution rates for Fe-phases were significantly lower than those for Mn-phases, indicating that over time, the varnish would become relatively depleted in Mn, with a concurrent increase in the relative Fe content compared to unweathered varnish. This finding underlines the greater susceptibility of Mn-phases to dissolution under acidic conditions. In addition, this chemical weathering of mainly Mn-oxide-phases will likely also increase the varnish's vulnerability to physical alteration, as the dissolution of Mn-phases will lead to higher porosity of the varnish, creating new weak points where, for example, material is more likely to chip off.

The estimated Mn content in this model varnish was significantly higher than that suggested by p-XRF measurements. As described in Chapter 3.1.3, p-XRF measurements include contributions from the underlying weathered rind and areas where the varnish is not intact, both of which are characterised by significantly lower Mn concentrations. Consequently, the Mn content in the model varnish is more likely to be overestimated rather than underestimated relative to real-world conditions. Additionally, the artificial rainwater in the collected samples interacted with both, intact varnish areas with high Mn concentrations and other regions with lower Mn content. Therefore, the estimated dissolution rates are likely conservative and tend to result in lower values compared to actual environmental conditions.

Table 6.1: Estimated dissolution rates for a model varnish using the measured Fe and Mn concentrations in the artificial rainwater samples for both, the climate chamber and irrigation experiments at different pH values.

	Climate Chamber		**Irrigation experiments**				
pH	**5**	**7**	**3**	**4**	**5**	**6**	**7**
C_{Mn} (µg/L)	16.6	15.1	853.0	331.0	133.1	145.4	199.8
Mn dissolution rate (µg/year)	0.493	0.448	25.334	9.831	3.953	4.318	5.934
Dissolution rate$_{Mn}$ (µm/year)	0.017	0.016	0.879	0.341	0.137	0.150	0.206
Dissolution rate$_{Mn}$ (years/µm)	58	64	1	3	7	7	5
C_{Fe} (µg/L)	12.4	14.5	10.0	4.6	3.4	4.1	6.9
Fe dissolution rate (µg/year)	0.368	0.431	0.297	0.137	0.101	0.122	0.205
Dissolution rate$_{Fe}$ (µm/year)	0.011	0.013	0.009	0.004	0.003	0.004	0.006
Dissolution rate$_{Fe}$ (years/µm)	91	77	112	244	330	274	163

Given the recently observed pH values below 5 on Murujuga on certain occasions (MacLeod & Fish, 2021; MRAMP, 2023), which are associated with significantly higher Mn dissolution rates, it is possible that the samples used for the experiments, collected in 2019 and 2022, already exhibit a reduced Mn content compared to their original state. To investigate this possibility, an older sample collected in 1994 by Robert Bednarik was additionally analysed and its Mn content was measured. This sample showed significantly higher MnO concentrations and, particularly, lower Fe-Mn ratios (see Chapter 3.1.3.1). The MnO content and Fe-Mn ratios measured on this older sample also align more closely with the results of varnish samples analysed by other researchers (Potter & Rossman, 1979; Wayne et al., 2006; Goldsmith et al., 2014; Xu et al., 2019; Dorn, 2020; Harmon et al., 2021; Rabbachin et al., 2022).

As the p-XRF technique was used for these measurements, it is theoretically possible that the observed differences are due to variations in the thickness of the Mn-rich varnish layer. This is because p-XRF may measure not only the outermost varnish layer but also underlying materials, depending on the sample's characteristics. However, quantitative data from the EMP measurements further support the conclusion that the varnish on the sample from 1994 contains a significantly higher Mn content. Specifically, a mean Mn concentration of 18.4 wt. % was found in the 1994 sample, compared to only 9.6 wt. % in the samples collected in 2022.

Although the number of compared samples is by far too small to confirm definitively that the varnish on the 2022 samples was already depleted in Mn due to lower rainwater pH levels on Murujuga, which could have led to increased Mn dissolution rates over time, this hypothesis warrants further investigation. Additional research on this assumption could yield more reliable data with relatively little effort. It is recommended that older samples of varnish from Murujuga, such as those preserved in museums and private collections, as well as a larger number of recent varnish samples from Murujuga, will be analysed using p-XRF. This method enables fast, non-destructive measurements without the need for sample preparation, making it highly suitable for such a survey.

6.2 Classification of varnish types and weathering processes

The observed and classified different components of the rock sample surfaces have to be analysed separately to understand the weathering processes and degradation effects, and how they affect the different types of varnish as explained in the discussion of the results of the long-term weathering experiment (Chapter 4.3). Main distinguishable components, sorted by their observed vulnerability to simulated weathering, were (1) minor surface components such as secondary minerals that were deposited on the sample surfaces, which were identified in some cases as on one granophyre sample (NR3) as thin lepidocrocite layer or as fine albite aggregates on another granophyre sample (SR1), as well as organic material that was identified on some of the granophyre varnish surfaces (SA3 & NA3), (2) orange to brown varnish layers with a porous structure that overlaid darker, more dense parts of the varnish, as found on some of the gabbro (NA2, SA1 & SA2) and granophyre (NR1 & SR1) samples that are mainly composed of hematite, (3) more dense and dark, nearly black varnish layers with a low pore space that contain relatively high amounts of Mn-oxides and characterise the outermost layers on gabbro (NA1, NA3 & SA3) and granophyre (NR1 & SR1) samples used in the climate chamber experiment and in the irrigation experiments, as well as underlying layers that were uncovered on some of the gabbro samples (NA2, SA1 & SA2) used in the climate chamber experiment, (4) a mixture of orange to red and black varnish with very high Mn contents and medium density and pore space on some of the granophyre samples (NR2 & SR3), as well as (5) very dense, red to brown varnish layers with a very high Fe and low Mn content and metallic lustre on some of the granophyre samples (NR3 & SR2). Additionally some red varnish spots were identified that were also measured using p-XRF (Tab. 3.2) but were to small and occurred only on a few samples making it not possible to further characterise this type of varnish, which is why it was excluded in the following.

Type 1: Varnish with secondary minerals at the surface

The presence of secondary minerals that were quickly washed away or dissolved was only observed in the high-resolution optical images of two granophyre samples (NR3 & SR1) but due to the fast colour change and decrease of certain element concentrations over the first 15 to 35 days of the experiment, it is assumed that different amounts of secondary minerals were present on nearly all of the samples. Especially the fast decrease of the S content indicates that the material might have been deposited on the surfaces of the samples due to the SO_x emission on Murujuga, likely in form of sulphates like small gypsum crystals or other minerals (e.g. arcanite, glauberite, or thénaridte). It was not possible to identify any of these secondary mineral phases, except for lepidocrocite (γ-FeO(OH)) on one sample (NR3) and albite on another (SR1), but the decrease of S, P, Ca, and K concentrations (it is recalled that the change of Na concentrations could not be measured) on all samples is a reliable indication

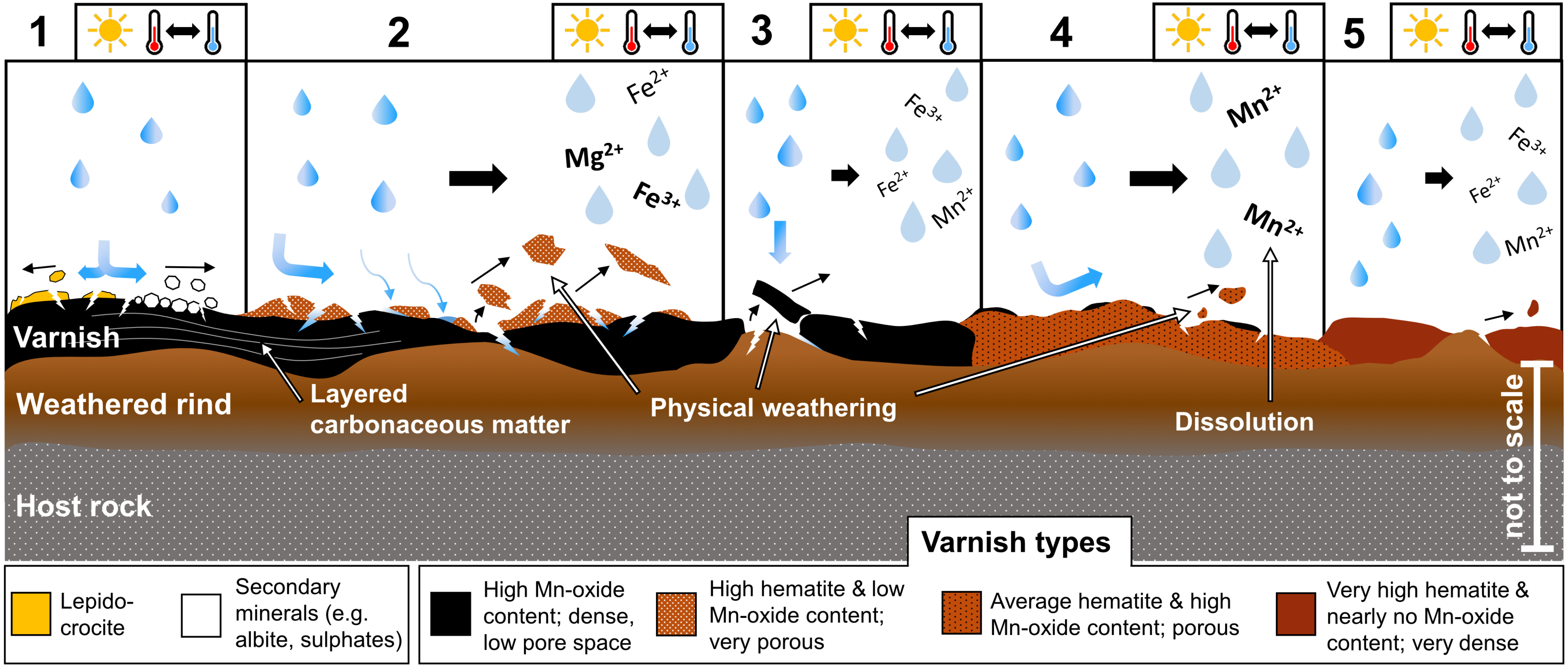

Figure 6.1: Schematic illustration of varnish types and observed surface degradation processes that determine respectively affect measured properties such as surface colour, chemistry, and weight. (1) Varnish areas with secondary minerals at the surface, (2) a porous, orange to brown varnish with underlying black varnish, (3) a dense, black varnish, (4) a red varnish with high Mn content and some pore space, and (5) a very dense red to brown varnish with very high hematite, i.e., high Fe content.

that material containing these elements was removed from the surface. The fast initial decrease of the S content observed in the irrigation experiments additionally supports this assumption, as well as the high amount of different elements in the water samples from the first irrigation experiment that are thought to be the results of secondary minerals that were washed away. The weathering processes were not directly observed but it is assumed that some of the material was already relatively loose before the start of the experiments, or quickly loosened due to a combination of physical effects like humidity and temperature changes, as well as due to chemical dissolution of some material, especially at interfaces between different components (Fig. 6.1). The material then was washed away by the simulated precipitation. Due to the measured contents of all elements analysed in the artificial rainwater samples it can be assumed that some of the material was also chemically dissolved. In addition some organic fibre was identified on two of the granophyre samples (SA3 & NA3), that was subsequently removed during the weathering experiment. Also some anatase and rutile crystals were identified in the varnish which could have been removed over the course of the weathering experiment.

Type 2: Orange to brown hematite-rich varnish

Porous orange to brown varnish layers on various samples partly disappeared over the course of the experiment. These layers contained comparably high amounts of Fe, mostly hematite, and less Mn and Al than the underlying darker layers, which were therefore believed to be richer in birnessite, todorokite, and kaolinite (Chapter 4.3.2.1. On this type of varnish the biggest changes were observed using the high-resolution optical images and other analytical methods. The gabbro samples with this type of varnish on them (SA1, SA2 & NA2) were the ones with the highest observed changes for multiple parameters and the samples with the most continuous changes over the course of the experiment, with gabbro sample NA2 forming an exception, where the measured colour change ΔE was relatively low. For these samples, it is assumed that after initially some looser parts of the varnish may have been washed away by rainwater, a mixture of physical and chemical alteration led to the observed changes (Fig. 6.1). The high Fe content in some of the rainwater samples proves that parts of at least the hematite were dissolved under both weathering conditions, but the overall weight change and the intensity of the observed surface changes are to high to explain all of the changes by dissolution only. It is noted that this type of varnish was found to be the most vulnerable among all types of varnish and that at pH 5, as well as pH 7 dissolution was observed. The changes at pH 7 were slightly lower as indicated by the observed colour change, the observed surface changes and the weight loss. The Fe-Mn ratio of this type of varnish is thought to be comparable for all samples to the measured spots of the orange varnish on the granophyre samples that ranged from 7 to around 20 (Tab. 3.2) and fits the anticipated high Fe and therefore hematite, as well as the low Mn content.

Type 3: Black Mn-oxide-rich varnish

The darkest type of varnish on the samples contained the highest amounts of Mn, which is mainly bound in birnessite and therefore has the lowest Fe-Mn ratios (Tab. 3.2). In addition to birnessite small amounts of todorokite, as well as kaolinite and hematite as the two other main components were found in this type of varnish. There was only one spot where a full removal of the black varnish was observed and additionally layers of the black varnish were uncovered in multiple spots under brighter varnish described as type (2). Due to the dense and compact structure and nearly black colour, no significant changes of this varnish type were visible in the high-resolution optical images. Nevertheless, the measured Mn concentrations in the rainwater samples, especially from the irrigation experiments, proved that significant amounts of the birnessite and probably todorokite were dissolved at every pH level. Due to the fact that only on one sample material chipped off and no complete removal of visible structures was observed in the high-resolution optical images it was assumed that this type of varnish is less sensitive to physical weathering effects than Type 2 and most of the observed changes were due to chemical weathering processes. On some samples, parts of the black varnish looked like they had already chipped off before the start of the weathering experiment, as aforementioned, which contradicts this assumption and indicates that this type of varnish may also be very vulnerable to physical weathering effects (Fig. 6.1). Here, it has to be taken into account that the relatively small number of samples and the limited time of the weathering make it plausible that by chance only on one sample chipping of material could be observed in the climate chamber experiment. The black varnish was found to be intergrown with carbonaceous matter.

It is known that the dissolution rates of Mn-phases like birnessite and todorokite are significantly higher than of hematite and kaolinite (see Chapter 5.3.2.2), which also indicates that the chemical weathering vulnerability of this type of varnish is higher. These chemical weathering effects were not visible in the high-resolution optical images and the µCT-scans, as the resolution of both techniques was not high enough to determine changes that small. Also the thickness of the varnish layer could not be monitored and therefore it was not possible to examine if the varnish might have become thinner over the course of the weathering.

The BSE images, as well as the element distribution and Raman images of parts of the black varnish showed that the varnish is layered and the outermost parts of this varnish type contain the most Mn, while the Fe content was higher in deeper layers. The kaolinite was primarily found in combination with the hematite in deeper layers of the varnish. The Mn-rich layers that are mostly composed of birnessite also contain significantly more S than the layers below. The analysed black varnish from an older sample provided by Robert Bednarik showed similar structures with layering and high Mn contents in the outermost layers of the varnish, as well as more kaolinite and hematite in the layers below. The overall Mn content in the older sample was significantly higher and therefore the Fe-Mn ratio was even lower (Chapter 3.1.3.2).

Over a longer period of time the black varnish will probably become Mn depleted, as the Mn minerals were found to dissolve faster than hematite, which might be already visible in the comparison of the older black varnish with the samples from this study, as aforementioned.

If the black varnish would be classified according to the classification system proposed by Macholdt et al. (2017), it would probably be a Type I varnish due to the observed layering and high Mn content (Macholdt et al., 2017). The observed high Mn content in the outermost layers in the element distribution maps (Chapter 3.1.3.2) contradict the findings of Goldsmith et al. (2014) who analysed varnish samples from other sources, where the outermost layers were depleted in Mn.

Type 4: Mn-oxide-rich reddish to brown varnish
Another varnish type with high Mn contents but a less dark and dense surface with some more pore space and more of a reddish to brown colour was only found on two of the granophyre samples (NR2 & SR3). The outstanding parameters of the rocks with this type of varnish were the high overall Mn content, as well as the high Mn concentrations in the artificial rainwater that was in contact with them. The observed changes varied significantly depending on the weathering conditions, but were mainly due to chipped off parts of the samples, which indicates a vulnerability to physical weathering effects (Fig. 6.1). It has to be noted that before material chips off cracks will form on the surface (Fig. 4.12a). This process is not entirely driven by physical weathering effects as these cracks form preferentially at interfaces that are more sensitive to chemical weathering and potentially already more porous.

For the sample weathered under acidic conditions the colour change and the visible changes in the high-resolution optical images were larger, which was mainly due to more material that was chipped off. The Mn concentrations were in a similar range for both weathering conditions, which indicates that the chemical weathering on this kind of varnish was in a similar range for both pH values and that the Mn-bearing phases were more sensitive to chemical alteration.

Type 5: Hematite-rich, brown to red varnish with a metallic lustre
The varnish with the most conspicuous composition and appearance was very dense with a metallic lustre and a brown to red colour with extraordinarily high Fe contents and negligible Mn on the surface. This type was only found on two of the granophyre samples (NR3 & SR2). This varnish type is believed to consist almost entirely of hematite, with smaller amounts of kaolinite and other minor components. Due to the low Mn content, the Fe-Mn ratios were exceptionally high, with values > 100. The measured surface changes were relatively small, with one sample exhibiting a minor instance of varnish chipping and the other showing a lepidocrocite layer that disappeared over the course of the experiment. The chipped off material demonstrates that this varnish is vulnerable to physical weathering effects.

As with other samples and varnish types, a significant amount of dissolved material was detected in the rainwater samples in contact with this varnish, indicating chemical alteration processes through mineral dissolution. However, the quantity of dissolved material from this varnish type is presumed to be relatively low due to its dense surface with minimal porosity. This is further supported by the comparatively low element concentrations in the rainwater samples associated with this varnish type.

It is assumed that all types of varnish contain small amounts of carbonaceous matter intergrown with the varnish. This carbonaceous matter originates from microorganisms, which are known to be crucial for varnish growth (see Chapter 1.4) and become incorporated into the varnish, as well as from organic material deposited on the surface, such as bird droppings or organic fibres, which were detected on the surface of some of the samples.

Overall, it can be concluded that the extent of physical and chemical weathering impact primarily depends on the type of varnish present on the sample surfaces. More porous and less dense varnish types were more susceptible to both chemical and physical alterations. These types of varnish were more likely to be found on the gabbro samples, making the varnish on the gabbro rock more vulnerable to alteration. Denser and less porous varnish types also showed vulnerability to physical alteration, such as chipping, but they were less prone to chemical weathering due to their reduced surface area. Nevertheless, chemical alteration during rainfall events occurred on all varnish types albeit with varying extents. For most of the varnish types it was observed that under slightly acidic conditions at pH 5 more changes were observed than at pH 7.

7 Summary and conclusions

Since many decades, it is disputed whether industrial development on the Murujuga Peninsula in the north of Western Australia affects the weathering rates of the local rocks due to the extensive release of industrial pollutants, such as NO_x and SO_x, which lower the surface and rainwater pH on the peninsula. This issue is of significant interest, as the local rocks host over a million petroglyphs, which are feared to be endangered due to the industrial emissions. These examples of Aboriginal rock art are of great importance to the local Aboriginal community and represent one of the most significant cultural heritage sites in Australia. As there is currently no scientific consensus on whether the increase in industrial pollutant emissions adversely affects the conservation of the petroglyphs, further research remains necessary.

Therefore, the hypothesis tested in this study is if anthropogenic pollution from various industrial sites on Murujuga accelerates the degradation of the Aboriginal petroglyphs, which are carved in the rock varnish of the different rocks on the peninsula. For this an experimental programme was designed that involves detailed analyses of the rock varnish on rock samples from Murujuga, a number of irrigation experiments of varnish-bearing samples from Murujuga with different pH conditions, as well as a semi-actualistic long-term artificial weathering experiment over a total of 12 months in a climate chamber under controlled, Murujuga-like conditions with different artificial rainwater compositions and pH levels, to determine:

(1) the chemical and mineralogical composition of the rock varnish and the differences between various types of varnish found on Murujuga rocks (see Chapter 3.1.3)

(2) the pH dependence of the dissolution rates of the main components of the rock varnish (see Chapter 5)

(3) the weathering processes and their effects on the surfaces of different rocks from Murujuga at different pH levels that were observed on Murujuga in the past and are observed on Murujuga at the present day, as well as the amount of changes observed depending on the pH level (see Chapter 4)

(4) the composition of the microbial community and its change depending on weathering conditions over time.

(1) Chemical and mineralogical composition of the rock varnish

The analysis of the chemical and mineralogical composition of the rock varnish samples with Raman spectroscopy, p-XRF, EMP, and XRD revealed that the varnish on Murujuga can be well categorised by its colour. The darkest, nearly black varnish is dense, with low porosity and a high Mn content. The orange and red varnish types contain less Mn and their porosity and density varies, depending on the chemical composition and the type of host rock. These differences are substantial, ranging from dense, Fe-rich varnish with metallic lustre and low Mn content to highly porous, brighter varnish, which was found to be particularly vulnerable to weathering and was predominantly found on gabbro rocks. The main mineral components of the different varnish types are birnessite ($(Na,Ca)(Mn^{4+},Mn^{3+})_2O_4 \bullet 1.5H_2O$), hematite ($Fe_2O_3$), and kaolinite ($Al_2Si_2O_5(OH)_4$) in varying proportions, alongside minor phases such as todorokite ($(Ca,Na,K)(Mn^{4+},Mn^{3+})_6O_{12} \bullet nH_2O$), quartz ($SiO_2$), anatase ($TiO_2$), rutile ($TiO_2$), and carbonaceous matter. All crystalline phases are found in the varnish as nm to µm sized crystals and the proportions of the main phases control the varnish colour, with black varnish containing the highest amount of birnessite and todorokite. Additionally lepidocrocite (γ-FeO(OH)) and albite ($NaAlSi_3O_8$), as well as rutile and anatase (TiO_2) were found on individual samples on the surface and were intergrown with the underlying varnish layer.

It was observed, that the black varnish also exhibits fine layering, with the outermost parts enriched in Mn and S compared to the underlying layers, which contain more Fe. The Mn content of the used samples collected in 2019 and 2022 is significantly lower than on an older sample from Murujuga collected in 1994, even in areas with exclusively black varnish. It is also lower than in other rock varnish samples analysed by researchers collected at other locations (Potter & Rossman, 1979; Wayne et al., 2006; Goldsmith et al., 2014; Xu et al., 2019; Dorn, 2020; Harmon et al., 2021; Rabbachin et al., 2022). The Fe-Mn ratios of the recently collected samples were therefore significantly higher.

(2) pH dependence of the main components dissolution rates

To determine the pH dependence of the dissolution rates of the main components in the varnish irrigation experiments were carried out. Here, varnish-bearing rock samples from Murujuga were irrigated with artificial rainwater with pH 8.0, 7.0, 6.0, 5.0, 4.0, and 3.0 and samples of the artificial rainwater, that was in contact with the rock varnish, were analysed using ICP-OES. It was determined that the dissolution rates of the main components, and thus the elements Al, Fe, Mn, and Si contained within these phases, increased under acidic conditions, except for Si. The dissolution rates and element concentrations of Fe, Al, and Si, and consequently of kaolinite and hematite, were lower compared to those of birnessite and todorokite and therefore the Mn concentrations in the rainwater samples. Hematite was identified as the most stable phase, with dissolution rates believed to increase significantly only below pH 4. The observed rates and their pH dependence were consistent with the findings of other researchers (Schwertmann, 1991; Martin, 2005; Black et al., 2017b). Kaolinite and birnessite (as well as todorokite) exhibited increased dissolution rates at pH $<$ 5, with the Mn-oxide-phases being particularly vulnerable to a decrease in pH. The dissolution rates of birnessite and todorokite were significantly higher, resulting in mean Mn concentrations in the artificial rainwater of approximately 800 ppb at pH 3. This greater vulnerability of kaolinite and especially birnessite and todorokite to pH changes and towards more acidic conditions aligns with findings from prior studies (Polzer & Hem, 1965; Parc et al., 1989; Cama et al., 2002; Martin, 2005; Lefkowitz et al., 2013; MacLeod & Fish, 2021).

Measurable amounts of all analysed elements were detected at every tested pH level, indicating that small amounts of surface minerals were dissolved at all pH levels tested. This finding contradicts earlier studies that suggested dissolution of Fe, Mn, and Al only begins at pH 3 or below (Ramanaidou et al., 2017). However, the observed dissolution at pH levels $>$ 3 does not necessarily contradict the stability of the rock varnish or the preservation of the petroglyphs. The rock varnish is known to grow simultaneously above a certain pH level, although the precise threshold below which varnish does not grow remains uncertain. Different studies propose varying assumptions regarding the critical pH limit (Bednarik, 2009; MacLeod & Fish, 2021).

(3) Weathering processes and their effects

In the long-term climate chamber experiment the weathering processes and their effects on the surfaces of different rocks from Murujuga were tested at different pH levels. The used rock samples were analysed regularly using colour and p-XRF measurements. Additionally surface changes were monitored using high-resolution optical microscopy and µ-CT. In addition the weight loss of the samples was monitored and samples of the artificial rainwater that was in contact with the rock varnish and DNA samples were collected. Glass dosimeters from the Fraunhofer ISC were used to quantify the simulated alteration and to enable a comparison of the simulated conditions.

The colour, chemical composition, and surface properties changed significantly on the samples during the accelerated weathering experiment, especially during the first one to three weathering steps, which spanned over 5 to 35 days in total. The varnish, particularly on the gabbro samples, was vulnerable to alteration, and under slightly acidic conditions (pH 5), the observed changes were significantly higher than under neutral conditions (pH 7). Similar trends were observed for the granophyre samples, but to a lesser extent.

Parts of the observed changes were attributed to physical weathering effects, where secondary minerals were washed away, minerals became loosened and subsequently removed, and small parts of some samples chipped off. These effects are believed to have been driven by simulated solar radiation, temperature changes, and the physical impact of the artificial rainwater rinsed over the samples. The changes observed during the initial stages of the experiment were mainly due to these effects. Notably, the S, P, Ca, and K content on the surfaces decreased significantly during this first periods, suggesting that phases containing S, believed to form on surfaces due to the deposition of SO_x emissions on Murujuga, as well as residues of bird droppings containing high amounts of P, were washed away.

Additionally, some observed changes were believed to result from chemical weathering effects, resulting in the dissolution of minerals on the sample surfaces. The differences in element concentrations measured in the different used types of artificial rainwater that had been in contact with the different rocks were smaller than expected in the long-term weathering experiment in the climate chamber. Nevertheless, the overall changes observed at pH 5 were significantly greater than at pH 7. These dissolution processes and the mineral related pH dependence were further analysed and better understood using the data from the irrigation experiments, as mentioned earlier.

The combination of these weathering processes led to rapid changes during the first 5 to 35 days across all samples, driven primarily by physical weathering effects, as outlined earlier. During this period, significant changes in colour and chemical composition of the surfaces were observed. After this initial phase, the rate of change slowed but remained measurable across all samples, with significantly larger changes occurring in the sample group subjected to acidic conditions. These changes were attributed to a combination of chemical and physical weathering effects, resulting in further chemical and colour changes on the sample surfaces. Additionally, significant changes were observed in the high-resolution optical images of the sample surfaces, and a notable weight loss was detected on all samples. The observed changes varied depending on the varnish type and the type of host rock.

On the gabbro samples with orange to brown and porous varnish, the largest changes were observed. Here, wide areas of the varnish were removed over the duration of the experiment and the underlying, darker, and Mn-richer varnish was uncovered. The gabbro samples with a denser and darker varnish experienced fewer changes and the dark varnish appeared to be less vulnerable. On the granophyre samples with the most diverse varnish on the surface, the observed changes were the highest. Here, some parts of the orange to brown varnish were also removed, uncovering the darker and denser black varnish underneath. In addition, some secondary minerals, mainly albite, was washed away. The other granophyre samples experienced fewer changes, even though the surface of two samples was not as dense as that of the last two granophyre samples, which also experiences lesser changes.

The use of glass dosimeters from the Fraunhofer ISC in the climate chamber experiment enabled the testing of the suitability of different glass types under Murujuga-like conditions, as well as the quantification of the simulated alteration. These glass dosimeters demonstrated that the simulated alteration was greater under acidic conditions. For future research, these dosimeters could be a valuable tool to compare the weathering simulated in the climate chamber with real-world conditions on the peninsula.

(4) Composition of the microbial community

The gabbro samples exhibited significant shifts in microbial diversity and composition across treatments, with acidic conditions favouring acidophilic taxa such as *Rubrobacter* and neutral conditions promoting a broader range of taxa. The granophyre samples showed a more stable microbial diversity and composition, with core taxa such as *Proteobacteria* and *Actinobacteriota* dominating across treatments under different pH conditions. Taxa associated with iron and manganese cycling, such as *Geodermatophilus* and *Deinococcota*, were more abundant under acidic conditions in gabbro samples, suggesting a functional response to environmental stress, while under neutral conditions in both rock types the diversity and evenness of the microbial community increased, with a notable enrichment of *Cyanobacteria* and *Firmicutes.*

The findings from this study provide new insights into the microbial ecology of Murujuga rock varnish and emphasize the influence of environmental changes, particularly pH fluctuations, on microbial community composition and function. These findings align with previous research, such as the study by Krinsley et al. (2017) on Mn-enhancing budding bacteria in rock varnish, which also highlighted the role of microbial communities in the formation of rock varnish under environmental stress.

While the microbial communities associated with rock varnish are still not fully understood (see Chapter 1.4), it is clear that they play a crucial role in biogeochemical cycling, particularly the cycling of metals like Mn and Fe. As industrial activities and environmental changes, such as acid rain, continue to impact these ecosystems, further research is needed to understand how these microbial communities adapt to changing conditions and how their activities influence the preservation of rock varnish and associated rock art. Future research should focus on elucidating the specific microbial metabolic pathways involved in rock varnish formation, as well as the role of rare taxa in these processes.

Conclusions

The results of the different experiments made it possible to make ballpark estimates of the varnish dissolution rates as a function of the rainwater pH. These estimated dissolution rates, calculated using the pH dependent element concentrations, measured in the artificial rainwater samples, and a model varnish, were relatively high, particularly for the birnessite and todorokite in the varnish, which are known to be more susceptible to alteration than hematite. The most important finding was that these dissolution rates increased significantly at $\mathrm{pH} < 5$. The dissolution rates for hematite, kaolinite, and the Mn-oxide-phases are believed to lead to a depletion of Mn in the varnish over time if the regrowth rates of the varnish components are slower than the dissolution rates on Murujuga.

As no dust deposition, which is critical for the regrowth of varnish, was simulated in the climate chamber experiment, it could not be assessed whether varnish would grow under the simulated conditions or whether the weathering rates exceeded the regrowth rates, which would lead to the removal of the varnish over an extended period of time. The precise growth rates of varnish on Murujuga have not yet been investigated, and overall, the knowledge regarding the growth rates of rock varnish remains limited but it is known that the growth rates are highly dependent on the local environmental conditions.

The observed low Mn content and the high Fe-Mn ratios in the varnish of the samples collected in 2019 and 2022, compared to the findings of other researchers analysing varnish from other locations and the Mn content and Fe-Mn ratios in a varnish sample from Murujuga collected in 1994, suggest that the newer samples might already be depleted in Mn due to more acidic conditions on Murujuga. However, as the number of samples in this study was very limited, this hypothesis could not be validated, necessitating further research.

All findings enhance the understanding of the mineralogy and the different types of varnish found on Murujuga, as well as their vulnerability to pH changes caused by industrial emissions and the associated pollution. It was shown that the dissolution rates of intact rock varnish from Murujuga are highly pH dependent, particularly for the dissolution of the primary Mn-bearing phase, birnessite. These dissolution rates were found to increase critically at pH < 5. Given that measured pH levels on Murujuga have often fallen below this critical threshold in recent years (MacLeod & Fish, 2021; MRAMP, 2023), it must be assumed that the dissolution of the varnish has already accelerated in the past and will continue to do so in the future if the pH of the rainwater and rock surfaces remains below this critical level.

The most important finding of this study is that there are significant differences in varnish alteration under neutral (pH 7) and more acidic (pH 5) conditions. It was demonstrated that varnish weathering is already accelerated at pH 5, even though the dissolution rates observed at pH 5 and pH 7 were within a comparable range. Overall, the changes of the colour, chemical composition, surface properties, and weight were greater in the sample groups weathered under acidic conditions (pH 5). The experiment also revealed significant differences between the different types of varnish and their relative vulnerability to weathering effects. The observed varnish alteration made it possible to classify different types of varnish and determine the weathering processes on the varnish (Fig. 6.1). In addition it was possible to characterise the varnish structure and chemical composition, as well as to identify the main mineral phases. The pH dependence of the dissolution of these main components could be determined and it was proven that the Mn-oxide-phases are most vulnerable to chemical weathering and dissolution rates increase at a pH < 5. The same applies to kaolinite, which has a significantly lower dissolution rate compared to the Mn-oxides. Hematite was found to be the most stable main component of the varnish with dissolution rates increasing only at pH < 4. Additionally, the experiments, including the analysis of the microbial community, showed that the varnish layers on the gabbro rocks are more vulnerable to alteration than the varnish on the granophyre rocks.

Overall, this study indicates that

(1) it is highly likely that the alteration of rock varnish on petroglyph-bearing rocks on Murujuga has already been accelerated due to the lower pH of rainwater and rock surfaces caused by industrial emissions,

(2) the dissolution rates of varnish minerals will further increase and with this the physical degradation of the varnish, e.g. by increased growth a salt crystals in pores and along interfaces if the pH drops significantly below 5 for extended periods, rather than only occasionally as it has been observed to date, and

(3) parts of the rock varnish may already be significantly depleted in Mn compared to the pre industrial state due to accelerated weathering. This accelerated weathering initially results in higher dissolution rates of Mn-oxide-phases, which are highly vulnerable to pH changes and are primarily composed of birnessite.

Further research implications
As aforementioned (Chapter 4.3.2.1), the experimental setup did not simulate dust deposition or atmospheric conditions. Consequently, it is very likely that varnish regrowth did not occur during the long-term weathering experiment and pollutants were only introduced to the samples during simulated rainfall events. It is crucial to determine the pH threshold below which varnish regrowth is inhibited, and additionally, to assess the regrowth rates of varnish on Murujuga. This would help answer the question of the critical pH level at which dissolution rates exceed regrowth rates and thus lead in the long term to an irretrievable loss of the rock varnish and therefore of the Murujuga petroglyphs.

Based on the findings of this study, it would be reasonable to address two other open questions that can be more easily resolved. First, it would be important to place glass dosimeters made of the MI and M5 glass types, which were also used in the climate chamber experiment, at various locations on Murujuga, with varying proximities to industrial sites. Suitable locations could include the 18 weather stations established by the Murujuga Rock Art Monitoring Program (MRAMP) across Murujuga, as well as sites unaffected by industrial emissions but with comparable weather conditions. In addition to the glass dosimeters, varnish-bearing rock samples composed of granophyre and gabbro, as well as metal aerosol dosimeters, should be placed at these sites.

Second, the glass dosimeters and rock samples should be analysed using the same methods employed in this study, excluding µ-CT. Portable devices can be used for p-XRF and colour measurements in the field. The glass dosimeters must be sent to the Fraunhofer ISC for analysis, necessitating longer intervals between measurements. This study could span over one to two years, allowing comparisons between the findings from the climate chamber experiment and the observed alterations under real-world conditions, as the accelerated climate chamber experiment can not represent the actual conditions precisely due to the limitations of the setup and the used acceleration factor that changes the chemical and physical processes, some of which cannot be accelerated at all. The analysis of glass dosimeters weathered on Murujuga facilitates direct comparisons of simulated weathering conditions and the observed extent of alteration with real-world conditions. Ensuring reproducibility and high accuracy is essential, especially when performing p-XRF and colour measurements, which should be conducted in a manner consistent with this study.

To further validate or refute the hypothesis that the varnish on Murujuga is already depleted in Mn due to elevated dissolution rates under current conditions, a large number of spots of the black varnish on Murujuga rocks should be analysed using p-XRF. This method is non-destructive and requires no sample preparation. Additionally, older samples collected on Murujuga at least 20 years ago should be examined. These samples could be sourced from museums or private collections. If the hypothesis is confirmed, it would provide further evidence that dissolution rates, particularly for Mn-oxide-phases like birnessite, have already accelerated under present-day conditions in comparison to the pre industrial conditions on Murujuga.

References

ABC News. (2020). Cyclone Damien damage closes Karratha Airport as flash flooding warning issued for inland WA. *https://www.abc.net.au/news/2020-02-10/cyclone-damien-damage-closes-karratha-airport-flooding-possible/11949352*. (Accessed: 2024-10-21)

ABC News. (2023). Federal government formally nominates Burrup peninsula and surrounding areas for UN world heritage listing. *https://www.abc.net.au/news/2023-02-10/burrup-rock-art-nominated-world-heritage-unesco-/101947896*. (Accessed: 2024-12-21)

Abdi, H., & Williams, L. J. (2010). Principal component analysis. *Wiley interdisciplinary reviews: computational statistics*, *2*(4), 433–459.

Albertsen, M., Karst, S. M., Ziegler, A. S., Kirkegaard, R. H., & Nielsen, P. H. (2015). Back to basics–the influence of DNA extraction and primer choice on phylogenetic analysis of activated sludge communities. *PloS one*, *10*(7), e0132783.

Appelo, C. A. J., & Postma, D. (2004). *Geochemistry, groundwater and pollution*. CRC press.

Australian Government, Bureau of Meteorology. (2023). Climate statisticts Karratha Aero. *Australian Government, Bureau of Meteorology*. (URL: http://www.bom.gov.au/climate/averages/tables/cw_004083_All.shtml, Accessed: 2024-10-21)

Bednarik, R. G. (1979). The potential of rock patination analysis in Australian archaeology - Part 1. *The Artefact*, *4*(3 & 4), 14–38.

Bednarik, R. G. (1994). Dampier rock art under siege. *The Artefact*, *17*, 79.

Bednarik, R. G. (2002). The survival of the Murujuga (Burrup) petroglyphs. *Rock Art Research: The Journal of the Australian Rock Art Research Association (AURA)*, *19*(1), 29–40.

Bednarik, R. G. (2007). The science of Dampier rock art [Series of parts]: Part 1. *Rock Art Research: The Journal of the Australian Rock Art Research Association (AURA)*, *24*(2), 209–246.

Bednarik, R. G. (2009). Experimental colorimetric analysis of petroglyphs. *Rock Art Research*, *26*(1), 55–64.

Bernardini, S., Bellatreccia, F., Casanova Municchia, A., Della Ventura, G., & Sodo, A. (2019). Raman spectra of natural manganese oxides. *Journal of Raman Spectroscopy*, *50*(6), 873–888.

Bird, C., & Hallam, S. J. (2006). A review of archaeology and rock art in the Dampier Archipelago. *A report prepared for the National Trust of Australia*

(WA).

Black, J. L., Box, I., & Diffey, S. (2017a). Inadequacies of research used to monitor change to rock art and regulate industry on murujuga ('Burrup Peninsula'), Australia. *Rock Art Research: The Journal of the Australian Rock Art Research Association (AURA)*, *34*(2), 130–148.

Black, J. L., MacLeod, I., & Smith, B. W. (2017b). Theoretical effects of industrial emissions on colour change at rock art sites on Burrup Peninsula, Western Australia. *Journal of Archaeological Science: Reports*, *12*, 457–462.

Bolyen, E., Rideout, J. R., Dillon, M. R., Bokulich, N. A., Abnet, C. C., Al-Ghalith, G. A., ... Caporaso, J. G. (2019). Reproducible, interactive, scalable and extensible microbiome data science using QIIME 2. *Nature biotechnology*, *37*(8), 852–857.

Bray, J. R., & Curtis, J. T. (1957). An ordination of the upland forest communities of southern Wisconsin. *Ecological monographs*, *27*(4), 326–349.

Broecker, W. S., & Liu, T. (2001). Rock varnish: Recorder of desert wetness? *GSA TODAY*, *11*(8), 4–10.

Bruker AXS. (2024a). DIFFRAC.EVA version 5.1.0.5. *https://www.bruker.com/en/products-and-solutions/diffractometers-and-x-ray-microscopes/x-ray-diffractometers/diffrac-suite-software/diffrac-eva.html*. (Accessed: 2024-10-24)

Bruker AXS. (2024b). TOPAS version 5. *https://www.bruker.com/en/products-and-solutions/diffractometers-and-x-ray-microscopes/x-ray-diffractometers/diffrac-suite-software/diffrac-topas.html*. (Accessed: 2024-10-24)

Callahan, B. J., McMurdie, P. J., & Holmes, S. P. (2017). Exact sequence variants should replace operational taxonomic units in marker-gene data analysis. *The ISME journal*, *11*(12), 2639–2643.

Cama, J., Metz, V., & Ganor, J. (2002). The effect of pH and temperature on kaolinite dissolution rate under acidic conditions. *Geochimica et cosmochimica acta*, *66*(22), 3913–3926.

Camuffo, D. (1992). Acid rain and deterioration of monuments: How old is the phenomenon? *Atmospheric Environment. Part B. Urban Atmosphere*, *26*(2), 241–247.

Carmichael, S. K., Bräuer, S. L., & Engel, A. (2015). Microbial diversity and manganese cycling: A review of manganese oxidizing microbial cave communities. *Microbial life of cave systems*, 137–160.

Castillo-Miranda, J. O., Torres-Jardón, R., García-Reynoso, J. A., Mar-Morales, B. E., Rodríguez-Gómez, F. J., & Ruiz-Ruárez, L. G. (2017). Mapping recession risk for cultural heritage stone in Mexico City due to dry and wet deposition of urban air pollutants. *Atmósfera*, *30*(3), 189–207.

Chaddha, A. S., Sharma, A., Singh, N. K., Shamsad, A., & Banerjee, M. (2024). Biotic-abiotic mingle in rock varnish formation: A new perspective. *Chemical Geology*, *648*, 121961.

Charola, A. E. (1987). Acid rain effects on stone monuments. *Journal of chemical* *education*, *64*(5), 436.

Chernyshova, I. V., Hochella Jr, M. F., & Madden, A. S. (2007). Size-dependent structural transformations of hematite nanoparticles. 1. Phase transition. *Physical Chemistry Chemical Physics*, *9*(14), 1736–1750.

Cinderby, S., Cambridge, H., Herrera, R., Hicks, W., Kuylenstierna, J., Murray, F., & Olbrich, K. (1998). Global assessment of ecosystem sensitivity to acidic deposition. *Stockholm Environment Institute*.

Comet Technologies Canada Inc. (2024). Dragonfly 2024.1. *https://dragonfly.comet.tech/*. (Montreal, Canada, Accessed: 2024-10-24)

Crewdson, M. (2008). Outdoor weathering must verify accelerated testing. *Q-Lab Weathering Research Service*, *1005*, 33034–1725.

Daly, M. J. (2009). A new perspective on radiation resistance based on Deinococcus radiodurans. *Nature Reviews Microbiology*, *7*(3), 237–245.

De Faria, D. L., Venâncio Silva, S., & de Oliveira, M. T. (1998). Raman microspectroscopy of some iron oxides and oxyhydroxides. *Journal of Raman spectroscopy*, *28*(11), 873–878.

Department of the Environment and Energy. (2023). National Pollutant Inventory. *Department of the Environment and Energy*. (URL: http://www.npi.gov.au/npidata/action/load/map-result/criteria/destination/ALL/lga/516/source-type/ALL/subthreshold-data/Yes/substance-name/All/year/2023, Accessed: 2024-10-21)

Di Turo, F., Proietti, C., Screpanti, A., Fornasier, M. F., Cionni, I., Favero, G., & De Marco, A. (2016). Impacts of air pollution on cultural heritage corrosion at European level: What has been achieved and what are the future scenarios. *Environmental Pollution*, *218*, 586–594.

Donaldson, M., & Bednarik, R. G. (2011). Understanding the Rocks: Rock Art and the Geology of Murujuga (Burrup Peninsula). *Rock Art Research*, *28*(1), 35–43.

Donze, F.-V., Audin, L., Schmitt, B., Taillefer, A., & Truche, L. (2024). Contribution of hyperspectral analysis in relative dating applied to Miculla petroglyphs (Peru). *Journal of Archaeological Science*, *169*, 106023.

Dorn, R. I. (2007). Rock varnish. *Geochemical sediments and landscapes*, 246–297.

Dorn, R. I. (2009). Desert rock coatings. *Geomorphology of desert environments*, 153–186.

Dorn, R. I. (2020). Anthropogenic interactions with rock varnish. *Biogeochemical cycles: Ecological drivers and environmental impact*, 267–283.

Dorn, R. I. (2024). Rock varnish revisited. *Progress in Physical Geography: Earth and Environment*, *48*(3), 389–419.

Duffy, N., Ramanaidou, E. R., Alexander, D., & Lau, D. (2017). Burrup Peninsula Aboriginal petroglyphs: Colour change and spectral mineralogy 2004-2016. *CSIRO Publishing*, *EP161761*. (URL: https://www.wa.gov.au/system/files/2020-10/DWER-Murujuga-Burrup-

Peninsula-Aboriginal-Petroglyphs-Colour-Change-Spectral-Miner.pdf, Accessed: 2024-08-19)

DWER. (2019). Murujuga rock art strategy. *Department of Water and Environmental Regulation, Perth.* (DWER is the Department of Water and Environmental Regulation, Western Australia)

Esposito, A., Ahmed, E., Ciccazzo, S., Sikorski, J., Overmann, J., Holmström, S. J., & Brusetti, L. (2015). Comparison of rock varnish bacterial communities with surrounding non-varnished rock surfaces: Taxon-specific analysis and morphological description. *Microbial ecology*, *70*, 741–750.

Flood, B., Allen, C., & Longazo, T. (2003). Microbial fossils detected in desert varnish. , 1633.

Furcas, F. E., Lothenbach, B., Isgor, O. B., Mundra, S., Zhang, Z., & Angst, U. M. (2022). Solubility and speciation of iron in cementitious systems. *Cement and Concrete Research*, *151*, 106620.

Garland, J. (1977). The dry deposition of sulphur dioxide to land and water surfaces. *Proceedings of the Royal Society of London. A. Mathematical and Physical Sciences*, *354*(1678), 245–268.

Garvie, L. A., Burt, D. M., & Buseck, P. R. (2008). Nanometer-scale complexity, growth, and diagenesis in desert varnish. *Geology*, *36*(3), 215–218.

Geisler, T., Dohmen, L., Lenting, C., & Fritzsche, M. B. K. (2019). Real-time in situ observations of reaction and transport phenomena during silicate glass corrosion by fluid-cell Raman spectroscopy. *Nature Materials*, *18*(4), 342–348.

Gentilli, J. (1971). Climates of Australia and New Zealand. *World Survey of Climatology, Elsevier Science.*

Giesen, M. J., Ung, A., Warke, P. A., Christgen, B., Mazel, A. D., & Graham, D. W. (2014). Condition assessment and preservation of open-air rock art panels during environmental change. *Journal of Cultural Heritage*, *15*(1), 49–56.

Gillett, R. (2006). Burrup Peninsula Air Pollution Study: Final Report. *CSIRO Marine and Atmospheric Research.*

Gillett, R. (2008). Burrup Peninsula air pollution study: Report for 2004/2005 and 2007/2008. *Department of Environment and Conservation, Western Australia.*

Gleeson, D., Leopold, M., Smith, B., & Black, J. (2018). Rock-art microbiome: Influences on long term preservation of historic and culturally important engravings. *Microbiology Australia*, *39*(1), 33.

Goldsmith, Y., Stein, M., & Enzel, Y. (2014). From dust to varnish: Geochemical constraints on rock varnish formation in the Negev Desert, Israel. *Geochimica et Cosmochimica Acta*, *126*, 97–111.

Harmon, R. S., Khashchevskaya, D., Morency, M., Owen, L. A., Jennings, M., Knott, J. R., & Dortch, J. M. (2021). Analysis of rock varnish from the Mojave Desert by handheld laser-induced breakdown spectroscopy. *Molecules*, *26*(17), 5200.

Hauke, K., Kehren, J., Böhme, N., Zimmer, S., & Geisler, T. (2019). In situ hyperspectral Raman imaging: A new method to investigate sintering processes of ceramic material at high-temperature. *Applied Sciences*, *9*(7), 130.

Heckel, P., Keener, T., Lu, M., & Álvarez, H. B. (2007). A summary of the International Workshop on the Influences of Air Quality on the Mayan Heritage Sites in Mesoamerica. *Environmental Manager*, 24–30.

Hem, J. D. (1963). Chemical equilibria and rates of manganese oxidation. *Water Supply Paper*, *1667*.

Hickman, A. H. (1997). Dampier, W.A. Sheet 2256, 1:100.000 Geological Series. *Geological Survey of Western Australia.*

Hickman, A. H., Huston, D. L., Van Kranendonk, M. J., & Smithies, R. H. (2006). Geology and mineralization of the west Pilbara–a field guide. *Geological Survey of Western Australia, Record*, *17*, 50.

Holmes, J. (2021). Tropical cyclone impacts on the Western Australian coast and extreme wind speeds in Region D. *Australian Journal of Structural Engineering*, *22*(2), 110–119.

Horiba. (2024). LabSpec 6 Spectroscopy Suite version 6. *https://www.horiba.com/deu/scientific/products/detail/action/show/Product/ labspec-6-spectroscopy-suite-software-1843/*. (Accessed: 2024-10-24)

House, W. A., & Orr, D. R. (1992). Investigation of the pH dependence of the kinetics of quartz dissolution at 25 C. *Journal of the Chemical Society, Faraday Transactions*, *88*(2), 233–241.

Hungate, B., Danin, A., Pellerin, N., Stemmler, J., Kjellander, P., Adams, J., & Staley, J. (1987). Characterization of manganese-oxidizing (MnII→ MnIV) bacteria from Negev Desert rock varnish: Implications in desert varnish formation. *Canadian Journal of Microbiology*, *33*(10), 939–943.

Huntsman. (2004). Araldite 2020 (XW 396/XW 397) Farbloses Zweikomponenten-Klebstoffsystem auf Epoxidharzbasis. *https://www.filzring.de/intern/datasheets/ARA-2000/TDB_ARA_2020_DE.pdf*. (Accessed: 2024-10-21)

Iler, R. K. (1979). The Chemistry of Silica: Solubility, Polymerization, Colloid and Surface Properties and Biochemistry of Silica. *New York, NY: John Wiley & Sons.*

International Organization for Standardization, S., Geneva. (2020). Colorimetry - Part 4: CIE 1976 L*a*b* colour space (ISO/CIE 11664-4:2019); German version EN ISO/CIE 11664-4:2019.

IPCC. (2023). Climate Change 2023: Synthesis Report. Contribution of Working Groups I, II and III to the Sixth Assessment Report of the Intergovernmental Panel on Climate Change [Core Writing Team, H. Lee and J. Romero (eds.)]. *IPCC, Geneva, Switzerland.*

Jang, J.-H., Dempsey, B. A., & Burgos, W. D. (2007). Solubility of hematite revisited: Effects of hydration. *Environmental science & technology*, *41*(21), 7303–7308.

Jones, D. S. (2004). The Burrup Peninsula and Dampier Archipelago, Western Australia: An introduction to the history of its discovery and study, marine habitats and their flora and fauna. *Records of the Western Australian Museum Supplement*, *66*, 27–49.

Julien, C., Massot, M., Baddour-Hadjean, R., Franger, S., Bach, S., & Pereira-Ramos,

J. (2003). Raman spectra of birnessite manganese dioxides. *Solid State Ionics*, *159*(3-4), 345–356.

Karačić, S., Modin, O., Hagelia, P., Persson, F., & Wilén, B.-M. (2022). The effect of time and surface type on the composition of biofilm communities on concrete exposed to seawater. *International Biodeterioration & Biodegradation*, *173*, 105458.

Konica Minolta. (2020). CR-410 Specifications. *https://www5.konicaminolta.eu/de/messgeraete/produkte/farbmessung/chroma-meter/cr-400-410/technische-daten.html.* (Accessed: 2024-10-21)

Krinsley, D. H., DiGregorio, B., Dorn, R. I., Razink, J., & Fisher, R. (2017). Mn-Fe-enhancing budding bacteria in century-old rock varnish, Erie Barge Canal, New York. *The Journal of Geology*, *125*(3), 317–336.

Krinsley, D. H., Dorn, R. I., DiGregorio, B. E., Langworthy, K. A., & Ditto, J. (2012). Rock varnish in New York: An accelerated snapshot of accretionary processes. *Geomorphology*, *138*(1), 339–351.

Krumbein, W. E., & Jens, K. (1981). Biogenic rock varnishes of the Negev Desert (Israel) an ecological study of iron and manganese transformation by cyanobacteria and fungi. *Oecologia*, *50*(1), 25–38.

Kruskal, W. H., & Wallis, W. A. (1952). Use of ranks in one-criterion variance analysis. *Journal of the American statistical Association*, *47*(260), 583–621.

Labus, M., & Bochen, J. (2012). Sandstone degradation: An experimental study of accelerated weathering. *Environmental Earth Sciences*, *67*, 2027–2042.

Lafuente, B., Downs, R. T., Yang, H., & Stone, N. (2015). The power of databases: the RRUFF project. *Highlights in Mineralogical Crystallography, T Armbruster and R M Danisi*, 1–30.

Lau, D., Ramanaidou, E., Furman, S., Cole, I., Hughes, T., & Hoobin, P. (2007). Field Studies of Rock Art Appearance–Final Report: Fumigation and Dust Deposition–Progress Report: Colour Change and Spectral Mineralogy. *CSIRO Division of Exploration and Mining, Western Australia.*

Lau, D., Ramanaidou, E. R., Hacket, A., Caccetta, M., & Furman, S. (2010). Burrup Peninsula Aboriginal petroglyphs: Colour change and spectral mineralogy 2004-2009. *CSIRO Publishing*, *Restricted Report P2010/408 CMSE(C)-2010-059*. (URL: https://www.wa.gov.au/system/files/2020-10/DWER-Murujuga-Burrup-Aboriginal-Petroglyphs-2004-2009.pdf, Accessed: 2024-08-19)

Law, W. B., Cropper, D., & Petchey, F. (2010). Djadjiling Rockshelter: 35,000 Years of Aboriginal Occupation in the Pilbara, Western Australia. *Australian Archaeology*, *70*(1), 68–71.

Lefkowitz, J. P., Rouff, A. A., & Elzinga, E. J. (2013). Influence of pH on the reductive transformation of birnessite by aqueous Mn (II). *Environmental science & technology*, *47*(18), 10364–10371.

Lingappa, U. F., Yeager, C. M., Sharma, A., Lanza, N. L., Morales, D. P., Xie, G., … Fischer, W. W. (2021). An ecophysiological explanation for manganese enrichment in rock varnish. *Proceedings of the National Academy of Sciences*, *118*(25), e2025188118.

Liu, C., Cui, Y., Li, X., & Yao, M. (2021). microeco: An R package for data mining in microbial community ecology. *FEMS microbiology ecology*, *97*(2), fiaa255.

Liu, T., & Broecker, W. S. (2000). How fast does rock varnish grow? *Geology*, *28*(2), 183–186.

Liu, T., & Broecker, W. S. (2008). Rock varnish evidence for latest Pleistocene millennial-scale wet events in the drylands of western United States. *Geology*, *36*(5), 403–406.

Macholdt, D., Jochum, K., Pöhlker, C., Arangio, A., Förster, J.-D., Stoll, B., . . . Anreae, M. O. (2017). Characterization and differentiation of rock varnish types from different environments by microanalytical techniques. *Chemical Geology*, *459*, 91–118.

MacLeod, I. (2005). Effects of moisture, micronutrient supplies and microbiological activity on the surface pH of rocks in the Burrup Peninsula. *Preprints for ICOM-CC Triennial Meeting, Den Haag, The Netherlands*, *2*, 386–93.

MacLeod, I. (2018). Surface chemistry of Burrup Rock art at the Yara monitoring sites. *Yara Pilbara Nitrates*, *Version 1.3*. (URL: https://www.yara.com.au/siteassets/about-yara/reports/rock-art-monitoring-reports/tan-plant-epbc-annual-rock-art-monitoring-report-2017.pdf/, Accessed: 2024-08-19)

MacLeod, I. (2019). Surface chemistry of Burrup Rock art at the Yara monitoring sites. *Yara Pilbara Nitrates*, *Version 1.1*. (URL: https://www.yara.com.au/siteassets/about-yara/reports/rock-art-monitoring-reports/tan-plant-epbc-annual-rock-art-monitoring-report-2018.pdf/, Accessed: 2024-08-19)

MacLeod, I. (2021). Surface chemistry of Burrup Rock art at the Yara monitoring sites. *Yara Pilbara Nitrates*, *Version 1.7*. (URL: https://www.yara.com.au/siteassets/about-yara/reports/rock-art-monitoring-reports/tan-plant-epbc-annual-rock-art-monitoring-report-2021.pdf/, Accessed: 2024-08-19)

MacLeod, I., & Fish, W. (2021). Determining decay mechanisms on engraved rock art sites using pH, chloride ion and redox measurements with an assessment of the impact of cyclones, sea salt and nitrate ions on acidity. *ICOM-CC 19th Triennial Conference Preprints, Beijing*, 17–21.

Markley, T., Wells, M., Ramanaidou, E., Lau, D., & Alexander, D. (2015). Burrup Peninsula Aboriginal Petroglyphs: Colour Changes and Spectral Mineralogy 2004–2014. *CSIRO, Australia Report*, *EP1410003*.

Marshall, C. P., Dufresne, W. J. B., & Rufledt, C. J. (2020). Polarized Raman spectra of hematite and assignment of external modes. *Journal of Raman Spectroscopy*, *51*(9), 1522–1529.

Martin, S. T. (2005). Precipitation and dissolution of iron and manganese oxides. *Environmental catalysis*, *1*, 61–82.

McDonald, J. (2005). Archaic faces to headdresses: The changing role of rock art across the arid zone. *Desert peoples: archaeological perspectives*, 116–141.

McDonald, J. (2015). I must go down to the seas again: Or, what happens when the sea comes to you? Murujuga rock art as an environmental indicator for Australia's north-west. *Quaternary International*, *385*, 124–135.

McDonald, J., & Veth, P. (2009). Dampier Archipelago petroglyphs: Archaeology, scientific values and National Heritage Listing. *Archaeology in Oceania*, *44*(S1), 49–69.

McKeown, D. A., & Post, J. E. (2001). Characterization of manganese oxide mineralogy in rock varnish and dendrites using X-ray absorption spectroscopy. *American Mineralogist*, *86*(5-6), 701–713.

McMurdie, P. J., & Holmes, S. (2013). phyloseq: An R package for reproducible interactive analysis and graphics of microbiome census data. *PloS one*, *8*(4), e61217.

MP Biomedicals. (2024). USER MANUAL FastDNA SPIN Kit for Soil. *https://www.mpbio.com/media/document/file/manual/dest/f/a/s/t/d/FastDNA_ SPIN_Kit_for_Soil_UM_2021_WEB.pdf*. (Accessed: 2024-11-22)

MRAMP. (2022). Monitoring studies data collection and analysis plan. *Department of Water and Environmental Regulation, Perth.* (MRAMP is the Murujuga Rock Art Monitoring Program, URL: https://www.wa.gov.au/system/files/2023-12/murujuga-rock-art-monitoring-studies-data-collection-analysis-plan.pdf, Accessed: 2024-08-19)

MRAMP. (2023). Technical Report on Monitoring Studies completed from March 2022 to March 2023. *Department of Water and Environmental Regulation, Perth.* (MRAMP is the Murujuga Rock Art Monitoring Program, URL: https://murujuga.org.au/wp-content/uploads/2023/12/Murujuga-Rock-Art-Monitoring-Program-First-Year-Studies-Report-2023.pdf, Accessed: 2024-08-19)

Mulvaney, K. (2009). Dating the Dreaming: Extinct fauna in the petroglyphs of the Pilbara region, Western Australia. *Archaeology in Oceania*, *44*(S1), 40–48.

Mulvaney, K. (2010). Murujuga Marni-Dampier Petroglyphs: Shadows in the landscape, Echoes across Time. *(PhD thesis). University of New England.*

Mulvaney, K. (2013). Iconic imagery: Pleistocene rock art development across northern Australia. *Quaternary International*, *285*, 99–110.

Mulvaney, K. (2022). Without them - what then? People, petroglyphs and Murujuga. *Histories of Australian Rock Art Research*, 155–172.

Murujuga Aboriginal Corporation. (2024). Murujuga Rock Art Strategy. *https://murujuga.org.au/our-land/rock-art-strategy/*. (Accessed: 2024-10-24)

Neumann, J. T. (2021). Experimental weathering of Aboriginal rock art from Murujuga, Western Australia: A proof of concept study. *(Unpublished Master thesis). University of Bonn.*

Neumann, J. T., Black, J. L., Hœrlé, S., Smith, B. W., Watkins, R., Lagos, M., ... Geisler, T. (2022). Artificial weathering of rock types bearing petroglyphs from Murujuga, Western Australia. *Heritage Science*, *10*(1), 77.

Norton, S. A., & Vesela, J. (2003). Acidification and acid rain. *Treatise on geochemistry*, *9*, 367-406.

Oksanen, J., Blanchet, F. G., Kindt, R., Legendre, P., Minchin, P. R., O'Hara, R. B., … Wagner, H. (2019). vegan: Community ecology package. *R package version*, *2.5*(6).

OriginLab Corporation. (2018). OriginPro version 9.5.1.195. *https://www.originlab.com.* (Northampton, MA, USA, Accessed: 2024-10-24)

Osram. (2023). Technisches Datenblatt Ultra Vitalux. *Osram technical service.*

Ostrooumov, M. (2017). Raman and infrared reflection spectroscopic study of mineralogical composition of iron-manganese nodules (Pacific and Indian Oceans). *Int. J. Exp. Spectrosc. Tech*, *2*, 2–12.

Oxford Instruments. (2013). X-MET7000 Series. *https://www.bergeng.com/mm5/downloads/oxford/X-MET-General-Brochure-Nov2013.pdf.* (Accessed: 2024-10-21)

Parc, S., Nahon, D., Tardy, Y., & Vieillard, P. (1989). Estimated solubility products and fields of stability for cryptomelane, nsutite, birnessite, and lithiophorite based on natural lateritic weathering sequences. *American Mineralogist*, *74*(3-4), 466–475.

Pedeferri, P. (2018). Pourbaix Diagrams. In: Corrosion Science and Engineering. *Engineering Materials. Springer*, 57–72.

Perry, R. S., & Kolb, V. M. (2004). From Darwin to Mars: Desert varnish as a model for preservation of complex (bio) chemical systems. *Instruments, methods, and missions for astrobiology VII*, *5163*, 136–144.

Perry, R. S., Kolb, V. M., Lynne, B. Y., Sephton, M. A., Mcloughlin, N., Engel, M. H., … Staley Jr, J. T. (2005). How desert varnish forms? *Astrobiology and Planetary Missions*, *5906*.

Pillans, B., & Fifield, L. K. (2013). Erosion rates and weathering history of rock surfaces associated with Aboriginal rock art engravings (petroglyphs) on Burrup Peninsula, Western Australia, from cosmogenic nuclide measurements. *Quaternary Science Reviews*, *69*(1), 98–106.

Polzer, W., & Hem, J. (1965). The dissolution of kaolinite. *Journal of Geophysical Research*, *70*(24), 6233–6240.

Potter, R. M., & Rossman, G. R. (1977). Desert varnish: The importance of clay minerals. *Science*, *196*(4297), 1446–1448.

Potter, R. M., & Rossman, G. R. (1979). The manganese- and iron-oxide mineralogy of desert varnish. *Chemical Geology*, *25*(1-2), 79–94.

Pourbaix, M. (1974). Atlas of electrochemical equilibria in aqueous solutions. *English transl., National Association of Corrosion Engineers, Houston, TX, U.S.A., Vol. 307.*

Přikryl, R., Lokajiček, T., Svobodová, J., & Weishauptová, Z. (2003). Experimental weathering of marlstone from Předni Kopanina (Czech Republic)—historical building stone of Prague. *Building and Environment*, *38*(9-10), 1163–1171.

Quast, C., Pruesse, E., Yilmaz, P., Gerken, J., Schweer, T., Yarza, P., … Glöckner, F. O. (2012). The SILVA ribosomal RNA gene database project: Improved data processing and web-based tools. *Nucleic acids research*, *41*(D1), D590–D596.

R Core Team and others. (2013). R: A language and environment for statistical computing. *Foundation for Statistical Computing, Vienna, Austria*, *URL: https://www.R-project.org/*.

Rabbachin, L., Pinar, G., Nir, I., Kushmaro, A., Pavan, M. J., Eitenberger, E., … Sterflinger, K. (2022). A multi-analytical approach to infer mineral - microbial interactions applied to petroglyph sites in the Negev Desert of Israel. *Applied Sciences*, *12*(14), 6936.

Ramanaidou, E. R., & Fonteneau, L. C. (2019). Rocky relationships: The petroglyphs of the Murujuga (Burrup Peninsula and Dampier Archipelago) in Western Australia. *Australian Journal of Earth Sciences*, *66*(5), 671–698.

Ramanaidou, E. R., Walton, G., & Winchester, D. (2017). Extreme weathering experiment on the Burrup Peninsula / Murujuga weathered gabbros and granophyres. *CSIRO Publishing*, *EP172193*. (URL: https://www.der.wa.gov.au/images/documents/our-work/consultation/Burrup-Rock-Art/Extreme-Weathering-Burrup-Report-2017-.pdf, Accessed: 2024-08-19)

Reis, S., Grennfelt, P., Klimont, Z., Amann, M., ApSimon, H., Hettelingh, J.-P., … Williams, M. (2012). From acid rain to climate change. *Science*, *338*(6111), 1153–1154.

Santos, S. P., Yang, Y., Rosa, M. T. G., Rodrigues, M. A. A., De La Tour, C. B., Sommer, S., … Romão, C. V. (2019). The interplay between Mn and Fe in Deinococcus radiodurans triggers cellular protection during paraquat-induced oxidative stress. *Scientific Reports*, *9*(1), 17217.

Sanyal, S. K., Etschmann, B., Hore, S. B., Shuster, J., & Brugger, J. (2024). Microbial adaptations and biogeochemical cycling of uranium in polymetallic tailings. *Journal of Hazardous Materials*, *465*, 133334.

Schwertmann, U. (1991). Solubility and dissolution of iron oxides. *Plant and soil*, *130*, 1–25.

Sesana, E., Gagnon, A. S., Ciantelli, C., Cassar, J., & Hughes, J. J. (2021). Climate change impacts on cultural heritage: A literature review. *Wiley Interdisciplinary Reviews: Climate Change*, *12*(4), e710.

Shannon, C. E. (1948). A mathematical theory of communication. *The Bell system technical journal*, *27*(3), 379–423.

Simpson, E. (1949). Measurement of Diversity. *Nature*, *163*, 688.

Sitzia, F., Lisci, C., & Mirao, J. (2021). Accelerate ageing on building stone materials by simulating daily, seasonal thermo-hygrometric conditions and solar radiation of Csa Mediterranean climate. *Construction and Building Materials*, *266*, 121009.

Smith, B. W., Black, J. L., Hoerle, S., Ferland, M. A., Diffey, S. M., Neumann, J. T., & Geisler, T. (2022). The impact of industrial pollution on the rock art of Murujuga, Western Australia. *Rock Art Research: The Journal of the Australian Rock Art Research Association (AURA)*, *39*(1), 3–14.

Sulzbach, M., & Geisler, T. (2024). The Replacement of Celestine ($SrSO_4$) by Strontianite ($SrCO_3$) in Aqueous Solution Studied In Situ and in Real Time Using Fluid-Cell Raman Spectroscopy. *Minerals*, *14*(2), 164.

Sun, H., Xu, G., Zhan, H., Chen, H., Sun, Z., Tian, B., & Hua, Y. (2010). Identification and evaluation of the role of the manganese efflux protein in Deinococcus radiodurans. *BMC microbiology*, *10*, 1–8.

Tebo, B. M., Johnson, H. A., McCarthy, J. K., & Templeton, A. S. (2005). Geomicrobiology of manganese (II) oxidation. *TRENDS in Microbiology*, *13*(9), 421–428.

Tidblad, J., Kucera, V., Ferm, M., Kreislova, K., Brüggerhoff, S., Doytchinov, S., . . . Karmanova, N. (2012). Effects of air pollution on materials and cultural heritage: ICP materials celebrates 25 years of research. *International Journal of Corrosion*, *2012*(1), 496321.

Tukey, J. W. (1949). Comparing individual means in the analysis of variance. *Biometrics*, 99–114.

UNESCO. (2020). Murujuga Cultural Landscape. *https://whc.unesco.org/en/tentativelists/6445*. (Accessed: 2024-12-21, UNESCO is the United Nations Educational, Scientific and Cultural Organization)

Unterwurzacher, M., & Mirwald, P. W. (2008). Initial stages of carbonate weathering: Climate chamber studies under realistic pollution conditions. *Environmental geology*, *56*, 507–519.

Veth, P., Bradshaw, E., Gara, T., Hall, N., Haydock, P., & Kendrick, P. (1993). Burrup Peninsula Aboriginal heritage project. *Unpublished report to the Department of Conservation and Land Management.*

Vinnicombe, P. (2002). Petroglyphs of the Dampier Archipelago: Background to development and descriptive analysis. *Rock Art Research: The Journal of the Australian Rock Art Research Association (AURA)*, *19*(1), 3–27.

Wayne, D. M., Diaz, T. A., Fairhurst, R. J., Orndorff, R. L., & Pete, D. V. (2006). Direct major- and trace-element analyses of rock varnish by high resolution laser ablation inductively-coupled plasma mass spectrometry (LA-ICPMS). *Applied Geochemistry*, *21*(8), 1410–1431.

Weather Underground. (2023). Weather History for YPKA. *https://www.wunderground.com/history/daily/au/gap-ridge/YPKA/date/2011-3-5*. (Accessed: 2024-10-21)

Weiss Technik. (2021). Technische Beschreibung ClimeEvent C/180/70a/3 . *Weiss Technik manual.*

Wickham, H. (2016). *Data analysis.* Springer.

Wingate, M. (1997). Ion microprobe geochronology of baddeleyite and the use of mafic dyke swarms in testing Precambrian continental reconstructions. *(PhD thesis). Australian National University.*

Woodside. (2019). North West Shelf Project Extension: Environmental Review Document EPA Assessment No. 2186, EPBC 2018/8335, Revision 1 - December 2019. *https://www.epa.wa.gov.au/sites/default/files/PER_documentation2/NWSProject Extension-EnvironmentalReviewDocument.pdf*. (Accessed: 2024-08-19)

Wright, B. J. (1974). Dampier Archipelago Aboriginal sites. *Unpublished report for incorporation into the Pilbara Study Report, W.A. Museum, Perth.*

Xu, X., Li, Y., Li, Y., Lu, A., Qiao, R., Liu, K., … Wang, C. (2019). Characteristics of desert varnish from nanometer to micrometer scale: A photo-oxidation model on its formation. *Chemical Geology*, *522*, 55–70.

Yang, L., Nadeau, K., Grinberg, P., Brophy, C., Gedara, I. P., Meija, P., … McRae, G. (2015). SLRS-6: River water certified reference material for trace metals and other constituents. *Ottawa: National Research Council Canada*, *10*.

Yang, L., & Steefel, C. I. (2008). Kaolinite dissolution and precipitation kinetics at 22 C and pH 4. *Geochimica et Cosmochimica Acta*, *72*(1), 99–116.

Yara Pilbara. (2017). Baseline Air Quality Monitoring Report 2016-2017. *Yara Pilbara Nitrates Pty Ltd.*

Yara Pilbara. (2018). Ambient Air Quality Monitoring Report 2017-2018. *https://www.yara.com.au/siteassets/about-yara/reports/air-quality-monitoring-reports/650-200-rep-sec-0004.pdf/*. (Accessed: 2024-08-19)

Yara Pilbara. (2019). Ambient Air Quality Monitoring Report 2018-2019. *https://www.yara.com.au/siteassets/about-yara/reports/air-quality-monitoring-reports/650-200-rep-sec-0006.pdf/*. (Accessed: 2024-08-19)

Yara Pilbara. (2020). Ambient Air Quality Monitoring Report 2019-2020. *https://www.yara.com.au/siteassets/about-yara/reports/air-quality-monitoring-reports/650-200-rep-sec-0007.pdf/*. (Accessed: 2024-08-19)

Yara Pilbara. (2021). Ambient Air Quality Monitoring Report 2020-2021. *https://www.yara.com.au/siteassets/about-yara/reports/air-quality-monitoring-reports/650-200-rep-sec-0008.pdf/*. (Accessed: 2024-08-19)

Yara Pilbara. (2022). Ambient Air Quality Monitoring Report 2021-2022. *https://www.yara.com.au/siteassets/about-yara/reports/air-quality-monitoring-reports/650-200-rep-sec-0009.pdf/*. (Accessed: 2024-08-19)

Zhang, H., Xu, Z., Chen, D., Hu, B., Zhou, Q., Chen, S., … Zhang, C. (2021). Adsorption mechanism of water molecules on hematite (1 0 4) surface and the hydration microstructure. *Applied Surface Science*, *550*, 149328.

Appendix

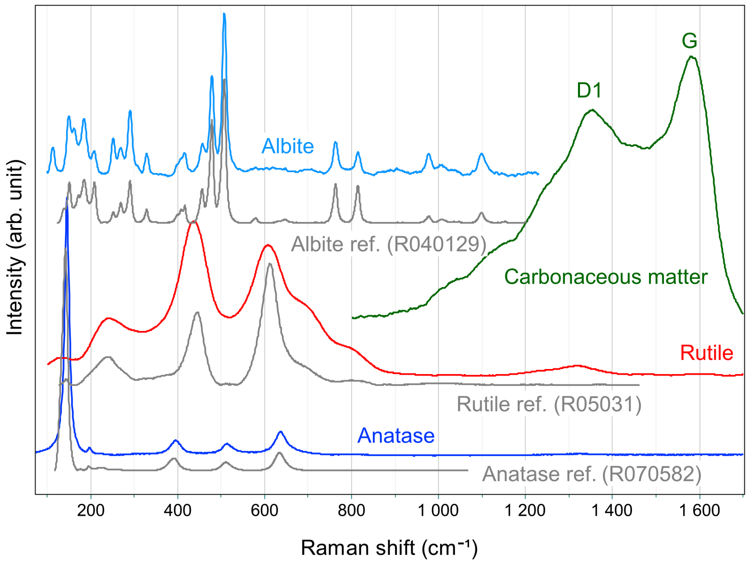

Figure A1: Representative Raman spectra from anatase, rutile, albite, and carbonaceous matter, characterized by two broad bands labelled D1 and G (see Neumann et al., 2022). The reference spectra were taken from the RRuff Raman database (Lafuente et al., 2015).

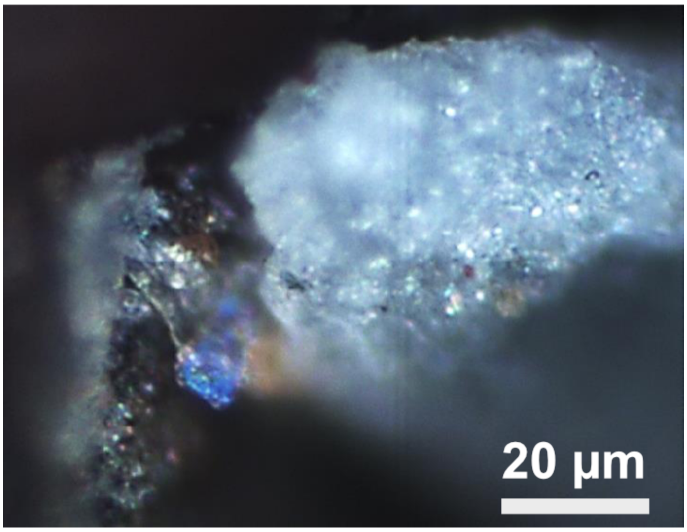

Figure A2: Image taken with the optical microscope of the used Raman spectrometer showing an area of white grains that were identified as albite on the piece of granophyre from which the samples SR1 and NR1 were cut.

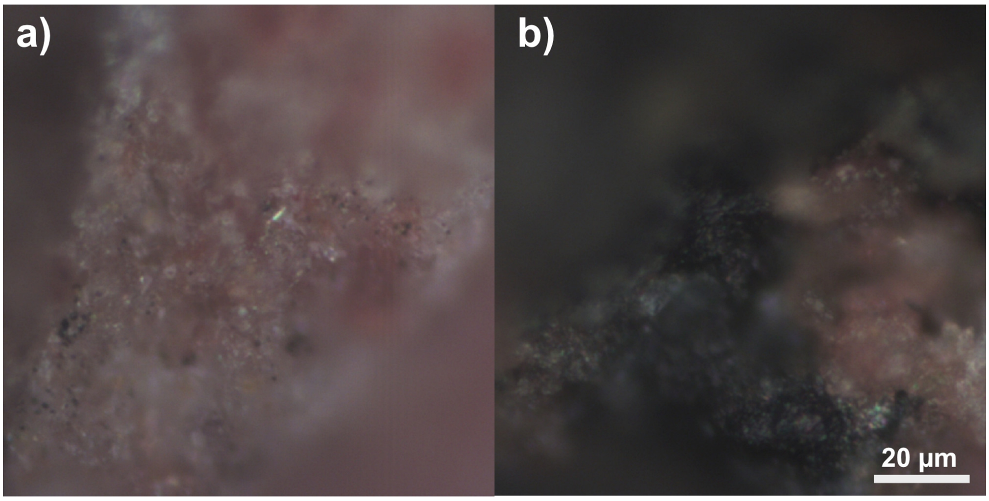

Figure A3: Images taken with the optical microscope of the used Raman spectrometer showing (a) an area of orange varnish on a granophyre sample (NR3) and (b) an area of black varnish on a gabbro sample (NA2). In both images the nano-crystalline structure is visible with a mixture of black, red, and white crystals that are highly likely birnessite, hematite, and kaolinite crystals, respectively.

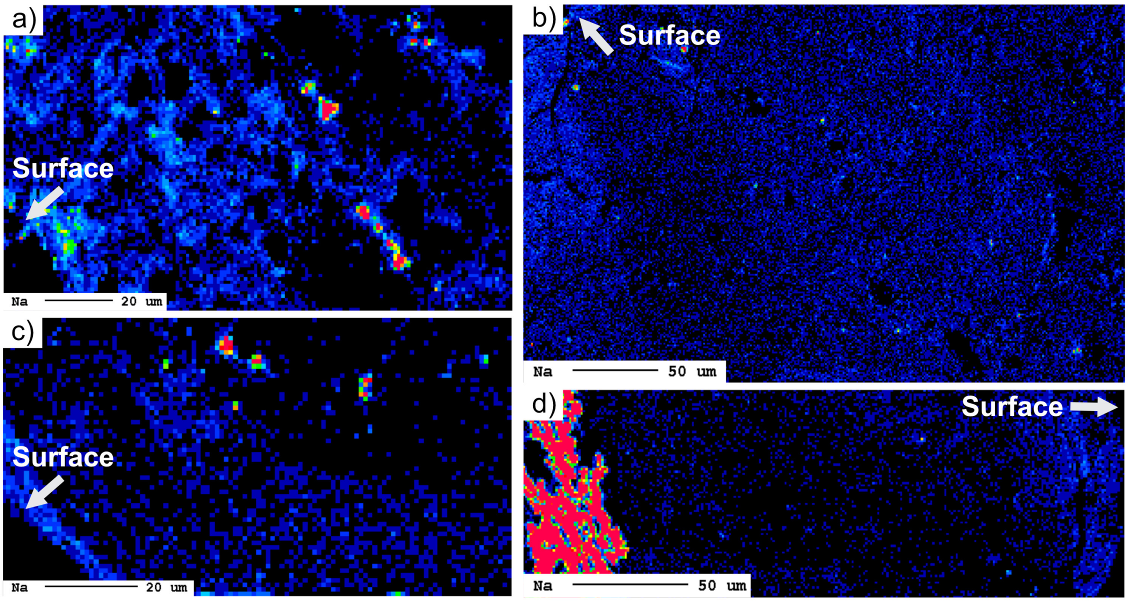

Figure A4: Element distribution maps for Na of the analysed thin sections from gabbro sample (a) NA1 and granophyre samples (b) NR1 and(c) NR2, as well as (d) from the granophyre sample collected in 1994 by Robert Bednarik.

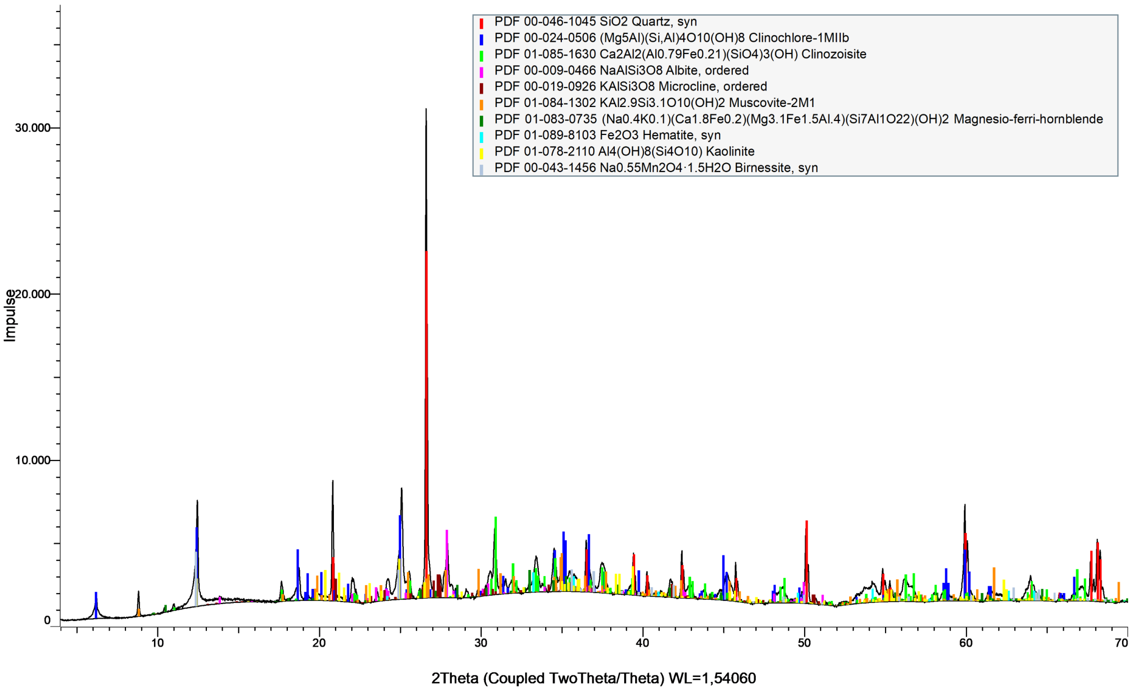

Figure A5: XRD data of the gabbro powder sample containing rock varnish and parts of the underlying weathered rind analysed using EVA (Bruker AXS, 2024a).

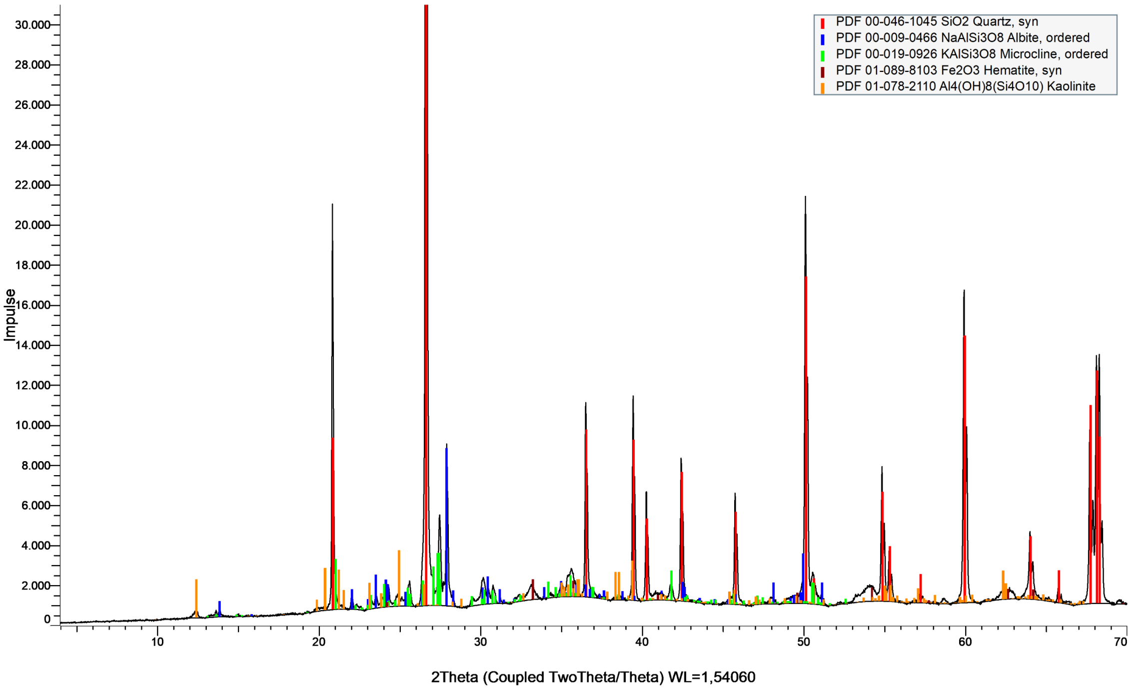

Figure A6: XRD data of the granophyre powder sample containing rock varnish and parts of the underlying weathered rind analysed using EVA (Bruker AXS, 2024a).

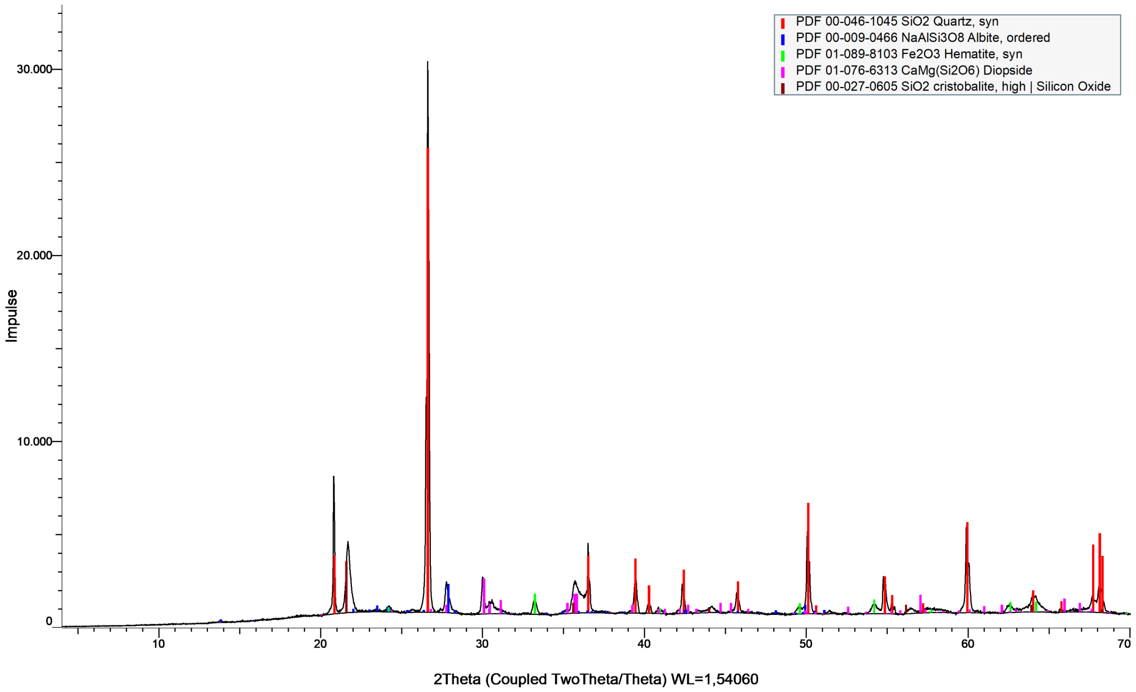

Figure A7: XRD data of the collected residue from the tank used for the climate chamber experiment on the neutral weathering side analysed using (Bruker AXS, 2024a).

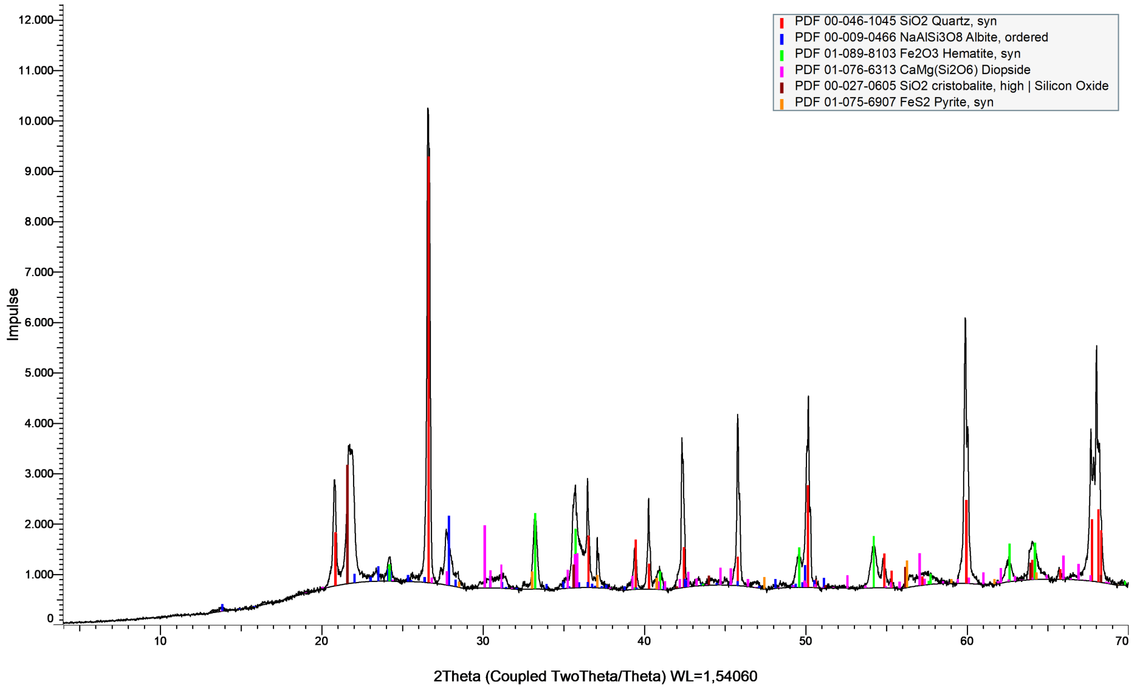

Figure A8: XRD data of the collected residue from the tank used for the climate chamber experiment on the acidic weathering side analysed using (Bruker AXS, 2024a).

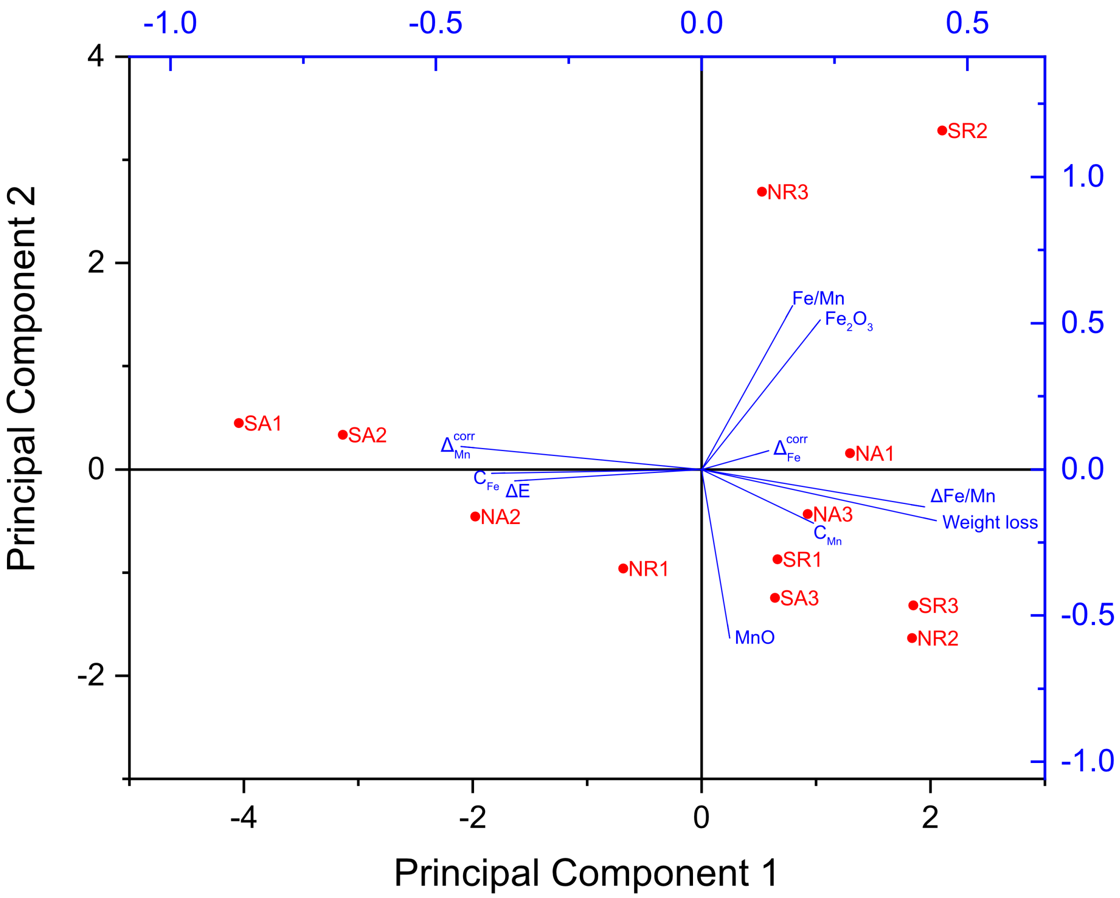

Figure A9: PCA of the results acquired after the end of the weathering experiment. Only the parameters related to Fe and Mn, as well as the colour change (ΔE) and loss of weight are displayed. These include the measured Fe and Mn concentrations on the sample surfaces before the start of the weathering experiment (Fe_2O_3 & MnO), the percentage changes in Fe and Mn concentrations compared to pre-weathering measurements ($\Delta_{\mathrm{Fe}}^{\mathrm{corr}}$ & $\Delta_{\mathrm{Mn}}^{\mathrm{corr}}$), the concentrations of Fe and Mn in the collected rainwater samples (C_{Fe} & C_{Mn}), and the Fe-Mn ratio (Fe/Mn), as well as its change (ΔFe/Mn). All used rock samples are shown as red dots. Samples with a 'S' as first letter were weathered at pH 5.0 and samples with a 'N' as first letter were weathered at pH 7. A second letter 'A' indicates gabbro samples and a second letter 'R' indicates granophyre samples.

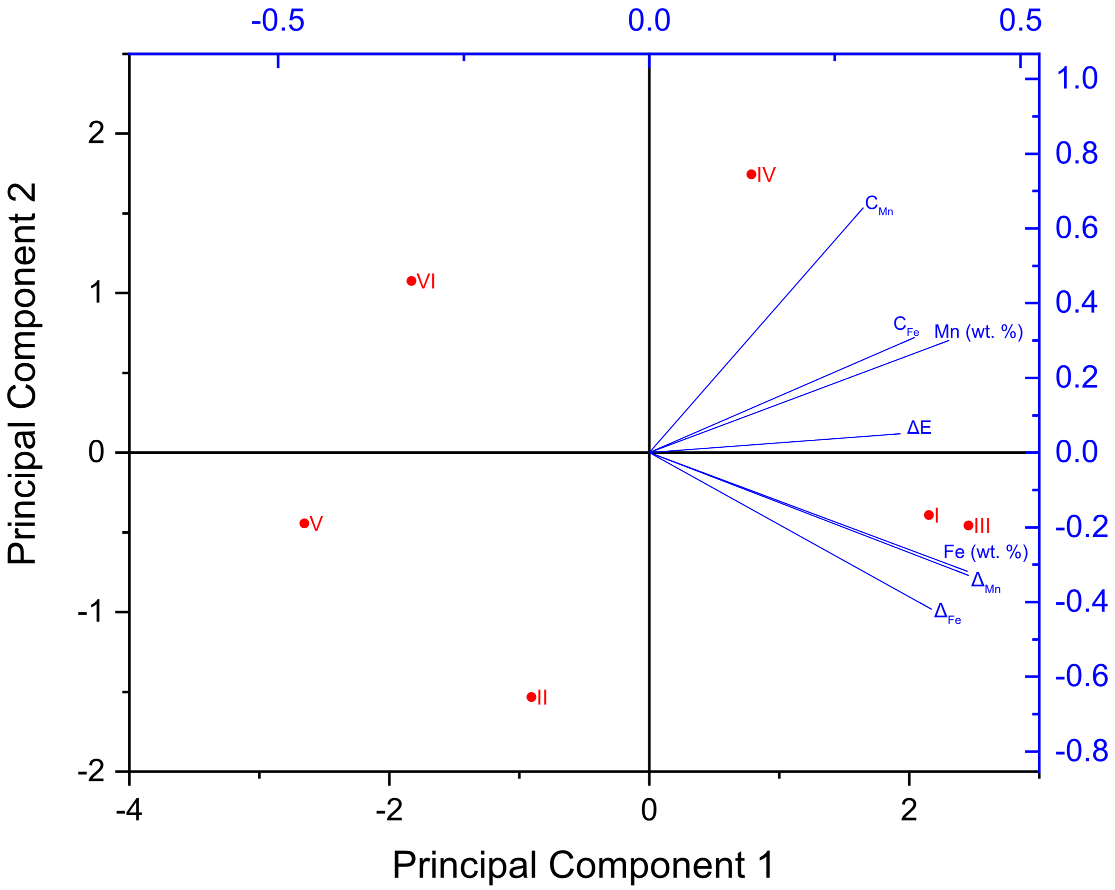

Figure A10: PCA of the results acquired after the end of the irrigation experiments. Only the parameters related to Fe and Mn, as well as the colour change (ΔE) are displayed. These include the measured concentrations of Fe and Mn on the surface (Fe % Mn (wt. %)), the percentage changes in Fe and Mn concentrations compared to pre-weathering measurements (Δ_{Fe} & Δ_{Mn}), and the sum of the Fe and Mn concentrations in the collected rainwater samples (C_{Fe} & C_{Mn}). All used rock samples are shown as red dots with (I-III) gabbro and (IV-VI) granophyre samples.

Table A1: ΔE values of all samples weathered in the climate chamber, as well as the reference samples, at each measurement step. All errors (95 %) are within ± 0.06.

Time (d)	**5**	**15**	**35**	**60**	**90**	**120**	**180**	**240**	**300**	**360**
NA1	0.20	1.09	1.35	1.36	1.51	1.53	1.62	1.61	1.52	1.52
NA2	0.59	0.88	0.91	0.93	0.56	0.56	0.35	0.37	0.34	0.70
NA3	0.53	1.17	1.26	1.25	1.35	1.23	1.28	1.26	1.23	1.20
NR1	1.64	2.93	3.77	3.76	4.24	4.20	4.23	4.11	4.23	4.20
NR2	0.65	0.69	0.68	0.70	0.83	0.57	0.53	0.64	0.49	0.47
NR3	0.79	1.05	1.22	1.25	1.36	1.24	1.41	1.38	1.25	1.23
SA1	1.70	2.13	2.31	2.12	3.37	3.21	3.67	4.33	4.90	5.42
SA2	0.92	0.83	0.81	1.36	3.05	2.80	3.55	4.16	4.39	4.82
SA3	0.44	1.13	1.12	1.14	1.10	1.08	1.23	1.32	1.22	1.18
SR1	0.65	3.48	3.78	3.85	3.97	3.78	3.80	3.86	3.89	3.86
SR2	0.57	0.68	0.77	0.53	1.03	0.95	1.06	1.02	1.06	0.97
SR3	1.08	1.50	1.64	1.67	1.92	1.79	1.84	1.83	1.69	1.62
RA1	0.14	0.08	0.07	0.13	0.21	0.14	0.15	0.31	0.26	0.20
RA2	0.24	0.09	0.12	0.13	0.12	0.23	0.32	0.51	0.43	0.14
RR1	0.28	0.30	0.40	0.51	0.51	0.55	0.53	0.41	0.66	0.81
RR2	0.14	0.14	0.10	0.33	0.17	0.23	0.26	0.20	0.17	0.41

Table A2: Step-to-step ΔE values of all samples weathered in the climate chamber, as well as the reference samples, at each measurement step. All errors (95 %) are within ± 0.06.

Time (d)	**5**	**15**	**35**	**60**	**90**	**120**	**180**	**240**	**300**	**360**
NA1	0.20	0.94	0.27	0.04	0.18	0.13	0.27	0.03	0.34	0.08
NA2	0.59	0.42	0.25	0.14	0.72	0.42	0.25	0.49	0.18	0.39
NA3	0.53	0.65	0.15	0.03	0.12	0.25	0.07	0.09	0.17	0.04
NR1	1.64	1.37	1.00	0.24	0.58	0.20	0.12	0.12	0.43	0.40
NR2	0.65	0.21	0.15	0.25	0.13	0.27	0.09	0.12	0.25	0.20
NR3	0.79	0.31	0.33	0.06	0.15	0.14	0.18	0.08	0.23	0.16
SA1	1.70	0.64	0.70	0.23	1.56	0.21	0.66	0.71	0.63	0.53
SA2	0.92	0.67	0.41	0.82	1.69	0.30	0.77	0.61	0.27	0.43
SA3	0.44	0.71	0.09	0.10	0.08	0.17	0.21	0.09	0.23	0.08
SR1	0.65	3.07	0.51	0.10	0.16	0.22	0.11	0.09	0.22	0.11
SR2	0.57	0.22	0.10	0.26	0.52	0.15	0.20	0.04	0.08	0.12
SR3	0.44	0.71	0.09	0.10	0.08	0.17	0.21	0.09	0.23	0.08
RA1	0.14	0.10	0.06	0.10	0.10	0.19	0.06	0.21	0.20	0.07
RA2	0.24	0.16	0.21	0.15	0.25	0.13	0.21	0.22	0.15	0.30
RR1	0.28	0.07	0.14	0.13	0.16	0.18	0.26	0.13	0.28	0.32
RR2	0.14	0.11	0.14	0.24	0.20	0.09	0.17	0.07	0.03	0.28

Table A3: Results of the Tukey HSD (Tukey, 1949) test for the analysed DNA samples from the gabbro rocks.

Comparison	Difference	Lower Bound	Upper Bound	Adjusted p-value
Acidic-d5 vs Acidic-d360	-0.20	-0.95	0.54	0.88
Day 0 vs Acidic-d360	1.69	0.94	2.43	0.00
Neutral-d360 vs Acidic-d360	0.82	0.08	1.57	0.03
Neutral-d5 vs Acidic-d360	1.09	0.25	1.92	0.01
Day 0 vs Acidic-d5	1.89	1.15	2.64	0.00
Neutral-d360 vs Acidic-d5	1.03	0.28	1.77	0.01
Neutral-d5 vs Acidic-d5	1.29	0.46	2.12	0.00
Neutral-d360 vs Day 0	-0.86	-1.61	-0.12	0.02
Neutral-d5 vs Day 0	-0.60	-1.43	0.23	0.19
Neutral-d5 vs Neutral-d360	0.26	-0.57	1.10	0.82

Table A4: Results of the Tukey HSD (Tukey, 1949) test for the analysed DNA samples from the granophyre rocks.

Comparison	Difference	Lower Bound	Upper Bound	Adjusted p-value
Acidic-d5 vs Acidic-d360	0.42	-2.09	2.93	0.90
d0-ASW vs Acidic-d360	-0.52	-3.77	2.72	0.99
Day 0 vs Acidic-d360	0.05	-2.47	2.56	1.00
Neutral-d360 vs Acidic-d360	0.04	-2.47	2.55	1.00
Neutral-d5 vs Acidic-d360	0.36	-1.85	2.58	0.99
d0-ASW vs Acidic-d5	-0.95	-4.50	2.60	0.91
Day 0 vs Acidic-d5	-0.38	-3.28	2.52	1.00
Neutral-d360 vs Acidic-d5	-0.38	-3.28	2.52	1.00
Neutral-d5 vs Acidic-d5	-0.06	-2.71	2.59	1.00
Day 0 vs d0-ASW	0.57	-2.98	4.12	0.99
Neutral-d360 vs d0-ASW	0.57	-2.99	4.12	0.99
Neutral-d5 vs d0-ASW	0.89	-2.46	4.24	0.92
Neutral-d360 vs Day 0	0.00	-2.90	2.90	1.00
Neutral-d5 vs Day 0	0.32	-2.33	2.97	1.00
Neutral-d5 vs Neutral-d360	0.32	-2.32	2.97	1.00